Effects of Upstream Roughness on Turbulent Flow over a Forward-Facing Step

By

Ali Nematollahi

A Thesis submitted to the Faculty of Graduate Studies of

The University of Manitoba

in partial fulfillment of the requirements of the degree of

DOCTOR OF PHILOSOPHY

Department of Mechanical Engineering

University of Manitoba

Winnipeg, Manitoba

Canada

ABSTRACT

This study reports an experimental investigation of the effects of upstream roughness on the turbulent boundary layer over a forward-facing step. Two types of upstream roughness were investigated, including a transitionally rough 16-grit sandpaper ($k_s^+ \approx 69$) and fully rough staggered cubes ($k_s^+ \approx 500$). A two-dimensional two-component time-resolved particle image velocimetry (2D-2C TR-PIV) method was used to measure the mean velocities, Reynolds stresses, temporal auto-correlations and frequency spectra of the flow field to quantify the influence of upstream roughness on the downstream evolution of the turbulence over the step. The results indicate that upstream roughness decreased the vortex shedding frequency. Roughness also decreased the reattachment length by enhancing the streamwise turbulence intensity level, reducing the magnitude of backflow and suppressing the vortex shedding frequency in comparison to the smooth wall. In the recirculation region, upstream roughness reduced the mean streamwise velocity only in the outer layer. The Reynolds stresses remained relatively unchanged by the sandpaper roughness but were significantly modified by the cube roughness. Downstream of the leading edge, the staggered cubes increased the streamwise Reynolds stress both near the wall and outside the shear layer but decreased the wall-normal Reynolds stress and Reynolds shear stress within the shear layer. These modifications are inversely proportional to distance in the recirculation region. The life times of the streamwise and wall-normal velocity fluctuations increase with streamwise distance and are much longer in the redevelopment region than in the recirculation region.

The quadrant decomposition method and joint probability density functions were used to characterize the dominant motions producing the Reynolds shear stress. Multi-point statistics such as two-point spatial and space-time correlations were used to quantify the impact of large upstream roughness on the downstream evolution of the separated shear layer over the step.

ACKNOWLEDGMENTS

I would like to acknowledge the invaluable guidance and support of my supervisor, Professor Mark Francis Tachie. I would also like to thank my Ph.D. committee, Professor David Kuhn and Professor Tricia Stadnyk for their valuable feedback and constructive suggestions throughout my research program. I am thankful to the external examiner, Professor Greg Kopp for his critical review and suggestions. I would also like to acknowledge the essential technological support provided by Mr. Dave Tataryn, Mr. Irwin Penner, and Mr. Daniel Rossong as well as the valuable knowledge and safety training from Mr. Paul Krueger. The financial support of the Natural Sciences and Engineering Research Council (NSERC) of Canada and the University of Manitoba is gratefully acknowledged. Last but not least, my deepest gratitude goes to my parents (Ahmad and Fatemeh) and my siblings (Azadeh, Maryam, and Mohammad) for their unconditional love and support. Finally, sincere gratitude to all my friends who contributed to the success of my program.

DEDICATION

This thesis is dedicated to my father (Ahmad), who was the best teacher in my life and passed away by the end of my program unfortunately, my lovely mother (Fatemeh), my sisters (Azadeh and Maryam), and my brother (Mohammad) for their love, patience, and supports throughout this program.

TABLE OF CONTENTS

LIST OF TABLES

LIST OF FIGURES

NOMENCLATURE

a	proper orthogonal decomposition temporal coefficient
B	logarithmic law constant
C_f	skin friction coefficient
d_l	light sheet thickness (mm)
d_s	width of the Airy function (mm)
d_t	particle image diameter (mm)
D_a	aperture diameter (mm)
d_p	Diameter of tracer particles (μm)
E_{uu}	frequency spectra of the streamwise velocity fluctuations (m^2/s)
E_{vv}	frequency spectra of the wall-normal velocity fluctuations (m^2/s)
f	frequency (Hz)
f'	focal length (mm)
$f^{\#}$	f-number of camera lens
Fr_H	Froude number ($\frac{U_o}{\sqrt{gH_u}}$)
$F_{u'}$	flatness factor of the streamwise fluctuating velocity
$F_{v'}$	flatness factor of the wall-normal fluctuating velocity
g	acceleration due to gravity (m/s^2)
G	Clauser shape parameter
h	step height (mm)
h_r	upstream bubble height (mm)
H	shape factor
H_q	hyperbolic hole size

H_r	downstream bubble height (*mm*)
H_u	upstream water depth (*mm*)
I	particle image intensity
k	roughness height (*mm*)
k_s	equivalent sand grain roughness height (*mm*)
K	turbulent kinetic energy (m^2/s^2)
K'	acceleration parameter
l_r	upstream reattachment length (*mm*)
L	step length (*mm*)
L_r	downstream reattachment length (*mm*)
M	Magnification factor (*pixel*/*mm*)
N	number of samples
N_Q	space fraction
p	instantaneous pressure (*Pa*)
p'	fluctuating pressure (*Pa*)
P	mean pressure (*Pa*)
P_x	streamwise distance between cubes (*mm*)
P_z	spanwise distance between cubes (*mm*)
Q	contribution to the Reynolds shear stress from a given quadrant (m^2/s^2)
R_{uu}	temporal auto-correlations of the streamwise velocity fluctuations
R_{vv}	temporal auto-correlations of the wall-normal velocity fluctuations
Re_h	Reynolds number based on the step height ($U_e h/\nu$)
Re_θ	Reynolds number based on momentum thickness ($U_e \theta/\nu$)

S_k	Stokes number (τ_p/τ_f)
S_Q	detector function
St_o	Strouhal number (fh/U_e)
$S_{u'}$	skewness factor of the streamwise fluctuating velocity
$S_{v'}$	skewness factor of the wall-normal fluctuating velocity
t	time (s)
T	total sampling time (s)
T^u	integral time scale of the streamwise velocity fluctuations (s)
T^v	integral time scale of the wall-normal velocity fluctuations (s)
u	streamwise instantaneous velocity (m/s)
u'	streamwise fluctuating velocity (m/s)
u_{rms}	streamwise turbulent intensity (m/s)
$\langle u'^2 \rangle$	streamwise Reynolds normal stresses (m^2/s^2)
$\langle u'^2 v' \rangle$	wall-normal transport of u'^2 (m^3/s^3)
$-\langle u'v' \rangle$	Reynolds shear stress (m^2/s^2)
$\langle u'v'^2 \rangle$	wall-normal transport of Reynolds shear stress (m^3/s^3)
U	streamwise mean velocity (m/s)
U_c	convection velocity (m/s)
U_e	local maximum mean velocity (m/s)
U_o	freestream velocity at the upstream location (m/s)
U_s	slip velocity (m/s)
U_τ	friction velocity (m/s)
v	wall-normal instantaneous velocity (m/s)

v'	wall-normal fluctuating velocity (*m/s*)
v_{rms}	wall-normal turbulent intensity (*m/s*)
$\langle v'^2 \rangle$	wall-normal Reynolds normal stresses (m^2/s^2)
$\langle v'^3 \rangle$	wall-normal transport of v'^2 (m^3/s^3)
V	wall-normal mean velocity (*m/s*)
W	step width (*mm*)
x	streamwise coordinate (*mm*)
y	wall-normal coordinate (*mm*)
y_0	virtual origin (*mm*)
z	spanwise coordinate (*mm*)

Greek

ε	dissipation of turbulent kinetic energy (m^2/s^3)
ψ	stream function
δ	turbulent boundary layer thickness (*mm*)
δ^*	displacement thickness (*mm*)
δ_ω	vorticity thickness (*mm*)
κ	von Kármán constant
ν	kinematic viscosity (m^2/s)
ν_t	eddy viscosity (m^2/s)
θ	momentum thickness (*mm*)
ρ	density (kg/m^3)
ρ_p	density of seeding particles (m^3/s)

ρ_f	density of working fluid (m^3/s)
ΔB	roughness shift
ΔU_{max}	velocity defect (m/s)
λ	wavelength of laser light source (nm)
λ_{ci}	unsigned swirling strength (s^{-1})
λ_z	streak spacing (mm)
Λ_{ci}	signed swirling strength (s^{-1})
Π	Coles wake parameter
τ_f	fluid characteristic time scale (s)
τ_p	particle response time (s)
τ_w	wall shear stress (N/m^2)
ω_z	mean vorticity (s^{-1})
ω'_z	fluctuating vorticity (s^{-1})

Superscript

$(\ )^+$	normalization by inner variables

Acronyms

APG	adverse pressure gradient
AR	aspect ratio (W/h, L/h)
BFS	backward-facing step
BR	blockage ratio (h/H_u)
CB	cube
CCD	charge-coupled device

CFD	computational fluid dynamics
CMOS	complementary metal-oxide semiconductor
DMD	dynamic mode decomposition
DNS	direct numerical simulation
FFS	forward-facing step
FFT	fast Fourier transform
HWA	hotwire anemometry
IA	PIV interrogation area
LDV	laser Doppler velocimetry
LES	large eddy simulation
LSE	linear stochastic estimation
Nd:YAG	Neodymium: Yttrium Aluminum Garnet
Nd:YLF	Neodymium: Yttrium Lithium Fluoride
PIV	particle image velocimetry
POD	proper orthogonal decomposition
PTU	programmable timing unit
RANS	Reynolds-averaged Navier-Stokes
SM	smooth
SP	sandpaper
TKE	turbulent kinetic energy
TR	time-resolved
ZPG	zero pressure gradient

Copyright Notice

1. With permission from Cambridge University Press for using Figure 2.2:

   Adrian, R. J., Meinhart, C. D., and Tomkins, C. D., "Vortex organization in the outer region of the turbulent boundary layer", Journal of Fluid Mechanics, 422, 1–54, 2000.

2. With permission from Cambridge University Press for using Figure 2.3:

   Kiya, M., and Sasaki, K., "Structure of large-scale vortices and unsteady reverse flow in the reattaching zone of a turbulent separation bubble", Journal of Fluid Mechanics, 154, 463-491, 1985.

3. With permission from American Society of Mechanical Engineers for using Figure 2.3:

   Sasaki, K., and Kiya, M., "Three-dimensional vortex structure in a leading-edge separation bubble at moderate Reynolds numbers", Journal of Fluids Engineering, 113(3), 405-410, 1991.

CHAPTER 1

INTRODUCTION AND OBJECTIVES

1.1 Introduction

Separated and reattached turbulent flows are of enduring interest in fluids engineering as they play a key role in the transport and mixing of fluids. The prototypical configuration for studying flow separation and reattachment is the forward-facing step (FFS). The FFS has many useful engineering applications, including manufacturing discontinuities on aircraft wings, swept wing applications, and air-flow over electronic chips. Apart from its technological applications, forward-facing steps in the form of blunt obstacles are also frequently observed in environmental flows such as bridge piers, large buildings and other man-made obstacles. Unsteady flow phenomena such as induced vortex fields, cross-winds and recirculation near these obstructions often lead to undesirable effects such as structural vibrations and noise. The FFS flow is frequently used as a benchmark for testing turbulence models. Nevertheless, our understanding of important features such as shear layer separation and reattachment and the physical mechanisms responsible for its unsteadiness is still incomplete.

The flow of an incompressible turbulent boundary layer over a FFS produces dynamic behaviour of considerable complexity. Figure 1.1 shows a schematic of a two-dimensional forward-facing step in an open channel. The Cartesian coordinate system is aligned with the mid-span of the test section; the x-coordinate points in the streamwise direction, while the y-coordinate is aligned with the wall-normal direction; $x = 0$ is at the leading edge of the step and $y = 0$ is on the upstream wall. The upstream boundary layer of freestream velocity U_o and thickness, δ, approaches the FFS of height, h. The adverse pressure gradient induced by the step causes the flow to separate upstream of the front face of the step. At a certain height, say, h_r, from the bottom wall the flow reattaches on the front face of the step. The flow separates again at the leading edge of the step and reattaches on the top face of the step after some distance, say, L_r, hereinafter referred to as the reattachment length. The maximum height of the recirculation region on the top face of the step is denoted by H_r. The region beyond the reattachment point is referred to as the redevelopment region. Several interesting phenomena documented in the literature on the FFS flow are worth noting, including a relatively more stable upstream separation bubble (Moss and Baker 1980; Leclercq et al. 2001), flapping motion of the shear layer leading to unsteady reattachment (Largeau and Moniere 2007), substantially higher wall-pressure fluctuations on the step compared to the upstream boundary layer (Efimstov et al. 1999; Camussi et al. 2008), and the bifurcation of the shear layer in the redevelopment region (Bradshaw and Wong 1972; Kiya and Sasaki 1983).

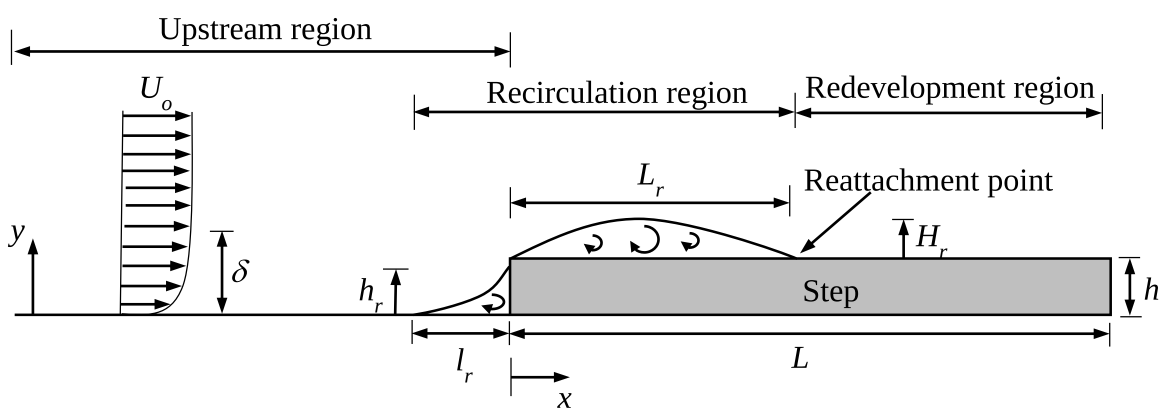

Figure 1.1: Schematic of a forward-facing step (FFS).

A consistent trend in the archival literature on FFS flows is that most earlier investigations have been conducted primarily over smooth walls. Although these studies have helped to enhance our understanding of the flow, questions still remain as to the exact impact of the step on the flow characteristics and the evolution of the large-scale structures in the presence of wall roughness. Roughness effects on the zero pressure gradient (ZPG) turbulent boundary layer have been known for decades, which include increase in the wall shear stress, and enhancements of the turbulence intensities and Reynolds stresses, by margins that may extend well into the outer parts of the boundary layer. In practice, roughness effects may arise due to either the presence of manufacturing defects on test surfaces, corrosion, abrasion or deposition of small particles over time. Due to the high sensitivity of the FFS flow to on-coming disturbances (Wilhelm et al. 2003; Marino and Luchini 2009), the imposition of additional perturbations such as wall roughness can lead to an extremely more complex fluid dynamics structure when compared to the canonical smooth wall flow.

1.2 Governing Equations

The governing equations are the continuity, momentum, and transport equations for Reynolds shear stress and turbulence kinetic energy (TKE) for an incompressible turbulent boundary layer:

Continuity

$$\frac{\partial U_i}{\partial x_i} = 0 \tag{1.1}$$

Momentum

$$\frac{\partial U_i}{\partial t} + U_j \frac{\partial U_i}{\partial x_j} = -\frac{1}{\rho}\frac{\partial P}{\partial x_i} + \frac{\partial}{\partial x_j}\left(\nu \frac{\partial U_i}{\partial x_j} - \langle u'_i u'_j \rangle\right) \tag{1.2}$$

Reynolds stress transport equation

$$\begin{aligned}\frac{\partial \langle u'_i u'_j \rangle}{\partial t} + U_k \frac{\partial \langle u'_i u'_j \rangle}{\partial x_k} &= -\left(\langle u'_i u'_k \rangle \frac{\partial U_j}{\partial x_k} + \langle u'_j u'_k \rangle \frac{\partial U_i}{\partial x_k}\right) + \langle \frac{p'}{\rho}\left(\frac{\partial u'_i}{\partial x_j} + \frac{\partial u'_j}{\partial x_i}\right) \rangle - 2\nu \langle \frac{\partial u'_i}{\partial x_k}\frac{\partial u'_j}{\partial x_k} \rangle \\ &+ \frac{\partial}{\partial x_k}\left(\nu \frac{\partial \langle u'_i u'_j \rangle}{\partial x_k} - \langle u'_i u'_j u'_k \rangle - \langle \frac{p'}{\rho}\left[u'_i \delta_{jk} + u'_j \delta_{ik}\right] \rangle\right)\end{aligned} \tag{1.3}$$

TKE transport equation

$$\frac{\partial K}{\partial t} + U_j \frac{\partial K}{\partial x_j} = -\langle u'_i u'_j \rangle \frac{\partial U_i}{\partial x_j} + \frac{\partial}{\partial x_j}\left(\nu \frac{\partial K}{\partial x_j} - \langle K u'_j \rangle - \langle \frac{p'}{\rho} u'_j \rangle\right) - \nu \langle \left(\frac{\partial u'_i}{\partial x_j} + \frac{\partial u'_j}{\partial x_i}\right)\frac{\partial u'_i}{\partial x_j} \rangle \tag{1.4}$$

In equations (1.1) – (1.4), the flow variables are defined as follows: x is the coordinate direction, U and u' are the mean and fluctuation velocities, respectively; ρ is the density; P and p' are the mean thermodynamic (static) and fluctuating pressures of the fluid, respectively; K is the turbulent kinetic energy and ν is the kinematic viscosity. The second-order terms $\langle u'_i u'_j \rangle$ correspond to the Reynolds stresses.

1.3 Research Motivation and Objectives

Despite their prevalence in practical engineering and environmental applications roughness effects on forward-facing step flows have received very little attention within the near-wall turbulence research community when compared to the smooth-wall counterpart. Also, although the characteristics of the flow over smooth forward-facing steps have been extensively investigated, majority of investigators reported only the one-dimensional profiles of the mean velocity and Reynolds stresses. Mostly, this is due to the limitations of the measurement methodologies employed. Single-point measurement methods such as hot-wire anemometry (HWA) and laser Doppler velocimetry (LDV) are incapable of measuring the often-sought multi-point statistics such as two-point correlations directly without using approximations. On the other hand, most flows studied with whole-field laser techniques such as particle image velocimetry (PIV) were not sufficiently resolved in order to fully capture the relevant turbulence scales. Thus, experimental data is still lacking on the impact of the FFS on the evolution of the turbulent structures in the flow. Nevertheless, with the development of high-repetition rate lasers and high-speed cameras in recent times, high-resolution PIV methods such as time-resolved particle image velocimetry (TR-PIV) are now available. The high spatial and temporal resolutions provided by TR-PIV facilitates the accurate measurement of the turbulence scales and multi-point statistics such as two-point spatial correlations and two-point space-time correlations. To date, no experimental study has applied the time-resolved PIV technique to characterize the turbulent boundary layer over a forward-facing step with upstream wall roughness.

In order to fulfill the need for well-qualified, temporally resolved rough-wall turbulent boundary layer experiments over forward-facing steps, a 2D-2C TR-PIV system is applied. The overarching goal of this study is to systematically investigate the effects of upstream wall roughness on the spatio-temporal characteristics of separating and reattaching turbulent flows over a forward-facing step with upstream deep turbulent boundary layer using both single- and multi-point statistics. This will advance physical understanding of the statistical properties and coherent structures of separating-reattaching turbulent flows. Also, the results obtained from this study can provide comprehensive benchmark datasets that will help Computational Fluid Dynamics (CFD) experts to improve the accuracy of turbulence models and validate their numerical results.

1.4 Organization of the Report

The remainder of this report is organized as follows: In Chapter 2, a detailed literature survey is presented on previous investigations of separated and reattached turbulent flows over FFS with and without wall roughness. The coherent structures in the unperturbed boundary layer and in separated shear layers are reviewed and their methods of eduction explored in this investigation are presented. Chapter 3 describes the experimental setup and test conditions investigated. Details of the time-resolved PIV (TR-PIV) system used are explained as well as the operating principle of TR-PIV. In Chapter 4, the results of the investigation are presented and discussed. Finally, in Chapter 5, the experimental results are summarized and the major conclusions are highlighted along with future work.

CHAPTER 2

LITERATURE REVIEW

2.1 Overview

In this chapter, previous studies of separated and reattached turbulent flows such as those produced by two-dimensional blunt flat plates and forward-facing steps (FFS) immersed in a turbulent boundary layer are reviewed. Turbulent shear flows with separation and reattachment have long been the subject of many investigations. In calculations of flow past obstacles, the obstacle is treated as a source of perturbation to the initial turbulent boundary layer. According to Bradshaw and Wong (1972), the strength of perturbation can be classified based on the relative height, h/δ of the obstacle as: weak perturbation ($h/\delta << 1$), where the velocity and length scales of the flow are altered without significant change in the stress ratios and two-point correlations; strong perturbation ($h/\delta \approx 1$), where the turbulence structure is significantly modified; and overwhelming perturbation ($h/\delta >> 1$), where the boundary layer changes into a free shear layer such as wake or mixing layer.

Separated and reattached turbulent flows investigated in the past employed a variety of techniques to characterize the state of the boundary layer. These include computational fluid dynamics (CFD) and experimental methods. CFD methods such as Reynolds-averaged Navier-Stokes (RANS) modelling, direct numerical simulation (DNS) and large-eddy simulation (LES) rely on the processing power of the computer to solve the discretized differential equations of fluid motion. Nevertheless, the complex nature of the flow in the recirculation and recovery regions renders the numerical prediction of practical flows a formidable task. This makes it more attractive to use experimental techniques such as hotwire anemometry (HWA), laser Doppler velocimetry (LDV) and particle image velocimetry (PIV) for turbulence measurements. Being pointwise measurement techniques, HWA and LDV are more challenging for examining the large-scale coherence of the velocity fluctuations. On the other hand, time-resolved PIV (TR-PIV) does not only capture the large-scale coherent structures but also provides instantaneous two-dimensional velocity fields for visualizing the temporal evolution of the instantaneous structures.

2.2 Characteristics of the Upstream Turbulent Boundary Layer

In an open channel, the flow upstream of a forward-facing step can be treated as a zero pressure gradient (ZPG) turbulent boundary layer (e.g., Tachie et al. 2001). Classical theory of wall turbulence indicates that the boundary layer is a composite fluid layer consisting of both inner and outer regions (e.g., von Karman 1930; Prandtl 1932). For a ZPG turbulent boundary layer flow, as shown schematically in Figure 2.1, the inner layer corresponds to the region extending from the wall ($y/\delta = 0$) to $y/\delta \approx 0.1$ (Pope 2000), where δ is the boundary layer thickness defined as the distance from the wall to the wall-normal location where the local mean streamwise velocity (U) is 99% of the freestream velocity (U_e). In the inner region, the turbulence dynamics depend on the friction velocity, U_τ, the fluid kinematic viscosity, ν, and the distance from the wall (y). This leads to two types of scaling parameters for the inner region, namely, the viscous length scale, ν/U_τ, and the viscous time scale, ν/U_τ^2. In the outer layer ($y^+ = 50$ to $y = \delta$), the wall acts to retard the fluid velocity in a manner that is independent of viscosity, but depends on the distance from the wall, and the outer variables δ and U_e. At sufficiently high Reynolds numbers, an overlap region exists between the outer and inner layers. For smooth boundary layers, the overlap region follows a logarithmic mean velocity profile of the form (Millikan 1938),

$$U^+ = (1/\kappa)\, ln(y^+) + B \tag{2.1}$$

where κ is the von Kármán constant, B is an additive constant, and subscript ($^+$) denotes normalization by inner variables. Typical values of the constants κ and B are $\kappa = 0.41$ and $B = 5.0$; or $\kappa = 0.40$ and $B = 5.5$.

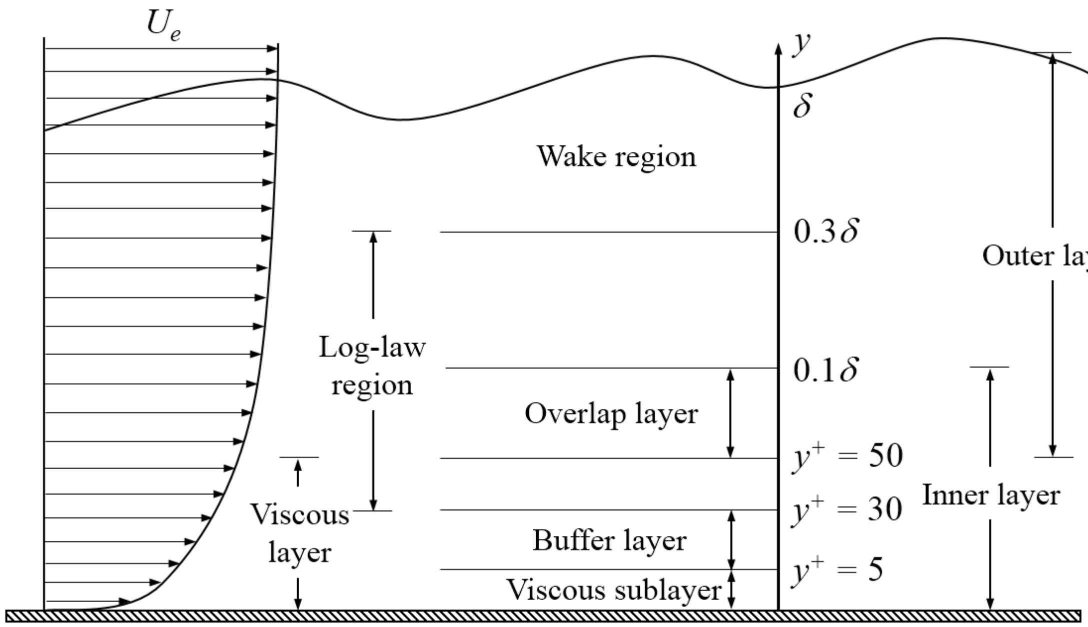

Figure 2.1: Schematic of the various regions of the turbulent boundary layer.

To account for the wake of the boundary layer, Coles (1956) proposed a logarithmic profile of the form

$$U^+ = (1/\kappa)\, ln(y^+) + B + (\Pi/\kappa)w(y/\delta) \tag{2.2}$$

where Π is the wake parameter and the function $w(y/\delta)$ is called the "law of the wake". For ZPG turbulent boundary layers, the wake parameter was found to be approximately 0.55 (Coles 1956). The drag characteristics of the wall or boundary are quantified by the wall shear stress, $\tau_w = \rho U_\tau^2$, and the skin friction coefficient, $C_f = 2(U_\tau/U_e)^2$. The skin friction coefficient is an asymptotic function of Reynolds number that increases with freestream turbulence level and surface roughness for a given Reynolds number. Typical values of $C_f \approx 0.0044 – 0.0048$ have been observed for low Reynolds numbers turbulent boundary layers over smooth walls (e.g., Tachie et al. 2000).

The turbulent boundary layer is often characterized by one or more integral parameters. These include the displacement thickness, momentum thickness and shape factor. The displacement thickness (δ^*), defined as the wall-normal distance by which the wall will have to be moved into the fluid for a potential flow at velocity, U_e to have the same mass flux over the wall, is given by

$$\delta^* = \int_0^\delta \left(1 - \frac{U}{U_e}\right) dy \tag{2.3}$$

Similarly, the momentum thickness (θ), which measures the momentum flux deficit occurring in the boundary layer due to fluid retardation, is given by

$$\theta = \int_0^\delta \left(\frac{U}{U_e}\right)\left(1 - \frac{U}{U_e}\right) dy \tag{2.4}$$

The ratio of the displacement thickness to the momentum thickness gives the dimensionless boundary layer shape factor:

$$H = \frac{\delta^*}{\theta} \tag{2.5}$$

When the flow is subjected to a roughness perturbation, the effect of roughness is to disrupt the turbulence structure, especially in the immediate vicinity of the wall. It has been suggested that when the roughness height k is large enough, the modifications in the mean velocity, turbulence intensities and Reynolds stresses can extend well into the outer layer (e.g., Krogstad et al. 1992; Jimenez 1998). Based on data compiled from studies over a wide range of roughness elements, Jimenez (1998) concluded that smooth and rough wall boundary layers will exhibit outer layer similarity if the relative roughness height k/δ is less than 2%.

The effect of the wall roughness is to enhance the drag characteristics and produce a shift in the logarithmic mean streamwise velocity profile. By accounting for the roughness shift and enhanced wake generated by roughness elements, the rough wall mean velocity profile satisfies the log law of the form

$$U^+ = (1/\kappa)ln(y + y_o)^+ + B - \Delta B^+ + (\Pi/\kappa)w(y/\delta) \qquad (2.6)$$

where ΔB^+ is the roughness shift, y is the wall-normal distance measured from the roughness crest and y_o is the virtual origin, which depends on the size and distribution of the roughness elements. The roughness Reynolds number, $k^+ = kU_\tau/\nu$, is an important parameter in rough-wall flows. When k^+ is small, the flow is said to be hydraulically smooth, whereupon the turbulent eddies shed by the roughness are completely damped by viscous forces. As k^+ increases, the flow becomes transitionally rough so that viscosity no longer completely affects the eddies produced by the roughness elements. The net effect is that both form drag by the roughness elements and viscous drag contribute to the overall skin friction. At sufficiently large k^+, the flow becomes fully rough and form drag is the pre-dominant contributor to skin friction. A more universal roughness parameter termed the equivalent sand grain roughness height, k_s, was also proposed by Nikuradse (1933) for comparing roughness effects among different flows, irrespective of roughness type. The scale k_s represents the size of monodisperse sand grains to provide the same skin friction coefficient as the roughness under investigation. Using the dimensionless equivalent sand grain roughness height, k_s^+, Schlichting (1979) suggested that the flow may be considered hydraulically smooth for $0 < k_s^+ \leq 5$, transitionally rough for $5 < k_s^+ < 70$, and fully rough for $k_s^+ \geq 70$.

2.3 Turbulent Structures

The archival literature presents overwhelming evidence of the existence of orderly structures in wall bounded flows. These orderly structures, also known as coherent structures, are believed to be responsible for providing the generation and self-sustaining mechanism for turbulence. According to Robinson (1991), a coherent structure may be defined as a three-dimensional region of the flow field over which at least one fundamental flow variable (e.g., velocity, density or pressure) exhibits significant correlation with itself or with another variable with length and time scales larger than the smallest scales of turbulence scales. Evidence of their presence in turbulence, for instance, is seen in the non-zero Reynolds shear stress and the two-point spatial and temporal correlations. Various coherent structures have been identified in ZPG turbulent boundary layers, both near the wall and in the outer region. In the wall region, these include low-speed streaks with average spanwise spacing of approximately 100 wall units (Kline et al. 1967), bursts (Grass 1971), sweeps and ejections (Corino and Brodkey 1969); quasi-streamwise vortices (Blackwelder and Eckelmann 1979), Q2/Q4 events (Wallace et al. 1972), where Q2 and Q4 are the second and fourth quadrants of the plane of instantaneous streamwise and wall-normal velocity fluctuations, and inclined shear layers (Brown and Thomas 1977; Schoppa and Hussain 2000). In the outer layer, the flow has been observed to be dominated by loop-like vortices (Head and Bandyopadhyay 1981), large-scale three-dimensional bulges (Blackwelder and Kaplan 1976) as well as structures called very large scale motions, VLSM (Kim and Adrian 1999).

Figure 2.2 shows a schematic of a loop-like vortex (called a hairpin vortex) often observed in the logarithmic region. A number of studies have emphasized the hairpin vortex as a simple coherent structure that explains many of the features observed in ZPG turbulent boundary layers. Theodorsen (1952) described the hairpin vortex as either a symmetric or asymmetric hairpin-like structure, and its modified versions, that produce regions of intense negative streamwise and positive wall-normal velocity fluctuations under a clearly defined spanwise rotating vortex head. In Figure 2.2, the vortex consists of a spanwise rotating head that is connected to the neck inclined at an angle of approximately 45° to the streamwise (x) direction. The neck is connected to the two quasi-streamwise legs which correspond to the counter-rotating quasi-streamwise vortices near the wall. Also, due to their rotation, the quasi-streamwise vortices induce regions of negative streamwise velocity fluctuations corresponding to the low-speed streaks near the wall. The vortex head when viewed in the streamwise wall-normal plane corresponds to spanwise vortex cores whose vorticity are of the same sign as the mean shear. Such spanwise vortices are called prograde vortices, while those with vorticity opposite to that of the mean shear are called retrograde vortices (Wu and Christensen 2006). The spanwise rotation of the vortex head induces Q2 motions or ejections underneath the vortex, accompanied by opposite Q4 or sweep-type motions outboard of the vortex. The opposing Q2 and Q4 motions form an inclined shear layer, and where their velocity fluctuation magnitudes cancel out creates a region of stagnation flow along the edge of the shear layer.

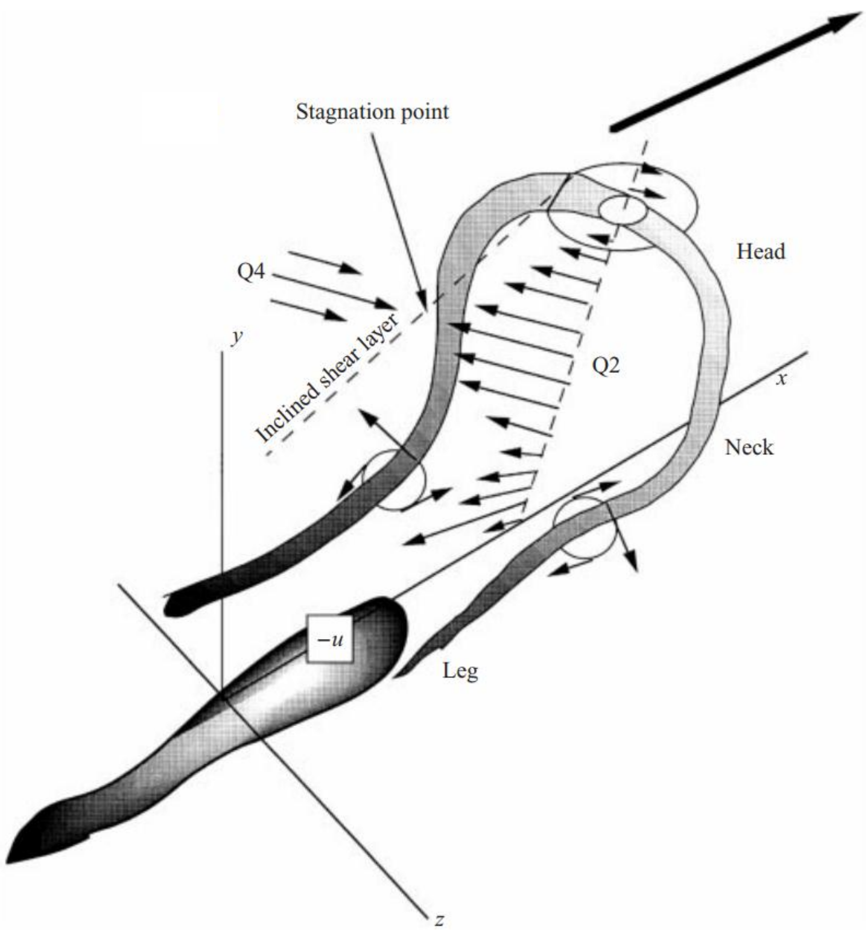

Figure 2.2: Schematic of a hairpin vortex taken from Adrian et al. (2000).

Although a considerable amount of work has already been done to understand the dynamics of coherent structures very little is known of the details of the turbulence structure in the separated shear layer. It is widely accepted that the behaviour of large-scale vortices in the recirculation region does not only affect the flow properties in the separation bubble but in the developing region also. Figure 2.3 shows a schematic of the coherent structures observed in the recirculation region.

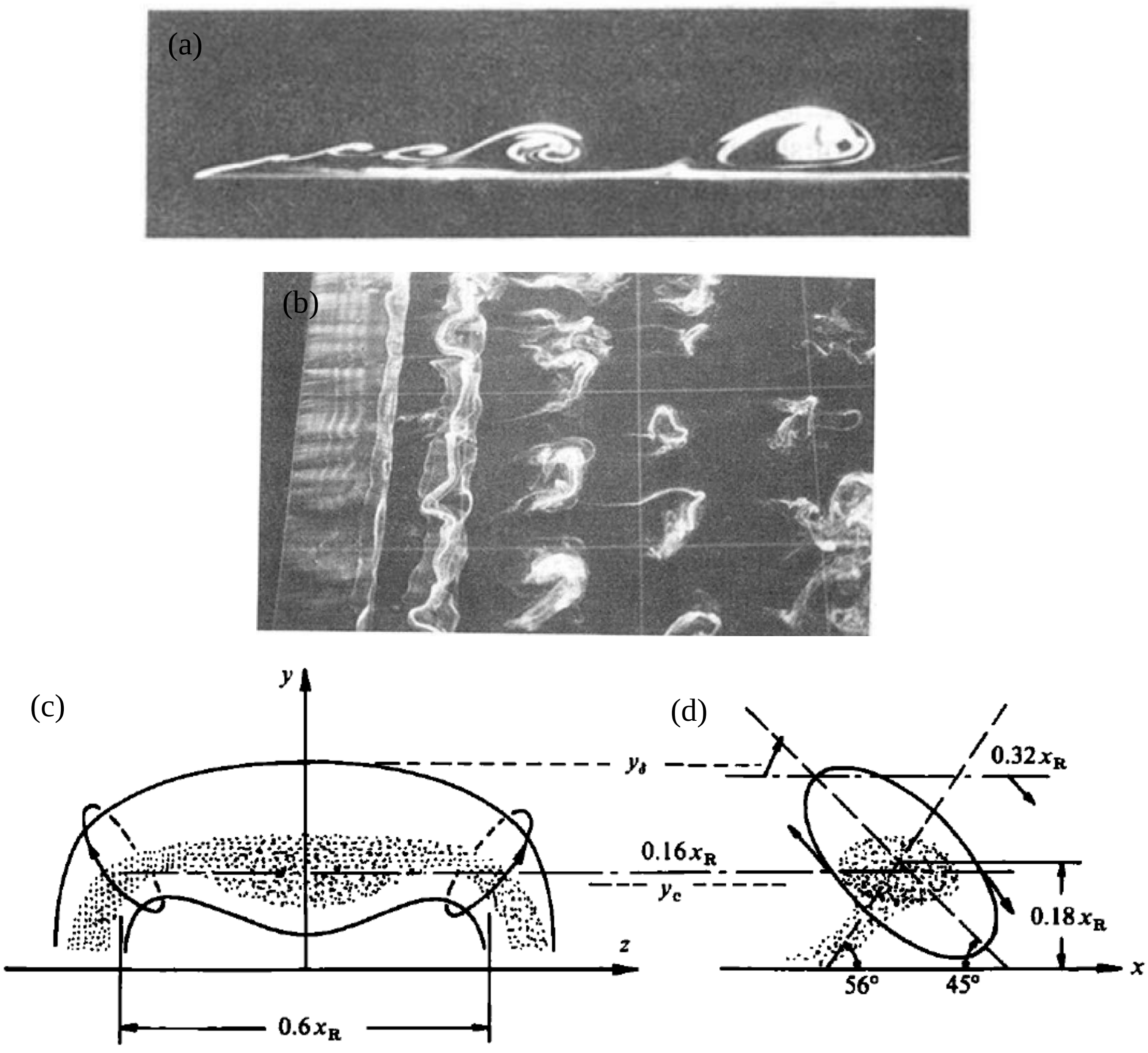

Figure 2.3: Schematic of the large-scale vortices in a separated and reattaching shear layer taken from Sasaki and Kiya (1991) and Kiya and Sasaki (1985), (a) side view of the vortices; (b) top view of the vortices; (c) structure in the *y*-*z* plane and (d) structure in the *x*-*y* plane.

It has been shown (e.g., Hillier and Cherry 1981; Eaton and Johnston 1981) that the turbulence in the separated shear layer is characterized by three-dimensional low-frequency unsteady motions responsible for the production and transport of the Reynolds stresses in the shear layer. As shown in Figure 2.3, in the streamwise-wall-normal plane, these structures bear a resemblance to the hairpin vortex and have been attributed to the large-scale vortices shed upstream of the reattaching zone. Measurements presented by Kiya and Sasaki (1983, 1985) suggest that the large-scale vortices are shed from the separation bubble at a frequency of approximately $f = 0.6U_e/L_r$, where U_e is the freestream velocity of the approach boundary layer. Kiya and Sasaki (1983) reported that the vortices are propagated at a convection velocity of approximately $0.5U_e$, and exhibit an average streamwise separation of roughly $(0.6 – 0.8)L_r$. Spanwise flow visualizations by Dimaczek et al. (1989) revealed the existence of streaky structures, separated by a spanwise spacing of $\lambda_z/h \approx 0.4 – 0.8$. They observed that these were the same quasi-streamwise legs of the hairpin vortices emanating from the upstream region and propagating over the step. Experimental and numerical results presented by Pollard et al. (1996) over a range of Reynolds numbers ($1500 \leq Re_h \leq 6700$) indicate that the spanwise spacing of the streaks is a function of Reynolds number. At the lowest Reynolds number (1500) the streak spacing λ_z/h was found to be approximately 2.8, while at the highest Reynolds number it was found to be approximately 0.95. The authors concluded that the streaks and their spacing in the recirculation region are the result of a mechanism triggered by Taylor-Gortler like vortices.

2.4 Review of Separated and Reattached Turbulent Flows over Smooth FFS

Numerous studies have been conducted in the past to quantify the impact of different flow conditions on the mean flow and turbulence characteristics over smooth FFS and rectangular blunt plates. Some previous experiments and numerical simulations that are of interest to the present investigation are summarized in Table 2.1. The summary includes the type of measurement or computational technique used, Reynolds number, relative step height and quantities reported.

Table 2.1: Summary of previous studies on FFS (smooth and rough)

Author(s)	**Technique**	h (*mm*)	Re_h	*BR* (h/H_u)	δ/h	L_r/h	**Analysed Parameters**
Awasthi et al. (2014)	HWA (CC-Air)	3.65– 58.3	6640 – 213000 (Smooth)	0.002 – 0.033	1.62 – 26.02	2.3 – 4.2	U, P
Sherry et al. (2010)	Planar PIV (OC-Water)	15 – 45	1400 – 19000 (Smooth)	0.018 – 0.056	0.83 – 2.5	1.9 – 3.8	$U, \langle u'^2 \rangle, -\langle u'v' \rangle$
Camussi et al. (2008)	TR-PIV (CC-Water)	20	8800 – 26300 (Smooth)	—	5.0	1.5 – 2.1	U, P
Largeau and Moriniere (2007)	HWA and PIV (CC-Air)	30 – 50	76900 – 128200 (Smooth)	0.06 – 0.11	0.3	3.50 – 3.75	$U, \langle u'^2 \rangle, \langle v'^2 \rangle, -\langle u'v' \rangle, P$
Leclercq et al. (2001)	LDA (CC-Air)	50	170000 (Smooth)	0.14	0.7	3.2	U, K, P
Rifat et al. (2016)	Planar PIV (OC-Water)	12.0	3400 (Rough)	0.2	4.7	1.26 – 1.78	$U, V, -\langle u'v' \rangle$
Shao and Agelin-Chaab (2016)	Planar PIV (CC-Water)	6.0	1600 – 4800 (Rough)	0.11	4.7	1.2 – 2.3	$U, V, \langle u'^2 \rangle, \langle v'^2 \rangle, -\langle u'v' \rangle$, *POD*
Essel and Tachie (2015)	Planar PIV (CC-Water)	9.0	4940 – 8650 (Rough)	0.2	3.0 – 3.8	1.3 – 2.2	$U, K, \langle u'^2 \rangle, \langle v'^2 \rangle, -\langle u'v' \rangle$, *quadrant analysis, two-point correlation*
Essel et al. (2015)	Planar PIV (CC-Water)	9.0	2040 – 9130 (Rough)	0.2	2.4 – 3.7	1.2 – 2.2	$U, V, \omega, \langle u'^2 \rangle, \langle v'^2 \rangle, -\langle u'v' \rangle, K$
Ren and Wu (2011)	Planar PIV (CC-Air)	6.35	3450 (Rough)	0.01	8.0	1.17	$U, \langle u'^2 \rangle, \langle v'^2 \rangle, -\langle u'v' \rangle$, *quadrant analysis, PDF*

OC: Open channel; CC: Closed channel

Due to the presence of two separation regions in these cases the flow structure is relatively more complex compared to other separated and reattached turbulent flows. Previous studies have revealed that the upstream recirculation region of a forward-facing step contains near stagnant fluid and is not significantly affected by changes in Reynolds number (Moss and Baker 1980; Leclercq et al. 2001; Addad et al. 2003). These studies have shown that generally, the flow separates from the upstream wall at a distance of approximately $0.8-1.5h$ upstream of the step and reattaches to the front face of the step at approximately $0.6-0.65h$. Previous observations on the salient features of the turbulent boundary over a smooth FFS are summarized in the next sections.

2.4.1 The Flow in the Recirculation Region

The primary recirculation region, the simplest characteristic scale of which is the reattachment length, is known to exhibit strong low Reynolds number effects. Ota et al. (1981), for instance, observed a seven-fold increase in length of a recirculation bubble transitioning from laminar to turbulent flow over a flat plate as the Reynolds number increased from 40 to 2000. At higher Reynolds numbers, the length of the separation bubble remained either relatively invariant with Reynolds number or decrease with increasing Reynolds number, depending on the nose angle of the leading edge of the plate. The Reynolds number invariance of the recirculation region at large Reynolds numbers was also observed by Hillier and Cherry (1981) for a blunt flat plate ($34000 < Re_h < 80000$), and by Djilali and Gratshore (1991) using a flat plate at zero incidence to the fluid stream. In the latter study, the Reynolds number was varied from 25000 to 90000.

The effects of turbulent intensity on the recirculation bubble have also been examined in detail. Hillier and Cherry (1981) investigated the effects of turbulent intensity in flow over a two-dimensional blunt flat plate. The turbulent intensity, which was varied from 1.0% to 6.5%, was produced using different grids. It was shown that the size of the separation bubble contracted substantially (about 40%) as the turbulent intensity increased. The effect of turbulent intensity on the reattachment length over a blunt flat plate at Re_h = 26000 was also investigated by Kiya and Sasaki (1983). The freestream turbulence was generated using circular rods of different diameters placed at different locations upstream of the plate. The reattachment length decreased by about 70% as the turbulent intensity was increased from 1.0% to 7.0%. Similar results were obtained by Nakamura and Ozono (1987) for the separated boundary layer over a blunt flat plate, noting that the effect of turbulence intensity was monotonic irrespective of Reynolds number. Yaghoubi and Mahmoodi (2004) performed a series of experiments over a finite blunt flat plate at Re_h = 15000 to 36000 to investigate the separated shear layer for different values of the plate length to thickness ratio (L/h = 4.0 to 9.0). A reduction in reattachment length of approximately 25% was observed when the turbulent intensity level increased from 0.56% to 1.8%, but it was found that the effect diminishes as the plate length to thickness ratio decreases. In a more recent study conducted by Shu and Lia, (2017), the effect of turbulent intensity generated by diverse types of grids was investigated. It was shown that the size of the recirculation bubble over the blunt flat plate decreased from 3.42h to 1.26h when the turbulent intensity was increased from 3.1% to 9.5%.

Sherry et al. (2010) investigated the effects of Reynolds number, Re_h and relative boundary layer thickness, δ/h on FFS in a turbulent boundary layer. The Reynolds number was varied from 1400 to 19000 and δ/h varied in the range $0.83 \leq \delta/h \leq 2.5$. It was found that for a given value of δ/h, the reattachment length increased linearly with Reynolds number up to 8500, beyond which no significant change in reattachment length was observed. It was reported that when $\delta/h < 1$, the influence of the upstream boundary layer is minimal. Conversely, when $\delta/h > 1$, the reattachment length is significantly affected by the Reynolds number.

Hattori and Nagano (2010) studied the state of the upstream boundary layer over a FFS using DNS. The Reynolds number varied from Re_h = 900 to 3000 and δ/h varied from 1.5 to 3. A counter gradient diffusion phenomenon (negative Reynolds shear stress) was observed near the leading edge of the step at the low Reynolds number (Re_h = 900) but this phenomenon vanished at higher Reynolds numbers ($1800 \leq Re_h \leq 3000$). Distributions of the second invariant of the velocity gradient tensor revealed that the flow over the step has finer-scale vortical structures at higher Reynolds numbers than at lower Reynolds numbers. Through a quadrant analysis of the mean Reynolds shear stress it was shown that ejections contributed more to the mean Reynolds stress than sweeps.

2.4.2 Development of the Reattached Boundary Layer

Although there have been many investigations of the separated shear layer over the FFS, only a few studies examined the redevelopment of the boundary layer after reattachment. On the other hand, extensive studies have been conducted in the past on the separation and recovery of the turbulent flow over blunt flat plates (Ruderich and Fernholz 1986; Castro and Epik 1998) and backward-facing steps (Tani et al. 1961; Bradshaw and Wong 1972; Jovic 1993; Song 2000). One key observation reported in the literature is the splitting or bifurcation of the shear layer after reattachment. This results in the deflection of part of the reattached flow back into the recirculation region, while the other part continues downstream (Bradshaw ad Wong 1972). A number of previous investigators including, Tani et al. (1961), Mueller and Robertson (1963), and Coles and Hirst (1969) expressed the view that the mean velocity profile after about 50 step heights ($x/h \approx 50$) recovers to the standard profile and still follows the log law of the wall in the recovery region. However, evidence presented by Bradshaw and Wong (1972) suggests that the outer part of the boundary layer develops much more slowly than the inner region. Castro and Epik (1998) presented the argument that it is not possible for the inner layer, which is dynamically linked to the outer layer, to fully recover while the outer flow is significantly different from that of the standard boundary layer.

In their blunt plate experiment, Ruderich and Fernholz (1986) employed hot-wire and pulsed-wire anemometry to measure the mean velocities, Reynolds stresses and spectra of velocity fluctuations at a Reynolds number of Re_h = 14000. The profiles of the mean streamwise velocity and Reynolds stresses were self-similar in a short region bounding the reattachment point. Results obtained from the pulsed-wire measurements revealed that the logarithmic law of the wall holds neither in the recirculation region nor in a region about half the length of the recirculation downstream from the reattachment point.

Tachie et al. (2001) performed open-channel experiments over a FFS to investigate the redevelopment of the separated and reattached turbulent boundary layer. The Reynolds numbers based on the freestream velocity and water depth were in the range $960 \leq Re_h \leq 1890$. A laser Doppler anemometer (LDA) was used to conduct the flow measurements. It was observed that the mean velocity profiles collapsed onto the corresponding upstream profiles at $x/h \geq 50$, while the integral parameters such as the friction coefficient and shape factor recovered to within 5% of their upstream values. In case of the turbulence field, it was found that even at $x/h \approx 100$, the streamwise turbulence intensity profiles did not collapse on the upstream profiles. Similar results were reported by other investigators of reattached and recovering turbulent flows over BFS (e.g., Yoo et al. 1992; Jovic 1993; Song and Eaton 2004).

Shah and Tachie (2007) performed particle image velocimetry measurements of the mean velocities and Reynolds stresses over a FFS in an open channel. Two step heights were investigated ($\delta/h \approx 8$ and 5), corresponding to two Reynolds numbers of $Re_h \approx 1900$ and 2800. The integral parameters decreased to minimum values at the separation point followed by sharp increases immediately downstream of the step and then levelling off to values slightly higher than upstream. Their results indicate that the mean streamwise velocity relaxes more quickly to the self-similar values than the mean wall-normal velocity. At their last measurement station (x/h = 50), the Reynolds stresses follow the same curve irrespective of δ/h although their magnitudes still exceed the upstream values in the inner region.

Another subject of interest that has received significant research attention is the influence of separation and reattachment on the wall pressure fluctuations (e.g., Farabee and Casarella 1984; Efimtsov et al. 1999; Fiorentini et al. 2006; Camussi et al. 2008; Becker et al. 2010; Awasthi et al. 2014; Scheit et al. 2013). The study of pressure fluctuations is of fundamental importance in aeroacoustics applications because of the sound and vibrations induced by the fluctuations.

Farabee and Casarella (1984) examined the flow characteristics of the turbulent boundary layer (Re_h = 21000) in a FFS flow with relative boundary layer thickness $\delta/h \approx 2.5$. A hot-wire anemometer was used for the velocity measurements while a pressure transducer was used for the fluctuating pressure measurements. Their results indicate that the mean (static) pressure distribution is strongly adverse immediately upstream of the step, highly favourable at the top of the step, and returns rapidly to ZPG conditions further downstream. Distributions of the frequency spectra upstream of the step show high pressure fluctuation levels at least up to 6 step heights as well as rapid variation in pressure fluctuation up to the onset of the secondary separation. Downstream of the step, they found that the maximum value of pressure fluctuations occurs at the reattachment point and that the flow remains highly energized (relatively high p_{rms} values) after reattachment, at least up to 36 step heights. The pressure spectrum downstream of the step is elevated at low and high frequencies as well, indicating the presence of larger structures in the reattachment region.

Efimtsov et al. (1999) conducted an experimental study of wall-pressure fluctuations over a FFS in a wind tunnel. The Reynolds number of the approach flow was in the range $600 \leq Re_h \leq 6400$, while the ratio of the displacement thickness to step height varied between 5 and 100. They found that the pressure fluctuations due to the FFS exceed those on a smooth wall by up to about 30 dB. One-dimensional profiles of the pressure fluctuations at selected upstream locations up to the step revealed a monotonic increase in pressure fluctuations from far upstream down to the step. Frequency spectra of the pressure fluctuations depict that the energy containing range of the pressure spectra is independent of Reynolds number while the spectral density of the dissipation range increases with Reynolds number.

A time-resolved PIV (TR-PIV) method coupled with pressure measurements was used by Fiorentini et al. (2006) to measure the velocities and wall pressure fluctuations over a FFS in an open channel. The Reynolds number of the unperturbed boundary layer ($\delta^*/h \approx 0.5$) varied from 4400 to 26300. Profiles of the pressure fluctuation spectra were used to evaluate the impact of the FFS on the spectral power law regions. They reported that the pressure spectrum exhibits a $-7/3$ power law region that widens for reference locations closer to the leading face of the step, albeit independent of Reynolds number. Over the step, increasingly lower values of the exponent were observed corresponding to a decrease in spectral energy as the flow propagates downstream.

A time-resolved PIV was also used by Camussi et al. (2008) to measure both the spatial and temporal statistics over a FFS in an open channel. For the approach flow, the Reynolds number ranged from 8800 to 26300, while the displacement thickness to step height ratio was kept constant at $\delta^*/h \approx 0.5$. Mean velocity contours and values of the reattachment length suggest that the characteristics of the secondary recirculation region are independent of Reynolds number as was reported by previous investigators (e.g., Bowen and Lindley,1977; Sherry et al. 2010; Essel et al. 2015). It was observed that the reattachment point downstream of the step is strongly unsteady, and corresponds to the location of maximum amplitude of the coefficient of pressure. Distributions of pressure-velocity temporal correlations revealed that downstream of the step, the wall pressure fluctuations have a strong coherence indicative of the large-scale vortical structures in the separated shear layer downstream of the step.

Awasthi et al. (2014) performed velocity and pressure measurements of the turbulent flow over a FFS in a wind tunnel. They used a Pitot tube and a HWA to measure the velocities and pressure transducers to measure to the static pressure. Reynolds number (Re_h) from 6640 to as high as 213000 were investigated for three values of the relative boundary layer thickness ($\delta/h \approx 2$, 7 and 26). Similar to the study of Sherry et al. (2010), two flow regimes were found: the first regime is for $Re_h < 3000$ where L_r is a strong increasing function of Reynolds number, and the second regime is for $Re_h > 3000$ where L_r is independent of Reynolds number. It was found that the increase with Reynolds number is more dramatic at lower values of the relative boundary layer thickness than at higher values. As the boundary layer approached the step, low frequency pressure fluctuations on the wall intensify and become more organized in the spanwise direction. At the secondary separation point, low frequency pressure fluctuations develop a strong spanwise correlation that can exceed their upstream levels by over two orders of magnitude. Over the step, it was observed that the pressure fluctuations were most strongly enhanced at lower frequencies, suggesting more energetic structures in the separated and reattaching shear layer.

2.5 Separated and Reattached Turbulent Flows over FFS with Wall Roughness

Despite their numerous practical applications, roughness effects on separated and reattached turbulent flows over FFS are not extensively documented. Of the handful of studies that investigated roughness effects, only conventional (non-time resolved) PIV systems were used to characterize the flow (e.g., Ren and Wu 2011; Wu and Ren 2013; Essel et al. 2015; Essel and Tachie 2015; Shao and Agelinchaab 2016; Rifat et al. 2016). Ren and Wu (2011), for example, investigated the effects of roughness on separated and reattached flow over a FFS in a wind tunnel. Velocity measurements were performed over smooth and rough steps with a smooth upstream boundary layer at a Reynolds number of Re_h = 3450 and relative boundary layer thickness of δ/h = 8. A 3D and highly irregular topographical roughness replicated from a realistic turbine blade was used to produce the roughness. Their results showed that wall roughness reduced the mean velocities as well as the Reynolds stresses over the step in comparison to the smooth wall. Quadrant analysis revealed that roughness reduced the shear stress contributions from both ejections and sweeps.

Essel et al. (2015) and Essel and Tachie (2015) investigated the effects of upstream roughness and Reynolds number on the reattachment and redevelopment regions of the FFS in a fully developed channel. Sand grain of mean diameter 1.5 mm was used as the upstream roughness. The Reynolds numbers based on the step height and maximum mean streamwise velocity of the approach flow were in the range $2040 \leq Re_h \leq 9130$. It was observed that the mean reattachment length of the primary recirculation region increased with increasing Reynolds number for the smooth wall up to a Reynolds number of approximately 6400; beyond this critical Reynold number it remained constant. Over the rough wall, the mean reattachment length was unaffected by Reynolds number. For the sand grain roughness, the dimensionless equivalent sand grain roughness height k_s^+ varied from 8 to 198. It was observed that at comparable Reynolds numbers, the upstream rough wall reduced the reattachment length by about 40% compared to the smooth wall. It was suggested that the reduction in L_r was not due to the upstream roughness *per se* but could be attributed partly to the reduction in mean velocity and higher turbulence intensity in the shear layer. The turbulent kinetic energy and Reynolds shear stress were independent of the roughness condition in the immediate vicinity of the wall. In the separation bubble, the integral scales were independent of the upstream roughness for reference locations in the inner region, but the size of the scales were enhanced for reference locations further from the wall. In the recovery region, the effect of upstream roughness gradually diminished as the boundary layer developed downstream.

In a more recent investigation, Shao and Agelinchaab (2016) performed measurements over smooth and rough forward-facing steps at three Reynolds numbers (Re_h = 1600, 3200, and 4800) in a fully developed channel. Two roughness conditions were investigated, including sandpaper 24 grit (k_s = 1.7 *mm*) and sandpaper 36 grit (k_s = 1.37 *mm*). It was found that the reattachment length increased with increasing Reynolds number over the smooth wall but decreased with wall roughness at similar Reynolds number. They reported that the profiles of the mean velocity and Reynolds stresses did not attain self-similarity even at 60 step heights downstream of the leading edge of the step.

The impact of upstream roughness produced by a 36-grit sandpaper (k_s^+ = 13) and sand grain roughness (k_s^+ = 176) on the separated and reattached flow over a smooth FFS was investigated by Rifat et al. (2016) in an open channel. It was observed that the upstream roughness increased the turbulent intensity near the wall by about 14% and 35%, respectively for the sandpaper and sand grain roughness conditions in comparison to the smooth-wall case. On the other hand, upstream roughness dampened the physical sizes of the mean velocity and turbulence intensities and reduced the reattachment length on top of the step compared to the smooth wall condition.

2.6 Eduction of Coherent Structures

Several quantitative methods have been developed in the literature for extracting coherent structures from turbulent flows. Most of these are comprehensively discussed in many previous articles, including Hussain (1983) and Adrian et al. (2000). Those explored in this investigation are quadrant decomposition, swirling strength, linear stochastic estimation (LSE), and proper orthogonal decomposition (POD). The mathematical details and the algorithmic implementation of these approaches are discussed next.

2.6.1 Quadrant Decomposition

Quadrant decomposition is used to investigate the relative contributions of the coherent motions to the mean Reynolds shear stress. The method consists of sorting the instantaneous Reynolds shear stress values into the four quadrants of the u'–v' plane based on the signs of u' and v'. The first quadrant (Q1: $u' > 0$ and $v' > 0$), referred to as the outward interaction term, contains outward motion of high-speed fluid; the second quadrant (Q2: $u' < 0$, $v' > 0$) contains the motions associated with ejection of low-speed fluid away from the wall; the third quadrant (Q3: $u' < 0$ and $v' < 0$), also called the inward interaction term, contains the inward motion of low-speed fluid; and the fourth quadrant (Q4: $u' > 0$ and $v' < 0$) contains an inrush of high-speed fluid (or sweeps). Thus, Q2 and Q4 events contribute to positive Reynolds shear stress ($-\langle u'v' \rangle$), while Q1 and Q3 events contribute to the negative Reynolds shear stress.

Following Lu and Willmarth (1973), the mean Reynolds shear stress at a given (*x*,*y*) location is decomposed into contributions from the quadrants excluding a hyperbolic hole of size H_q (see Figure 2.4) as

$$\langle u'v' \rangle_Q(x, y, H_q) = \frac{1}{N}\sum_{i=1}^{N} u'_i\,(x, y) v'_i(x, y) S_Q(x, y, H_q) \tag{2.7}$$

where *N* is the total number of instantaneous velocity vectors (= total number of PIV snapshots) at a given (*x*,*y*) location and S_Q is a detector function given by

$$S_Q(x, y, H_q) = \begin{cases} 1 & if\ |u'_i(x, y)v'_i(x, y)|_Q \geq H_q u_{rms}(x, y) v_{rms}(x, y) \\ 0 & \text{Otherwise} \end{cases} \tag{2.8}$$

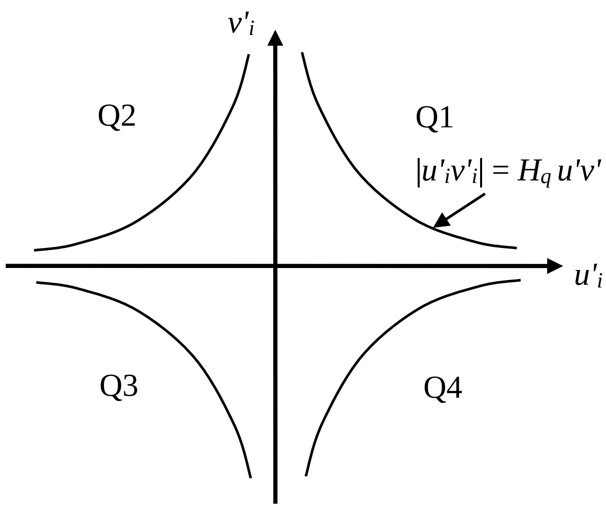

Figure 2.4: A sketch of the four quadrants and hole region of the *u'*-*v'* plane.

The hole size H_q represents a threshold on the strength of the Reynolds shear stress producing events, with H_q = 0 allowing all *u'v'* events to be included in the decomposition, and higher values of H_q allowing the inclusion of only increasingly intense Reynolds shear stress producing events. The contribution to the Reynolds shear stress from the hole region is given by

$$\langle u'v' \rangle_Q(x, y, H_q) = \frac{1}{N}\sum_{i=1}^{N} u'_i\,(x, y) v'_i(x, y) S_h(x, y, H_q) \tag{2.9}$$

where

$$S_h(x,y,H_q) = \begin{cases} 1 & if\ |u'_i(x,y)v'_i(x,y)| < H_q u_{rms}(x,y)v_{rms}(x,y) \\ 0 & \text{Otherwise} \end{cases} \tag{2.10}$$

By accumulating the values of S_Q, the space fraction N_Q can be calculated as

$$N_Q(x,y,H) = \frac{\sum S_Q(x,y,H)}{N} \tag{2.11}$$

2.6.2 Swirling Strength

Swirling strength is a term used to describe the imaginary part of the complex eigenvalues of the velocity gradient tensor and provides a means for identifying vortex cores in a flow field. In three dimensions, the local velocity gradient tensor will have one real eigenvalue λ_r, and a pair of complex conjugate eigenvalues ($\lambda_{cr} \pm i\lambda_{ci}$) when the discriminant of its characteristic equation is positive (Zhou et al. 1999). Chong et al. (1990) observed that when complex eigenvalues occur, fluid particle trajectories about the eigenvector corresponding to λ_r exhibit a spiralling motion with a period of magnitude λ_{ci}^{-1}. For a planar PIV velocity field, the complete local velocity gradient tensor is unavailable. Thus, only a two-dimensional swirling strength can be calculated using the in-plane velocity gradients (Adrian et al. 2000; Hutchins et al. 2005), and which in the *x*-*y* plane is formulated as

$$\begin{vmatrix} \frac{\partial U}{\partial x} - \lambda & \frac{\partial U}{\partial y} \\ \frac{\partial V}{\partial x} & \frac{\partial V}{\partial y} - \lambda \end{vmatrix} = 0 \tag{2.12}$$

This is a quadratic equation with solution given by

$$\lambda = \frac{1}{2}\left(\frac{\partial U}{\partial x} + \frac{\partial V}{\partial y}\right) \pm \frac{1}{2}\sqrt{\underbrace{\left(\frac{\partial U}{\partial x} + \frac{\partial V}{\partial y}\right)^2}_{b^2} - \underbrace{4\left(\frac{\partial U}{\partial x}\frac{\partial V}{\partial y} - \frac{\partial V}{\partial x}\frac{\partial U}{\partial y}\right)}_{4ac}} \tag{2.13}$$

Since the swirling strength, λ_{ci}, is defined at a location where the solution is complex, the magnitude of swirling strength associated with the spanwise vortex core at that location becomes

$$\lambda_{ci,z} = \frac{1}{2}\sqrt{\left|b^2 - 4ac\right|} \quad \text{where } 4ac > b^2. \tag{2.14}$$

In this form, the swirl has no sign information. Sign is however recovered by multiplying $\lambda_{ci,z}$ by the sign of the local in-plane instantaneous fluctuating vorticity. Using notation from previous studies (e.g., Wu and Christensen 2006), the instantaneous signed swirling strength is given by

$$\Lambda_{ci,z} = \lambda_{ci,z}\left(\frac{\omega_z'}{|\ \omega_z'\ |}\right) \tag{2.15}$$

where ω_z' is the instantaneous fluctuating vorticity.

The advantage of swirling strength, $\lambda_{ci,z}$ over the vorticity, ω_z, is that $\lambda_{ci,z}$ can be used to unambiguously differentiate between regions with vorticity arising from pure rotation and those with vorticity originating from shear.

2.6.3 Linear Stochastic Estimation (LSE)

Stochastic estimation is a least-square method for approximating conditional averages based on a set of prescribed events. The technique was first applied by Adrian (1977) to estimate the conditionally averaged flow structures associated with turbulent boundary layers.

In general, the conditional average of a function U denoted $\overline{U \mid E}$ where E is a set of event data is defined as (Adrian et al. 1989)

$$\overline{U \mid E} = \int \frac{f(U,E)}{f(E)} U dU \tag{2.16}$$

where $f(U, E)$ is the joint probability density function of U and E, and $f(E)$ is the probability density function of E. While equation (2.16) is the best estimate of the conditional average, its direct computation is impractical due to the large number of events that must be included for the results to converge. The stochastic estimate of the conditional average $\overline{U \mid E}$ where U_i is the i^{th} component of velocity is obtained by expanding the conditional average in a Taylor series about $E = 0$, and truncating the series at some level (Adrian et al. 1989). Thus, assuming $E = (E_1, E_2, E_3, ..., E_N)$, where the E_i's are fluctuations with respect to the mean, $\overline{U \mid E}$ is expanded as follows (Adrian et al. 1989):

$$\overline{U_i \mid E} = L_{ij} E_j + M_{ijk} E_j E_k + N_{ijkl} E_j E_k E_l + ... \tag{2.17}$$

The unknown coefficients L, M, N, ... are determined by requiring that the mean-square error between the approximation and the conditional average be minimized,

$$\overline{[\overline{U_i \mid E} - L_{ij} E_j - M_{ijk} E_j E_k - N_{ijkl} E_j E_k E_l - ...]^2} = \text{Minimum}. \tag{2.18}$$

In the case of linear stochastic estimation, only the first term in equation (2.17) is retained. The minimization leads to the orthogonality principle which states that the error must be statistically uncorrelated with each of the data. That is,

$$\overline{\left[\langle U_i \mid E \rangle - L_{ij} E_j\right] E_k} = 0\,, \quad i = 1, 2, 3 \quad j, k = 1, 2, 3, ..., N. \tag{2.19}$$

which on simplification yields

$$\overline{E_j E_k} L_{ij} = \overline{U_i E_k}\,, \qquad j, k = 1, 2, 3, ..., N. \tag{2.20}$$

Expanding equation (2.20) for indices j and k leads to a linear system of equations (or the Yule-Walker equations) which can be solved for the estimation coefficients L_{ij}.

$$\begin{aligned}
\overline{U_i E_1} &= L_{i1} \overline{E_1 E_1} + L_{i2} \overline{E_1 E_2} + ... + L_{iN} \overline{E_1 E_N} \\
\overline{U_i E_2} &= L_{i1} \overline{E_2 E_1} + L_{i2} \overline{E_1 E_2} + ... + L_{iN} \overline{E_2 E_N} \\
&\ldots\ldots\ldots\ldots\ldots\ldots\ldots\ldots\ldots\ldots\ldots\ldots \\
&\ldots\ldots\ldots\ldots\ldots\ldots\ldots\ldots\ldots\ldots\ldots\ldots \\
\overline{U_i E_N} &= L_{i1} \overline{E_N E_1} + L_{i2} \overline{E_N E_2} + ... + L_{iN} \overline{E_N E_N}
\end{aligned} \tag{2.21}$$

For a scalar event E at the reference location (x_{ref}, y_{ref}), equation (2.21) reduces to

$$\overline{U_i(x_{ref}+\Delta x, y)\cdot E(x_{ref}, y_{ref})} = L_i\,\overline{E(x_{ref}, y_{ref})\cdot E(x_{ref}, y_{ref})} \tag{2.22}$$

from which the corresponding LSE coefficient is obtained as

$$L_i = \frac{\overline{U_i(x_{ref}+\Delta x, y)\cdot E(x_{ref}, y_{ref})}}{\overline{E(x_{ref}, y_{ref})^2}} \tag{2.23}$$

Then, using equations (2.22) and (2.23), the LSE of the conditional average of the i^{th} component of velocity (u or v) is given by

$$\overline{U_i(x_{ref}+\Delta x, y)\,|\,E(x_{ref}, y_{ref})} = \frac{\overline{U_i(x_{ref}+\Delta x, y)\cdot E(x_{ref}, y_{ref})}}{\overline{E(x_{ref}, y_{ref})^2}}\,E(x_{ref}, y_{ref}) \tag{2.24}$$

Equation (2.24) allows the reconstruction of the average velocity field associated with a given value of E (Christensen and Adrian 2001). The event E can be set as u or v, a single component of vorticity vector (e.g. ω_z) or swirling strength $\Lambda_{ci,z}$.

2.6.4 Proper Orthogonal Decomposition (POD)

Proper orthogonal decomposition (POD) is used to extract coherent structures from an ensemble of data by decomposing the data into an infinite series of spatial eigenfunctions. The POD eigenfunctions provide an optimal basis for expansion of the flow in the sense that their energy convergence is more rapid than any other representation. The POD method was first introduced by Lumley (1967) for analysis of turbulent flows. Its advantage is that it is a more objective method for educing coherent structures in comparison to conditional averaging techniques such as LSE which require *a priori* knowledge of the presence of a coherent structure in the flow.

Mathematically, the goal of POD is to seek orthogonal spatial eigenfunctions, $\Phi(x)$ so that each member $U(x, t)$ of an ensemble of instantaneous realizations can be expressed as

$$U(x,t) = a_0\Phi_0(x) + \sum_{n=1}^{\infty} a_n(t)\Phi_n(x) \tag{2.25}$$

where $a_n(t)$ are time coefficients. The zeroth eigenfunction, or Mode 0, Φ_0, represents the mean flow field while subsequent modes contain the fluctuations. Following Berkooz et al. (1993), the values of the eigenfunctions are chosen to maximize a functional of the form

$$\frac{\overline{\left|(U,\Phi)\right|^2}}{(\Phi,\Phi)} \tag{2.26}$$

where the operation (g, h) between two functions g and h denotes the inner product given by

$$(g,h) = \int_{\Omega_x} g(x)\,h^*(x)\,dx \tag{2.27}$$

In equation (2.27), the function $h^*(x)$ is the complex conjugate of $h(x)$. Applying a calculus of variations procedure on equation (2.26) with the restriction that $(\Phi,\Phi) = 1$ leads to a Fredholm integral equation of the form

$$\int_{\Omega_x} \langle u(x)u(x')\rangle \Phi(x')dx' = \lambda\Phi(x) \tag{2.28}$$

where the kernel $\langle u(x)u(x')\rangle$ is the two-point auto-covariance function. Solving equation (2.28) for $\Phi(x)$ and eigenvalues λ requires the auto-covariance function to be calculated at all spatial points in the domain Ω_x. In practical applications such as PIV, where high spatial resolution is required, the number of grid points is usually very large leading to an extremely large eigenvector problem.

In the present study, the POD analysis is carried out using the Sirovich's (1987) method of snapshots. The snapshot method facilitates the computation of the two-point auto-covariance from a relatively small number ($N < M$) of instantaneous realizations or snapshots where M is the number of grid points. The methodology consists of the following steps. First, all the fluctuating velocity components from the N realizations are arranged in a matrix U as follows:

$$U = \left[U^1 \; U^2 \; \cdots U^N \right] = \begin{bmatrix} u_1^1 & u_1^2 & \cdots & u_1^N \\ \vdots & \vdots & \vdots & \vdots \\ u_M^1 & u_M^2 & \cdots & u_M^N \\ v_1^1 & v_1^2 & \cdots & v_1^N \\ \vdots & \vdots & \vdots & \vdots \\ v_M^1 & v_M^2 & \cdots & v_M^N \end{bmatrix} \tag{2.29}$$

The cross-covariance matrix is then calculated as (Sirovich 1987):

$$C = \tfrac{1}{N}(U^T U) \tag{2.30}$$

which is symmetric and positive definite. The corresponding eigenvalue problem is

$$CV^n = \lambda^n V^n \tag{2.31}$$

The eigenvectors V^n are arranged according to the size of the eigenvalues

$$\lambda^1 > \lambda^2 > \cdots > \lambda^N \geq 0 \tag{2.32}$$

where each eigenvalue represents the amount of the total variance explained by a given POD mode.

From the eigenvectors, the eigenfunctions or modes, Φ^n, are constructed as

$$\Phi^n = \frac{\sum_{i=1}^{N} V_i^n U^i}{\left\| \sum_{i=1}^{N} V_i^n U^i \right\|}, \qquad n = 1, 2, ..., N \tag{2.33}$$

where V_i^n is the i^{th} component of the eigenvector corresponding to eigenvalue λ^n, and the L_2-norm for a vector **x** is given by

$$\|\mathbf{x}\| = \sqrt{x_1^2 + x_2^2 + \cdots + x_M^2} \tag{2.34}$$

Writing the matrix of POD eigenmodes as $M = \left[\Phi^1 \; \Phi^2 \; \cdots \Phi^N \right]$, the temporal coefficients $a_n(t)$ are determined by projecting the fluctuating field onto the eigenmodes as

$$a^n = M^T U^n \tag{2.35}$$

which because of the orthogonality of the eigenfunctions are uncorrelated in time with mean square values equal to the eigenvalues λ^n,

$$\overline{a_n(t)a_m(t)} = \delta_{nm}\lambda^n \tag{2.36}$$

Using equation (2.22), the fluctuating part of the n^{th} snapshot can be reconstructed as (Sirovich 1991):

$$U^n = \sum_{n=1}^{N} a_n(t)\Phi^n \tag{2.37}$$

Since the POD is performed on the fluctuating velocity fields, the n^{th} eigenvalue, λ^n, represents the turbulent kinetic energy (tke) contribution of the n^{th} POD mode, Φ^n, with Mode 1 contributing the most energy, followed by Mode 2, and so on. The fractional contribution of mode Φ^n to the total tke is given by (Sen et al. 2007):

$$e_n = \frac{\lambda^n}{\sum_{i=1}^{N} \lambda^i} \tag{2.38}$$

Lower-order modes are representative of the large-scale coherent structures of the flow while higher-order modes correspond to the small-scale and less energetic turbulent structures. The cumulative energy contained in modes 1 to m is given by

$$E_m = \sum_{i=1}^{m} e_i \tag{2.39}$$

It must be noted that because the lower-order modes contribute much more energy than the higher-order ones, only the first few modes may be necessary to reconstruct the essential features of the flow. Using equation (2.37), a low-order representation of an instantaneous flow field based on the first m ($< N$) leading modes can be reconstructed as

$$U_L^n = \sum_{n=1}^{m} a_n \Phi^n \tag{2.40}$$

The accompanying residual field composed of the motions from the discarded higher-order modes is then calculated as

$$U_R^n = U^n - \sum_{n=1}^{m} a_n \Phi^n \tag{2.41}$$

2.6.5 Energy Spectra

Energy spectra describe the distribution of energy among the various scales of turbulence. The spectral representation of a turbulent flow considers turbulence to be made up of a hierarchy of scales, including large scales of wavelength or size comparable to the size of the flow domain, and small scales of significantly shorter wavelength. The large scales extract energy from the mean flow to provide the kinetic energy for the turbulence, while the small scales, formed because of the continuous stretching or straining of the large scales by the mean deformation, drain energy from the large scales to be dissipated by viscosity.

In near-wall turbulence, the large scales are anisotropic due to the strain imposed by the mean deformation. Kolmogorov (1941) hypothesized that at sufficiently high Reynolds numbers the small-scale motions are statistically steady, isotropic and independent of the detailed structure of the large scales and the mean deformation rate. This hypothesis, popularly referred to as K41 in the literature, implies that while the large scales may be flow dependent, the small scales are universally similar for all kinds of turbulent flows.

Figure 2.5 shows a schematic of the turbulence energy spectra often observed in high Reynolds number turbulent flows. At high Reynolds numbers an intermediate range of scales is observed between the small and large scales across which inter-scale energy transfer occurs and is known as the inertial subrange. For the inertial subrange, Kolmogorov postulated that the energy transfer depends solely on the value of the average dissipation rate ε and proposed the relation

$$E(k,t) = C_K \varepsilon^{2/3} k^{-5/3} \tag{2.42}$$

where the value of the constant C_K for the three-dimensional spectrum is given by Monin and Yaglom (1975) as 1.5 ± 0.1.

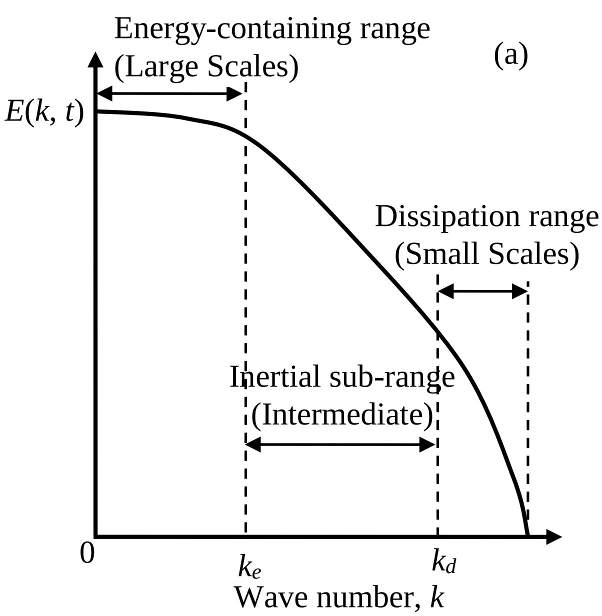

Figure 2.5: Schematic of the turbulent kinetic energy spectrum. (a) Wavenumber spectrum, (b) Frequency spectrum.

From the energy spectrum the average dissipation rate ε can be calculated as (Nelkin 1994):

$$\varepsilon = 2\nu \int_0^\infty k^2 E \, dk \tag{2.43}$$

The dissipation spectrum is given by

$$D(k,t) = k^2 E(k,t) \tag{2.44}$$

The quantity $E(k, t)$ represents the turbulent kinetic per unit mass, per unit wavenumber in all three velocity components (Nelkin 1994). It is obtained as the surface integral of the Fourier transform of one-half the trace of the cross-correlation tensor (Pope 2000) over a sphere of radius $k = (k_1^2+k_2^2+k_3^2)$. Since $E(k, t)$ provides no directional information, the one-dimensional energy spectral density E_{ii} and cross-spectral density E_{ij} are found more useful and are the spectra considered in the present data analysis. The cross-spectral density is defined as

$$E_{ij}(k_x, y) = \int_{-\infty}^{\infty} R_{ij}(r_x, y)\, e^{-jk_x r_x}\, dr_x \tag{2.45}$$

where R_{ij} is the one-dimensional two-point cross-covariance function given by

$$R_{ij}(r_x, y) = \langle u_i(x, y, t) u_j(x + r_x, y, t) \rangle \tag{2.46}$$

Using the properties of the Fourier transform, the spectrum may also be calculated in a more computationally efficient manner. Following Hong and Katz (2011), the cross-spectral density was estimated along the streamwise direction as

$$E_{ij}(k_1, y) = \frac{L}{2\pi N^2} \langle F_i(k_1, y) F_j{}^*(k_1, y) \rangle \tag{2.47}$$

where L is the length of the flow domain, N is the number of points and k_1 is the wavenumber in the streamwise direction. The quantity F_i denotes the Fourier transform of the velocity field given by (Doron et al. 2001):

$$F_i(k_1, y) = \sum_n u_i(x_n, y) W(x_n, y) e^{-jk_1 x_n} \tag{2.48}$$

where W is a windowing function and F^* is the complex conjugate of F.

$$\int_0^{\infty} E_{ij}(k_1)\, dk_1 = \langle u_i u_j \rangle \tag{2.49}$$

Following Pope (2000), the frequency spectra can be estimated from the temporal correlation of a stationary random process as

$$E(f, y) = \frac{1}{2\pi} \int_{-\infty}^{\infty} R_{ii}(x, y, \Delta t) e^{-jft} dt \tag{2.50}$$

where R is temporal auto-covariance of the velocity fluctuation u or v given by

$$R_{ii}(x, y, \Delta t) = \langle u_i(x, y, t) u_i(x, y, t + \Delta t) \rangle \tag{2.51}$$

In equations (2.50) and 2.51, Δt is the temporal separation. Both the spatial and temporal (frequency) spectra are explored in this investigation.

2.7 Summary

Separated and reattached turbulent flows over smooth forward-facing steps and blunt rectangular plates have been investigated extensively in the past by means of experimental methods as well as numerical simulations. From these studies, the following conclusions can be drawn: The reattachment length of the primary recirculation region decreases almost linearly with increasing freestream turbulence intensity but is an increasing function of Reynolds number up to a critical Reynolds number. The value of the critical Reynolds number decreases with background turbulence level. Beyond the critical Reynolds number, the reattachment length remains relatively constant. Also, the increase with Reynolds number is more dramatic at lower values of the relative boundary layer thickness than at higher values.

The mean (static) pressure is adverse upstream of the FFS with largest value occurring close to the step, favourable on top of the step, and returns to equilibrium conditions (or ZPG) as the flow evolves downstream. The largest pressure coefficient, root-mean-square pressure fluctuation and highest spectral energy occur at the mean reattachment point.

The values boundary layer integral parameters such as the skin friction coefficient and boundary layer shape factor decrease to minimum values at the separation point followed by sharp increase immediately downstream of the step, though they level off to slightly higher values than observed upstream. The mean streamwise velocity relaxes more quickly to the self-similar values than the mean wall-normal velocity, turbulence intensities and Reynolds stresses.

In the presence of wall roughness, place either upstream or on top of the step, the reattachment length is reduced by the presence of wall roughness both upstream of the step and over the step. In the presence of upstream roughness, the reattachment length is relatively invariant with Reynolds number.

Wall roughness also reduces the mean velocity both upstream and downstream of the step. On the contrary, while the turbulence intensities and Reynolds stresses are enhanced by roughness in the unperturbed case, reductions are observed over the step when compared to a smooth wall. Roughness also reduces the contributions of Reynolds shear stress producing events: ejections and sweeps, leading to reduction of the mean Reynolds shear stress.

CHAPTER 3

EXPERIMENTAL SETUP AND MEASUREMENT PROCEDURE

This chapter presents details of the experimental setup used for the velocity measurements. These include a description of the test section, the principles of time-resolved particle image velocimetry (TR-PIV) and a summary of the test conditions investigated.

3.1 Test Section

The experiments were conducted in an open recirculating water channel as shown in Figure 3.1. The test section of the channel is 6000 mm long, and has a cross section of dimensions 600 mm × 450 mm. The side and bottom walls of the channel were fabricated from smooth 31.8 mm thick Super Abrasion Resistant (SAR) transparent acrylic plates that facilitate optical access. A smooth step of nominal height, h = 15 mm and length L = 2400 mm, spanning the entire width of the channel, was positioned 3600 mm from the inlet of the channel. The aspect ratio, AR (= W/h) was approximately 40, which is four times larger than the minimum value of $W/h \approx 10$ (Brederode and Bradshaw 1972) required to ensure the flow is nominally two-dimensional at the mid-span of the channel. The flow in the channel was driven by an impeller pump that delivers a maximum flow rate of 33950 LPM. A 40HP variable-speed drive motor was used to regulate the speed of the pump. The flow in the channel was driven by a centrifugal pump through a series of flow conditioning units, including a perforated plate, a hexagonal honey-comb, mesh screens and a 4.88:1 converging section. The resulting fine-scale flow at the inlet was triggered by a 100 mm wide sandpaper 16-grit to promote a rapid transition of the approach boundary layer to turbulence.

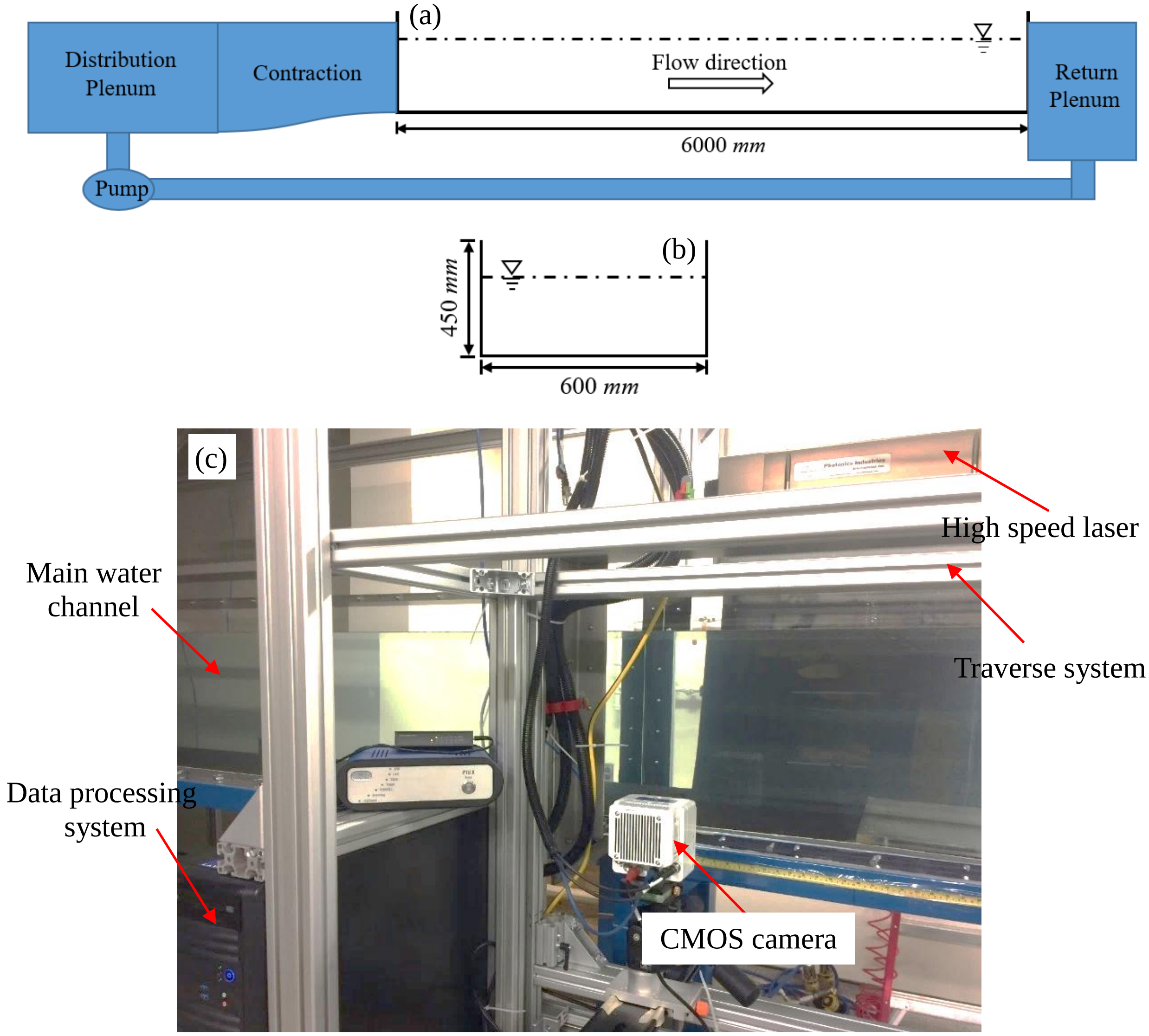

Figure 3.1: Picture of test facility used for flow measurements: (a) front view of the water channel; (b) side view of the water channel and (c) experimental facility.

3.2 Description of Wall Roughness

In addition to the upstream smooth wall, two replaceable upstream rough-wall conditions were investigated: a 16-grit sandpaper of average roughness height, 1.54 mm, which was glued to a 6 mm acrylic insert (Figure 3.2b), and staggered cubes of height, k = 3 mm, and spacing $P_x = P_y$ = 6 mm, which were glued to a 3 mm acrylic insert (Figure 3.2c). The average roughness height of the sandpaper was measured using a SMZ800N optical stereo microscope that yielded a sample standard deviation, skewness and kurtosis of approximately 0.42 mm, 0.63 and 3.08, respectively.

The two types of roughness elements used in this study are shown in Figure 3.3.

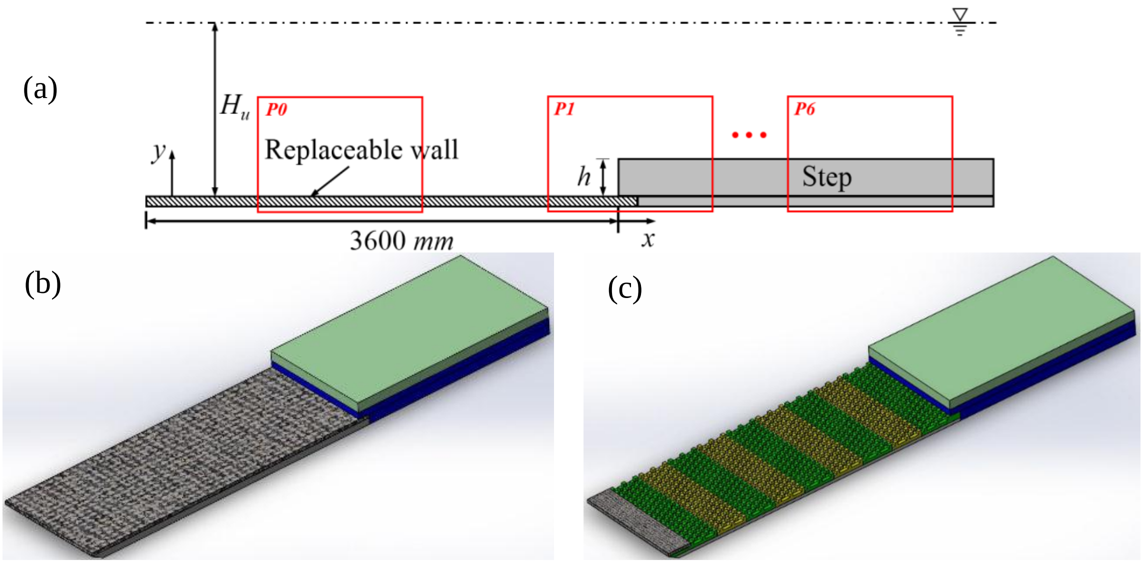

Figure 3.2: Schematic of the FFS with replaceable upstream wall (not drawn to scale): (a) test section with FFS (smooth wall); (b) replaceable rough wall made from sandpaper 16-grits; and (c) replaceable rough wall made from cubes.

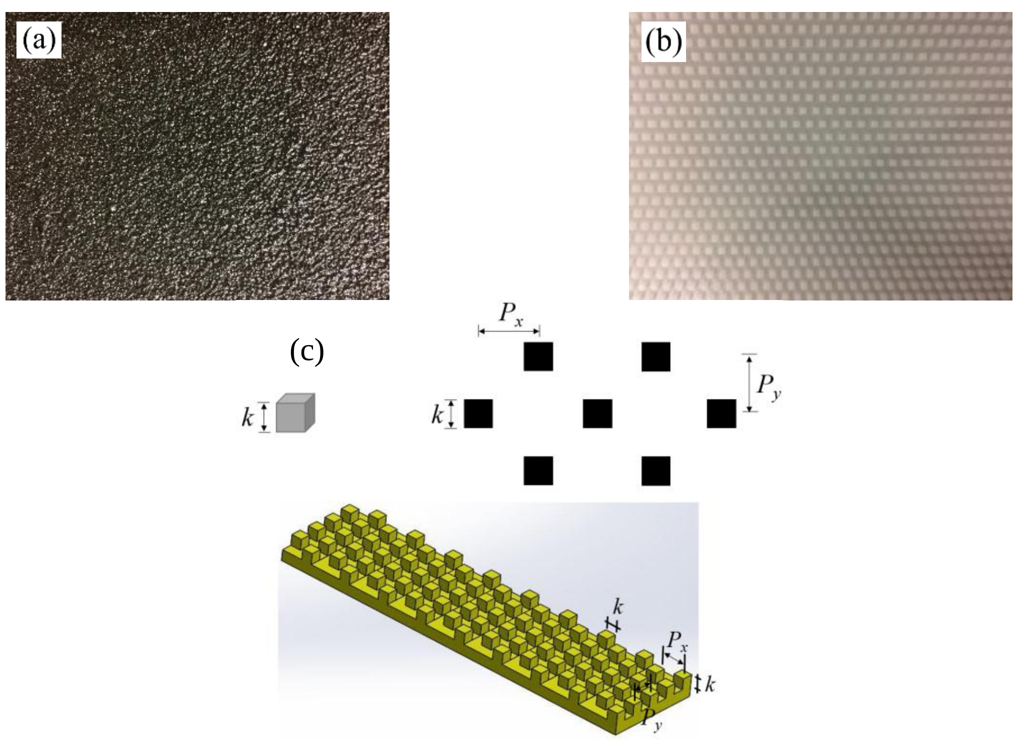

Figure 3.3: Types of roughness elements used: (a) 16-grit sandpaper; (b) and (c) staggered cubes.

3.3 Test Conditions

The step height, h, was kept constant for all three cases at 15 mm. The upstream water depth, H_u, was about 415 mm for all cases, leading to a blockage ratio ($BR = h/H_u$) of 0.03. The measurements were made in the mid-span ($z/h \approx 0$) in seven measurement planes, P0 to P6, corresponding to the upstream station, the recirculation and redevelopment regions, respectively. For the smooth and rough walls, the velocity of the approach flow was approximately 0.520 m/s, corresponding to a Reynolds number of 7800, based on the freestream velocity and step height. In all cases, the Froude number, $Fr_H = U_o/\sqrt{(gH_u)}$, was approximately 0.25, which ensured that the effects of surface waves on the quality of results were minimal. For ease of reference, the test conditions for the smooth upstream wall, sandpaper and cube roughness are denoted by the acronyms SM, SP and CB, respectively.

3.4 Time-Resolved Particle Image Velocimetry

In the last few decades particle image velocimetry (PIV) has been established as a whole-field measurement methodology for simultaneously measuring the velocities in both 2D (planar) and 3D (volumetric) flow regions. A typical setup is depicted schematically in Figure 3.4. The flow is seeded with small neutrally buoyant particles whose response times are much shorter than the fluid time scale so that their velocities approximate the fluid velocity. The area of interest (AOE) also known as the field of view (FOV) is illuminated by a pulsed sheet of high-intensity laser light, fired at precise time intervals. The images of the light scattered by the particles are captured and recorded by a high-speed camera. Image processing methods are then applied to estimate the displacement of the particles within the images. The displacement is divided by the time interval between laser pulses to yield the velocity.

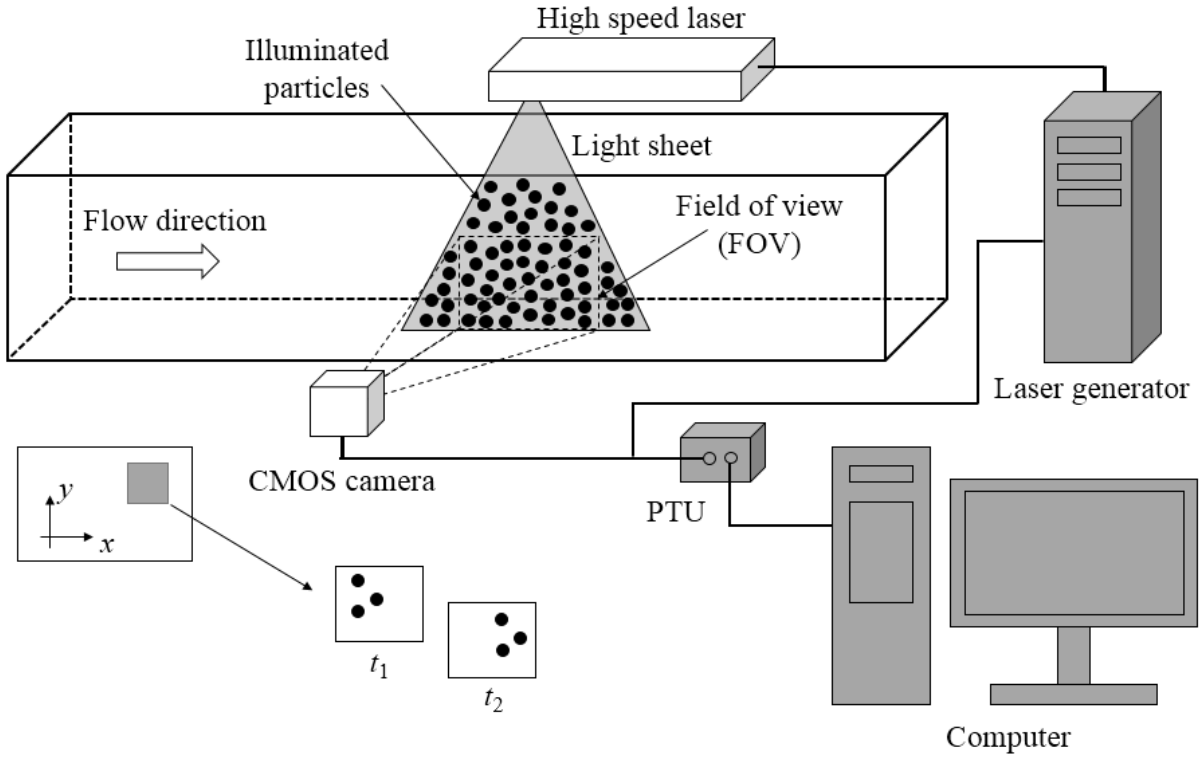

Figure 3.4: A typical setup of a planar TR-PIV system.

3.4.1 Particle Illumination and Recording

Lasers are widely used to illuminate seeding particles in PIV due to their high-energy density monochromatic light that can be formed into thin sheets of light. A laser consists of three main components, namely, the laser material consisting of atomic or molecular gas, semiconductor or solid material; the pump source that excites the laser material by electromagnetic energy or chemical energy, and the mirror arrangement allowing an oscillation within the laser material. To provide light sheets of high intensity, laser beams with good and stable properties as well as high energy pulses are required. One such laser is the Neodymium: Yttrium Aluminum Garnet (Nd:YAG) semi-conductor type laser in which the laser beam is generated by excited Nd^{3+} ions. The excitation is produced by pumping the laser material with electromagnetic energy. The excited ions are then promoted to higher energy levels after absorbing photons of electromagnetic energy. If the energy released on subsequent fall back to their unexcited state is in phase with the exciting photons light amplification by stimulated emission is said to occur. Frequency doubled Nd:YAG lasers emit infra-red radiation whose frequency is doubled to produce green light of wavelength 532 nm. The pulses of the laser are triggered by means of a quality switch (Q-switch). The most important property of a laser system that determines its suitability for flow measurement is the pulse repetition rate. For most commercially available Nd:YAG lasers, the pulse repetition rate is limited to 10 to 15 Hz. These are often adequate for most low-speed applications. However, the need for high-speed, time-dependent turbulence applications has led to the development of high-repetition rate lasers capable of delivering pulse bursts of up to 1 kHz – 1 MHz. An example is the Neodymium: Yttrium Lithium Fluoride (Nd:YLF) dual-pulse laser with a pulse width of about 129 ns and wavelength 527 nm that delivers a total energy of 30 – 60 mJ/Pulse at 1 kHz – 10 kHz.

The intensity of the light sheet produced by the laser is considered to follow a Gaussian distribution of the form

$$I = I_o \exp\left(-8z^2 / d_l^{\,2}\right) \tag{3.1}$$

where I_o is the peak intensity of the sheet and d_l is the light sheet thickness, defined at the $I_o e^{-2}$ intensity level (that is, where $z = d_l/2$).

In order to capture the images of the illuminated particles, high-spatial resolution cameras such as the charge-coupled device (CCD) camera are used. The cameras are synchronized with the laser to allow image acquisition within the duration of the pulse. However, typical commercially available CCD cameras are limited to the acquisition of relatively few image pairs per second (e.g., 4 image pairs/second or 4Hz). On the contrary, the development of high-speed cameras such as the complementary metal-oxide semiconductor (CMOS) camera makes it possible to achieve up to kilohertz (kHz) image acquisition rates. When coupled with the high-repetition rate lasers, the CMOS camera becomes an extremely valuable tool for performing time-resolved PIV measurements. The availability of the high-speed CMOS cameras allows turbulence research into rapidly evolving time-dependent flow phenomena as found in separating and reattaching flows around bluff bodies.

In practical applications, the images recorded by the camera are acquired in one of two ways: i.e., either as a single-frame/multi-exposure or multi-frame/single-exposure acquisition. In single-frame/multi-exposure mode, two or more exposures are recorded on the same frame, leading to multiple images of the same particle within the frame. The method is successful only when a relatively small number of particles are involved since too many particles in the flow can result in overlapping images. The single exposure also leads to directional ambiguity as there is no way to decide which image comes from the first illumination or the second illumination. The directional ambiguity is solved by using the multi-frame/single-exposure mode.

The particle image intensity is approximated by a two-dimensional Gaussian distribution of the form

$$I_p(x, y) = I \exp\left[-8\left(\left(x - x_p\right)^2 + \left(y - y_p\right)^2\right) / d_t^{\,2}\right] \tag{3.2}$$

where I is the laser sheet intensity distribution given by equation (3.1), (x_p, y_p) is the location of the peak intensity and d_t is the particle image diameter given by (Adrian 1991):

$$d_t = \left(M^2 d_p^{\,2} + d_s^{\,2}\right)^{1/2} \tag{3.3}$$

where M is the magnification and d_s is the width of the Airy function of a diffraction limited lens. For a camera of f-number, $f^{\#} = f'/D_a$, where f' is the focal length and D_a the aperture diameter, the Airy function width is given by (Adrian 1991):

$$d_s = 2.44(1 + M) f^{\#} \lambda \tag{3.4}$$

where λ is the wavelength of the light. Knowing the particle intensity distribution, the corresponding particle pixel value is the integral over the area of the pixel:

$$I_{px}(x,y) = I \iint \exp\left(-8 \frac{(x - x_p)^2 + (y - y_p)^2}{d_t^{\,2}} \right) dxdy \tag{3.5}$$

3.4.2 Statistical Evaluation of Recorded Images

The images acquired by the camera are processed numerically using convolution algorithms to determine the average displacement of the particles within the image. The algorithm first divides the image into a number of smaller regions called interrogation areas (*IA*). To calculate the particle displacement for a given *IA*, the pixel intensity values are statistically correlated with one another over the same *IA* (auto-correlation), or with the pixel intensity values of a corresponding *IA* in another image (cross-correlation). A detailed discussion of the mathematical background of the two correlation methods in PIV can be found in Westerweel (1997) and Raffel et al. (1998).

3.5 Measurement Procedure

A high-resolution 2D-2C TR-PIV system, which consists of a high repetition-rate laser source, a high-speed camera, and data acquisition system was used to measure the data. The flow was seeded with 10 μm silver coated hollow glass spheres with specific gravity of 1.4 and illuminated by a Photonics DM30-527DH dual-head high-speed Nd:YLF laser, that emits green light up to a maximum of 30 mJ/pulse for each laser at λ = 527 nm. A high speed 12-bit $f^{\#}$2.8 Phantom VEO-340L complementary metal-oxide semiconductor (CMOS) camera with 806 frame rate at a full resolution of 2560 pixel × 1600 pixel was used to capture the images. The pixel pitch of the camera was 10 μm. In the present experiments, the images were acquired at a rate of 1047 Hz at a reduced resolution of 1920 pixel × 1600 pixel. The field of view of the camera was set to approximately 88 mm × 73 mm (i.e., 5.8h × 4.8h) for the SM in the x and y directions. Due to the significantly thicker boundary layers over the sandpaper (SP) and cube roughness (CB), the field of view was increased to 131 mm × 109 mm (8.7h × 7.3h) for the rough-wall cases.

Table 3.1: Summary of TR-PIV experimental parameters

Parameter	Value
Camera pixel pitch	10 μm
Laser power	30 mJ/Pulse
Aperture ($f^{\#}$)	2.8
Light sheet thickness	1 mm
Field of view (FOV)	88 × 73 mm^2 (SM); 131 × 109 mm^2 (SP and CB)
Pulse separation (Δt)	5 μs
Magnification (M)	0.22 (SM); 0.15 (SP and CB)
Diameter of tracer particles (d_p)	10 μm
Slip velocity (U_s)	2.18×10^{-5} m/s
Particle response time (τ_p)	2.22×10^{-6} s
Stokes number (S_k)	0.00085 (SM); 0.0015 (SP); and 0.0027 (CB)
Image sampling frequency (f)	1047 Hz
Sampling time (T)	17s (SM); 23s (SP and CB)

The TR-PIV experimental parameters are summarized in Table 3.1. The corresponding magnification factors were respectively 0.22 for the smooth wall and 0.15 for SP and CB. The slip velocity of particles was estimated as (Raffel et al. 1998):

$$U_s = \frac{d_p^2(\rho_p - \rho_f)}{18\rho_f \nu} g \tag{3.6}$$

where ρ_p and ρ_f are the density of seeding particles and working fluid (water), respectively. Also, the response time of the seeding particles was estimated as

$$\tau_p = \frac{d_p^2(\rho_p - \rho_f)}{18\rho_f \nu} \tag{3.7}$$

The fluid characteristic time scale, τ_f, herein taken as the viscous timescale, ν/U_τ^2, was approximately 2.60×10^{-3} s, 1.48×10^{-3} s and 8.16×10^{-4} s for SM, SP and CB, respectively. The corresponding values of the Stokes number, $S_k = \tau_p/\tau_f$, were 0.00085, 0.0015 and 0.0027 for SM, SP and CB, respectively. These values are within the recommended range of $S_k \leq 0.05$ proposed by Samimy and Lele (1991).

Detailed velocity measurements were made first in Plane 0 upstream of the step (with the field of view centered at $x/h = -20$) to characterize the upstream smooth and rough wall turbulent boundary layers. This was followed by successive measurements in planes P1 to P6 spanning the recirculation and redevelopment regions. For the smooth and rough test condition, 18000 and 24000 instantaneous image pairs were acquired in each measurement plane, respectively. The sample sizes of 18000 and 24000 were confirmed in a convergence analysis (Appendix A) to be sufficient for the statistics to converge. The data acquisition was controlled using commercial software (DaVis version 8.4) supplied by LaVision. The experiment was designed to have the particle image diameter between 2–4 pixels to minimize the effect of peak-locking. The particle displacement was calculated using the adaptive multigrid cross-correlation algorithm, starting with a *IA* size of 128 × 128 pixels with 50% overlap and decreasing it to 32 × 32 pixels with 75% overlap. The processing procedure used a multi-pass FFT with a one-dimensional Gaussian peak-fitting function to determine the average particle displacement within the interrogation window to sub-pixel accuracy. The resulting vector spacing in the streamwise and wall-normal directions were $0.024h \times 0.024h$ for the smooth wall and $0.036h \times 0.036h$ for sandpaper and cube roughness. At 32 × 32 pixels (75% overlap), the spacing between vectors in physical units were 0.37 mm and 0.37 mm in the x and y directions respectively for SM. The corresponding spacing between vectors for SP and CB were 0.55 mm and 0.55 in the x and y directions, respectively. In viscous wall units, these dimensions correspond to 7.3, 14.3 and 19.3 for the smooth wall, sandpaper and cube roughness, respectively.

3.6 Uncertainty Estimates

In their most recent publication, Coleman and Steele (2009) defined an uncertainty in a measured result as a term used to describe the degree of goodness of the measured result. This implies that a measurement uncertainty has a direct impact on the reliability of the measurement. Thus, the identification and mitigation of sources of experimental uncertainty is of paramount significance to the present investigation. In any given experiment, two types of uncertainty can be identified: systematic uncertainties and random uncertainties. There are several sources of systematic uncertainty in PIV that tend to bias the measurement results. These include particle response to fluid motion, light sheet positioning, light pulse timing, seeding density, out-of-plane motion and interrogation area (IA) size. Random uncertainties, on the other hand, describe measurement uncertainties whose magnitude does not change during the measurement period (Coleman and Steele 2009).

Uncertainties in the TR-PIV results were estimated using the correlation statistics method proposed by Wieneke and Prevost (2014), in which the computed displacement field is used to compare correlated interrogation areas in the first and second image frames. A sub-pixel interpolation function is then fitted to the cross-correlation function, which is subsequently used to estimate the root-mean-square value of the displacement error. Details of the uncertainty estimation procedure are presented in Appendix B. Based on this approach, the uncertainty in the instantaneous streamwise velocity for the upstream smooth wall, sandpaper, and cube roughness at the 95% confidence level were estimated to be ±1.0%, ±2.1% and ±3.0%, respectively. Using the uncertainty propagation methodology suggested by Sciacchitano and Wieneke (2016), the uncertainties in the mean velocity, streamwise Reynolds stress, wall-normal Reynolds stress and Reynolds shear stress for the upstream smooth wall condition were estimated to be ±1.5%, ±1.8%, ±1.8%, and ±3.5%, respectively. The corresponding values for the SP are respectively, ±2.0%, ±2.2%, ±2.2%, and ±6.1% and for CB are ±3.1%, ±2.3%, ±2.3%, and ±7.9%, respectively.

CHPTER 4

RESULTS AND DISCUSSION

In this chapter, the statistical properties of the flow obtained within the three regions of the flow: upstream region, recirculation region and redevelopment region for the upstream smooth- and rough-wall conditions are discussed.

4.1 Upstream Boundary Layer Characteristics

The velocity measurements made at x/h = –20 were analysed in order to characterize the state of the approach boundary layer upstream of the step. The boundary layer characteristics for the upstream smooth- and rough-wall conditions are summarized in Table 4.1. These include the freestream velocity, U_o, boundary layer and displacement thicknesses δ and δ^*, respectively, momentum thickness, θ, shape factor, H (= δ^*/θ), relative boundary layer thickness, δ/h, momentum thickness Reynolds number, Re_θ, and velocity scales, $U|_h$, $u_{rms}|_h$, and $v_{rms}|_h$, measured at the height of the step ($y = h$). The boundary layer thickness was estimated as the distance from the wall to wall-normal location where the mean streamwise velocity reaches 99% of the freestream velocity. The shape factor of H = 1.39 observed over the smooth wall is within the range of typical values of 1.3 – 1.4 documented for ZPG turbulent boundary layers over smooth walls (e.g., Karlsson 1978; Smith and Smits 1994; Tachie et al. 2000). Over the sandpaper and cube roughness, the shape factor value is increased by approximately 10% and 36%, respectively, because the rough walls increase the mass flux deficit (δ^*) more substantially than the momentum flux deficit (θ) upstream of the FFS. For the smooth and rough walls, the value of δ/h corresponds to the $\delta/h = O$ (1) Bradshaw and Wong's (1972) classification, indicating a strong perturbation of the boundary layer by the FFS. Because roughness enhanced the momentum flux deficit, the values of the momentum thickness Reynolds number are approximately 70% and 72% higher over the sandpaper roughness and staggered cubes, respectively, in comparison to the smooth wall. As expected, roughness reduced the mean streamwise velocity and enhanced the streamwise and wall-normal turbulence intensities at the step height. Also summarized in Table 4.1 are the values of the skin friction coefficient, $C_f = 2(U_\tau/U_e)^2$ and dimensionless equivalent sandgrain roughness, $k_s^+ = k_s U_\tau/\nu$, where U_τ is the friction velocity and ν is the kinematic viscosity. The values of the friction velocity were estimated by a Clauser chart fit of the logarithmic mean velocity profiles $U^+ = (1/\kappa) \ln y^+ + B$ and $U^+ = (1/\kappa)\ln(y + y_o)^+ + B - \Delta B^+$ to the mean velocity data over the smooth and rough walls, respectively, where $\kappa = 0.41$ and $B = 5.0$ are the logarithmic law constants, ΔB^+ is the roughness function ($\Delta B^+ = 0$ for a smooth wall) and y_o is the virtual origin. The results indicate a 63% enhancement in skin friction by the sandpaper roughness and a more than a three-fold increase in friction by the cube roughness. The dramatic increase in skin friction by the cubes is consistent with the relatively large value of the corresponding equivalent sandgrain roughness height. Following Schlichting (1979), the value of $k_s^+ \approx 503$ suggests that the cube roughness is fully rough ($k_s^+ > 70$) while the sandpaper roughness is transitionally rough ($k_s^+ < 70$). It should be mentioned that the precision uncertainty in the boundary layer thickness (δ), displacement thickness (δ^*), and momentum thickness (θ) for SM was estimated as ±4.1%, ±8.0%, and ±6.5%, respectively. The corresponding values for the SP were ±5.2%, ±9.7%, and ±7.2% and for the CB were ±5.9%, ±11.2%, and ±7.6%. The uncertainties in the friction velocity (U_τ) were estimated to be ±3.0%, ±5.0%, and ±6.0% for SM, SP, and CB, respectively. Accordingly, the uncertainty in skin friction coefficient, C_f, was estimated to be ±4.3%, ±7.0%, and ±9.1% for SM, SP, and CB, respectively.

Table 4.1: Summary of upstream boundary layer parameters and drag characteristics

Parameters	**SM**	**SP**	**CB**
U_o (m/s)	0.517	0.527	0.515
U_τ (m/s)	0.019	0.026	0.035
δ (mm)	64.8	100.3	100.4
δ^*(mm)	11.04	20.02	25.52
θ (mm)	7.8	13.0	13.5
H	1.39	1.52	1.89
δ/h	4.3	6.7	6.7
Re_θ	4032	6877	6952
$U\|_h/U_o$	0.738	0.631	0.587
$u_{rms}\|_h/U_o$	0.071	0.089	0.110
$v_{rms}\|_h/U_o$	0.042	0.056	0.062
C_f	0.0030	0.0049	0.0092
k_s^+	---	69	503

4.2 Flow Characteristics in the Separated and Reattached Region

4.2.1 Instantaneous Flow Visualization

For all the test cases investigated, the flow in the separated and reattached region was observed to be highly unsteady and dominated by large-scale coherent structures. To provide insight into the instantaneous large-scale structures in the separated shear layer a Galilean decomposition was applied to the instantaneous velocity fields. Figure 4.1 shows time-sequenced plots of the Galilean decomposition of the instantaneous velocity fields for the upstream smooth wall condition. The vector plots were obtained by subtracting a constant convection velocity of approximately U_c = $0.8U_o$ from the instantaneous streamwise velocities. The decomposition reveals the presence of streamwise-aligned vortex cores representing the heads of the spanwise vortices produced by the Kelvin-Helmholtz roll up of the separated shear layer. The vortex cores are inclined at angles of approximately 10º – 15º over the step in the downstream direction. In order to elucidate the vortical structures in the flow the swirling strength criterion (λ_{ci}) proposed by Zhou et al. (1999) was used. Because the complete 3D velocity gradient tensor was inaccessible, the 2D velocity gradient tensor was used in estimating the values of the swirling strength, $\lambda_{ci,z}$, in the x-y plane. A similar approach has been used in previous planar PIV measurements of canonical turbulent shear flows (Hutchins et al. 2005; Tay et al. 2015). The instantaneous $\lambda_{ci,z}$ distribution was decomposed into prograde (negative) and retrograde (positive) swirling strength in order to differentiate between clockwise and counter-clockwise swirling motions, respectively. Contours of the prograde (blue $\lambda_{ci,z}$ patches) and retrograde (red $\lambda_{ci,z}$ patches) were superimposed on the vector fields as shown in Figure 4.1. The plots depict a larger proportion of prograde swirling motions compared to retrograde swirling motions in the separated shear layer. The prograde swirling patches are located along the edge of the shear layer and coincide with the spanwise vortex cores. This implies that prograde vortices are more dominant features of the separated shear layer than retrograde vortices. Additional flow structures revealed by the Galilean decomposition include low-speed motions (ejections) away from the leading edge and top surface of the step and high-speed motions (sweeps) towards the wall further downstream. As explained by Tomkins and Adrian (2003), these motions are induced by the spiralling motion of the vortex cores. The appearance of the vortical structures in all the vector fields provides an indication that these structures are recurrent features of the separated and reattached shear layer over the FFS.

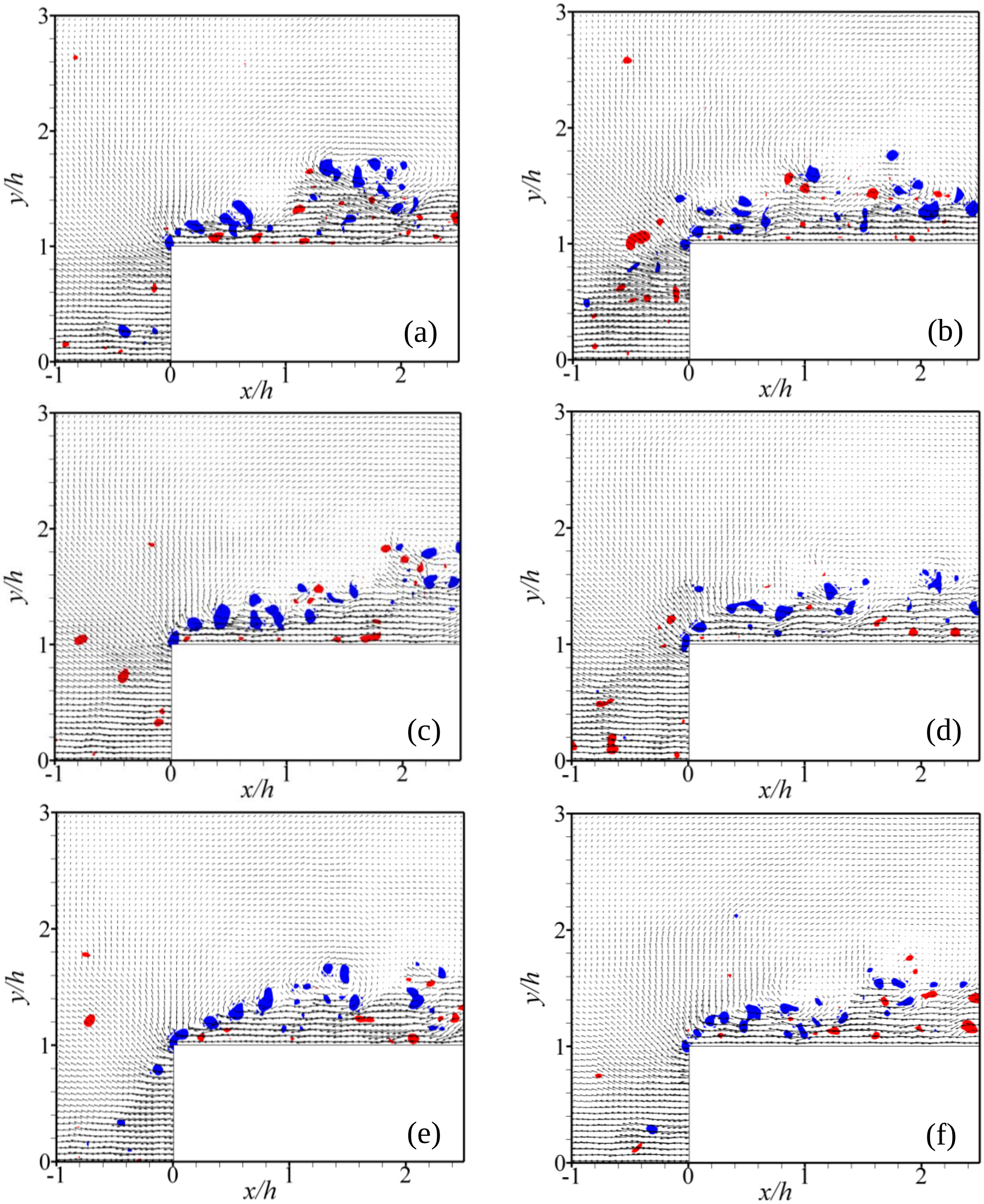

Figure 4.1: Time-sequenced plots of the Galilean decomposition of the instantaneous flow fields over the FFS for the upstream smooth (SM) wall condition: (a) t = 0s (t/T = 0); (b) 2.0s (t/T = 69); (c) 4.0s (t/T = 139); (d) 6.0s (t/T = 208); (e) 8.0s (t/T = 277); (f) 10.0s (t/T = 347).

Figure 4.2 shows the time-sequenced plots of the vector fields for the upstream sandpaper roughness. In this case a constant convection velocity of $U_c \approx 0.7U_o$ was subtracted from the velocity fields to reveal the vortices. For the most part, the coherent structures in the time-sequenced plots are qualitatively similar to those observed for the smooth wall case, except for a reduced streamwise inclination of the spanwise vortices. This would suggest that the transitionally rough 16-grit sandpaper ($k_s^+ \approx 69$) has no significant impact on structure organization over the FFS.

Figure 4.3 shows the Galilean decomposition over the FFS for the upstream staggered cubes with $U_c \approx 0.9U_o$. The plots show frequent large-scale ejections away from the step, extending well into the outer parts of the flow compared to the smooth wall and sandpaper roughness. These large-scale ejections are caused by vigorous eruptions of fluid from the FFS by the cube roughness and are consistent with the relatively large drag characteristics (C_f and k_s^+) observed for the staggered cubes. The plots also show a significantly larger proportion of non-zero swirling strength, which are distributed over a wider area of the flow field than was observed for the cases with the upstream smooth wall and sandpaper roughness. These results are in agreement with previous boundary layer measurements (Volino et al. 2011) over staggered cubes that attributed the violent eruptions to strong Reynolds shear stress producing events in the shear layer.

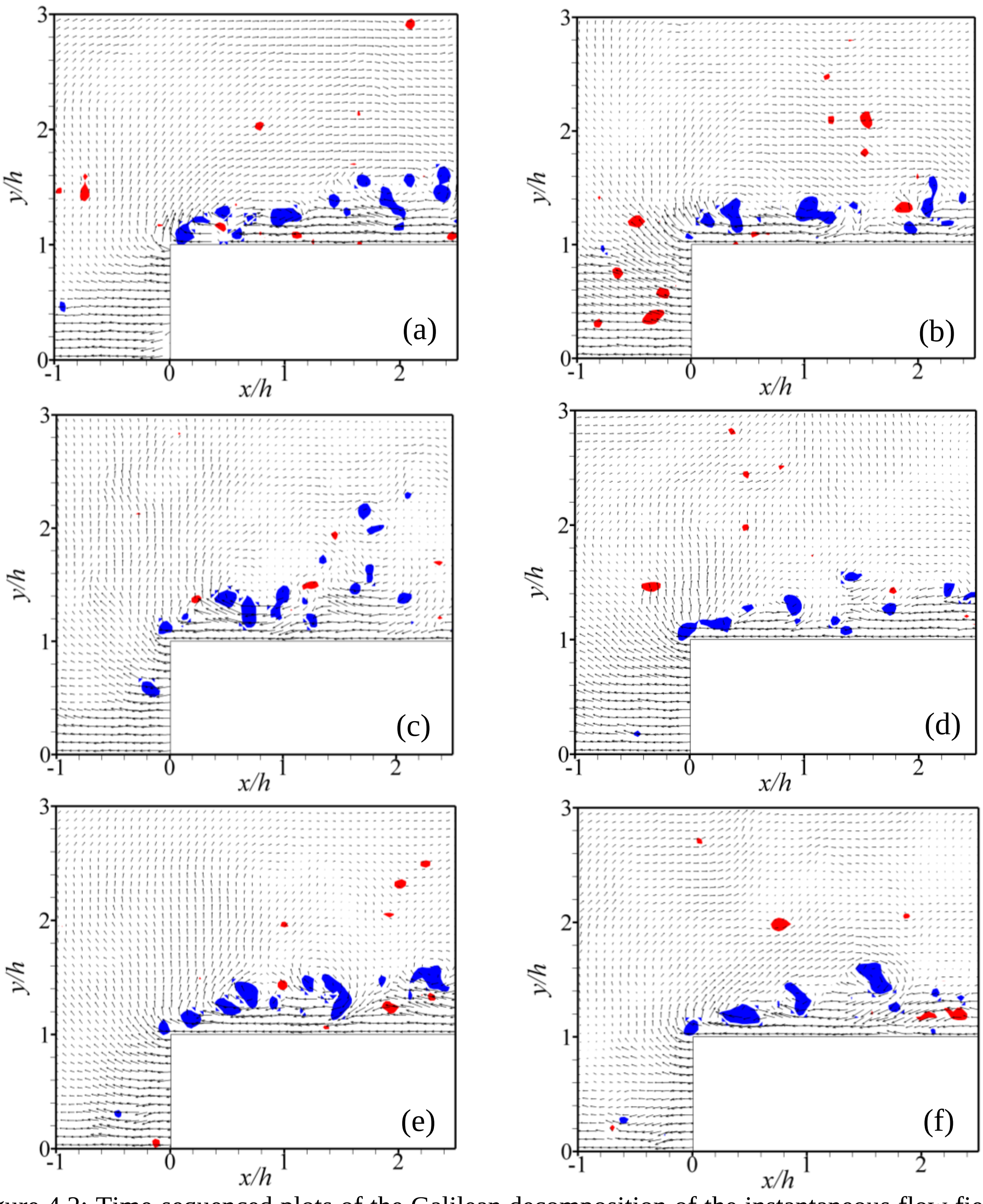

Figure 4.2: Time-sequenced plots of the Galilean decomposition of the instantaneous flow fields over the FFS for the upstream sandpaper (SP) roughness condition: (a) t = 0s (t/T = 0); (b) 2.0s (t/T = 69); (c) 4.0s (t/T = 139); (d) 6.0s (t/T = 208); (e) 8.0s (t/T = 277); (f) 10.0s (t/T = 347).

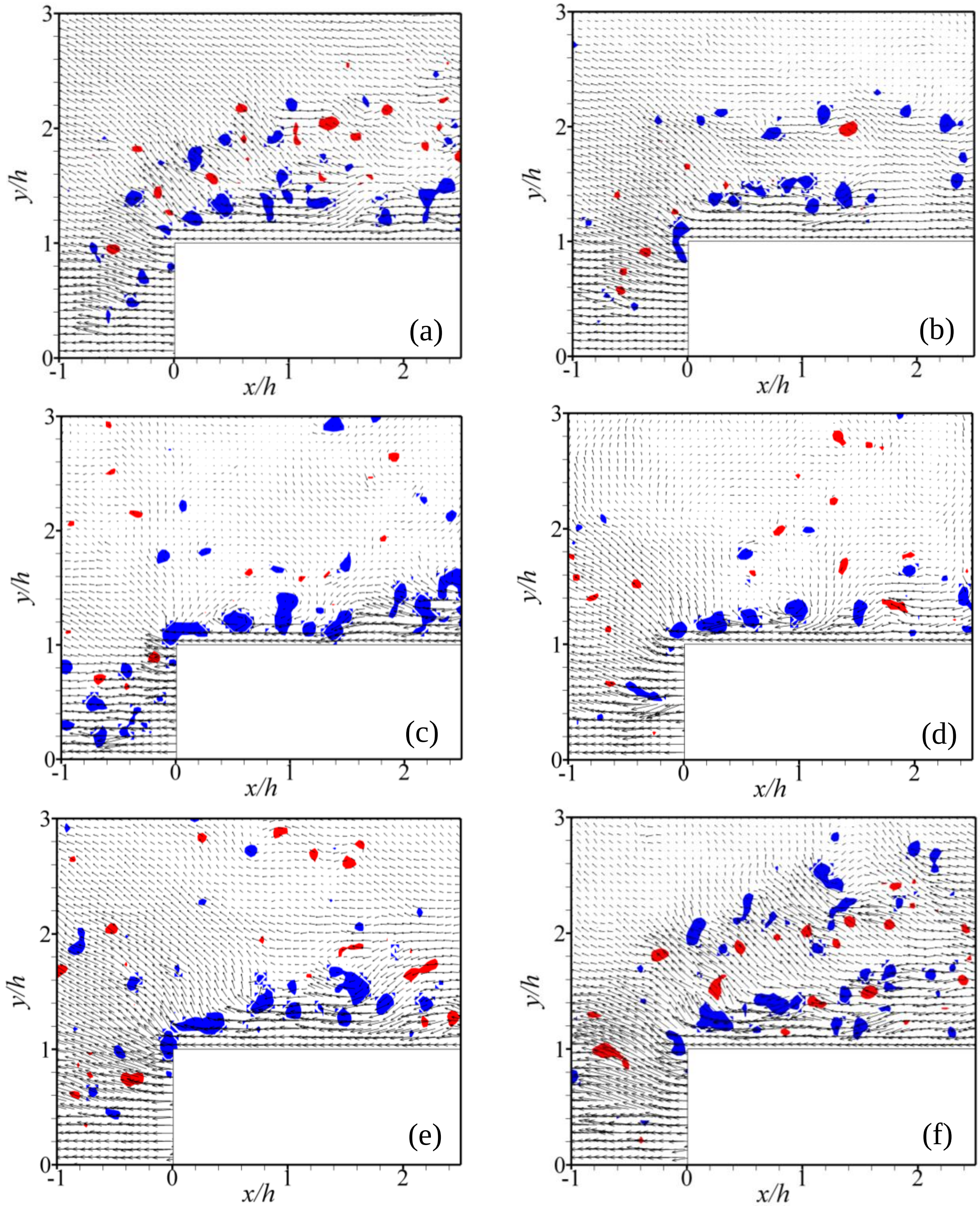

Figure 4.3: Time-sequenced plots of the Galilean decomposition of the instantaneous flow fields over the FFS for the upstream cube (CB) roughness condition: (a) t = 0s (t/T = 0); (b) 2.0s (t/T = 69); (c) 4.0s (t/T = 139); (d) 6.0s (t/T = 208); (e) 8.0s (t/T = 277); (f) 10.0s (t/T = 347).

4.2.2 Flapping of the Separated Shear Layer

The literature identifies two main mechanisms as the factors responsible for the large-scale unsteadiness of the separated and reattached shear layer over the step. These include the Kelvin-Helmholtz roll up of the vortices shed from the leading edge of the step, and the low-frequency oscillation (flapping) of the shear layer. Previous investigations (e.g., Ota et al. 1981; Driver et al. 1987) concluded that the flapping of the shear layer leads to the streamwise oscillation of the instantaneous reattachment point. To investigate flapping of the shear layer the distributions of the temporal auto-correlation of the velocity fluctuations were calculated. For a given reference location (x_{ref}, y_{ref}) and time lag, τ, the temporal auto-correlations were estimated as

$$R_{AA}(x_{ref}, y_{ref}, \tau) = \langle A(x_{ref}, y_{ref}, t) A(x_{ref}, y_{ref}, t+\tau) \rangle / [\sigma_A(x_{ref}, y_{ref}) \sigma_A(x_{ref}, y_{ref})] \quad (4.1)$$

where A denotes the quantity whose auto-correlation function is required and σ_A is the root-mean-square value of A. The temporal auto-correlations R_{uu} and R_{vv}, calculated at the edge of the shear layer near the leading edge of the step ($x/h \approx 0.01$), are shown in Figures 4.4(a) and 4.4(c), respectively. Near the leading edge, the auto-correlations for the smooth and rough walls exhibit a long tail. Similar observations were reported by various investigators (e.g., Ota and Motegi 1983; Kiya and Sasaki 1983; Djilali and Gartshore 1991), who attributed it to the flapping of the shear layer. The distributions also exhibit a high-frequency oscillation with temporal separation (t) due to the large-scale vortices shed from the leading edge of the step. The dimensionless vortex shedding frequency or Strouhal number estimated from the peak values of the frequency spectra, E_{uu} and E_{vv} near the leading edge (Figures 4.4(b) and 4.4(d)) were approximately St_o = 0.103 (3.38Hz), 0.067 (2.35Hz) and 0.059 (2.09Hz), respectively, for the upstream smooth wall, sandpaper and cube roughness. The Strouhal number of 0.103 observed over the smooth wall is in good agreement with the value of approximately 0.1 reported by Pearson et al. (2011) for a FFS flow. The vortex shedding frequency is reduced by the wall roughness in comparison to the smooth wall. Previous bluff body experiments (e.g., Achenbach and Heinecke 1981; Ausoni et al. 2007) suggested that there is a direct connection between the upstream conditions and the vortex shedding frequency. For instance, the vortex shedding frequency was found to increase linearly with an increase in the velocity upstream of smooth and rough airfoils (Ausoni et al. 2007). The lower shedding frequencies observed for the present rough wall cases are in concert with the reduction in the mean streamwise velocity at the step height for these cases.

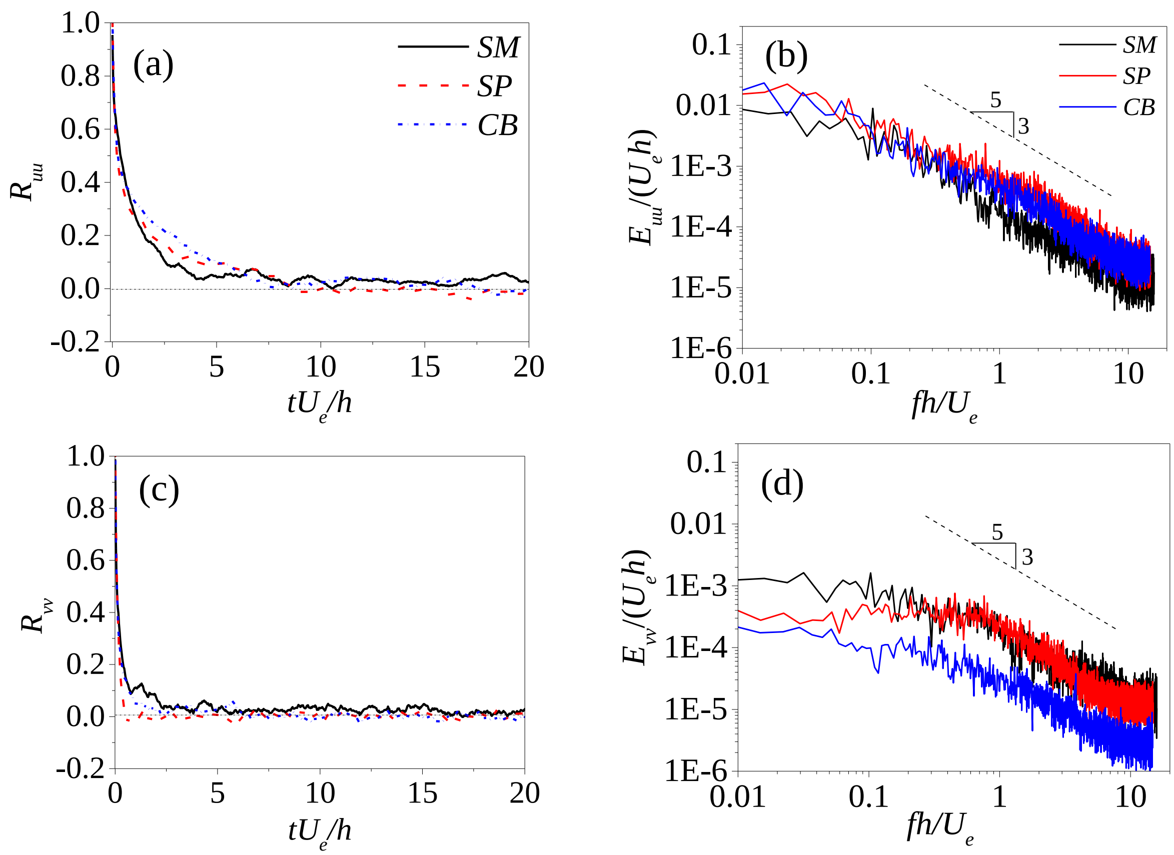

Figure 4.4: Temporal auto-correlations of the velocity fluctuations and energy spectrum near the leading edge of the FFS: (a) R_{uu} vs. dimensionless t; (b) E_{uu} vs. dimensionless f; (c) R_{vv} vs. dimensionless t; (d) E_{vv} vs. dimensionless f.

4.2.3 Distributions of the Mean Velocities and Reynolds Shear Stress

Figure 4.5 shows the iso-contours of the normalized mean streamwise velocity, U/U_o, and the stream function, Ψ, in the recirculation region, where U_o is the freestream velocity of the approach boundary layer.

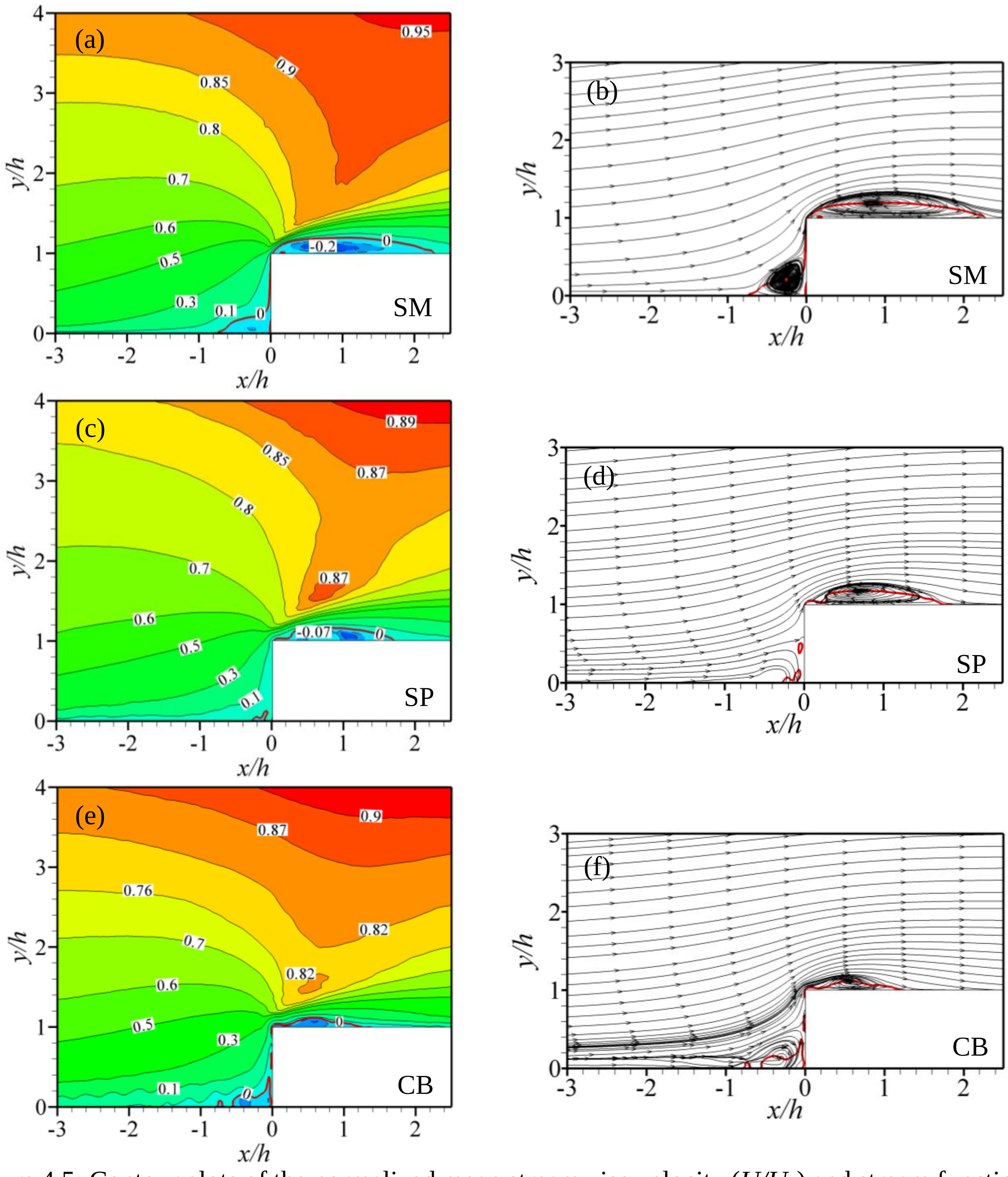

Figure 4.5: Contour plots of the normalized mean streamwise velocity (U/U_o) and stream function over the smooth and rough walls. Top-left to bottom-left: Contours of the mean streamwise velocity. Top-right to bottom-right: Streamlines over the smooth and rough walls.

Figure 4.5(a) shows the mean streamwise velocity contours for the upstream smooth-wall condition. In the vicinity of the step, the flow is decelerated and deflected due to the obstruction caused by step. As observed in previous studies (Chou and Chao 2000; Largeau and Moriniere

2007), the flow is deflected both in the wall-normal and spanwise directions. While the upstream separation is caused by secondary currents within the upstream corner of the step, the separation downstream of the step is due to the sudden change in direction of the flow over the leading edge. The flow separation upstream and downstream of the step results in backflow in both regions depicted as regions of negative mean streamwise velocity. The recirculation bubble in both regions is defined as the area of the flow enclosed by the zero-mean velocity contour line ($U/U_o \approx 0$). The strongest backflow is observed in the primary (downstream) recirculation region, amounting to approximately 20% of the approach velocity. The corresponding mean velocity distributions over the sandpaper and cube roughness are shown in Figures 4.5(c) and 4.5(e), respectively. The distributions over the rough walls bear a close resemblance to the smooth wall except for the smaller primary recirculation zones in these cases compared to the smooth wall. The maximum backflow over the sandpaper and cubes are substantially reduced to about 9% and 4% of the approach velocity, respectively. These results suggest that the upstream roughness has a damping effect on flow separation downstream of the step. This is consistent with the damping of the vortex shedding process over the rough walls.

The streamlines shown in Figures 4.5(b), 4.5(d) and 4.5(f) for the smooth wall, sandpaper and cube roughness, respectively, depict the extents of the recirculation regions for the smooth and rough wall cases. Each plot also shows the zero-mean velocity contour level, superimposed to facilitate the estimation of the mean reattachment lengths, L_r and l_r, of the primary and secondary recirculation regions, respectively. From the streamlines, the centres of the primary recirculation bubble for the smooth wall, sandpaper and cube roughness were estimated to be approximately ($0.82h$, $1.19h$), ($0.68h$, $1.17h$) and ($0.55h$, $1.11h$), respectively. These results indicate a monotonic decrease in the values of the x and y coordinates of the center of the bubble with increasing upstream roughness effect. It should be noted that among all three surface conditions, only the smooth wall and cube roughness exhibit complete streamline reversal in the secondary (upstream) recirculation region. Over the sandpaper, the results were affected by laser light reflection from the roughness elements, leading to difficulties in capturing flow reversal by the camera.

Table 4.2 provides a summary of the mean reattachment lengths, L_r and l_r, as well as the vertical extents, H_r and h_r, of the primary and secondary recirculation regions, respectively. The reattachment length L_r was estimated as the distance from the leading edge of the step to the reattachment point downstream of the step (that is, the x-location where $U/U_o \approx 0$ contour line makes contact with the top face of the FFS), while the reattachment length l_r was estimated as the distance from the upstream separation point to the vertical face of the step (see Figure 1.1). The height of the primary recirculation region (H_r) was estimated as the vertical distance from step to the highest point on the $U/U_o \approx 0$ contour level, while the height of the secondary recirculation region (h_r) was estimated as the distance from the upstream wall to the y-location where the $V/U_o \approx 0$ contour level touches the vertical face of the step. For the smooth wall, the primary reattachment length, $L_r \approx 2.27h$, is in good agreement with the value of $2.5h \pm 0.5\%$ obtained by Sherry et al. (2010) at $Re_{\mathrm{h}} \approx 7500$ for $\delta/h > 1$. The presence of the sandpaper and cube roughness led to reductions of approximately 22% and 45%, respectively, in the primary reattachment length. The upstream reattachment length of $l_r \approx 0.74h$ over the smooth wall is approximately 8% less than the value of approximately $0.8h$ previously reported for FFS flows (Leclercq et al. 2001; Largeau and Moriniere 2007). The rough-wall value of $l_r \approx 0.76h$ suggests that the upstream reattachment length is nearly independent of roughness upstream of the step and agrees with previous observations that the upstream recirculation region of a FFS is relatively stable and independent of upstream disturbances (Pearson et al. 2013). The height of the primary recirculation region for the upstream smooth wall is within the range of $H_r/h \leq 0.5 – 0.8$ reported in the literature (Mohsen 1967; Moss and Baker 1980). In the presence of upstream roughness, however, the value of H_r/h is diminishing, albeit by nearly the same amounts (≈ 20% and 44% for SP and CB, respectively) as for L_r/h. The literature shows that the size of the primary recirculation bubble is highly sensitive to changes in the external turbulence intensity (Hillier and Cherry 1981; Kiya and Sasaki 1983; Largeau and Moriniere 2007), and that an increase in the turbulence intensity contracts the recirculation bubble over the step. In this context, the reductions in L_r/h and H_r/h can be attributed to enhanced turbulence levels over the rough walls ($u_{rms}|_h$ ≈ 8.9% and 11%, respectively, for SP and CB) compared to the smooth wall ($u_{rms}|_h$ ≈ 7.1%). The height of the secondary recirculation region is approximately $h_r \approx 0.56h \pm 3\%$ for the smooth wall and cube roughness. This is within 7% of the value of approximately 0.6h reported in previous boundary layers over FFS (Moss and Baker 1980; Leclercq et al. 2001). Despite the diminishing effect of upstream roughness on L_r/h and H_r/h, the ratio L_r/H_r is relatively invariant with roughness ($L_r/H_r \approx 6.5 \pm 0.19$). The results also indicate that the ratio l_r/h_r is relatively independent of the upstream roughness perturbation.

Table 4.2: Summary of reattachment lengths and heights of the primary and secondary recirculation bubbles

Test	L_r/h	l_r/h	H_r/h	h_r/h	L_r/H_r	l_r/h_r
SM	2.27	0.74	0.34	0.54	6.67	1.37
SP	1.78	---	0.28	---	6.36	---
CB	1.23	0.76	0.19	0.58	6.47	1.31

The effects of upstream roughness on flow acceleration over the step are examined in Figure 4.6. The deflection of the flow by the step leads to mean flow acceleration so that the freestream velocity over the step is higher than that upstream. Figure 4.6(a) shows the streamwise development of the normalized freestream velocity, $U_e^* = U_e/U_o'$, within the range $-1.5 \leq x/h \leq 3.5$, where U_o' is the value of U_e at $x/h = -1.5$. For the upstream smooth wall, U_e^* increases almost linearly within $-1.5 \leq x/h \leq 1.0$ but drops off to near-constant values thereafter. Over the rough walls, the variation of U_e^* with streamwise distance is significantly slower when compared to the smooth wall. This is because of the deceleration of the approach boundary layer by the upstream roughness. The rough-wall distributions take a relatively longer streamwise distance to level out because of the inhomogeneities introduced by the roughness.

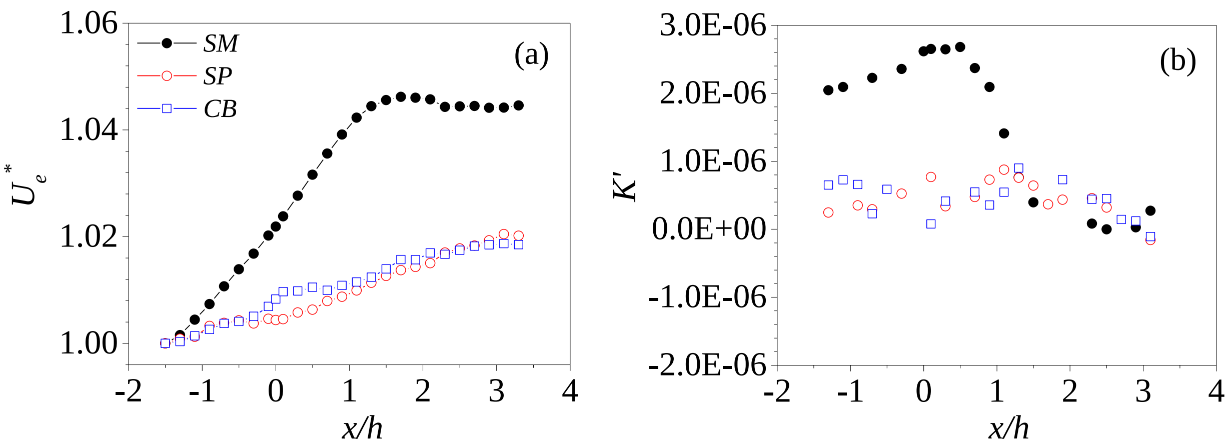

Figure 4.6: Streamwise development of the (a) freestream velocity and (b) acceleration parameter.

Figure 4.6(b) shows the streamwise development of the acceleration parameter, K', estimated as $K' = (\nu/U_e^2)(dU_e/dx)$, at the y location of the maximum mean streamwise velocities, where ν is the kinematic viscosity. In all cases, the value of K' is less than the critical value of $K' \approx 3.5 \times 10^{-6}$ required for an accelerated flow to become relaminarized (Moretti and Kays 1965; Sreenivasan 1982). As expected, the values of K' over smooth wall are substantially higher than over the rough walls within $-1.5 \leq x/h \leq 1.0$. The higher acceleration over the smooth wall will also contribute to a delay in reattachment downstream of the step in the smooth-wall case. For the rough walls, the acceleration parameter is relatively invariant with streamwise distance and is an order of magnitude smaller than for the smooth wall within $-1.5 \leq x/h \leq 1.0$. Further downstream, smooth and rough wall results are nearly similar.

The contours of the mean wall-normal velocity, V/U_o, are presented in Figures 4.7(a), 4.7(c) and 4.7(e), for the smooth wall, sandpaper and cube roughness, respectively. The deflection of the

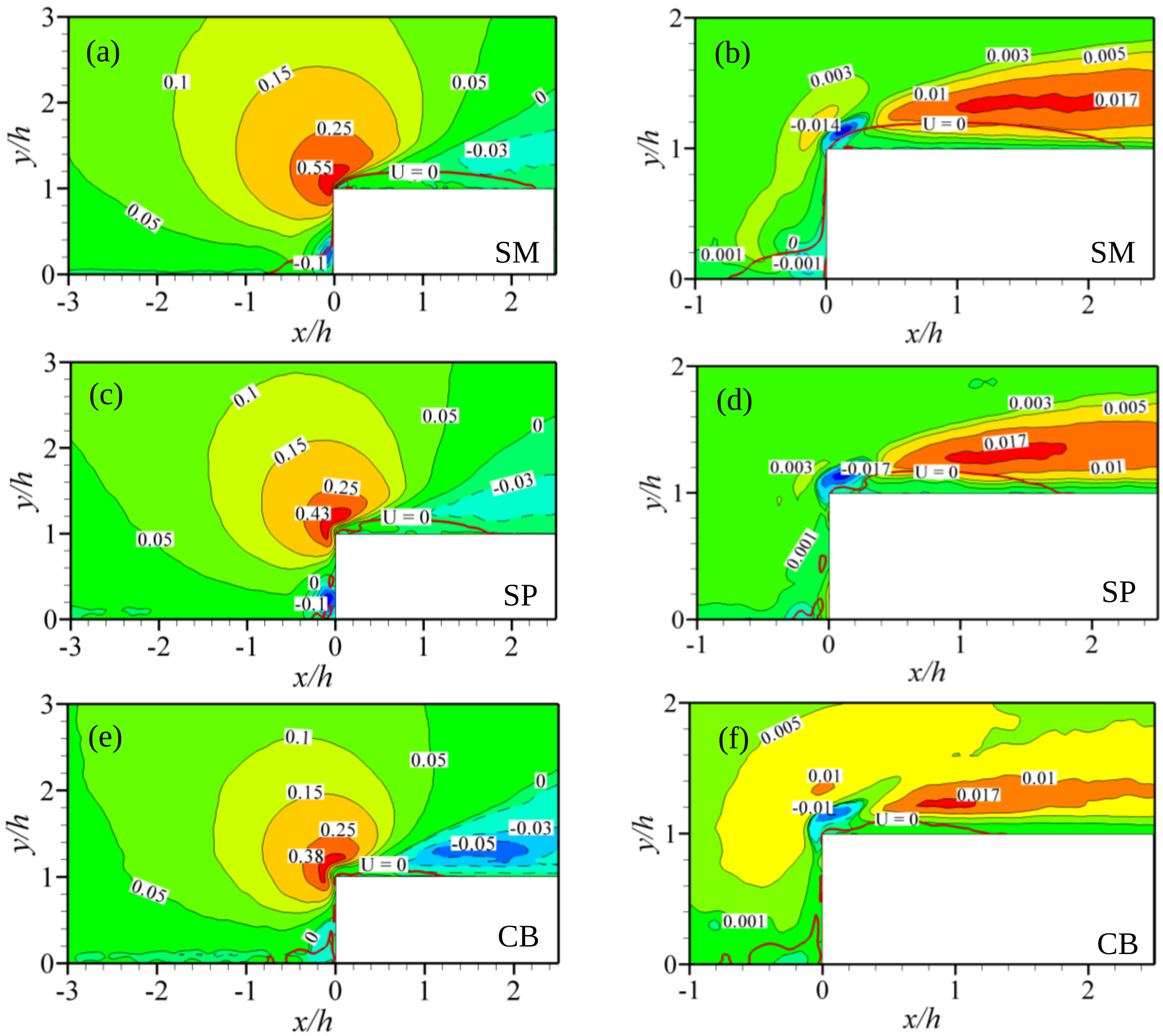

Figure 4.7: Contour plots of the mean wall-normal velocity and Reynolds shear stress over the smooth and rough walls. Top-left to bottom-left: Contours of the mean wall-normal velocity. Top-right to bottom-right: Contours of the Reynolds shear stress over the smooth and rough walls.

flow by the step produces an upwash of fluid near the leading edge of the step. This creates near the leading edge a high positive mean wall-normal velocity, whose magnitude is decreasing with increasing upstream roughness condition. The mean continuity equation for the two-dimensional FFS is given by

$$\partial U/\partial x + \partial V/\partial y = 0 \tag{4.2}$$

As the mean flow accelerates over the step, $\partial U/\partial x > 0$. The continuity equation would imply that $\partial V/\partial y < 0$, as evident in the contours above the separated shear layers. For the rough walls, the flow is undergoing retardation because of the enhanced drag so that $\partial U/\partial x$ is decreasing. To satisfy continuity, $\partial V/\partial y$ must increase. This occurs by means of the reductions in V occurring over smaller wall-normal distances than observed for the smooth wall. This is consistent with the reduction in size of the mean wall-normal velocity contours observed for the rough walls. As the upwash is swept over the step by the high-momentum outward flow ($U > 0$, $V > 0$), the flow near the step reverses direction. This leads to a downwash towards the step, producing regions of negative mean wall-normal velocity downstream of the leading edge. Some of this wall-ward-moving high-momentum fluid ($U > 0$, $V < 0$) is entrained by the primary shear layer to overcome the momentum deficit created by the separation but the effect diminishes with increasing upstream roughness. It should be pointed out that although the downwash towards the wall is more intense with increasing upstream roughness, the streamwise inclination of the $V/U_o \approx 0$ contour level is nearly independent of the roughness effect. A line-fit through the $V/U_o \approx 0$ contour level yields a streamwise inclination angle of approximately 29.5º ± 0.5º for the smooth and rough walls.

Figures 4.7(b), 4.7(d) and 4.7(f) show the contour plots of the Reynolds shear stress, $-\langle u'v'\rangle/U_o^2$ for tests SM, SP and CB, respectively. For the smooth wall, the distribution shows a small region of negative Reynolds shear stress close to the leading edge of the step, as well as an extended region of positive Reynolds shear stress both upstream and downstream of the leading edge. The maximum values of positive Reynolds shear stress ($-\langle u'v'\rangle/U_o^2 \approx 0.17$) occur over the step, which suggest a strong turbulent mixing process that entrains high-momentum freestream fluid into the recirculation region over the step. For the rough walls, the distributions are qualitatively similar and the peak value of the Reynolds shear stress remains approximately the same as for the smooth wall. However, the enclosed area of the maximum contour level is increasingly smaller for the rough-wall cases. It should be noted that the negative Reynolds shear stress near the leading edge of the step occurs also for the rough walls. The region of negative

Reynolds shear stress can be attributed to the presence of the small wall jet produced by the interaction between the upwash along the vertical face and the high-momentum fluid convecting in the streamwise direction. Similar negative Reynolds shear stress regions were reported by previous investigators of flow over smooth FFS (Sherry et al. 2010; Hattori and Nagano 2010) and over rough FFS (Ren and Wu 2011; Essel et al. 2015). Hattori and Nagano 2010 explained the occurrence of the negative Reynolds shear stress near the leading edge to be due to the counter-gradient diffusion phenomenon (CDP) that results in a negative contribution to the kinetic energy of turbulence.

4.2.4 Streamwise Growth of the Separated Shear Layer

The behaviour of the separated shear layer is often compared to a plane mixing layer. The growth of the plane mixing layer is commonly characterized using the vorticity thickness, δ_ω, defined as (Brown and Roshko 1974):

$$\delta_\omega = (U_e - U_{min})/(\partial U/\partial y)_{max} \tag{4.3}$$

where U_{min} is the local minimum mean streamwise velocity in the shear layer. For steady separated shear layers with recirculation, a linear growth of δ_ω has been observed for flow over blunt flat plates (Kiya and Sasaki 1983; Ruderich and Fernholz 1986) and backward facing steps (Eaton and Johnston 1980; Driver and Seegmiller 1985). Figure 4.8(a) first examines the streamwise development of the velocity difference $\Delta U_{max} = U_e - U_{min}$ over the step. For the smooth wall, the normalized velocity difference has a maximum value of approximately 1.1 at the center of the recirculation region. A similar value was reported in separated and reattached turbulent flow over a blunt flat plate (Castro and Haque 1987) and a backward facing step (Driver and Seegmiller 1985). The values of $\Delta U_{max}/U_e$ for SP and CB lie within 1.1 ± 3.5%, which are not significantly different from the smooth wall value.

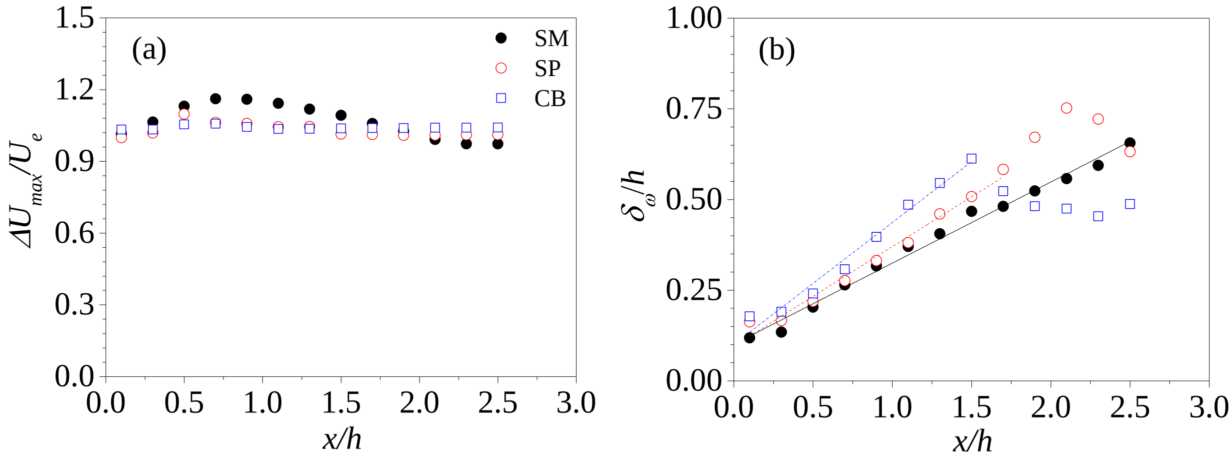

Figure 4.8: Streamwise development of (a) the velocity defect, $\Delta U_{\max}$, and (b) vorticity thickness, δ_w in the recirculation region.

The streamwise evolution of the vorticity thickness, δ_ω for the smooth and rough cases is examined in Figure 4.8(b). The distributions of δ_ω/h are almost linear over the respective streamwise extents of the recirculation regions. For the smooth wall, the growth rate $d\delta_\omega/dx$ was estimated to be approximately 0.224, which compares favorably with the range of values of 0.145 – 0.22 reported by Brown and Roshko (1974) for a single stream plane mixing layer. For the sandpaper and cube roughness, the growth rates are approximately $d\delta_\omega/dx$ = 0.275 and 0.336, respectively, which are about 30% and 50% higher than the smooth-wall value. The drop-off of the rough-wall profiles at larger x/h is due to these points falling outside the recirculation regions for the rough walls.

4.2.5 One-dimensional Profiles of Mean Velocity and Reynolds Stresses

Figure 4.9 presents the one-dimensional profiles of the mean streamwise velocity and Reynolds stresses in the primary recirculation region. The mean velocity is normalized by U_e, while the Reynolds stresses are normalized by U_e^2. The profiles were plotted at three successive streamwise locations: $x/L_r \approx 0$, 0.5 and 1.0 in the recirculation region in order to examine the streamwise evolution of the mean velocity and Reynolds stresses. For each statistic, the corresponding smooth-wall profile obtained at the upstream location, $x/h \approx -20$, is superimposed on the plots for reference.

The profiles from the various streamwise locations are staggered relative to one another with the origin, 0, redefined on the top axes to indicate the correct intervals for the axes. It should be noted that after accounting for the step height, the correct wall-normal location of the top surface of the step is $y/h \approx 1$.

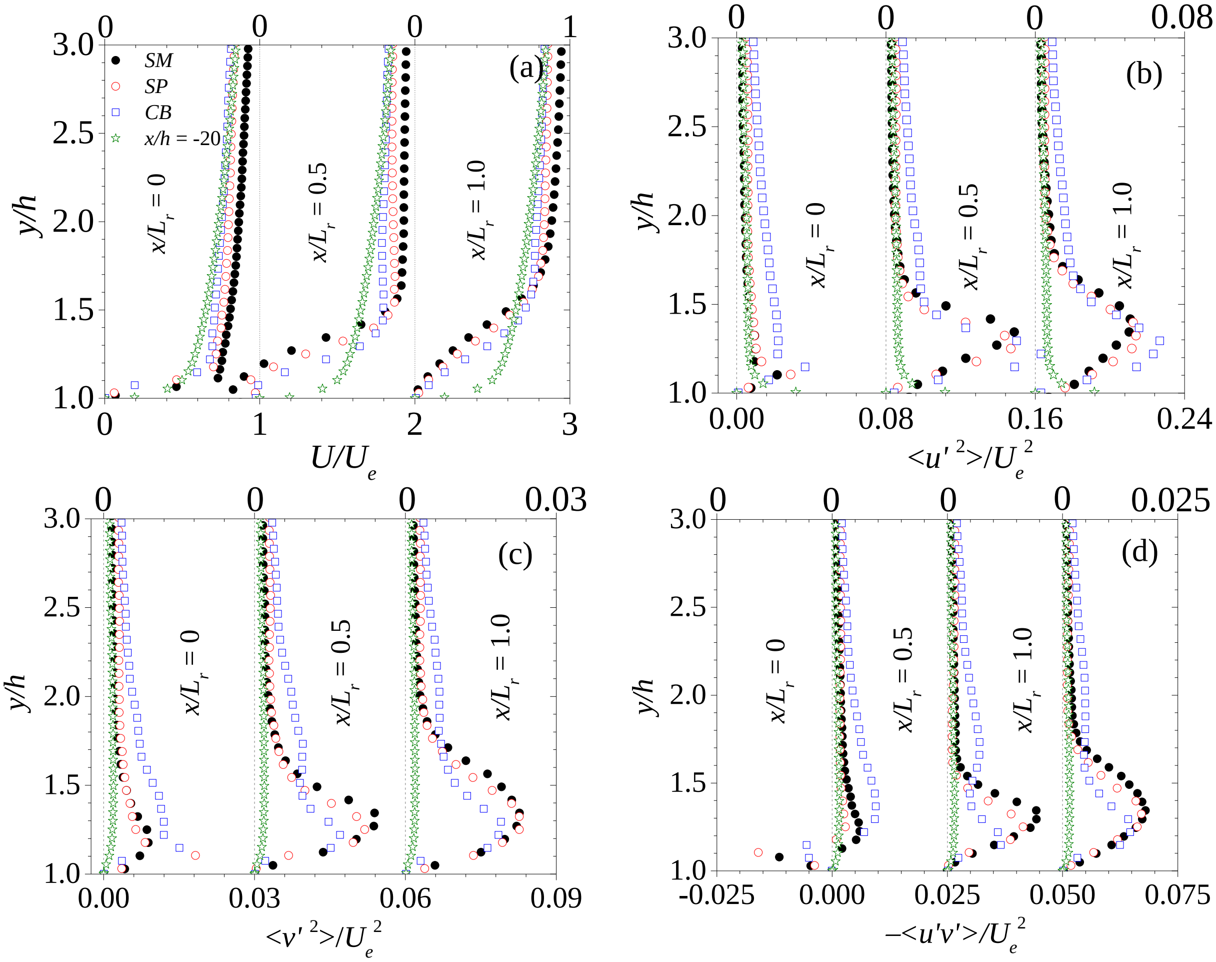

Figure 4.9: Streamwise evolution of the one-dimensional profiles over the FFS for the upstream smooth and rough wall conditions: (a) streamwise mean velocity; (b) streamwise Reynolds stress; (c) wall-normal Reynolds stress; (d) Reynolds shear stress.

The dimensionless mean streamwise velocity profiles (Figure 4.9(a)) at the leading edge of the step indicate a decrease in velocity with upstream roughness for the entire range of y/h. However, all three profiles at $x/L_r \approx 0$ are 'fuller' in comparison to the upstream profile due to the flow acceleration. At the mid- and reattachment points of the recirculation region the influence of acceleration is felt only in the outer parts of the flow. However, for the rough walls the outer part is moving more slowly while the inner part is moving faster than the smooth wall. Within the shear layer the mean velocity profiles develop an inflection point (for example, $y/h \approx 1.3$ at $x/L_r \approx 0.5$ and $y/h \approx 1.4$ at $x/L_r \approx 1.0$), reaching negative values due to the separation. The height of the inflection point grows with streamwise distance until about 2 step heights downstream of the reattachment point. The presence of an inflection point in the mean velocity profile leads to a Kelvin-Helmholtz type instability of the shear layer and the accompanying roll up of the shear layer into spanwise vortex cores. Figure 4.9(b) shows the profiles of the normalized streamwise Reynolds stress, $\langle u'^2 \rangle / U_e^2$. For the smooth-wall condition, the upstream profile reaches a peak value close to the wall because of the high levels of turbulence generated by the quasi-streamwise vortices in the wall region (Krogstad et al. 1992). At the leading edge of the step the peak value is reduced by about 32% compared to the upstream value. This reduction can be attributed to the breakdown of the quasi-streamwise vortices by the step. Over the step, the peak values of the streamwise Reynolds stress coincide approximately with the inflection points of the mean velocity profile, increasing rapidly to values that are substantially larger downstream of the leading edge than at $x/L_r \approx 0$. For example, at $x/L_r \approx 0.5$ and 1, the respective peak values are approximately 218% and 136% higher than at the leading edge. The peak values of $\langle u'^2 \rangle / U_e^2$ are also wider and their wall-normal locations are farther from the wall as the flow propagates downstream due to the effect of the roller vortices. At all three streamwise locations, $\langle u'^2 \rangle / U_e^2$ is unaltered by the sandpaper roughness within the experimental uncertainty limits. For the upstream cube roughness, the streamwise stress is substantially increased at $x/L_r \approx 0$ relative to the smooth wall with a peak that is approximately 69% larger than the corresponding smooth-wall value, albeit the differences diminish with increasing y/h across the boundary layer. At $x/L_r \approx 0.5$ and 1, the stress peaks are enhanced by approximately 21% and 31%, respectively, by the cube roughness, while the cubes' influence on the outer layer gradually diminishes as the flow moves downstream.

The streamwise evolution of the wall-normal stress is shown in Figure 4.9(c). The smooth-wall peak at the leading edge is more than four times as large as the upstream value but is lower than the peaks over the sandpaper and cube roughness by approximately 52% and 41%, respectively. The smooth-wall profile of $\langle v'^2 \rangle / U_e^2$ evolves similarly to that of the streamwise Reynolds stress in the shear layer, but the peak values are approximately 1/3 of those of the streamwise Reynolds stress, indicating the presence of strong anisotropy in the separated shear layer. For the smooth wall, the peak value of $\langle v'^2 \rangle / U_e^2$ at $x/L_r \approx 0.5$ and 1 are respectively 178% and 160% larger than at the leading edge of the step. Downstream of the leading edge, the disparity between the sandpaper and smooth-wall profiles gradually disappears as the influence of the sandpaper diminishes. On the contrary, cube roughness reduced the peak value of $\langle v'^2 \rangle / U_e^2$ at $x/L_r \approx 0.5$ and 1 by approximately 27% and 17%, respectively, in comparison to the smooth wall. It should be noted that reductions in wall-normal stress are limited to the region of negative mean wall-normal velocity ($V < 0$). Above this region ($V > 0$), the cubes increased the wall-normal stress relative to the smooth wall and sandpaper roughness. These discrepancies are consistent with the more rapid reduction in vortex shedding frequency by the cubes (Figure 4.4) but more intense ejections in the outer layer (Figure 4.3) than the smooth wall and sandpaper.

Profiles of the Reynolds shear stress, $-\langle u'v' \rangle / U_e^2$ (Figure 4.9(d)), are qualitatively similar to those of the wall-normal stress in the shear layer, except near the leading edge of the step where the profiles develop negative peak values due to the counter-gradient diffusion phenomenon. Evaluation of the production term in the turbulent kinetic energy equation,

$$P_K = -[\langle u'^2 \rangle \partial U/\partial x + \langle v'^2 \rangle \partial V/\partial y + \langle u'v' \rangle (\partial U/\partial y + \partial V/\partial x)], \tag{4.4}$$

near the leading edge of the step showed negative turbulence production for the smooth and rough walls (not shown). It was found that the negative turbulence production is predominantly due to the shear component, $-\langle u'v' \rangle(\partial U/\partial y + \partial V/\partial x)$, arising from negative $-\langle u'v' \rangle$ and positive $(\partial U/\partial y + \partial V/\partial x)$ near the leading edge of the step. As will be shown subsequently, the negative values of the Reynolds shear stress can be attributed to the dominance of negative Reynolds shear stress producing events near the leading edge. These events are accompanied by a turbulent transport of $-\langle u'v' \rangle$ away from the leading edge. The counter-gradient diffusion of Reynolds shear stress near the leading edge would imply that eddy-viscosity models based on the assumption of positive eddy viscosity will fail to properly predict the flow near the corner of the step (Essel et al. 2015). Downstream of the leading edge, the peak Reynolds shear stress for the smooth wall and sandpaper roughness are about an order of magnitude higher than the upstream smooth-wall value. This demonstrates the enhanced turbulence mixing of the separated shear layer compared to the nominally ZPG upstream turbulent boundary layer. As observed for wall-normal stress, the cube roughness reduced the peak value of the Reynolds shear stress by approximately 36% and 17% at $x/L_r \approx 0.5$ and $x/L_r \approx 1$, respectively, in comparison to the smooth wall.

4.2.6 Quadrant Decomposition of the Reynolds Shear Stresses

In order to investigate the dominant motions contributing to the mean Reynolds shear stress a quadrant decomposition was performed for the smooth- and rough-wall cases. Using the Lu and Willmarth's (1973) hyperbolic hole method, the contribution of each quadrant of the u'-v' plane to the mean Reynolds shear stress were estimated for $H_q = 0$, where the hole size of 0 represents Reynolds shear stress contributions from all events in the decomposition.

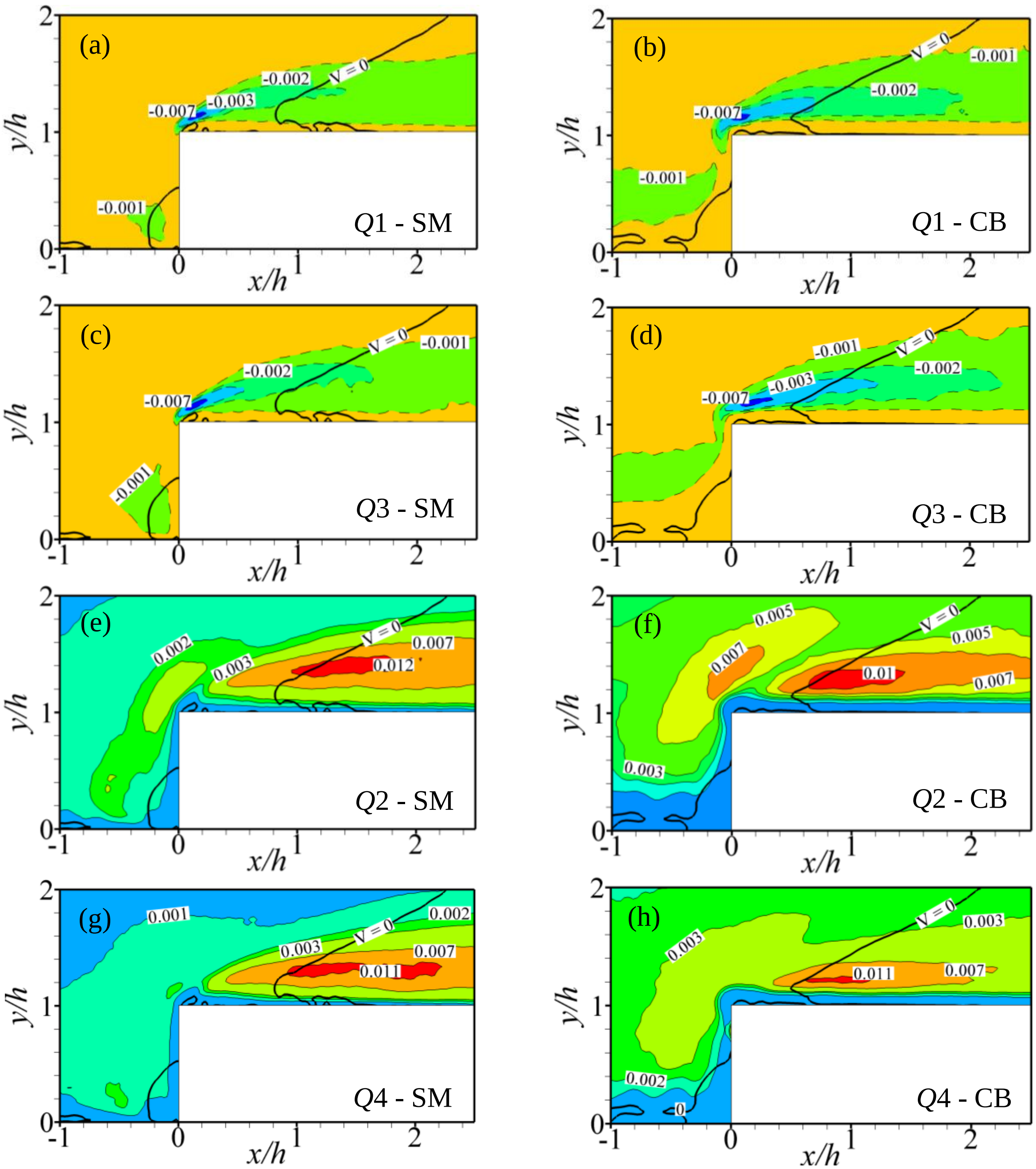

Figure 4.10: Contours of the quadrant decomposition of the Reynolds shear stress over the FFS for smooth wall and cube roughness.

Figure 4.10 presents the iso-contours of the contributions from the four quadrants: outward interactions (Q1), ejections (Q2), inward interactions (Q3) and sweeps (Q4) for the smooth wall and rough walls for a hyperbolic hole of size 0. Using a hole size of 0 ensures that all Reynolds shear stress events are included in the decomposition. It should be noted that only the smooth wall and cubes results are presented here because the sandpaper results were found to be similar to the smooth wall. The thick solid line in the plots corresponds to the $V = 0$ contour level superimposed to demarcate the regions of positive and negative mean wall-normal velocity. The results in Figures 4.10(a) to 4.10(d) indicate that the negative Reynolds shear stress at the leading edge, produced by the counter-gradient diffusion phenomenon, can be attributed to more prevalent Q1 and Q3 events near the leading edge in the smooth and rough cases. The identical peak value of –0.007 in all four plots suggest that the inward and outward interaction terms contributed nearly equally to the negative Reynolds shear stress near the leading edge of the step for both upstream conditions. However, the wider spread of the larger-magnitude contours ($-0.007 \leq -\langle u'v' \rangle / U_o^2 \leq -0.002$) of Q1 and Q3 in the cubes case would have a diminishing effect on the mean Reynolds shear stress downstream of the leading edge compared to the smooth wall. The contour plots in Figures 4.10(e) – 4.10(h) show that ejections (Q2) are the more dominant contributors to the Reynolds shear stress in the shear layer compared to sweeps (Q4). Above the leading edge of the step for CB (Figure 4.10(f)), a region of relatively intense ejections is observed, which is reminiscent of the large-scale ejections from the step observed in the instantaneous flow visualizations of CB (Figure 4.3). Other than this feature, the upstream roughness suppresses the ejection and sweep motions in comparison to the smooth wall, although the effect is more dramatic on Q4 than Q2. These results are qualitatively consistent with previous fully developed channel measurements with upstream wall roughness (Essel et al. 2015) and turbulent boundary layer measurements over a rough FFS (Ren and Wu 2011).

In order to compare the relative magnitudes of the quadrant contributions at specific locations over the step, one-dimensional profiles of the contributions are plotted in Figure 4.11. The peak values of Q1 and Q3 have the largest magnitude near the leading edge of the step and decrease with streamwise distance in the recirculation region. Downstream of the leading edge

($x/L_r > 0$), the smooth wall and sandpaper distributions are in agreement to within measurement uncertainty. However, the cube roughness produces an increase of approximately 43% in Q1 at the intermediate location, $x/L_r \approx 0.5$ when compared to the smooth wall that vanishes near the reattachment point (Figure 4.11(a)).

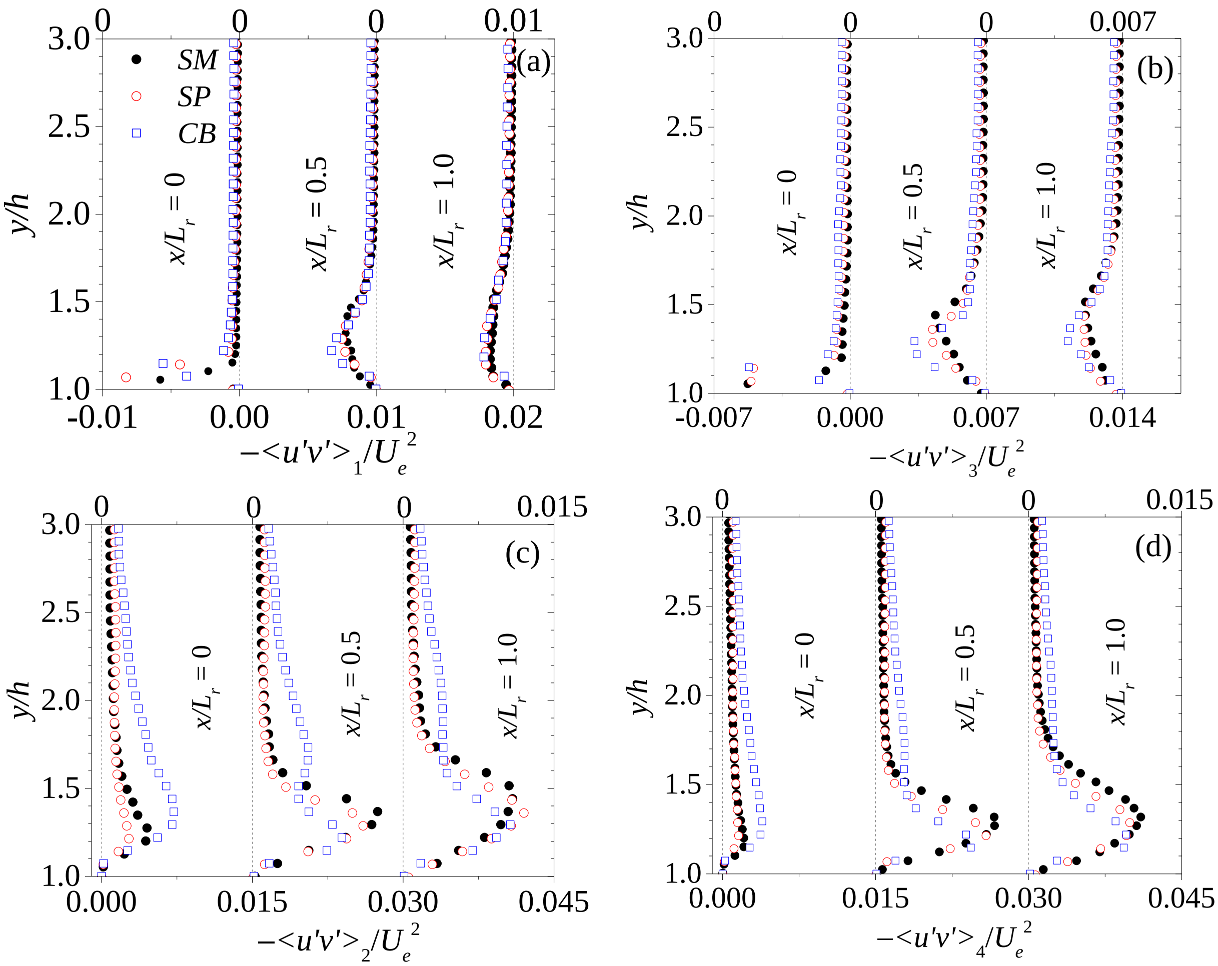

Figure 4.11: Profiles of the quadrant events over the step for the upstream smooth and rough wall conditions: (a) Quadrant 1: outward interactions ($Q1$); (b) Quadrant 3: inward interactions ($Q3$); (c) Quadrant 2: ejections ($Q2$); (d) Quadrant 4: sweeps ($Q4$).

Figure 4.11(b) shows that there is approximately a 36% increase in the peak value of Q3 from the smooth wall to the cube roughness at the center of the recirculation region. This difference increases to about 45% near the reattachment point over the step. Profiles of the Q2 (ejection) contributions are shown in Figure 4.11(c). Near the leading edge, the peak value of Q2 is reduced by the sandpaper by approximately 41% but enhanced by the cubes by approximately 59%. The lower peak of Q2 for SP can be attributed to a more substantial loss of Reynolds shear stress by counter-gradient diffusion near the corner of the step compared to SM and CB. Further downstream, the cubes reduced the Q2 contributions near the wall but produced enhancements in the outer layer. Downstream of the leading edge, differences are found between the sandpaper and smooth wall but these are within the measurement uncertainty. At $x/L_r \approx 0.5$ and $x/L_r \approx 1$, the near-wall reductions by the cube roughness are approximately 30% and 14%, respectively. The quadrant 4 profiles are presented in Figure 4.11(d). At $x/L_r \approx 0$, the peak values of Q4 are about 56%, 44% and 47% lower than those of Q2 for SM, SP and CB, respectively. Again, the cube roughness increases Q4 near the leading edge, albeit by a larger amount (75%) compared to the smooth wall and sandpaper. This is followed by reductions near the wall and enhancements above the shear layer for $x/L_r > 0$ in comparison to the smooth wall. The outer layer enhancements of Q2 and Q4 by the cubes are consistent with a similar trend in the Reynolds shear stress distributions but most of this is due to the effect of the cubes on Q2.

4.2.7 Turbulent Transport

The structural differences in the Reynolds stress producing motions are imprinted on the higher-order turbulence statistics, such as triple velocity correlations. In the Reynolds stress transport equations, the spatial gradients of the triple correlations determine the turbulent transport of the Reynolds stresses in the flow. The profiles of the triple correlations, representing turbulent transport in the wall-normal direction, are shown in Figure 4.12 non-dimensionalized by U_e^3. Figure 4.12(a) presents the profiles of the wall-normal turbulent transport of the streamwise Reynolds stress ($\langle u'^2v'\rangle$). Near the leading edge of the step ($x/L_r \approx 0.0$, $y/h \approx 1.1$), $\langle u'^2v'\rangle$ is negative for the smooth wall but positive for the sandpaper and cube roughness. The negative smooth wall

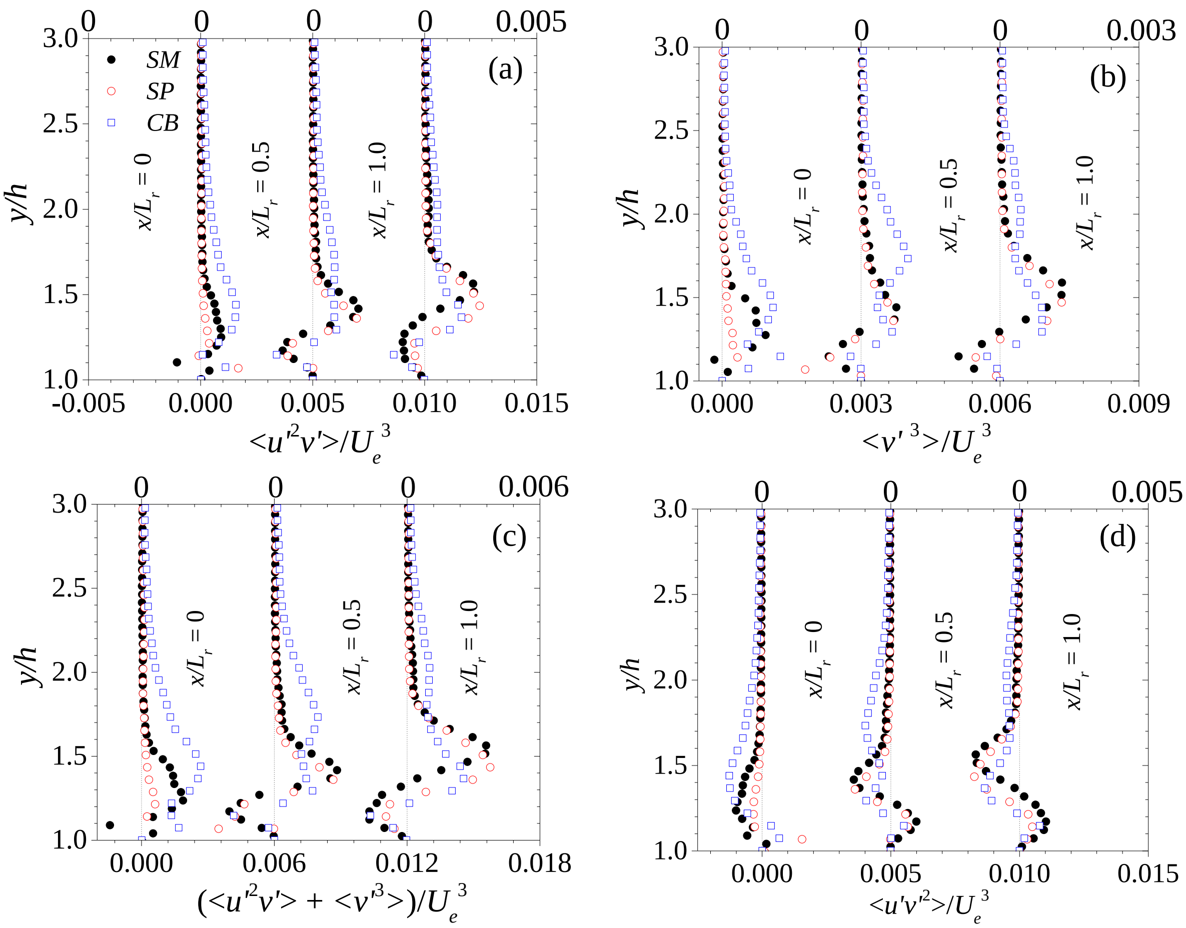

Figure 4.12: Profiles of the triple correlations over the step for the upstream smooth and rough wall conditions: (a) wall-normal transport of u'^2; (b) wall-normal transport of v'^2; (c) wall-normal transport of turbulent kinetic energy; (d) wall-normal transport of Reynolds shear stress.

value can be attributed to negative excursions in the wall-normal motions in this case and indicates the turbulent transport of streamwise Reynolds stress towards the leading edge. In contrast, the positive near-wall values of $\langle u'^2v' \rangle$ observed for the sandpaper and cube roughness are due to more frequent positive excursions of v' in these cases and indicate an upward transport of streamwise Reynolds stress away from the leading edge of the step. Similar results were noticed in the skewness factors of u' and v' (not shown) for the smooth and rough walls. Above the leading edge, a secondary peak develops in the profiles of $\langle u'^2v' \rangle$, that is approximately 62% and 295% higher for CB than SM and SP, respectively. These positive peaks would also imply an outward transport of $\langle u'^2 \rangle$ towards the outer parts of the flow away from the locations of high streamwise stress, which are $y/h \approx 1.3$ and 1.5 at $x/L_r \approx 0.5$ and 1, respectively. It should be noted that near the leading edge, $\langle u'^2 v' \rangle$ decays more rapidly with y/h in the sandpaper case than the smooth wall and cube roughness. This may be attributed to the high irregularity of the sandpaper roughness. Downstream of the leading edge, the profiles of $\langle u'^2 v' \rangle$ are antisymmetric about the edge of the separated shear layer, reaching peak values to either side of the edge of the shear layer. The negative peaks near the wall would imply a turbulent transport of u'^2 towards the wall, while the positive peaks would imply a turbulent transport u'^2 towards the outer layer. Above the recirculation bubble the magnitude of u'^2 transported by the wall-normal motion diminishes for CB because the cubes reduced the streamwise Reynolds stress in this region. In the outer flow, positive values are still observed for the cube roughness although they decay slightly with x/L_r.

Figure 4.12(b) shows profiles of the wall-normal turbulent transport of the wall-normal stress ($\langle v'^3 \rangle$). The profiles are qualitatively similar to those of $\langle u'^2 v' \rangle$, suggesting that the motions responsible for the wall-normal transport of the streamwise and wall-normal Reynolds stresses are similar. At $x/L_r \approx 0$, the wall-ward transport of v'^2 is much smaller than that of u'^2 for the upstream smooth wall condition. Away from the wall, the cube roughness increased the positive peak value of $\langle v'^3 \rangle$ by approximately 52% in comparison to the smooth wall and produced more than a four-fold increase in comparison to the sandpaper. In the downstream region, the increases produced by the cube in the outer layer are more substantial than were observed for $\langle u'^2 v' \rangle$ in Figure 4.12(a). At the same time, the near-wall negative values of $\langle v'^3 \rangle$ within the shear layer are attenuated for the cube roughness in comparison to the smooth wall and sandpaper roughness.

Figure 4.12(c) shows the profiles of the wall-normal transport of the turbulent kinetic energy, $\langle u'^2 v' \rangle + \langle v'^3 \rangle$. At $x/L_r \approx 0$, $\langle u'^2 v' \rangle + \langle v'^3 \rangle$ is negative for the smooth wall and positive for the sandpaper and cube roughness in the near-wall region. The negative near-wall value observed for SM suggests that the contribution to turbulent diffusion, $-\partial(\langle u'^2v'\rangle + \langle v'^3\rangle)/\partial y$ is positive. This indicates a gain in turbulent kinetic energy by diffusion near the leading edge. The positive near-wall values for the rough walls suggest that the mechanism for the turbulent transport of the turbulent kinetic constitutes a loss in energy as opposed to a gain in energy in the smooth wall case. In the downstream region, $-\partial(\langle u'^2v'\rangle + \langle v'^3\rangle)/\partial y$ is consistently positive in the proximity of the wall ($1.0 \leq y/h \leq 1.2$), indicating a gain in energy by diffusion at a rate that is nearly independent of upstream roughness. The near-wall gain in energy is fed by the loss in energy by diffusion within the adjacent region $1.2 \leq y/h \leq 1.5$. While the term $\langle u'^2v'\rangle + \langle v'^3\rangle$ decays rapidly with y/h beyond the location of positive peak value for SM and SP, there is substantial turbulent diffusion of the turbulent kinetic energy for the cubes. Within $1.5 \leq y/h \leq 1.8$ and $1.7 \leq y/h \leq 2.0$ at $x/L_r \approx 0.5$ and $x/L_r \approx 1.0$, respectively, there is a loss in energy by diffusion for CB, leading to a reduction in peak value of $\langle u'^2v'\rangle + \langle v'^3\rangle$ by approximately 57% and 74% for CB near $y/h \approx 1.5$ compared to SM and SP.

Figure 4.12(d) shows profiles of the wall-normal turbulent transport of the Reynolds shear stress ($\langle u'v'^2\rangle$). Near the leading edge, $\langle u'v'^2\rangle$ is predominantly positive within $1.0 \leq y/h \leq 1.1$. This is within the counter-gradient Reynolds shear stress zone of the leading edge. The positive near-wall values of $\langle u'v'^2\rangle$ suggest a turbulent transport of $u'v'$ away from the wall. This counter-gradient transport of Reynolds shear stress results in loss in Reynolds shear stress near the leading edge of the step. Within the recirculation region, the $\langle u'v'^2\rangle$ correlations remain positive in the wall region but the peak values are farther from the wall than observed near the leading edge. The correlation is also nearly independent of upstream roughness in the wall region. Further from the wall ($y/h >$ 1.3), there is a gain in Reynolds shear stress by turbulent diffusion fed by the loss in Reynolds shear stress by turbulent diffusion from the wall region. Although this is comparable for SM and

SP, it is smaller for CB so that the negative peak near $y/h \approx 1.4$ is reduced for CB in comparison to SM and SP.

4.2.8 Joint Probability Density Function Distributions

The joint probability density function (pdf), $P(u', v')$ defined as (Wallace and Brodkey 1977)

$$\langle u'v' \rangle = \iint_{-\infty}^{+\infty} u'v' P(u', v') du' dv' \tag{4.5}$$

is often used to investigate the correlation between the instantaneous velocity fluctuations. It should be noted that the integral in equation (4.5) is not a time average but a probability-weighted average of $u'v'(t)$. The joint pdfs were estimated by sorting the velocity fluctuations into equal-width 100 × 100 bins. Figure 4.13 shows the distributions of the joint pdfs at the three streamwise locations, $x/L_r \approx 0$, 0.5 and 1.0 for the smooth and rough walls. At $x/L_r \approx 0$ (top row), the joint pdfs were calculated at $y/h \approx 1.1$. At $x/L_r \approx 0.5$ (middle row), the calculations were done at $y/h = 1 + H_r/h$, which corresponds to the highest point on the mean dividing streamline. At $x/L_r \approx 1.0$ (bottom row), the distributions were calculated at $y/h \approx 1.1$. For non-isotropic turbulence, the contours of $P(u', v')$ are elliptical, where the innermost contours correspond to high-probability but weak Reynolds shear stress events and outermost contours correspond to strong but low-probability events. Thus, the total Reynolds shear stress will be a balance between the strong but low-probability joint events and the weak but high probability joint events. Near the leading edge (Figures 4.13(a), 4.13(b) and 4.13(c)), the distributions are inclined towards Q1 and Q3, indicating the predominance of outward and inward interactions in the determination of the Reynolds shear stress. These results are also consistent with the negative Reynolds shear stress values observed near the leading edge of the step for the smooth and rough walls. With increasing upstream roughness condition, the maximum contour becomes increasingly elongated in the third quadrant. The larger size and more elongated shape of the maximum contour for CB is in agreement with the relatively large spread of the higher contours levels in Q3 in the quadrant decomposition for CB.

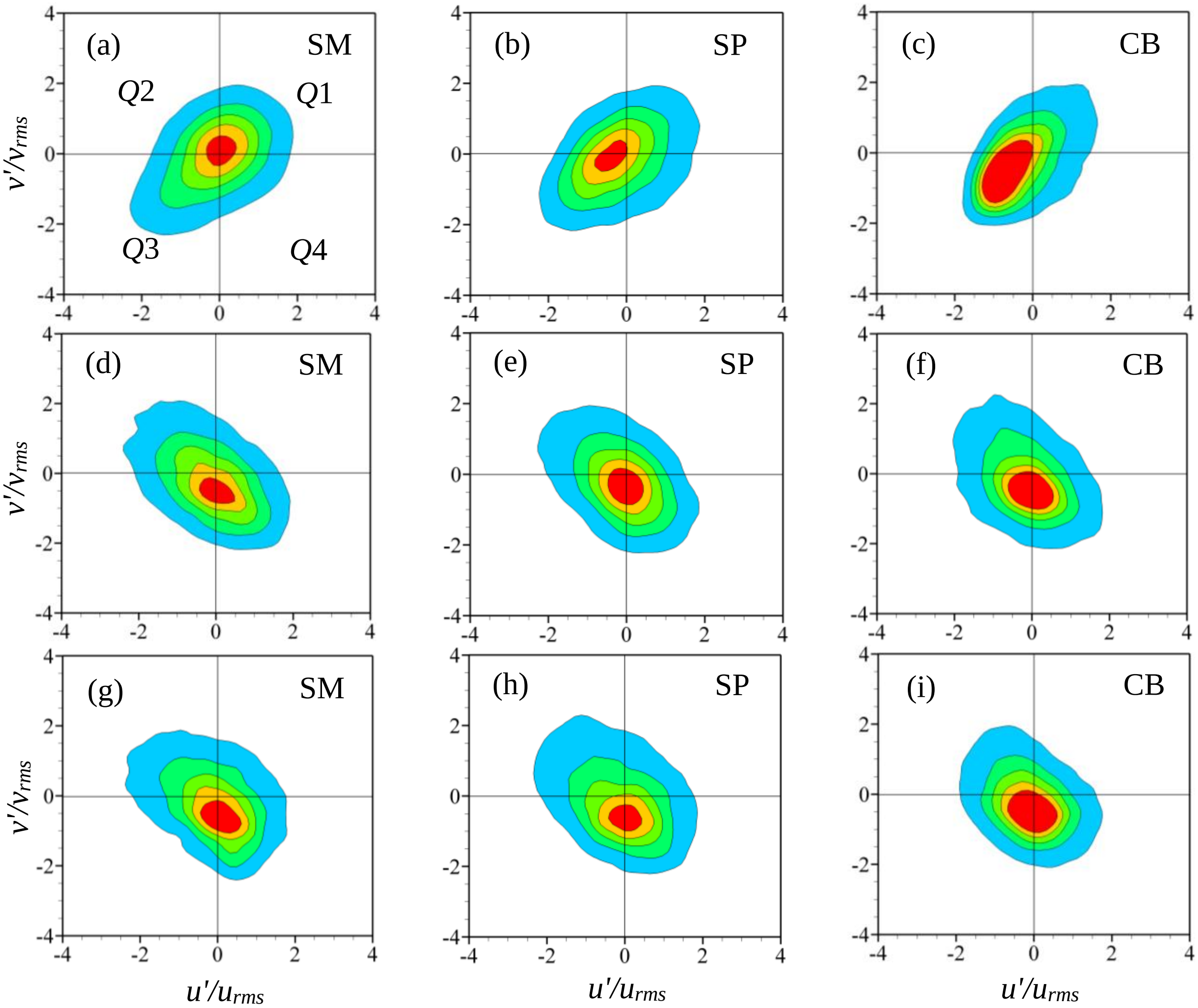

Figure 4.13: Contours of the joint PDF of the velocity fluctuations along the mean dividing streamline: (a) SM (x/L_r = 0, y/h = 1.1); (b) SP (x/L_r = 0, y/h = 1.1); (c) CB (x/L_r = 0, y/h = 1.1); (d) SM (x/L_r = 0.5, $y/h = 1 + H_r/h$); (e) SP (x/L_r = 0.5, $y/h = 1 + H_r/h$); (f) CB (x/L_r = 0.5, $y/h = 1 + H_r/h$); (g) SM (x/L_r = 1.0, y/h = 1.1); (h) SP (x/L_r = 1.0, y/h = 1.1); (i) CB (x/L_r = 1.0, y/h = 1.1). Contour levels are from 0.0005 to 0.0045 at intervals of 0.001. H_r is as defined in Figure 1.1.

At $x/L_r \approx 0.5$ (Figures 4.13(d), 4.13(e) and 4.13(f)), where the chosen wall-normal location also coincides with the location of $[-\langle u'v'\rangle/U_e^2]_{\max}$, the iso-probability contours are inclined towards Q2 and Q4. The Q2-Q4 inclination indicates the larger contributions of ejections and sweeps to the mean Reynolds shear stress at this location as observed in the quadrant decomposition. It can also be discerned that the contours for SM and SP are more elliptical than those for CB that show a slight expansion in Q2 and a contraction towards the highest probability contour in Q3. Despite the expansion in Q2, the resulting large-amplitude values have low probabilities, and therefore do not contribute as much as Q3. The closeness of the larger-amplitude contours in Q3 to the maximum contour suggest a non-negligible influence of Q3 in the determination of the Reynolds shear stress, which explains the reduction in the peak value of $-\langle u'v'\rangle/U_e^2$ for CB in comparison to SM and SP at this location. The contours presented at $x/L_r \approx 1.0$ (Figures 4.13(g), 4.13(h) and 4.13(i)) for SM, SP and CB are also predominantly skewed towards Q2 and Q4 in agreement with the more dominant contribution of ejections and sweeps to the Reynolds shear stress at this location. For a given surface, the joint pdfs are nearly independent of streamwise distance in the recirculation bubble.

Figure 4.14 shows the distributions of the joint pdfs at successive wall-normal locations ($y/h \approx 1.1$, 1.5, 2.0, 2.5) away from the leading edge of the step for SM (left column), SP (middle column) and CB (right column). Except for the joint pdfs close to the leading edge (Figures 4.14(a) – 4.14(c)), all distributions show a Q2-Q4 orientation because Q2 and Q4 motions contribute the largest to the Reynolds shear stress ($-\langle u'v'\rangle$). At $y/h \approx 1.5$, the maximum joint pdfs shift in favour of the second quadrant, indicating the dominance of ejections in producing the Reynolds shear stress compared to sweeps. The smaller size of the maximum contour for SP is consistent with the lower value of the corresponding Reynolds shear stress compared to SM and CB at $y/h \approx 1.5$. Away from the wall, the outermost (low-probability) contours do not show any systematic change in size, but the maximum probability contours generally diminish in size. Also, at $y/h \approx 2$ for SP, the maximum joint pdf contour is inclined towards the negative-u' axis, indicating the prevalence of negative-u' motions of relatively small amplitude of v'-fluctuations in the Reynolds shear stress signal.

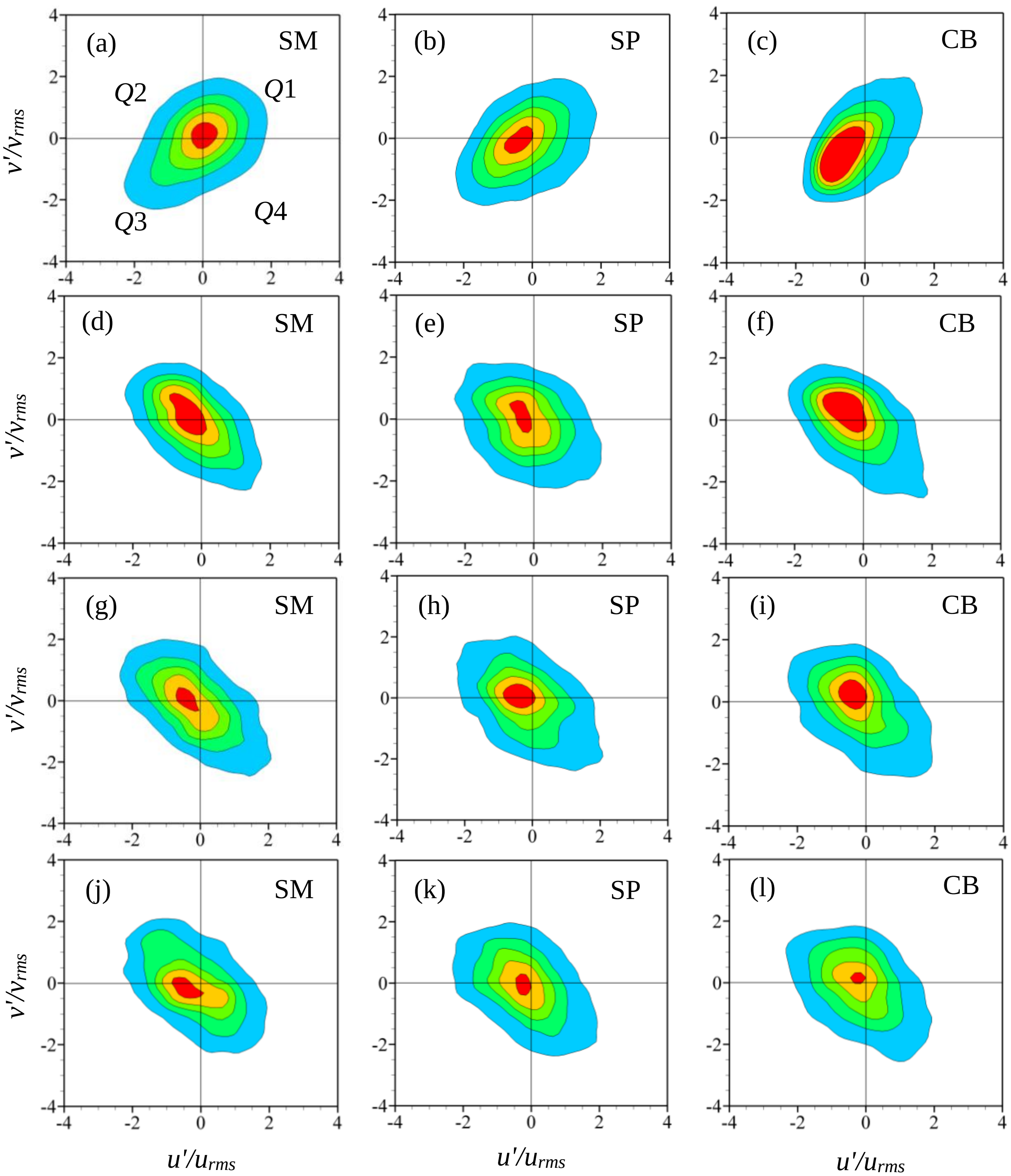

Figure 4.14: Contours of the joint PDF of the velocity fluctuations along the wall-normal direction: (a) SM (x/L_r = 0, y/h = 1.1); (b) SP (x/L_r = 0, y/h = 1.1); (c) CB (x/L_r = 0, y/h = 1.1); (d) SM (x/L_r = 0, y/h = 1.5); (e) SP (x/L_r = 0, y/h = 1.5); (f) CB (x/L_r = 0, y/h = 1.5); (g) SM (x/L_r = 0, y/h = 2); (h) SP (x/L_r = 0, y/h = 2); (i) CB (x/L_r = 0, y/h = 2); (j) SM (x/L_r = 0, y/h = 2.5); (k) SP (x/L_r = 0, y/h = 2.5); (l) CB (x/L_r = 0, y/h = 2.5). Contour levels are from 0.0005 to 0.0045 at intervals of 0.001.

At $y/h \approx 2.5$, the maximum probability for SP is inclined approximately towards Q2 and Q3. This is also noticed for smooth wall at this location. The prevalence of Q3 motions in the instantaneous signal would lead to a reduction in $-\langle u'v' \rangle$ for SP and SM at this location in relation to the cube roughness.

4.2.9 Temporal Correlations and Turbulence Spectra

Figure 4.15 shows the streamwise evolution of the temporal auto-correlations R_{uu} and R_{vv} at two wall-normal locations, $y/h \approx 1.1$ and 2, in the primary recirculation region of the step. Figure 4.15(a) shows the R_{uu} plots at $y/h \approx 1.1$. With increasing distance from the leading edge, the area of the time-correlated region of the auto-correlation ($R_{uu} > 0$) increases as the rolled-up eddies increase in size. A similar variation with streamwise distance was observed for flow over blunt flat plates (Swamy et al. 1979; Ota and Motegi 1983; Djilali and Gartshore 1991). Near the leading edge ($x/L_r \approx 0$), R_{uu} is slightly reduced by both the sandpaper and cube roughness at small temporal separations ($tU_e/h < 2$). At larger temporal separations, R_{uu} is enhanced by the cube roughness, but nearly indistinguishable for smooth wall and sandpaper. At the middle of the recirculation bubble ($x/L_r \approx 0.5$), the correlations are nearly independent of upstream roughness. At the reattachment location ($x/L_r \approx 1.0$), the values of R_{uu} for SM are mostly negative for $tU_e/h > 10$. This may be attributed to low-momentum fluid produced by the deceleration of flow near the reattachment location for SM. This is in agreement with the acceleration parameter profile for smooth wall which levels off much earlier than occurred for SP and CB. Figure 4.15(b) shows profiles of R_{uu} at $y/h \approx 2$. At this wall-normal location, the decay of the tails is more gradual than closer to the wall. This is because the scale of the structures increases as the measurement position moves away from the wall so that the structures survive much longer with time than the smaller-scale structures near the wall. While the auto-correlation is relatively unaffected by the sandpaper roughness, substantial enhancements are produced by the cube roughness. This increase with the cube roughness is consistent with the enhancements produced in the streamwise Reynolds stress for CB.

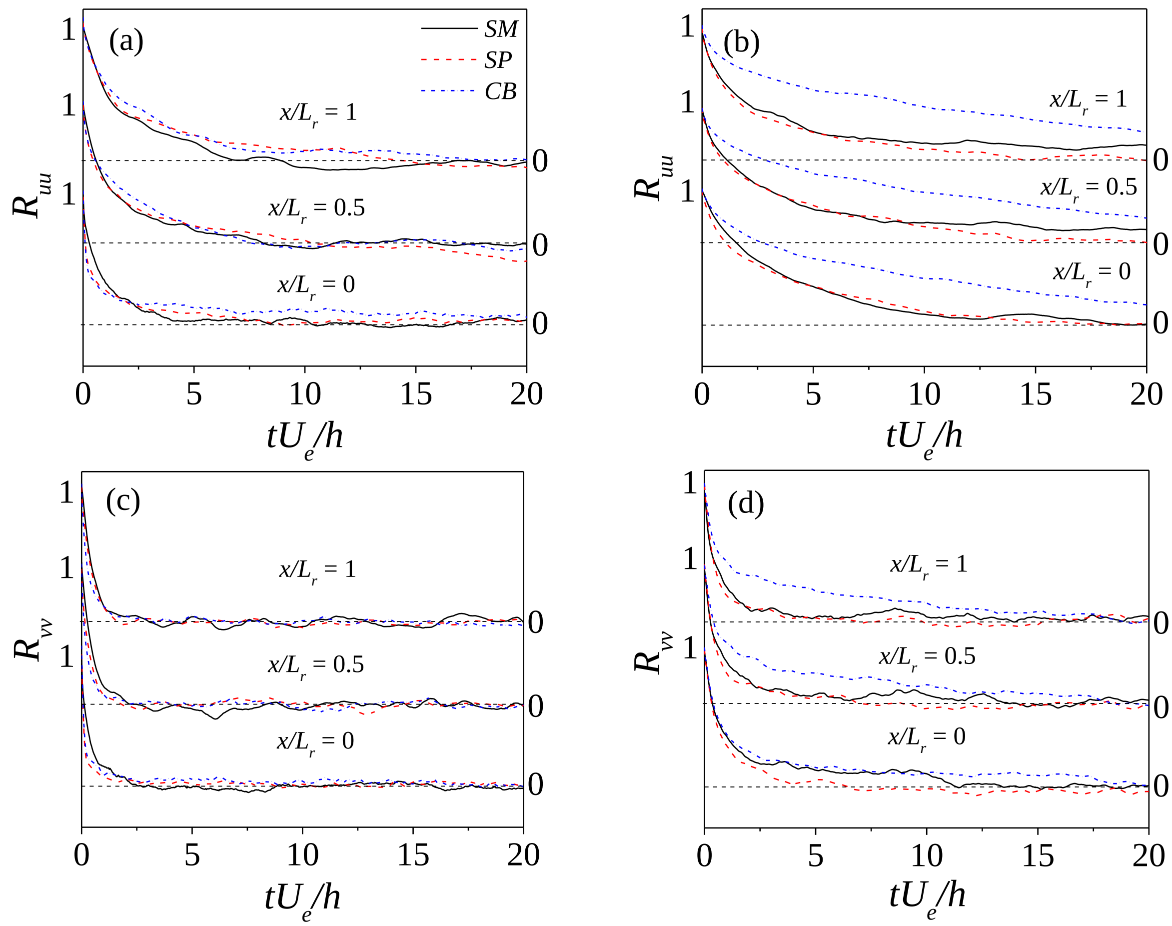

Figure 4.15: Streamwise evolution of the temporal autocorrelations, R_{uu} and R_{vv}, in the primary recirculation region: (a) R_{uu} profiles at y/h = 1.1; (b) R_{uu} profiles at y/h = 2; (c) R_{vv} profiles at y/h = 1.1; (d) R_{vv} profiles at y/h = 2.

The profiles of the wall-normal velocity auto-correlation, R_{vv} at $y/h \approx 1.1$ and 2 are presented in Figures 4.15(c) and 4.15(d), respectively. The plots indicate that R_{vv} decorrelates much faster than R_{uu}, and even more dramatically close to the wall. This suggests that the wall-normal motions such as those that produce the wall-normal Reynolds stress are less persistent in time than the larger-scale quasi-streamwise motions. At $y/h \approx 1.1$, R_{vv} is invariant with streamwise distance and nearly independent of upstream roughness. This suggests that the smaller-scale structures near the wall in the recirculation region are unaffected by upstream roughness and distance from the leading edge. Further from the wall ($y/h \approx 2$), R_{vv} decays faster for SP than SM and CB, while that of CB decays the slowest. The higher values of R_{vv} for CB are attributable to structures of larger time scales, and by inference, larger spatial scales than SM and SP. The dominance of large-time scale disturbances in the separated shear layer have been reported in the literature (e.g., Eaton and Johnston 1981; Cherry et al. 1984; Largeau and Moriniere 2007), where they were observed to produce a significant contribution to the low frequency part of the turbulence spectrum.

Figure 4.16 shows wall-normal profiles of the integral time scales, T^u and T^v of the u' and v' fluctuations, respectively, estimated from the temporal auto-correlation functions as

$$T^u = \int_0^\infty R_{uu}(t)dt \tag{4.6}$$

$$T^v = \int_0^\infty R_{vv}(t)dt \tag{4.7}$$

Following previous studies (Swamy et al. 1979; Ota and Motagi 1983), the integrals were performed from $t = 0$ to the first zero crossing of R_{uu} and R_{vv} on the temporal separation axis. The profiles of T^u normalized by U_e and h are shown in Figure 4.16(a). The time scales are relatively small close to the wall and have maximum values within the region of maximum Reynolds shear stress. The values then decay to relatively constant values in the outer parts of the flow. The streamwise integral time scale is relatively unchanged by the sandpaper roughness at all three streamwise locations shown. However, the peak values are increased by the cube roughness by approximately 52%, 87% and 110% at $x/L_r \approx 0$, 0.5 and 1.0, respectively, compared to the smooth wall. For the smooth wall, the peak value of T^u at the reattachment location ($x/L_r \approx 1.0$) are lower than those upstream. Bradshaw and Wong (1972) concluded that the shear layer at reattachment is split in two, where one part of the flow is deflected upstream into the recirculation region and the other part continues downstream. The authors suggested that this would lead to a reduction in eddy length and time scales as observed herein at least for SM. The profiles of the normalized values of T^v are shown in Figure 4.16(b). Near the leading edge, the sandpaper reduces the peak value of the time scale relative to the smooth wall and cube roughness, with the cube profile reaching the largest peak. Downstream of the leading edge, the differences between the SM and SP values are approximately 35%, while T^v is dramatically increased by the cube roughness. It should be noted that for the smooth wall, the value of T^v in the region of maximum Reynolds shear stress becomes increasingly smaller with streamwise distance within the recirculation.

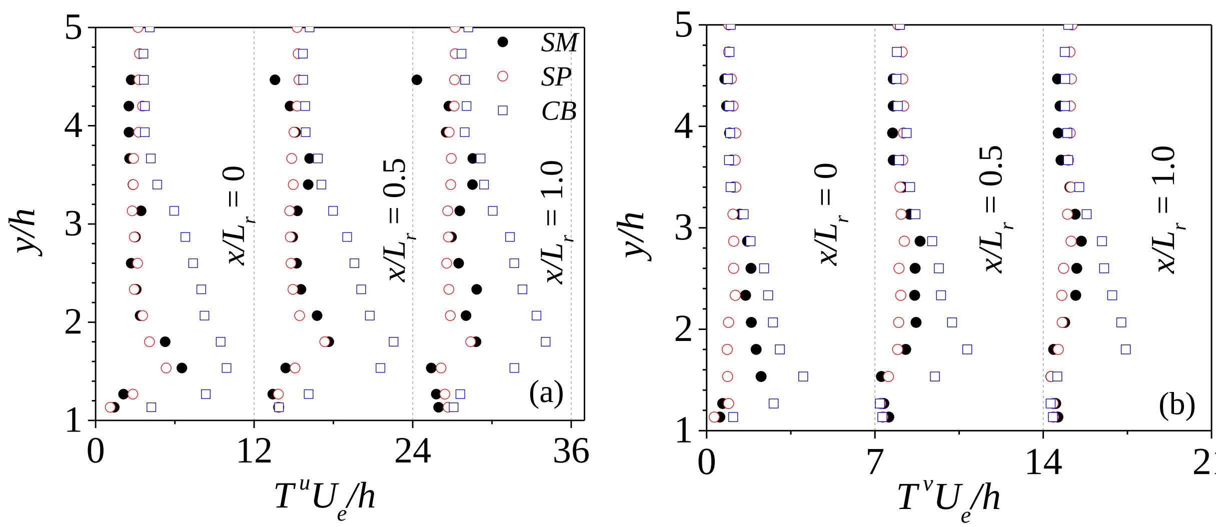

Figure 4.16: Wall-normal distribution of the integral time scales of the velocity fluctuations in the primary recirculation region: (a) integral time scale of the streamwise velocity fluctuations; (b) integral time scale of the wall-normal velocity fluctuations.

Figure 4.17 examines the frequency spectral density of the streamwise velocity fluctuations in the recirculation region. The spectra, normalized by U_e and h, are plotted at $y/h \approx 1.1$ and 2.0 at successive streamwise locations in the recirculation region. All the frequency spectra exhibit a noise floor which is typical of spectra estimated from PIV data. The frequency spectra density plots presented here are qualitatively similar to those presented by Pearson et al. (2013) for time-resolved PIV measurements over a forward-facing step. Near the wall (Figure 4.17(a)), the spectral density of the low frequency motions in the recirculation region is independent of upstream roughness. For the high frequency motions, on the other hand, the spectral density exhibits a tendency to increase with upstream roughness.

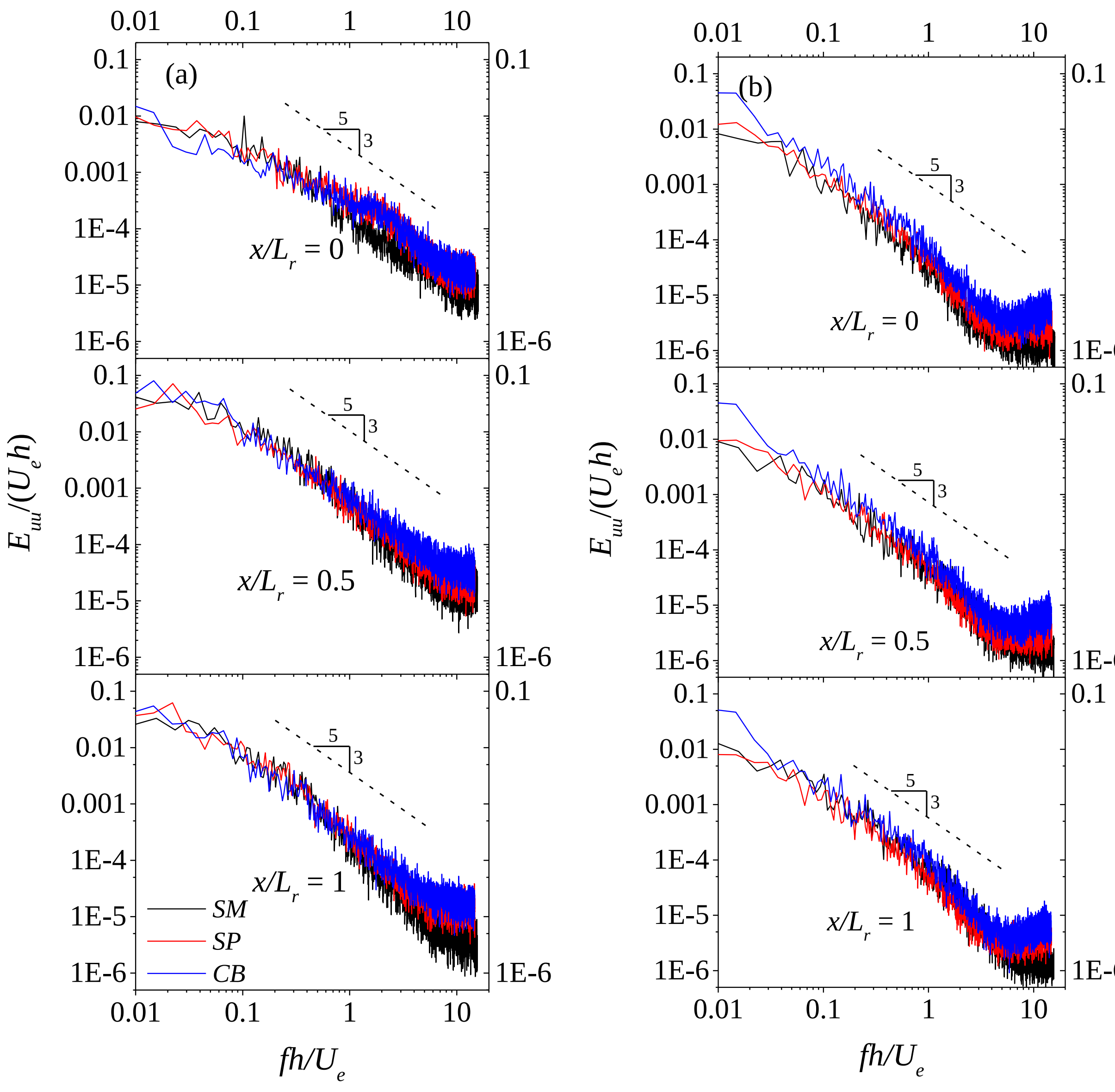

Figure 4.17: Frequency spectra of the streamwise velocity fluctuations (E_{uu}) in the primary recirculation region: (a) E_{uu} at y/h = 1.1; (b) E_{uu} at y/h = 2.

The effect of upstream roughness is more noticeable at $x/L_r \approx 1.0$. At $x/L_r \approx 0$, the spectra lack a distinct inertial subrange region (–5/3). However, further downstream, the spectra exhibit an inertial subrange of approximately one decade. Further from the wall (Figure 4.17(b)), the cube roughness enhances the spectral density of the low frequency motions at all three streamwise locations. This is similar to the observed enhancements in R_{uu} and the integral time scale T^u by the cube roughness in the outer region. There is still a weak increase in the spectral density of the high frequency motions with the cube roughness, indicating the injection of energy into the flow at the small scales as well as the large scales by the cube roughness.

Figures 4.18(a) and 4.18(b) show the corresponding frequency spectral density plots of the wall-normal velocity fluctuations, E_{vv}, at $y/h \approx 1.1$ and 2.0, respectively. Near the leading edge (Figure 4.18(a)), the spectral density is independent of upstream roughness, except for an intermediate region ($0.9 \leq fh/U_e \leq 2.5$) in which there is an increase with roughness. The increase can be attributed to high-frequency contributions from the large wall-normal velocity fluctuations near the leading edge for SP and CB. This is also consistent with the larger values of wall-normal Reynolds stress and wall-normal turbulent transport of v'^2 at $y/h \approx 1.1$ for the rough-wall cases compared to the smooth wall. Downstream of the leading edge, the low-frequency contributions to the wall-normal velocity fluctuations are suppressed by the cube roughness. This suppression occurs over a frequency range that is considerably larger at the reattachment location than at the middle of the recirculation bubble. These spectral modulations are in agreement with the attenuation of the peak values of $\langle v'^2 \rangle$ by CB observed in the recirculation region. At $y/h \approx 2.0$ (Figure 4.18(b)), the low-frequency contributions to E_{vv} are unaltered by the sandpaper but they are dramatically enhanced by the cube roughness in relation to the smooth wall and sandpaper. The largest enhancements are observed for $x/L_r > 0$, which are consistent with the increase in time scale of the turbulent structures with increasing distance from the leading edge. At high frequencies, the spectral density is increased by both the sandpaper and cube roughness compared to the smooth wall. This is also an indication of energy supply to the turbulence field at the scale of the smallest eddies that may be due to a turbulent-turbulent interaction mechanism that produces no net contribution to Reynolds stress.

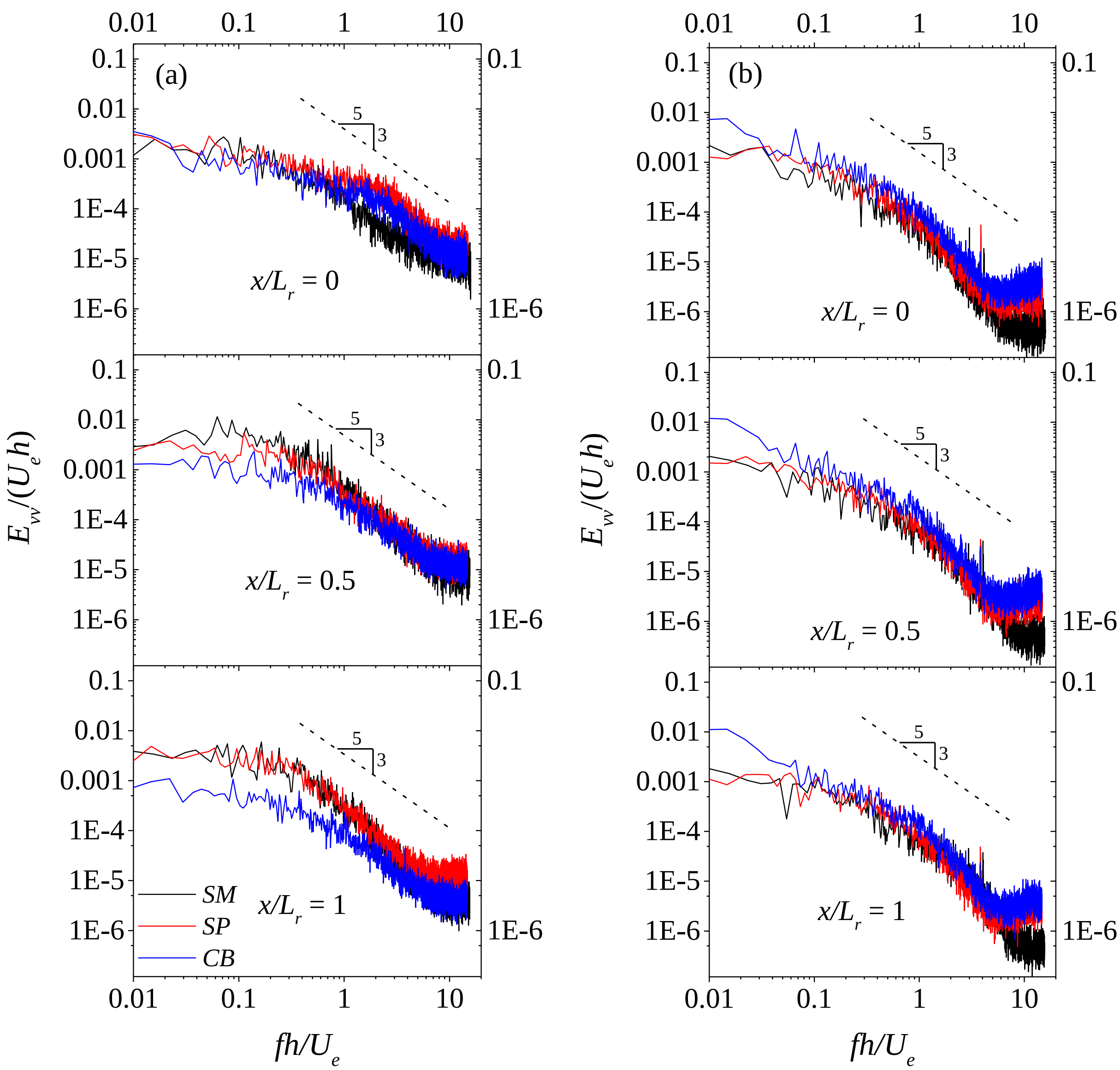

Figure 4.18: Frequency spectra of the wall-normal velocity fluctuations (E_{vv}) in the primary recirculation region: (a) E_{vv} at y/h = 1.1; (b) E_{vv} at y/h = 2.

4.3 Development of flow characteristics in the redevelopment region

To evaluate the effects of upstream roughness on the redevelopment of the flow characteristics downstream of reattachment, profiles of the turbulent quantities were plotted at various streamwise locations for the smooth and rough walls. Four streamwise locations at distances of 2, 12, 20 and

35 step heights from the reattachment location were selected for this evaluation. Figure 4.19 examines the redevelopment of the wall-normal profiles of the mean streamwise and wall-normal velocities after the reattachment. At each streamwise location, the profiles are compared to the corresponding distribution obtained at the upstream location, $x/h \approx -20$, over the smooth wall. During early redevelopment ($(x-L_r)/h \approx 2$), the mean velocities have not yet relaxed to the upstream distribution, and a slight roughness effect is noticed in this region. However, the profiles collapsed appreciably well for $(x-L_r)/h \geq 12$, indicating that sufficiently far downstream of reattachment, the mean flow is independent of upstream roughness. Previous investigations of separated and reattached wall-bounded turbulent flows (e.g., Song et al. 2000; Tachie et al. 2001) show that the mean flow recovery is very rapid downstream of reattachment.

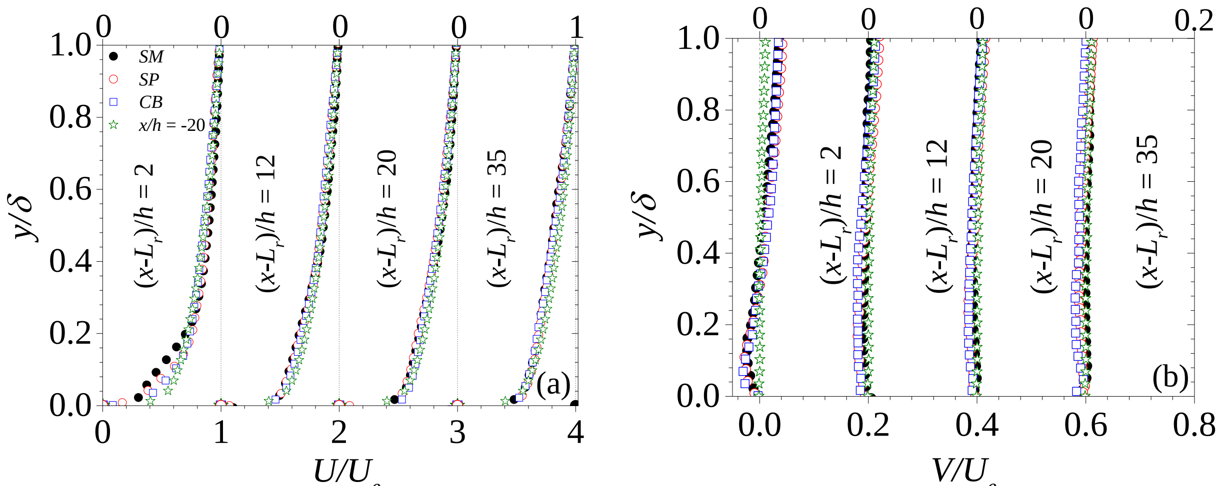

Figure 4.19: Streamwise evolution of the one-dimensional profiles of the mean velocities in the redevelopment region for the upstream smooth and rough wall conditions.

Figure 4.20 shows the streamwise development of selected boundary layer parameters in the mid-span of the step, including the skin friction coefficient, C_f, boundary layer shape factor, H, and the Clauser shape parameter, G. Figure 4.20(a) shows the values of the skin friction coefficient in the redevelopment region. The values for the smooth and rough walls were estimated using the Ludwieg-Tillman (1950) relation

$$C_f = 0.246 \times 10^{-0.678H} Re_\theta^{-0.268} \quad (4.8)$$

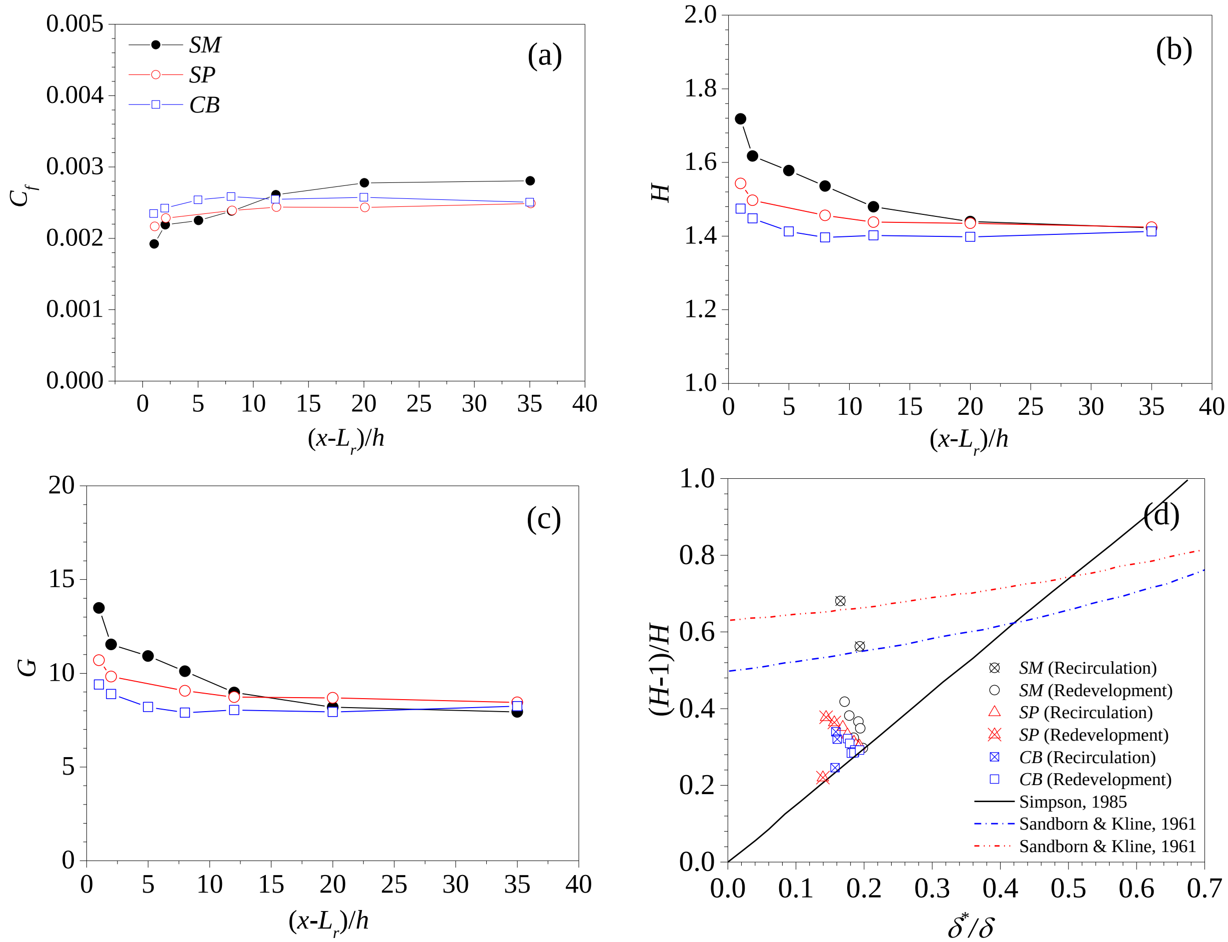

Figure 4.20: Streamwise evolution of the boundary layer integral parameters over the FFS for the upstream smooth and rough wall conditions: (a) friction coefficient, $C_f = 0.246 \times 10^{-0.678H}\mathrm{Re}_\theta^{-0.268}$; (b) shape factor, $H = \delta^*/\theta$; (c) Clauser shape parameter, $G = (2/C_f)^{1/2}(H-1)/H$; (d) $(H-1)/H$ versus δ^*/δ.

When used to estimate the skin friction coefficient at the upstream location, the Ludwieg-Tillman formula yields a value of approximately 0.0031 for the smooth wall, which is within 3% of the value of 0.0030 estimated using the Clauser chart method. The smooth-wall profile shows an increase with streamwise distance from a value of $C_f \approx 0.0019$ near reattachment and levels off at a value of approximately 0.0028. Within the measurement range, the rough- and smooth-wall values are fairly comparable, but altogether are less than the upstream smooth-wall measured value of $C_f \approx 0.0030$. The skin friction profiles are in qualitative agreement with data reported in the recovery region of a blunt flat plate (Ruderich and Fernholz 1986) and backward-facing steps (Adams and Johnston 1988; Jovic 1994). Figure 4.20(b) shows the profiles of the shape factor, H. The shape factor varies with streamwise distance and upstream roughness within the early redevelopment region but becomes invariant with distance and roughness for $(x-L_r)/h \geq 20$. Far downstream, the values of H are not significantly different from $H \approx 1.3 - 1.4$ for the standard ZPG turbulent boundary layer. The values of the Clauser shape factor, estimated as $G = (2/C_f)^{1/2}(H-1)/H$, are presented in Figure 4.20(c). The profiles of G closely mimic those of H, with values of approximately 13.5, 11 and 9.5 for SM, SP and CB, respectively, immediately downstream of reattachment. With increasing distance downstream of reattachment, G decreases to a relatively constant value of approximately 8.5 that is independent of upstream roughness. The converged value of $G \approx 8.5$ is about 25% larger than the value of 6.8 obtained by Coles (1962) for the ZPG turbulent boundary layer. Sandborn and Kline (1961) suggested that in the recirculation region, the mean velocity satisfies a family of power-law type velocity profiles. Figure 4.20(d) shows the profiles of $(H - 1)/H$ versus δ^*/δ for locations in the recirculation and redevelopment regions. In the plot, the straight line represents $(H - 1)/H = 1.5(\delta^*/\delta)$ which is considered to fit most non-separated turbulent boundary layers at high Reynolds number (Simpson 1989). The curved lines (from Sandborn and Kline 1961), intersecting the straight line, correspond to turbulent boundary layers undergoing separation or detachment. As can be seen, the two points from recirculation region for SM nearly coincide with the curves. Corresponding points for SP and CB fall below the detachment curves, indicating differences in boundary layer shape factor between the smooth and rough walls in the recirculation region. A possible manifestation of these differences can be seen even in the shape factor plots of Figure 4.20(b) close to reattachment, where the rough-wall values of H are lower than the smooth-wall value. For points in the redevelopment region, the profile either collapses on the straight line or lies close to it. Similar results were reported by Simpson (1989).

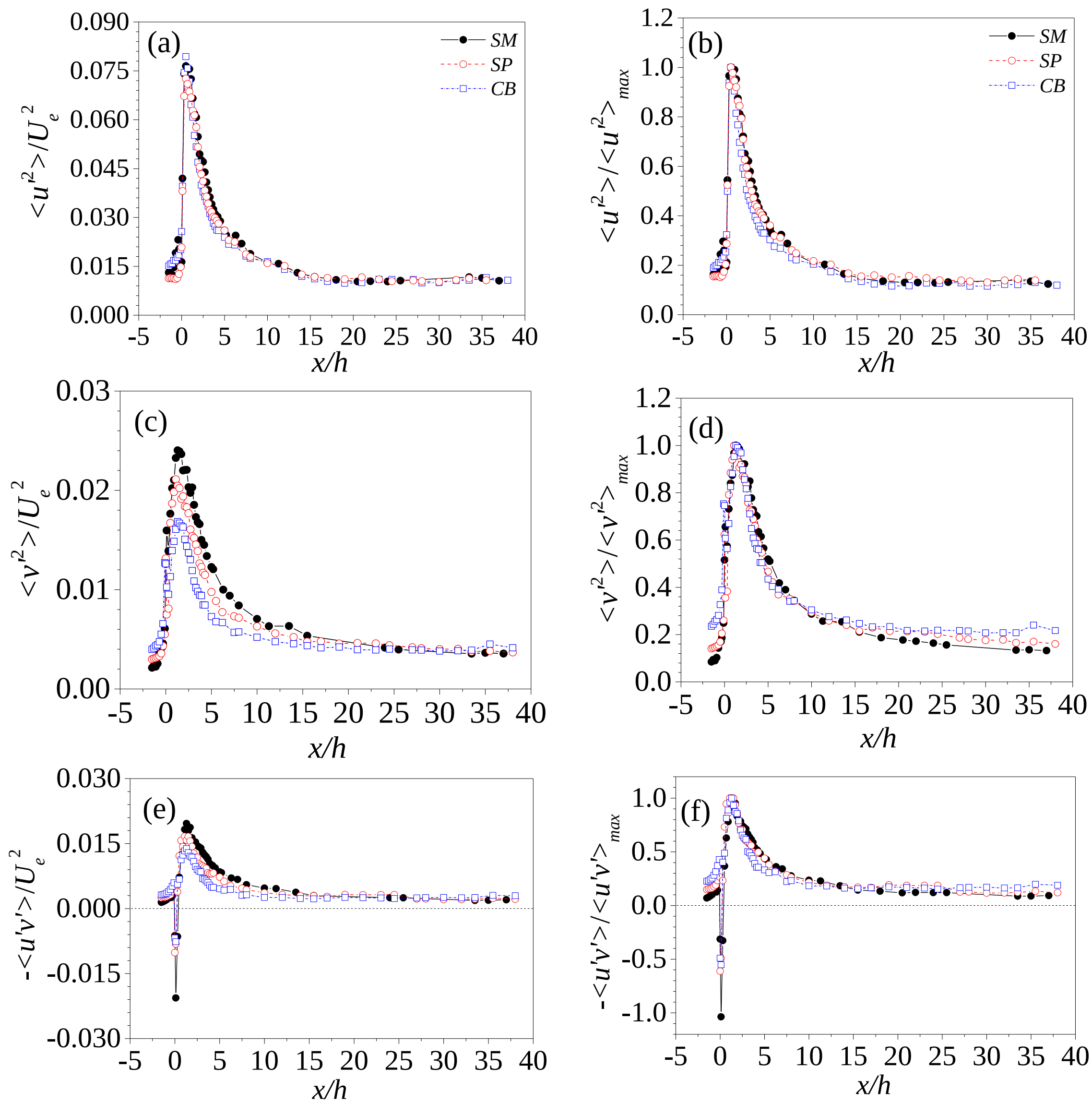

Figure 4.21: Streamwise evolution of the peak values of the (a,b) streamwise Reynolds stress; (c,d) wall-normal Reynolds stress, and (e,f) Reynolds shear stress.

Figure 4.21 examines the streamwise development of the peak values of the Reynolds stresses in the mid-span of the test section. In order to assess the behaviour of the peak Reynolds stress profiles near the leading edge of the step, the upstream region $-2 \leq x/h \leq 0$ is also included in the analysis. Two types of velocity scales were used to normalize the peak stresses: the local maximum mean streamwise velocity (Figures 4.21(a), 4.21(c) and 4.21(e)) and the maximum peak Reynolds stress (Figures 4.21(b), 4.21(d) and 4.21(f)).

The peak values of the streamwise Reynolds stress (Figure 4.21(a)) increase rapidly within the upstream region and undergo an abrupt change in magnitude to their maximum values near the leading edge of the step. The highest value is observed for the cube roughness, exceeding those of the smooth wall and sandpaper by approximately 4% and 10%. After reattachment, the peak values of $\langle u'^2 \rangle / U_e^2$ decay rapidly to a relatively constant value of 0.012 in the far downstream region. In the redevelopment region, the peak streamwise Reynolds stress is independent of upstream roughness. The decay of the Reynolds stress after reattachment is consistent with the idea of bifurcation of the large-scale eddies near reattachment (e.g., Bradshaw and Wong 1972). This effect reduces the strength of the eddies convecting with the redeveloping boundary layer to produce Reynolds stress in comparison to the rolled-up eddies in the separated shear layer. Figures 4.21(c) and 4.21(e) indicate that the peak values of wall-normal stress and Reynolds shear stress, respectively, also increase rapidly with streamwise distance near the leading edge of the step, reaching the largest peaks within the recirculation bubble. For the Reynolds shear stress, however, negative peaks are also observed in the profiles close to the leading edge due to the counter-gradient transport phenomenon. For both stresses, the maximum in the profiles are reduced by the upstream roughness, although the effect is less dramatic for the Reynolds shear stress values than the wall-normal stress. Also, the highest reductions were produced by the cube roughness in comparison to the smooth wall: approximately 12% and 30% reductions in $\langle v'^2 \rangle / U_e^2$ by SP and CB, respectively, but 15% and 30% in $-\langle u'v' \rangle / U_e^2$, by SP and CB, respectively, compared to the smooth wall. The streamwise decay of the Reynolds stresses in the redevelopment region to relatively constant values in the far downstream region have been reported in other separated and reattached boundary layer investigations, including flow over backward-facing steps (Moss and Baker 1980;

Jovic 1998) and blunt flat plates (Ruderich and Fernholz 1986; Castro and Epik 1998). When normalized by the maximum peak value, the profiles of the streamwise Reynolds stress (Figure 4.21(b)) and Reynolds shear stress (Figure 4.21(f)) collapse reasonably well over the step but the wall-normal Reynolds stress profiles (Figure 4.21(d)) show an increase with wall roughness in the far field of the redevelopment region.

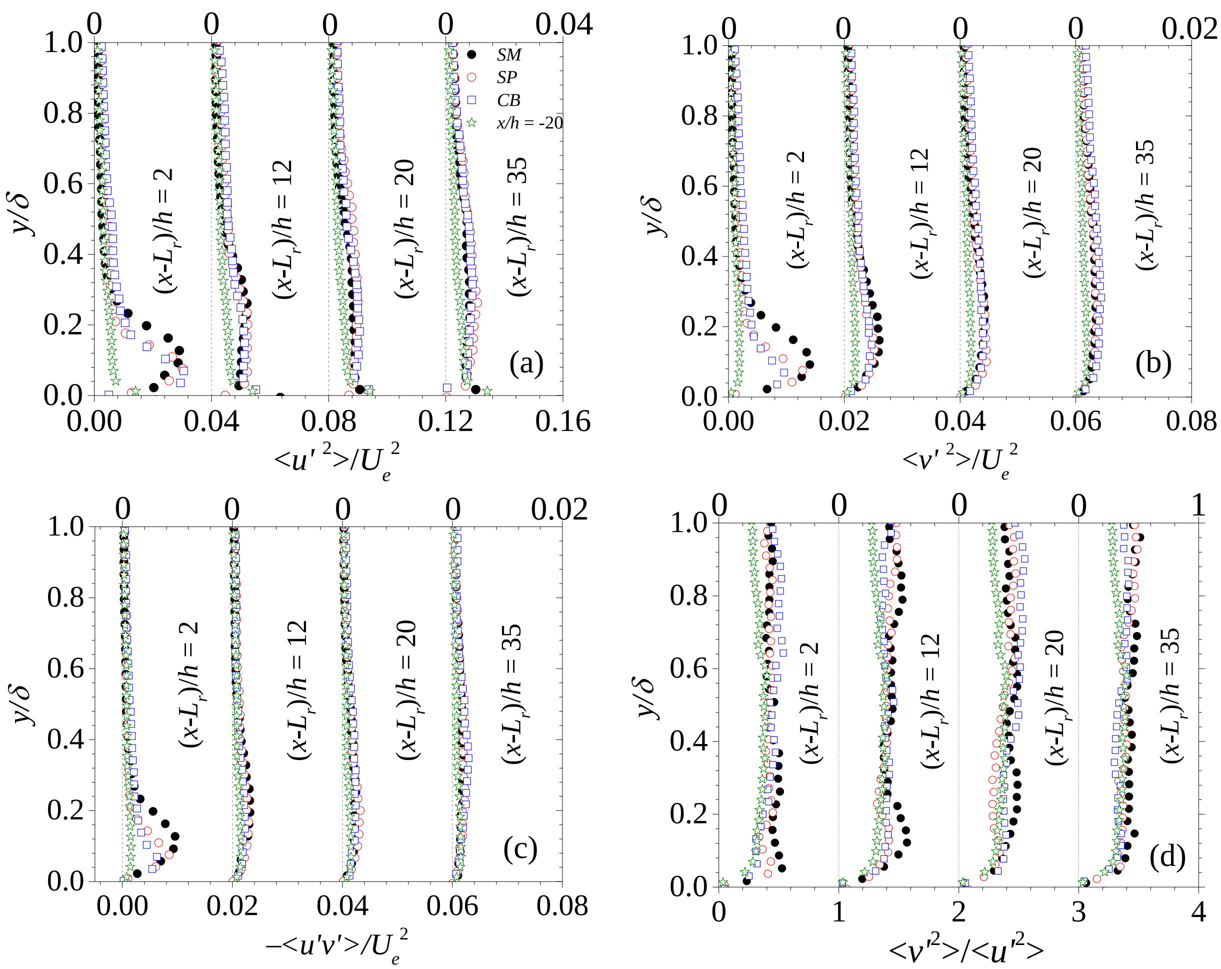

Figure 4.22: Streamwise evolution of the one-dimensional profiles of the Reynolds stresses in the redevelopment region for the upstream smooth and rough wall conditions: (a) streamwise Reynolds stress; (b) wall-normal Reynolds stress; (c) Reynolds shear stress; (d) normal stress ratio.

Figure 4.22 shows the evolution of the one-dimensional wall-normal profiles of the Reynolds stresses in the redevelopment region. For the smooth wall, the peak values of the Reynolds stresses (Figures 4.22(a) – 4.22(c)) are relatively higher than the upstream values and reductions are observed for the rough-wall profiles in comparison to the smooth wall in the early redevelopment region. Further downstream, the rough- and smooth-wall profiles collapse reasonably well, but do not fully recover to the upstream smooth wall distribution. For the smooth wall (SM), this implies that a longer redevelopment distance is required for the stresses to recover to the upstream profile. For the rough walls, on the other hand, this implies that upstream roughness still influences the velocity fluctuations far downstream of the step. Figure 4.22(d) shows the profiles of the normal stress ratio, $\langle v'^2\rangle/\langle u'^2\rangle$. These show discrepancies among the smooth- and rough-wall values and do not collapse on the upstream smooth-wall profile, even at the farthest downstream location.

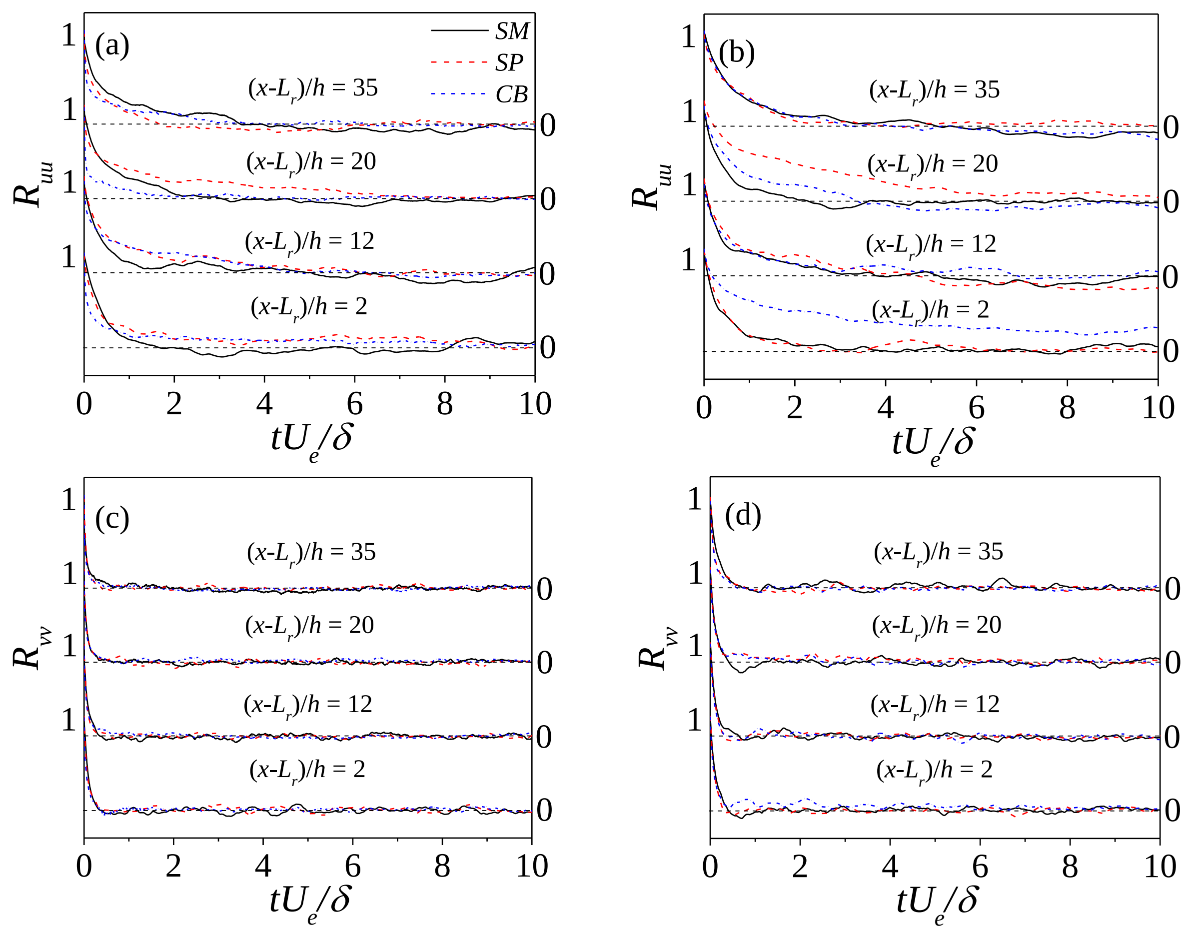

Figure 4.23: Streamwise evolution of the temporal autocorrelations, R_{uu} and R_{vv}, in the redevelopment region: (a) R_{uu} profiles at y/h = 1.1; (b) R_{uu} profiles at y/h = 2; (c) R_{vv} profiles at y/h = 1.1; (d) R_{vv} profiles at y/h = 2.

Downstream redevelopment of the temporal auto-correlations R_{uu} and R_{vv} is examined in Figure 4.23. Here, the values of the temporal separation were normalized by δ/U_e. The profiles of R_{uu} plotted at the wall-normal location $y/h \approx 1.1$ (Figure 4.23(a)) reveals appreciable differences between the smooth- and rough-wall results but these differences become less important in the far downstream region. The same conclusion applies to the profiles of R_{uu} at $y/h \approx 2$ (Figure 4.23(b)) although more substantial enhancements by the upstream cube roughness and sandpaper are observed at 2 and 20 step heights, respectively, downstream of reattachment. However, for both wall-normal locations, the region of positive R_{uu} between zero separation and the first zero crossing is larger in the redevelopment region than in the recirculation region. This is due to the increase in longitudinal extent of the large-scale vortices as the flow propagates downstream (Kiya and Sasaki 1985). The profiles of the auto-correlation of the wall-normal velocity fluctuation at both wall-normal locations (Figures 4.23(c) and 4.23(d)) suggest that the wall-normal auto-correlation in the redevelopment region is invariant with upstream roughness for dimensionless temporal separations larger than approximately 2.

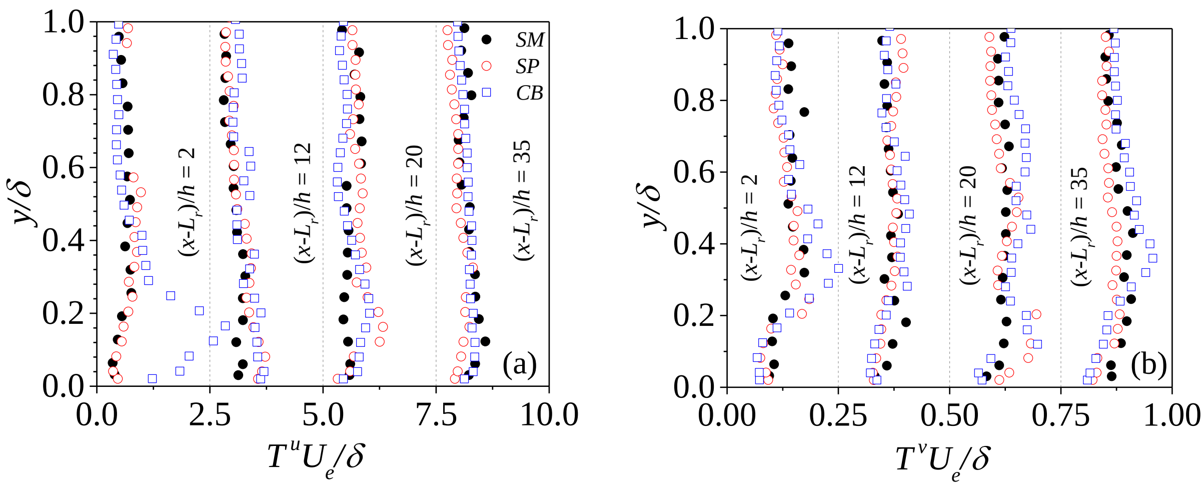

Figure 4.24: Wall-normal distribution of the integral time scales of the velocity fluctuations in the redevelopment region: (a) integral time scale of the streamwise velocity fluctuations; (b) integral time scale of the wall-normal velocity fluctuations.

Figure 4.24 shows the streamwise evolution of the of the integral time scales, T^u and T^v in the redevelopment region. During the early stages of redevelopment, the time scales are independent of the sandpaper roughness but have larger peak values for CB than the smooth wall and sandpaper. Further downstream, there is no systematic dependency of the time scales on upstream roughness.

Figures 4.25 and 4.26 show the frequency spectral density distributions of the streamwise and wall-normal velocity fluctuations, respectively, in the redevelopment region. There are significant differences between the smooth- and rough-wall profiles close to the wall, but the spectra exhibit near universality further from the wall. In Figure 4.25(a), an increase in spectral density at higher frequencies is observed for upstream rough-wall conditions, which is generally more substantial at larger distances from reattachment. This may be an indication of a merging of smaller eddies to form larger-scale eddies as the reattached boundary layer convects downstream in the recovery region for the rough walls. An imprint of such an inverse energy cascade process is noticed in Figure 4.26(a) for E_{vv} that show a general reduction in the spectral density for the rough walls compared to the smooth wall. This will arise when the smaller eddies responsible for E_{vv} are merged to form larger-scale vortices in the recovery region by the rough walls.

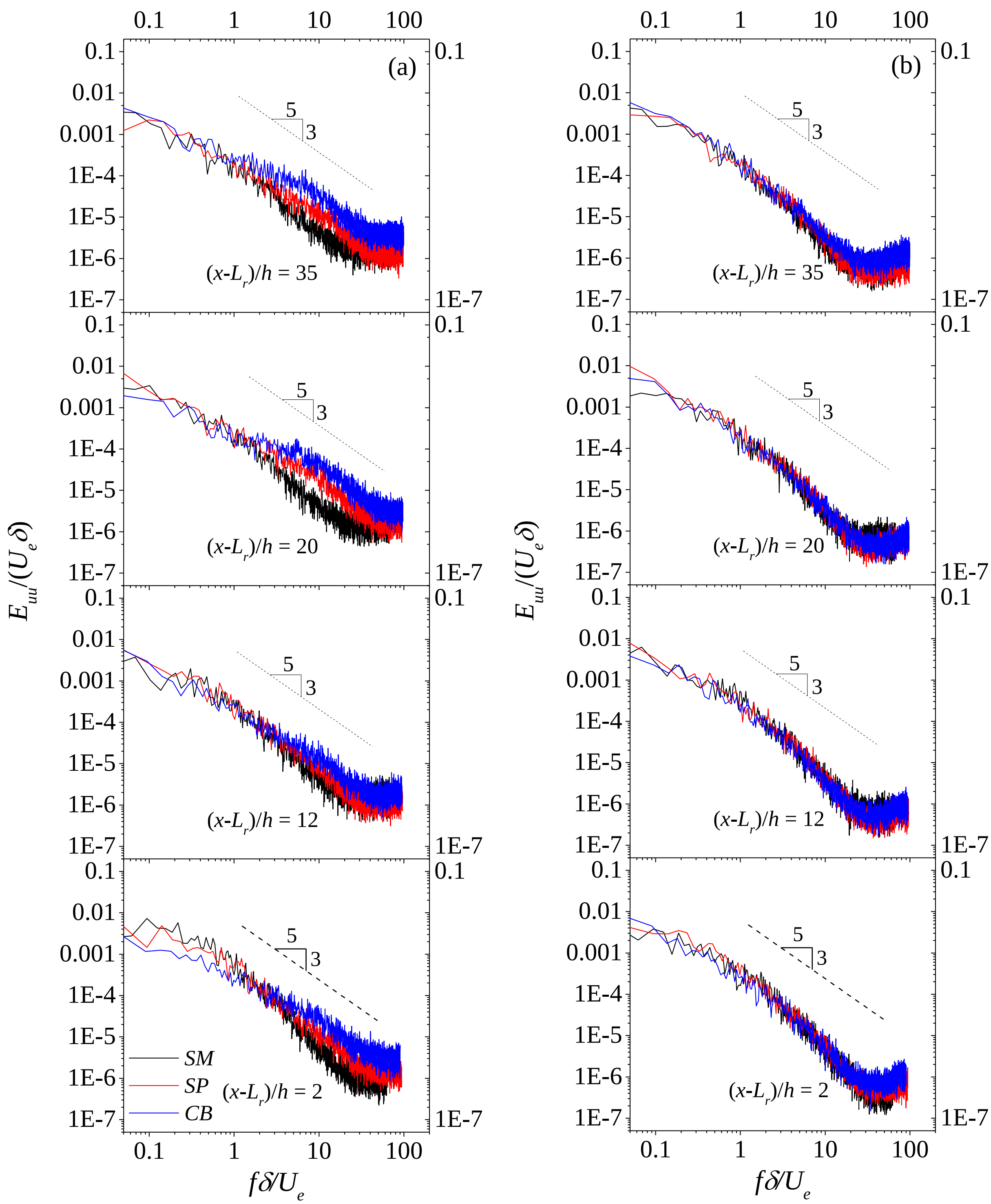

Figure 4.25: Frequency spectra of the streamwise velocity fluctuations (E_{uu}) in the redevelopment region: (a) E_{uu} at y/h = 1.1; (b) E_{uu} at y/h = 2.

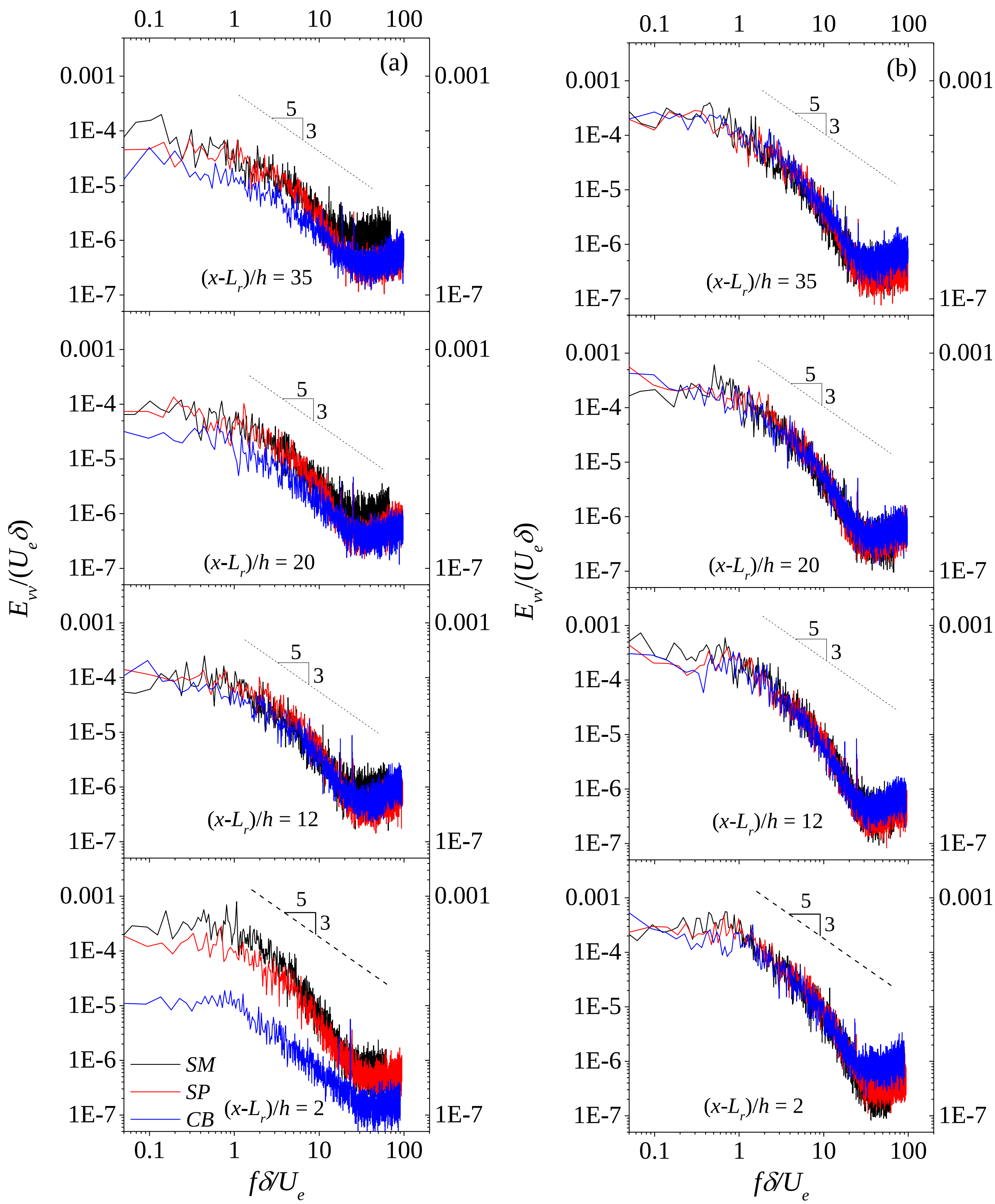

Figure 4.26: Frequency spectra of the wall-normal velocity fluctuations (E_{vv}) in the redevelopment region: (a) E_{vv} at y/h = 1.1; (b) E_{vv} at y/h = 2.

4.4 Effects of Upstream Roughness on the Coherent Structures in the Separated Shear Layer

The effects of upstream roughness on the single-point turbulent statistics were examined in the preceding sections. In this section, various multipoint turbulent statistics such as linear stochastic estimates of the velocity fields, two-point spatial and space-time correlations are used to provide insight into the evolution of the large-scale coherent structures in the separated shear layer. It should be noted however that in discussing these results, attention is given only to the smooth and cube roughness test conditions. The results for the sandpaper are not shown because no significant differences were observed in comparison to the smooth wall.

4.4.1 Linear Stochastic Estimation (LSE) of the Velocity Fields

The flow visualization results earlier (Figures 4.1 and 4.3) revealed the spanwise vortex cores produced by the Kelvin-Helmholtz roll up of the separated shear layer. Using contours of instantaneous swirling strength, these vortex cores were identified to be predominantly prograde vortices shed by the step. To obtain the average flow field associated with these prograde vortices a conditional average of the velocity fields was performed using the linear stochastic estimation (LSE) approach. Figure 4.27 shows the vector plots of the linear stochastic estimation in the recirculation region of SM and CB. The LSE calculations were conditioned on the presence of prograde swirling strength at the location $x/h = 0.6$ and $y/h = 1.3$. To prevent the obscuring of weaker motions away from the event location, the velocity vectors in the plots were set to unity by normalizing them with their respective magnitudes. The smooth wall vector field is shown in Figure 4.27(a). The LSE calculation shows a prograde vortex at the event location, demarcated by a red circle. This vortex is accompanied by two other swirling motions centered at ($x/h = 0.8$, $y/h = 1.5$) and ($x/h = 1.4$, $y/h = 1.4$).

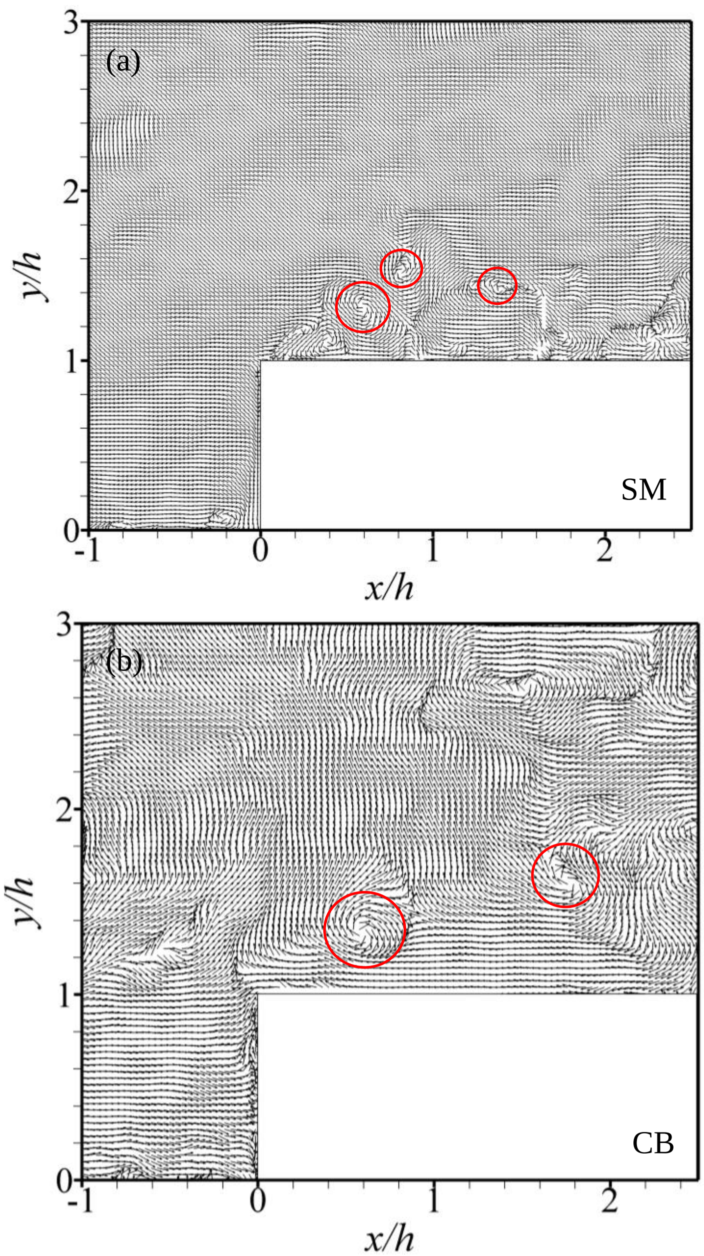

Figure 4.27: Linear stochastic estimate (LSE) of the velocity fields in the recirculation region for SM and CB based on a prograde event at x/h = 0.6 and y/h = 1.3.

Altogether, all three vortices lie along a crease in the velocity field that resembles a Karman vortex street. As shown by the Galilean decomposition, these vortices correspond to the spanwise vortex cores propagating at the same convection velocity downstream of the step. Application of the LSE method to the equilibrium smooth wall boundary layer in previous investigations (e.g., Christensen and Adrian 2001; Volino et al. 2009) indicated a region of large-scale ejections (Q2) between the wall and the vortex cores and an extended region of sweep-like (Q4) events above the crease. While the present smooth wall still shows a large-scale Q4 region above the vortices, there is very minimal ejection of fluid from the top face of the step in the recirculation. This is due to the boundary layer separation over the step.

The vector field obtained from the LSE of the rough wall boundary layer is shown in Figure 4.27(b). As expected, a strong prograde vortex is detected at the event location x/h = 0.6 and y/h = 1.3. However, due to the disruptive nature of the wall roughness, the flow over the step in this case is less organized than over the smooth wall. The rough wall result shows only one other vortex at x/h = 1.8 and y/h = 1.6 in addition to the event vortex. The fewer number of vortices is consistent with the reduced vortex shedding frequency observed for the rough wall cases. Also, the crease is less defined if not non-existent because of the smearing effect of wide variability in the convection velocities over the rough wall. In the place of the organized structure or Karman vortex street observed for the smooth wall, a large-scale region of ejections is observed over the step, which is similar to that observed in the Galilean decomposition for the cubes.

4.4.2 Estimation of Convection Velocities in the Recirculation Region

The spanwise vortex cores revealed by the linear stochastic estimation would be captured in the conditional average only if they were part of the same large-scale structure, or if they were propagating at the same convection velocity. Early investigators estimated the convection velocity of the large-scale structures in turbulence using the Taylor's (1938) frozen turbulence hypothesis. Taylor's (1938) hypothesis suggests that for a homogeneous turbulent flow the ∂/∂t term in the Navier-Stokes equations can be substituted according to the relation

$$\partial/\partial t = -U(\partial/\partial x) \tag{4.9}$$

where U is the local mean velocity. That is, the large-scale eddies may be considered as propagating downstream at a speed approximately equal to the local mean velocity. Despite its usefulness in coordinate transformation from temporal to spatial, the validity of the Taylor approximation has been questioned in certain cases. Lin (1953), for instance, showed that the Taylor hypothesis is invalid in the presence of large flow acceleration caused by shear. Fisher and Davies (1964) argued that in the mixing region of an axisymmetric jet there are uncertainties in the coordinate transformation from time to space due to mean shear and high turbulence intensities in the shear layer. Nevertheless, the Taylor approximation has been widely used in the past to analyze the spatial structure of both canonical (e.g., Choi and Moin 1990; Kim and Hussain 1993; Krogstad et al. 1998) and free shear (e.g., Browand and Wiedman 1976; Wygnanski et al. 1976; Sokolov et al. 1980) turbulent flows. Other techniques have also been used in the literature to estimate the convection velocity, including use of the phase velocity of velocity fluctuations (del Alamo and Jimenez 2009), core velocity of the spanwise vortices (Wu and Christensen 2010) and from space-time correlations (Favre et al. 1958, 1967; Goldschmidt et al. 1981). In this investigation, the values of the convection velocity, U_C, were estimated from the slope of the iso-contours of the longitudinal space-time auto-correlation function. This is similar to the *celerities* method described by Favre et al. (1967). Following Wallace (2014), the space-time correlation R_{AB}, between any two arbitrary quantities $A(x, y)$ and $B(x, y)$ was calculated as

$$R_{AB}(\Delta x, \Delta y, \tau) = \frac{\langle A(x_{ref}, y_{ref}, t) B(x_{ref} + \Delta x, y_{ref} + \Delta y, t + \tau) \rangle}{\sigma_A(x_{ref}, y_{ref}) \sigma_B(x_{ref} + \Delta x, y_{ref} + \Delta y)} \tag{4.10}$$

where the point (x_{ref}, y_{ref}) denotes the reference location, Δx and Δy are the spatial separations between A and B in the streamwise and wall-normal directions, respectively, τ is the temporal separation between the times t and $t + \tau$; σ_A and σ_B are the root-mean-square values of A and B at the space-time locations (x_{ref}, y_{ref}, t) and $(x_{ref} + \Delta x, y_{ref} + \Delta y, t + \tau)$, respectively.

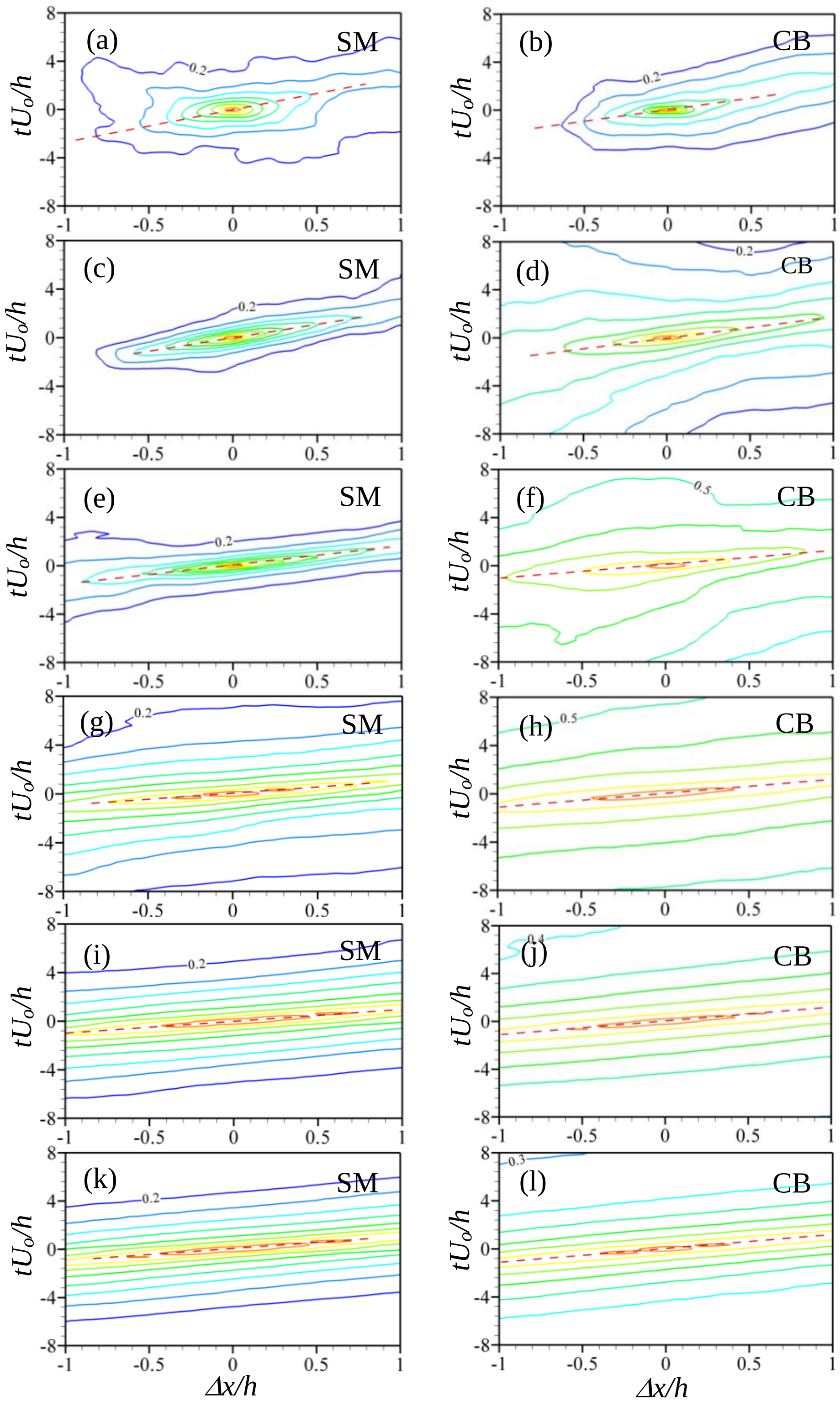

Figure 4.28: Iso-contours of the space-time auto-correlation function of streamwise velocity for SM and CB at x/L_r = 0.5, and y/h = 1.1, 1.3, 1.5, 2.0, 2.5 and 3.

Figure 4.28 shows the iso-contours of the space-time auto-correlation R_{uu} (Δx, 0, τ) at increasing wall-normal distances away from the step ($y/h \approx$ 1.1, 1.3, 1.5, 2.0, 2.5, 3.0) at the center of the primary recirculation bubble. The contours display the characteristic inclination with the positive direction of the streamwise spatial separation axis. This diagonal orientation is an indication that the turbulent structures are not only elongated in space but they are persistent in time as well. Near the wall, the contours are almost elliptical. Farther from the wall, the outermost contour lines are approximately parallel to ridge of the contours. The almost straight contour lines in the outer parts of the flow can be attributed to the larger-scale structures in the outer layer convecting at nearly the same speed as the mean flow. Also, with increasing distance from the wall, the temporal scales of the correlations are larger, which reinforces the idea that the outer layer is dominated by larger-scale eddies with longer lifetimes than eddies closer to the wall. Similar contours have been reported in the literature for both equilibrium turbulent boundary layers (Favre et al. 1967; Blackwelder and Kovasznay 1972; Nakagawa and Nezu 1981) and separated shear layers (Tinney and Ukeily 2009; Mohammed-Taifour and Weiss 2016). At the closest location to the wall, the effect of upstream cube roughness is negligible. At larger distances from the wall, the extent of significant correlation is considerably increased by the cube roughness when compared to the smooth wall. As shown by the LSE and flow visualization results, the rough wall correlations confirm the existence of larger and more persistent turbulent structures in the outer parts of the flow for the cubes than the smooth wall. Figure 4.29 shows the iso-contours of the wall-normal space-time auto-correlation function, R_{vv} (Δx, 0, τ). For a given wall-normal location, R_{vv} (Δx, 0, τ) is less spatially and temporally coherent than R_{uu} (Δx, 0, τ). This is because this correlation is caused by the small-scale spanwise vortices in the shear layer. Thus, the reduced temporal extents of the wall-normal space-time correlation may be attributed to a more rapid decorrelation of the small-scale eddies in time in comparison to the larger scale eddies.

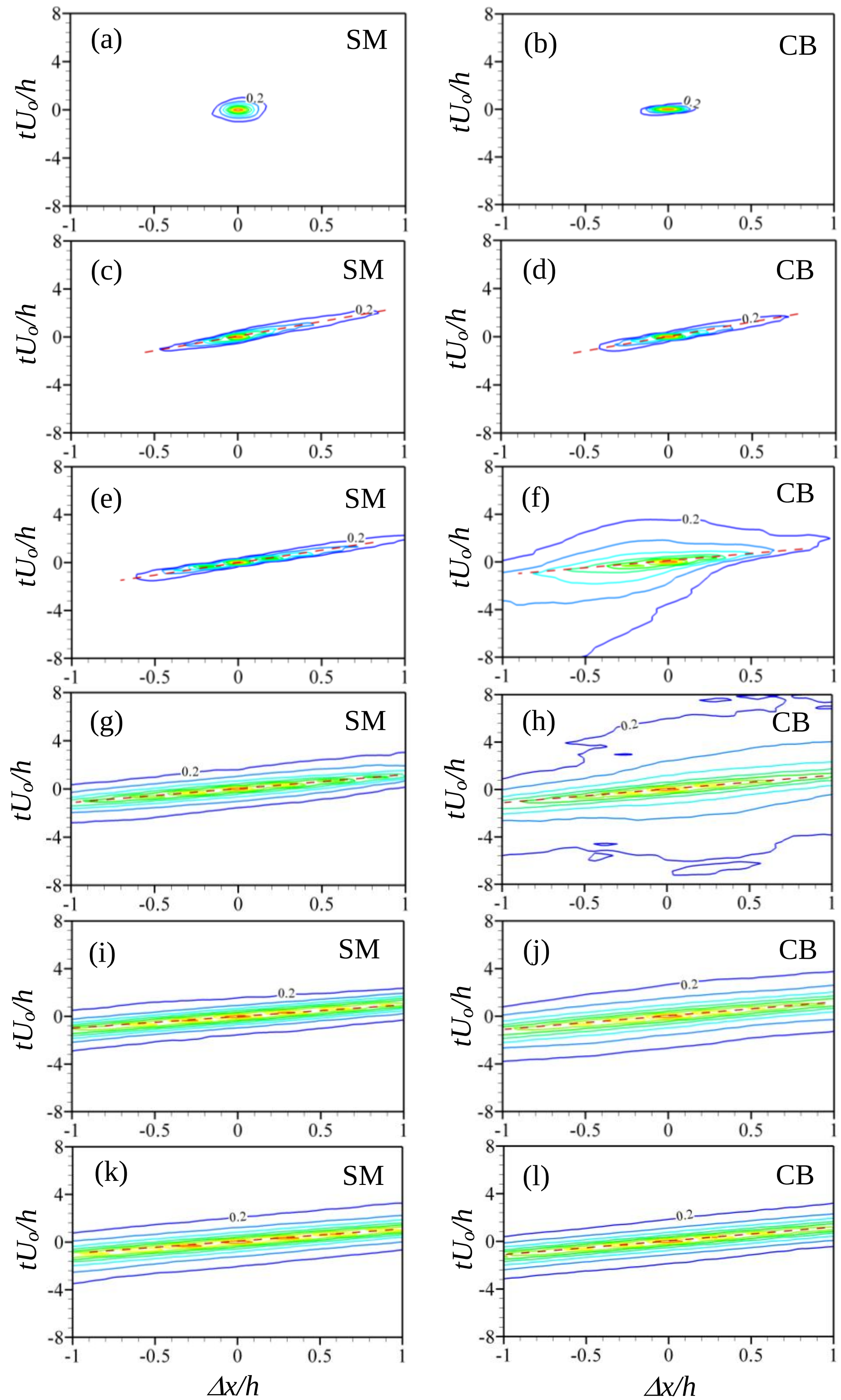

Figure 4.29: Iso-contours of the space-time auto-correlation function of wall normal velocity for SM and CB at x/L_r = 0.5, and y/h = 1.1, 1.3, 1.5, 2.0, 2.5 and 3.

Several authors (e.g., Tennekes 1975; Sanada and Shanmugasundaram 1992; Zhou and Rubinstein 1996; O'Gorman and Philip 2004; Zhao and He 2009) discussed the decorrelation process of the small-scale eddies. They suggested that their rapid reduction in time can arise either by the sweeping action of the larger-scale eddies or the local straining of the small eddies themselves. Close to the step, the cube roughness caused a further reduction in both the spatial and temporal spreads of the wall-normal space-time auto-correlation R_{vv} (Δx, 0, τ). This is qualitatively consistent with the damping action of the cubes on the wall-normal velocity fluctuations in the shear layer (Figure 4.9). On the contrary, at larger distances from the wall, a predominant increase in scale is observed for the rough wall compared to SM because the outer flow is characterized by more energetic v fluctuations in the rough wall case.

To estimate the convection velocities a least squares straight line was fitted to the locus of the maximum correlation along the ridge of the contours of R_{uu} (Δx, 0, τ). A comparison of the convection velocities calculated from the slope $\Delta x/\Delta\tau$ of the line is shown in Figure 4.30. In these plots, the values of U_c were normalized by the upstream freestream velocity (U_o). Figure 4.30(a) shows the effect of upstream roughness on the wall-normal variation of U_c/U_o at the center of the primary recirculation bubble. Near the wall ($y/h \leq 1.5$), the convection velocity increases rapidly with wall-normal distance. The results indicate that the small-scale structures are propagating at a much lower speed than that of the approach boundary layer and reflects the strong anisotropy of the flow close to the wall. In the wall region, the small-scale eddies are about 30% faster for CB compared to SM. Farther from the wall ($y/h > 1.5$), the convection velocity remains approximately constant, with the larger-scale structures convecting at nearly the same speed as the mean flow ($U_c \approx U_o$) for SM. For CB, on the other hand, a reduction in convection velocity is observed in comparison to the smooth wall, with the differences in U_c/U_o reaching about 21%. The results in Figure 4.30(a) suggests that the larger the structures, the smaller the convection velocity, and by inference, the longer their lifetime. Similar conclusions were reached by previous investigators (Favre et al. 1967; Kovasznay et al. 1970; Blackwelder and Kovasznay 1972). Figure 4.30(b) shows the streamwise evolution of the normalized convection velocity, measured at the location of maximum turbulence intensity. This location was chosen to highlight the convection velocities of the rolled-up eddies in the shear layer. Within the first half of the recirculation bubble, the convection velocity is a decreasing function of x/L_r. In both cases, a minimum value is reached near the center of the recirculation bubble. Within most of the shear layer, the values of U_c/U_o are nearly independent of upstream roughness. In the second half of the recirculation bubble, the normalized convection velocity is quasi-invariant with streamwise distance with a value of $U_c/U_o \approx 0.5$. A similar trend of nearly constant values has been reported for separated and reattached shear layers (Na and Moin 1998; Weiss et al. 2015).

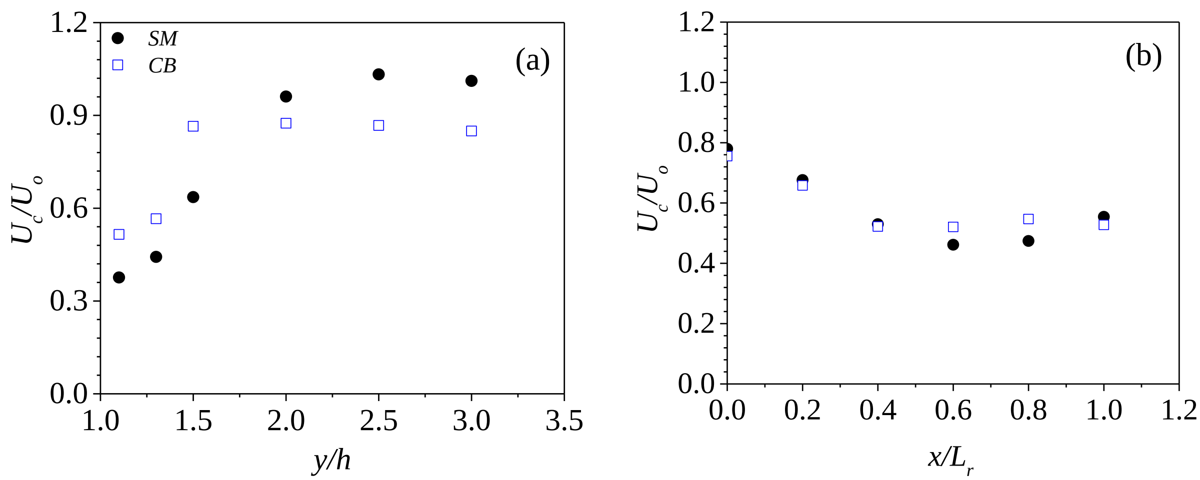

Figure 4.30: Normalised convection velocity (a) in the wall-normal direction at $x/L_r = 0.5$; (b) along the locus of maximum streamwise turbulence intensity in the recirculation region.

4.4.3 Two-point Spatial Correlations

The effects of upstream roughness on the two-point spatial correlations without time delay are examined in this section. These are useful for quantifying the average spatial dimensions of the coherent structures in the shear layer. The two-point correlation, R_{AB}^{S}, at the reference point (x_{ref}, y_{ref}) between the two quantities $A(x, y)$ and $B(x, y)$ was calculated as

$$R_{AB}^{S}(x_{ref}+\Delta x, y_{ref}+\Delta y) = \frac{\langle A(x_{ref}, y_{ref}) B(x_{ref}+\Delta x, y_{ref}+\Delta y)\rangle}{\sigma_A(x_{ref}, y_{ref})\sigma_B(x_{ref}+\Delta x, y_{ref}+\Delta y)} \qquad (4.11)$$

where Δx and Δy are the spatial separations in the streamwise and wall-normal directions and the superscript s is introduced to denote spatial correlation. Figure 4.31 shows iso-contours of R_{uu}^{s} centred at various streamwise locations ($x/L_r \approx 0.0$, 0.25, 0.5 and 1.0) along the locus of maximum turbulence intensity in the shear layer for SM and CB. In each plot, the highest and lowest contour levels are respectively 0.9 and 0.4, and the contours are at intervals of 0.1. The largest regions of high streamwise velocity correlation occur near the leading edge of the step (Figures 4.31(a) and 4.31(b)). The relatively strong spatial coherence of the u fluctuations here and their inclination to the vertical and top faces of the step are the imprints of the low-momentum fluid erupting diagonally from the corner of the step (see Figures 4.1 and 4.3). The R_{uu}^{s} correlation is even more pervasive for the cube roughness because the corner eruptions are strongly correlated with the larger-scale ejections in the shear layer compared to the smooth wall. For the smooth wall, the inclined structure decorrelates rapidly as the flow separates from the step, and is replaced by a streamwise-aligned structure whose size grows with distance from the leading edge. The enhancement in spatial correlation with downstream distance is consistent with growth of the vortical structures as the flow evolves downstream. For the rough wall, the inclined structure is more resilient to the flow separation due to the more dominant influence of the ejections from the step in comparison to the smooth wall. Also, for the wall roughness condition, the R_{uu}^{s} correlation contours at $x/L_r \geq 0.5$ bear a striking resemblance to those of attached turbulent boundary layers. This may have resulted from the reduced vortex shedding from the step in the case of the rough wall. The average streamwise inclination angle of the correlation was estimated to be approximately 11^{o}, which is in good agreement with the value of approximately 11^{o}-13^{o} reported for equilibrium turbulent boundary layers (Volino et al. 2007). As was observed in the temporal and space-time correlation results, for a given reference location, the effect of roughness is to enhance the spatial coherence of the fluctuations by increasing the average size of the turbulent structures.

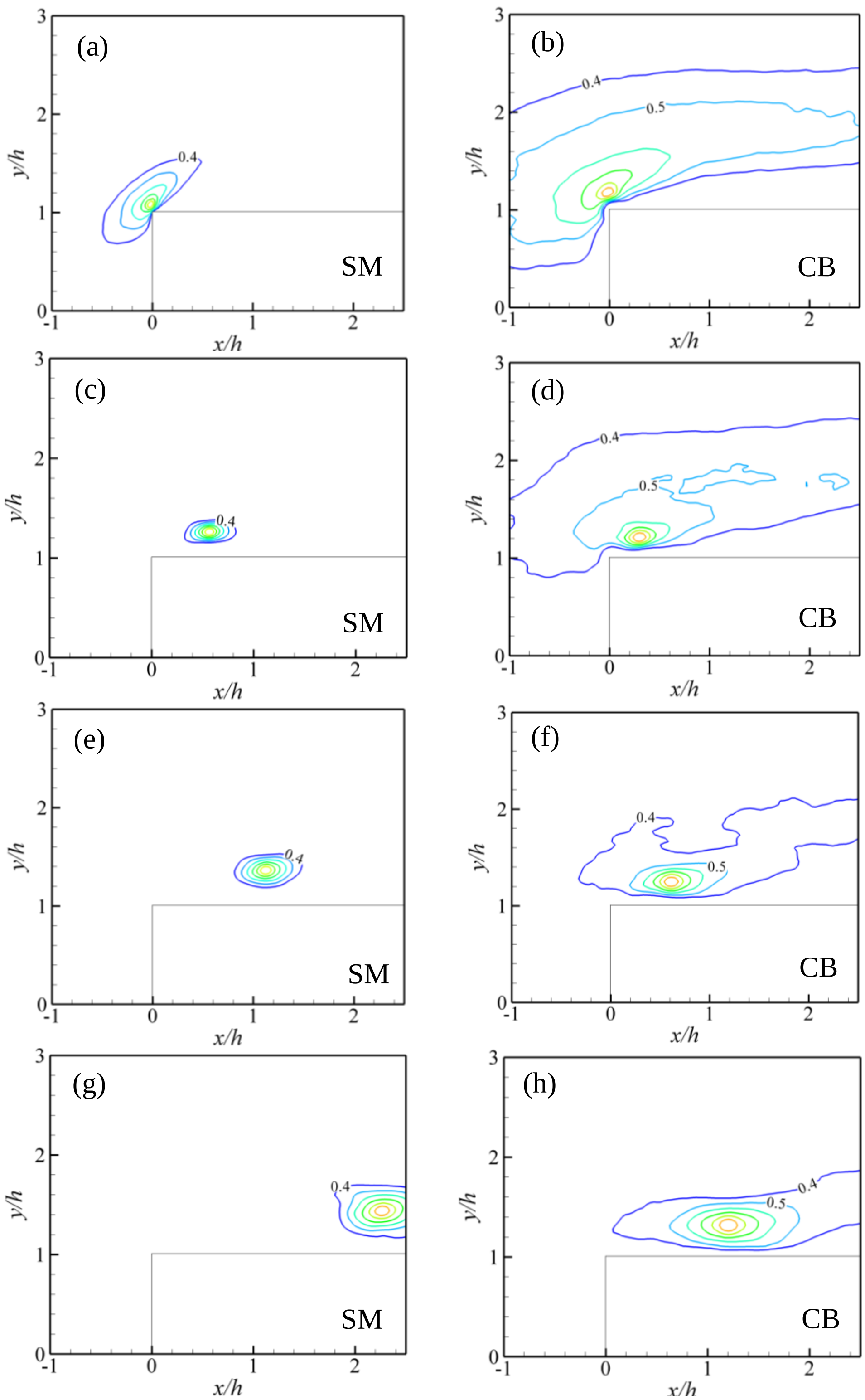

Figure 4.31: Iso-contours of the two-point spatial auto-correlation function of streamwise velocity (R_{uu}^{s}) along the locus of maximum streamwise turbulence intensity in the recirculation region.

The iso-contours of R_{vv}^{s} plotted versus Δx and Δy are shown in Figure 4.32. As expected, the contours are smaller and more compact than those of the streamwise fluctuating velocity auto-correlation function. The correlations are also inclined to the leading edge of the step as was observed for their streamwise counterparts. Downstream of the leading edge, the smooth wall R_{vv}^{s} correlation exhibits a characteristic shape that is elongated in the wall-normal direction and grows with increasing distance from the leading edge. This is consistent with the streamwise evolution of a turbulent mixing layer. For the cube roughness, on the other hand, the contours are relatively more circular and show a much less tendency to growth with streamwise distance than the smooth wall correlations. The roughly circular shapes in this case are another feature indicating quasi-similarity with equilibrium boundary layers. This is not unexpected since for the upstream rough walls, reattachment on the step and subsequent flow redevelopment occur much sooner than the smooth wall. Also, except near the leading edge, the correlation areas of the rough wall contours are much smaller than the smooth wall contours.

Figure 4.33 shows the contours of the spatial cross-correlation R_{uv}^{s} at the various streamwise locations for SM and CB. The two-point spatial cross-correlation provides information regarding the size and shape of the vortical structures responsible for mixing across the shear layer. It embodies the turbulent motions that transport low-momentum fluid from the wall into the faster moving outer layer and high-momentum fluid from the outer layer toward the wall. The plots show that the cross-correlation function has both positive and negative distributions in the shear layer. The positive correlations correspond to the Q1 ($u > 0$, $v > 0$) and Q3 ($u < 0$, $v < 0$) motions in the shear layer, while the negative correlations correspond to the Q2 ($u < 0$, $v > 0$) and Q4 ($u > 0$, $v < 0$) motions in the shear layer.

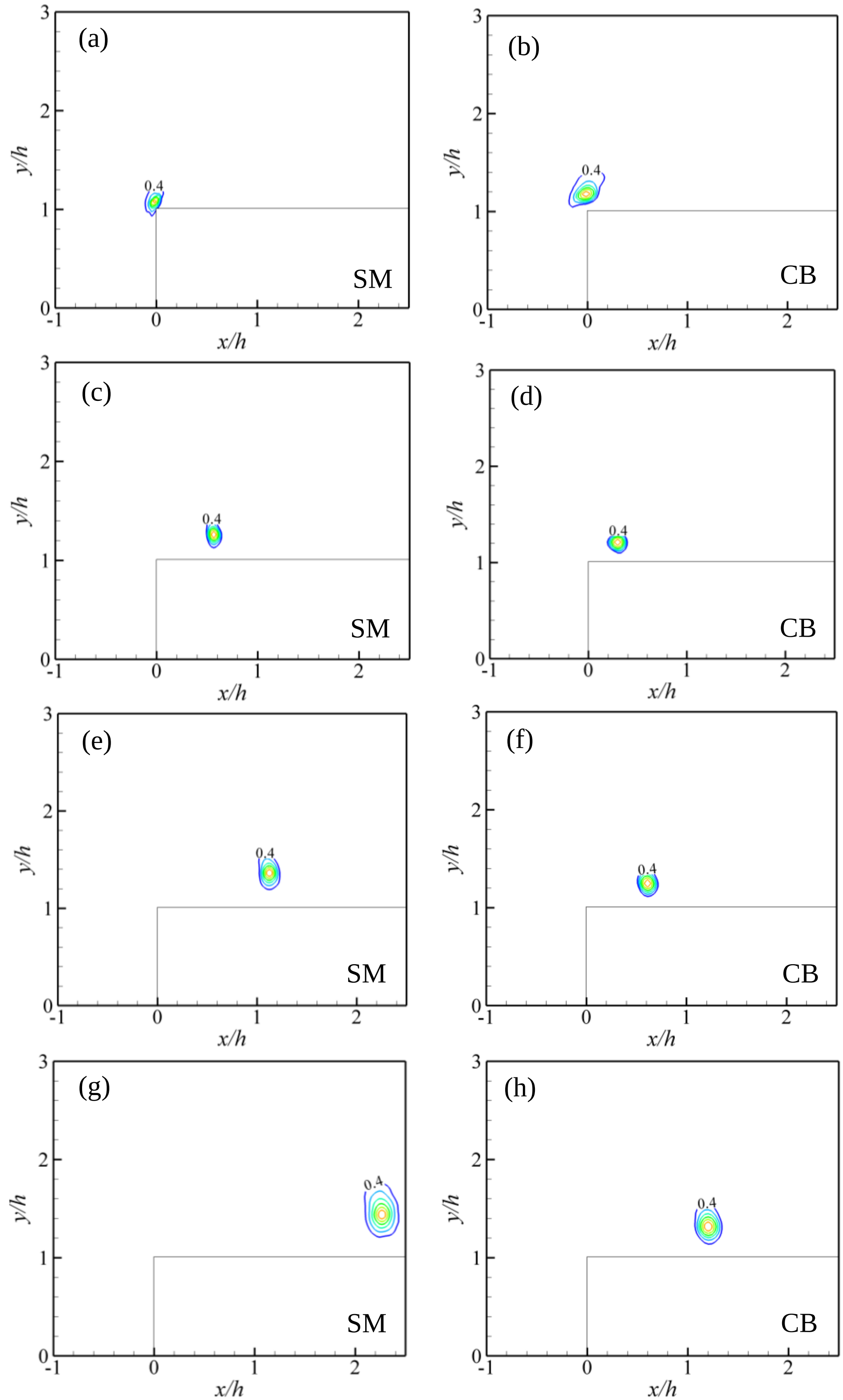

Figure 4.32: Iso-contours of the two-point spatial auto-correlation function of wall-normal velocity (R_{vv}^{s}) along the locus of maximum streamwise turbulence intensity in the recirculation region.

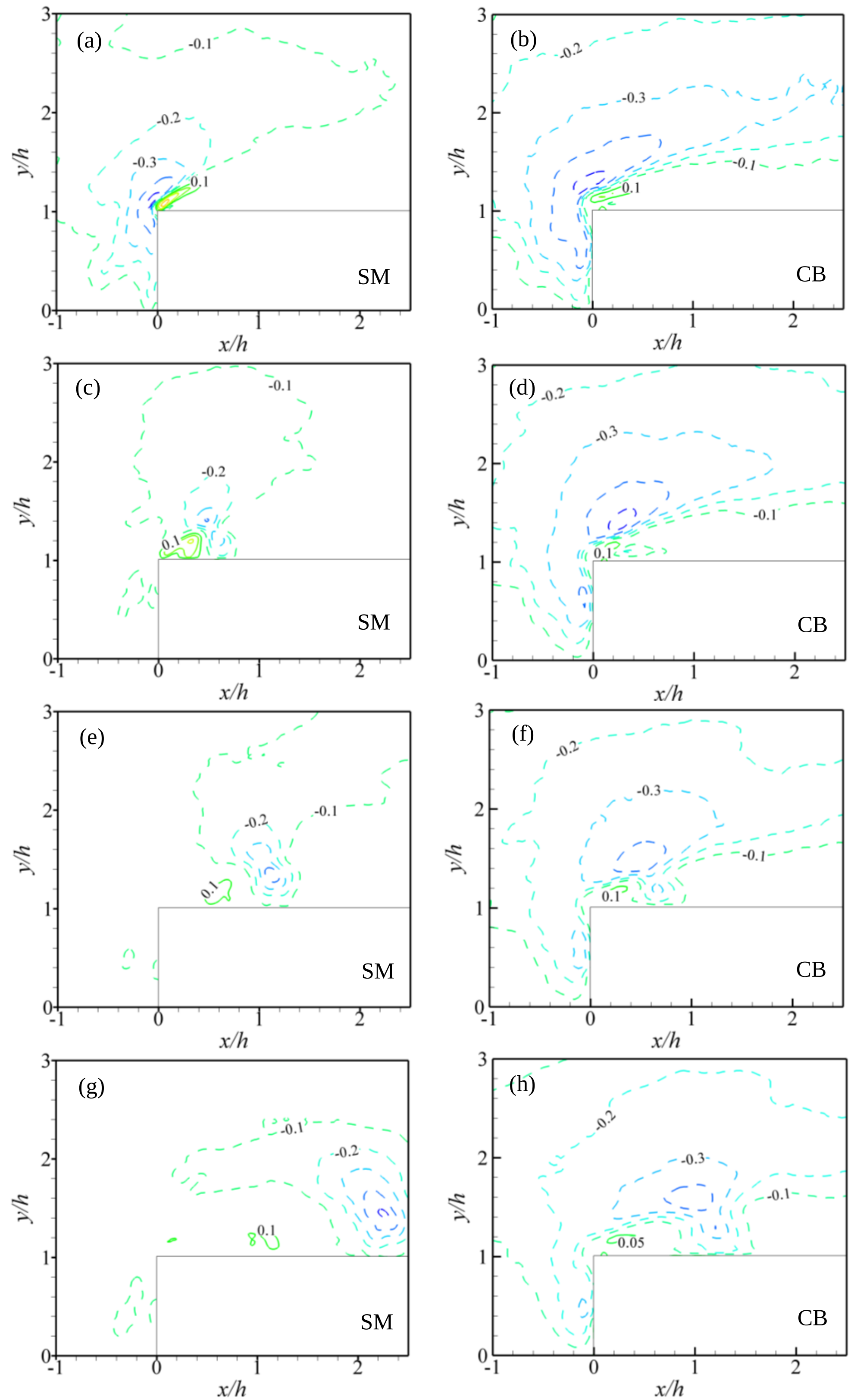

Figure 4.33: Iso-contours of the two-point spatial cross-correlation function (R_{uv}^{s}) along the locus of maximum streamwise turbulence intensity in the recirculation region (Contour levels are from -0.5 to -0.1 and 0.1 to 0.5 with the interval of 0.1).

The negative contours are of considerably larger spatial extent than the positive contours. This suggests that Q2 and Q4 are the dominant motions producing the Reynolds shear stress. The Q2 and Q4 structures are thus important parts of the turbulent mixing process, transporting low-speed fluid from the wall into the higher-speed regions and bringing high-speed fluid towards the wall, respectively. For the smooth wall, the streamwise evolution of the cross-correlation is similar to those of the *u* and *v* auto-correlations. For the cube roughness, the region of significant negative correlation remains massive for all reference locations in the recirculation region. This reflects the more dominant contributions of the Q2 and Q4 motions to the Reynolds shear stress in the quadrant decomposition for CB compared to SM. Also evident in the rough wall results are the diminishing size and magnitude of the positive correlations when compared to the smooth wall. This implies that rough wall flow is recovering more rapidly than the smooth wall.

To compare the average dimensions of the vortical structures the streamwise and wall-normal integral length scales of the velocity fluctuations were calculated. The integral length scales were estimated by integrating the one-dimensional profiles of the two-point spatial auto-correlation functions R^s_{uu} and R^s_{vv}. The streamwise and wall-normal integral length scales, $L^u{}_x$ and $L^u{}_y$, respectively, of the fluctuating streamwise velocity were estimated as follows:

$$L^u_x = \int_0^\infty R^s_{uu}(\Delta x, 0)dx \quad (4.12)$$

$$L^u_y = \int_0^\infty R^s_{uu}(0, \Delta y)dy \quad (4.13)$$

The profiles of $L^u{}_x$ and $L^u{}_y$ normalized by the step height are shown in Figures 4.34(a) and 4.34(b), respectively. The values of $L^u{}_x$ and $L^u{}_y$ were calculated at the leading edge (x/L_r = 0.0) and the two downstream locations x/L_r = 0.5 and 1.0. The corresponding profiles of the integral length scales obtained at $x/h \approx$ -20 over the smooth wall are included for reference. For the smooth wall, no significant differences were observed between the length scales at the leading edge and upstream location. Further downstream, the spatial scales in the shear layer are reduced in comparison to the upstream structures with the differences reaching about 70%. For the upstream roughness, however, a dramatic increase in the spatial scales is observed over a considerable extent of the separated shear layer relative to the smooth wall. For $L^u{}_x$ and $L^u{}_y$ the differences were found to average to about 138% and 68%, respectively within the shear layer.

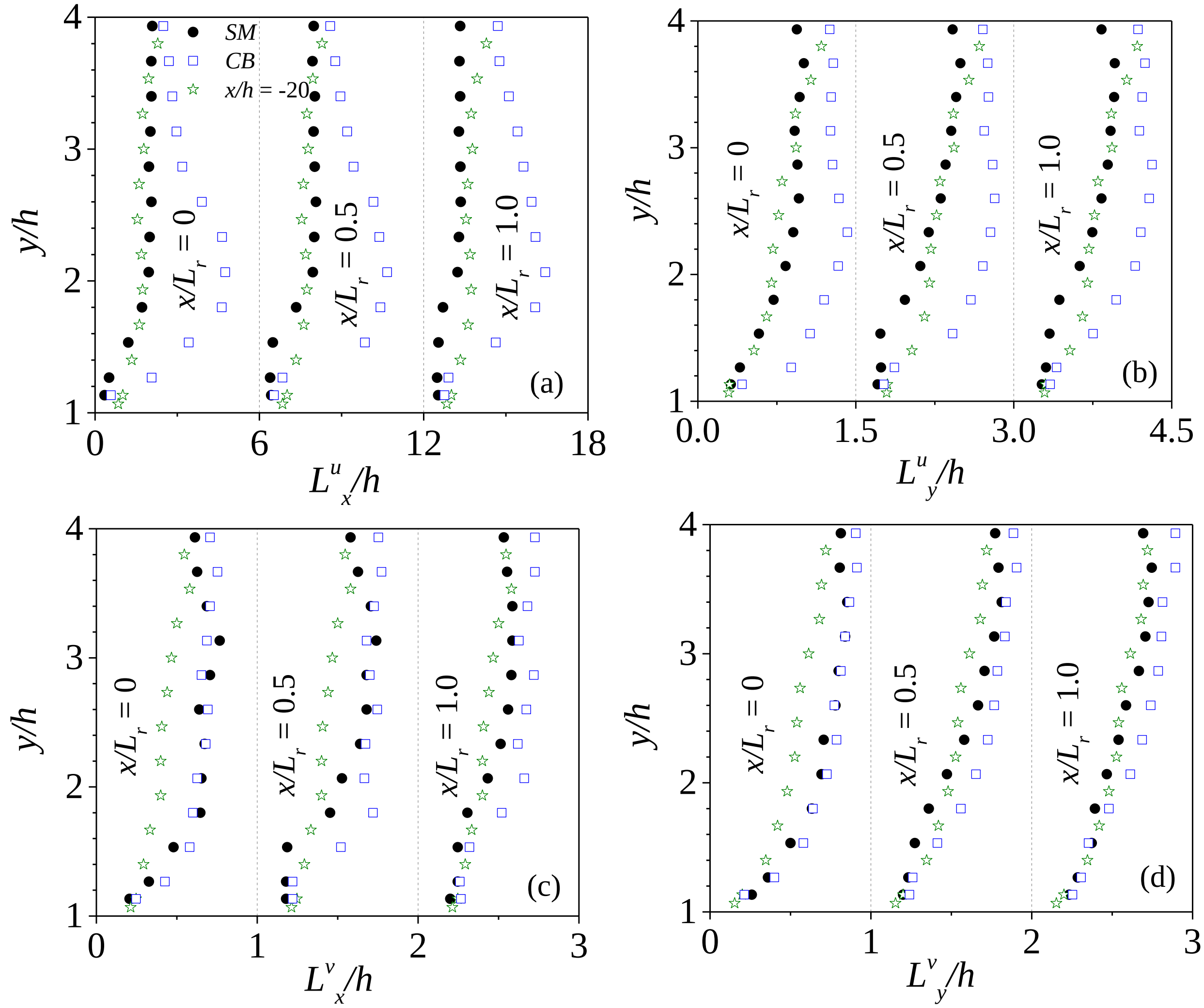

Figure 4.34: Wall-normal distribution of the length scales of the two-point spatial correlations in the primary recirculation region.

The streamwise and wall-normal integral length scales of the fluctuating wall-normal velocity, $L^v{}_x$ and $L^v{}_y$, respectively, were estimated as:

$$L_x^v = \int_0^\infty R_{vv}^s(\Delta x, 0)dx \tag{4.14}$$

$$L_y^v = \int_0^\infty R_{vv}^s(0, \Delta y)dy \tag{4.15}$$

The profiles of $L^v{}_x$ and $L^v{}_y$ are presented in Figures 4.34(c) and 4.34(d), respectively. For both spatial scales, the smooth and rough wall profiles at the leading edge are nearly indistinguishable, but are about 70% larger than the upstream smooth wall values within $1 \leq y/h \leq 3$. Downstream of the leading edge, the differences with the upstream values gradually diminish.

4.4.4 Space-Time Correlations with $\Delta x = 0$

Figure 4.35 shows the streamwise evolution of the iso-contours of the space-time correlation R_{uu} $(0, \Delta y, \tau)$. This correlation is often used to show the temporal evolution of the eddies ejected from the wall region. Therefore, it can be used to investigate the interconnection between the outer turbulent structure and events near the wall. At all four reference locations, the extent of significant correlation is much larger for the cube roughness than the smooth wall. The substantial streamwise elongation for CB is a further indication that the large eddy structure has a longer memory for CB than SM. The larger wall-normal extents of the CB correlations are indicative of the transport of events originating near the wall that reach much further into the outer layer than over the smooth wall. This is consistent with the large region of ejected fluid observed for CB over the step and reflects the higher levels of Reynolds stress in the outer layer for CB in comparison to SM.

The iso-contours of the wall-normal fluctuating velocity space-time auto-correlation R_{vv} $(0, \Delta y, \tau)$ are shown in Figure 4.36. The extents of the wall-normal correlation are significantly less than the streamwise correlation irrespective of the upstream roughness condition. This suggests that the wall-normal fluctuations have less influence on the eddies responsible for the inner-outer layer interaction.

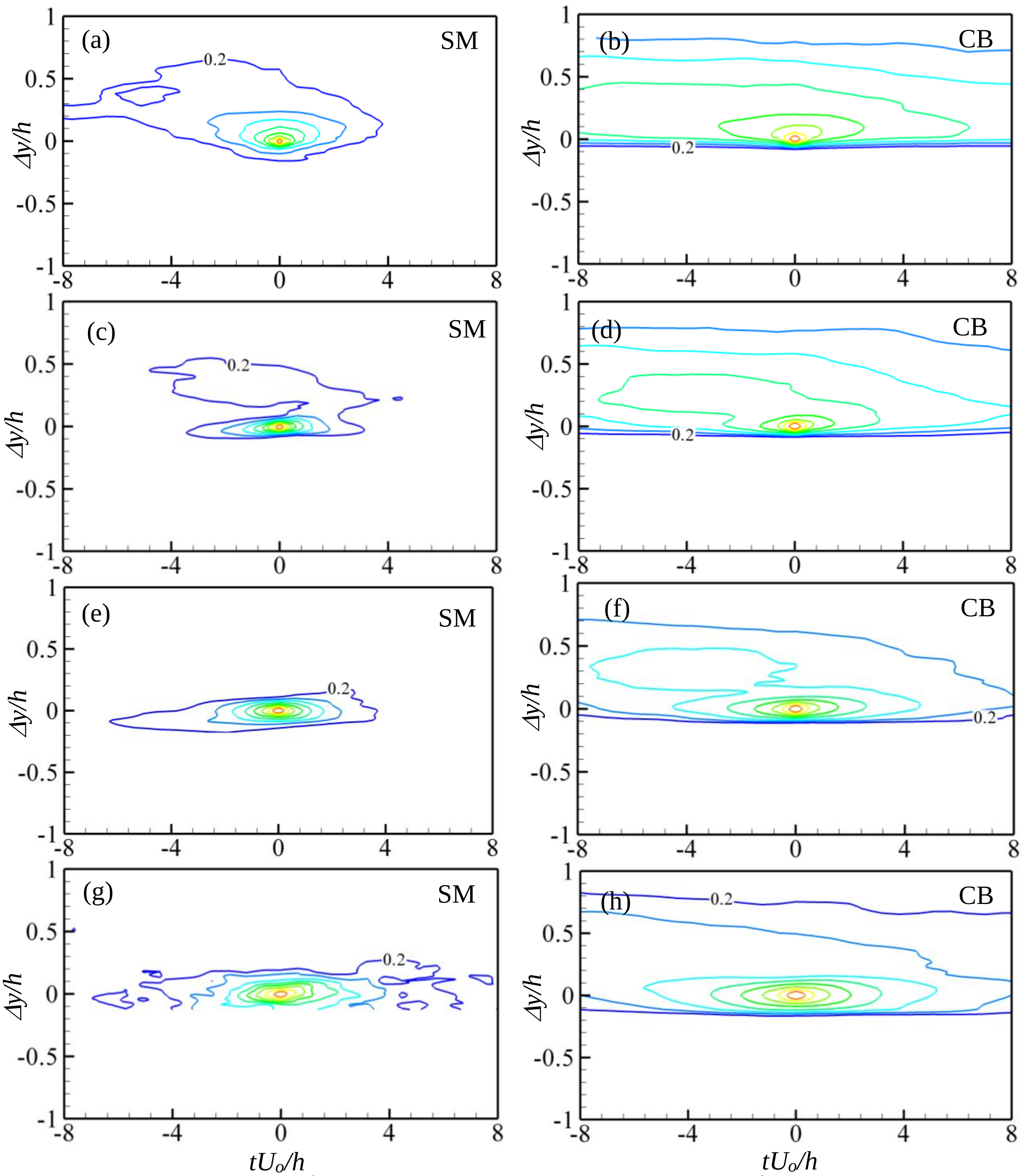

Figure 4.35: Iso-contours of two-point space-time auto-correlation of the streamwise velocity along the locus of maximum streamwise turbulence intensity in the recirculation region.

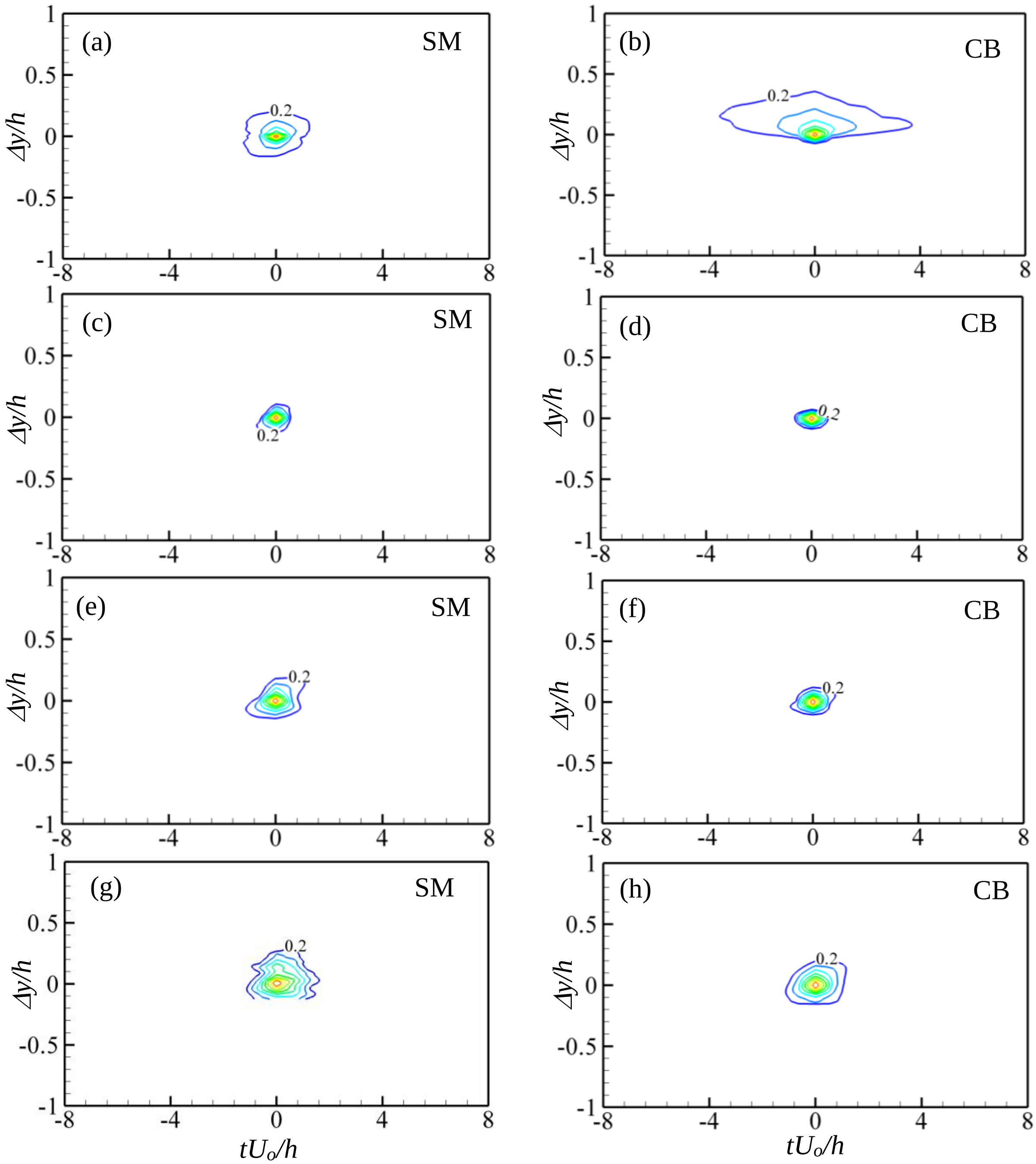

Figure 4.36: Iso-contours of two-point space-time auto-correlation of the wall-normal velocity along the locus of maximum streamwise turbulence intensity in the recirculation region.

4.4.5 Development of the Two-Point Correlations in the Recovery Region

Figure 4.37 examines the redevelopment of the profiles of the average dimensions of coherent structures in the recovery region. The evolution of the streamwise and wall-normal integral scales of R^s_{uu} are shown in Figures 4.37(a) and 4.37(b), respectively.

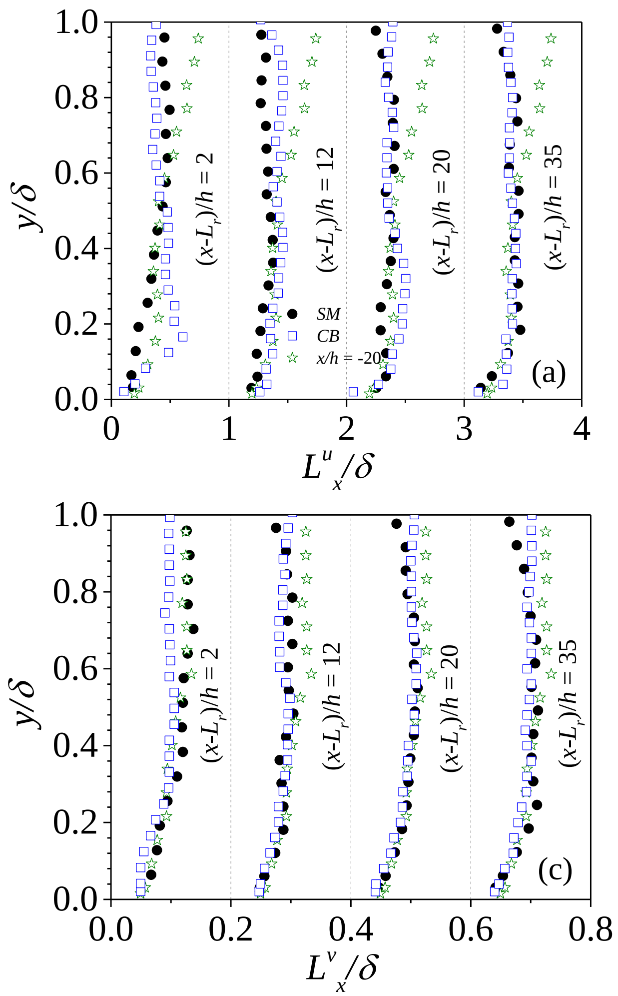

Figure 4.37: Wall-normal distribution of the length scales of the two-point spatial auto-correlations in the redevelopment region.

The spatial scales are nearly independent of upstream roughness, except in the region immediately downstream of reattachment. The structures in the wall region retain their spatial coherence over longer distances with the cube roughness compared to the smooth wall. For the rough wall, for instance, this caused increases of approximately 162% and 67% in the values of $L^u{}_x$ and $L^u{}_y$, respectively, at $(x\text{-}L_r)/h \approx 2$ in the reattached shear layer. The corresponding profiles for the wall-normal correlations, $L^v{}_x$ and $L^v{}_y$, are shown in Figures 4.37(c) and 4.37(d), respectively. Downstream of reattachment the smooth and rough wall profiles are nearly indistinguishable, suggesting a negligible influence of upstream roughness on the smaller eddies in the redevelopment region. All together, the four plots shown in Figure 4.37 suggest that inner layer evolves much more quickly than the outer layer. In the near-wall region, the profiles show nearly complete recovery to the upstream smooth wall distribution. In the outer layer the profiles did not recover to the upstream smooth wall profile even at the farthest downstream location. These observations are consistent with the measurements of Song and Eaton (2004) that showed that the inner layer recovers much faster than the outer layer for turbulent boundary layers downstream of reattachment.

4.5 Proper Orthogonal Decomposition (POD) of the Flow Fields

The snapshot POD method was applied to the flow fields to reveal the spatial and temporal characteristics of the dominant eddies in shear layer. For each upstream condition, the POD was performed for the three measurement planes P0, P2 and P5, corresponding to the upstream plane, recirculation region and part of the redevelopment region, respectively. To ensure that the optimum number of TRPIV snapshots was used in the decomposition, a convergence study was conducted in which increasing number of snapshots ($36 \leq N \leq 9000$) were used to perform the POD. The values of the fractional energy of the first POD mode are summarized in Table 4.3 for SM and CB. Except for plane 0 of SM it is clear that the decomposition converges for number of snapshots $N > 1800$. The upstream plane data of the smooth wall may have been affected by measurement noise causing λ_1^* to oscillate. Nevertheless, the values of the fractional energy in mode 1 converged to within 1%. For the smooth wall, the energy of mode 1 readjusts to the presence of the step as indicated by the decrease of λ_1^* from P0 to P2 and an increase to P5. The rough wall values on the other hand show a consistent increase from P0 to P5. Also, for a given measurement plane, the rough wall values are consistently larger than those over the smooth wall. This agrees with the spatial and space-time correlation results that showed that the rough wall flows possess more coherent large-scale vortical structures than the smooth wall flow. In the results presented subsequently, a sample size of $N = 6000$ was used to perform the POD.

Table 4.3: Energy convergence for increasing number of snapshots (N) of the first mode

Snapshots (N)	***SM***			***CB***		
	λ_1^* (P0)	λ_1^* (P2)	λ_1^* (P5)	λ_1^* (P0)	λ_1^* (P2)	λ_1^* (P5)
36	19.66	15.23	26.98	21.97	33.16	37.30
90	19.49	14.34	22.27	22.02	33.71	35.57
180	18.70	12.96	21.71	21.41	33.45	35.19
360	18.61	12.97	21.62	21.58	33.40	34.87
900	18.61	13.02	21.63	21.35	33.35	34.98
1800	18.69	13.01	21.63	21.37	33.21	35.00
3600	18.74	13.00	21.63	21.37	33.22	35.00
6000	18.72	13.00	21.63	21.37	33.22	35.00
9000	18.75	13.00	21.63	21.37	33.22	35.00

Figure 4.38 shows a comparison of the modal energy and cumulative modal energy distributions among the upstream and downstream planes. To avoid clatter of the data only the first 40 POD modes are plotted. The results in Figures 4.38(a) and 4.38(b) show that the first POD mode contributes to the largest fraction of the total TKE, while the contributions from the higher order modes decay very rapidly, reaching less than 2% from the 15th mode. Similar decay with increasing mode number has been reported in a wide range of flows including ZPG turbulent boundary layers (Sen et al. 2008; Wu and Christensen 2010), separated shear layers (Kostas et al. 2005; Sherry et al. 2010; Sampath et al. 2014; Iftekhar and Agelin-Chaab2016) and jets (Gordeyev and Thomas 2000; Iqbal and Thomas 2007; Shinneeb et al. 2008). The shape of the curves provides a rough indication of how fast the POD modal energy converges. In the recirculation region (Figure 4.38(a)), the enhanced growth of the structures by the cube roughness caused a more rapid convergence than was observed for the smooth wall. This contrasts with the upstream data where the smooth and rough walls converge at nearly the same rate. The results in Figure 4.38(b) reveal that the modal energy of the lowest-order modes does not recover to the upstream values, which is consistent with the spatial correlation results in the outer parts of the redevelopment region. The energy convergence is more clearly depicted in the profiles of the cumulative energy (Figures 4.38(c) and 4.38(d)). The results suggest a more rapid energy convergence in both the recirculation

and redevelopment regions of CB compared to SM. That is, in order to capture the same amount of total TKE, a smaller number of POD modes will be required in the case of CB than SM. For instance, to capture approximately 50% of the total TKE in the recirculation region, only the first 5 low-order modes are required for CB as opposed to 16 modes for the smooth wall. In the redevelopment region, even fewer modes are required (2 and 8 for CB and SM, respectively) to capture about 50% of the total TKE. The reduced number of low-order modes in the redevelopment region is indicative of faster energy convergence in this region compared to upstream and recirculation regions.

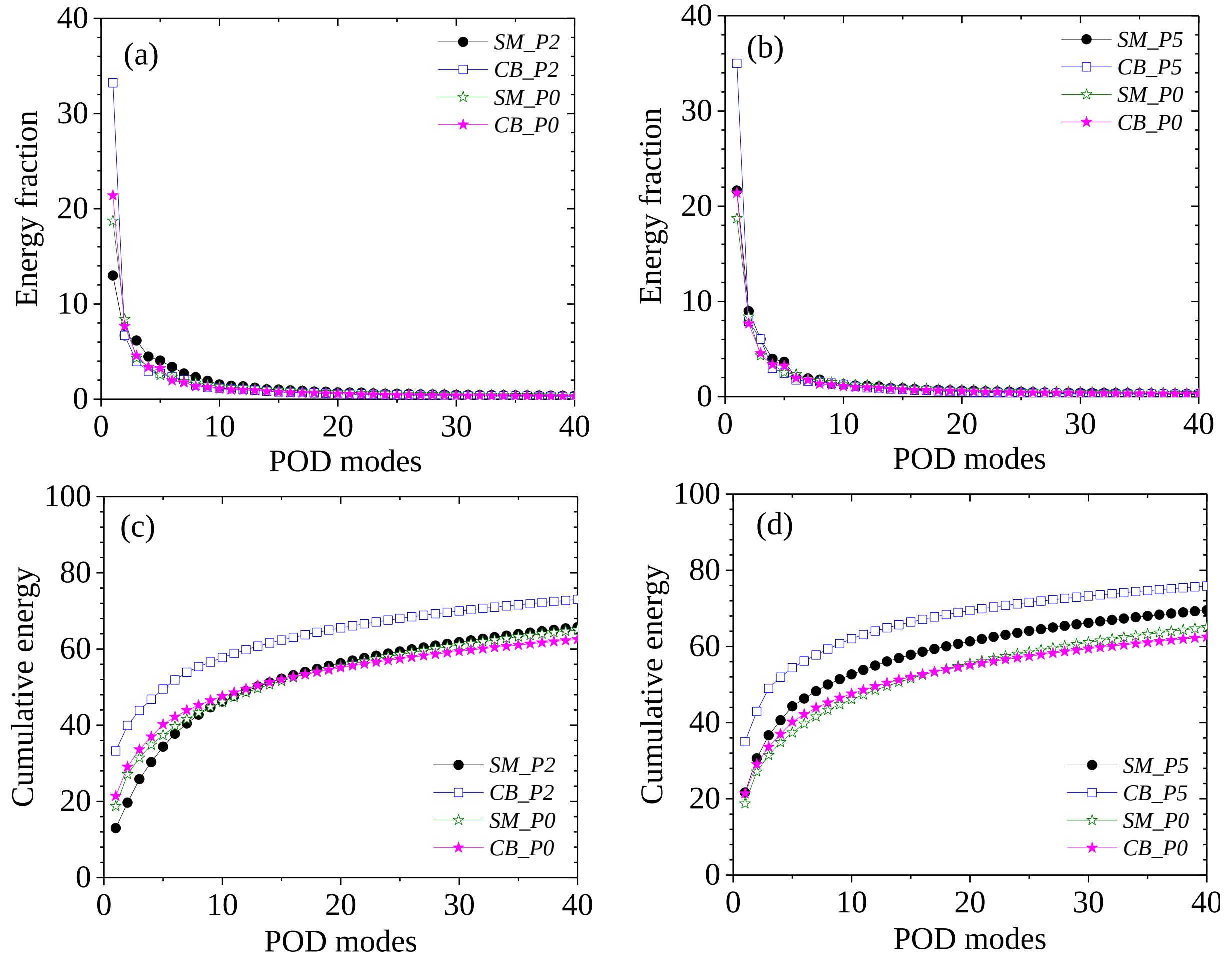

Figure 4.38: Distributions of modal and cumulative energy fraction for the first 40 modes.

The effects of upstream roughness on the spatial eigenmodes in the recirculation region are examined in Figure 4.39. The plots show the iso-contours of the streamwise component $\Phi_u(x, y)$ of the first five low-order POD modes. The percentage of total TKE contributed by the mode is indicated in each plot. As depicted in Figure 4.39(a) and 4.39(b) for SM and CB, respectively, the iso-contour of the first spatial mode encompasses the entire recirculation bubble. This suggests that the dynamics of the most dominant spatial mode are related to the physical mechanism responsible for the formation of the recirculation bubble. It has indeed been suggested in previous studies (e.g., Humble et al. 2009; Thacker et al. 2013; Mohamme-Taifour and Weiss 2016) that the first POD mode is exclusively associated with global velocity fluctuations within the recirculation bubble, which are linked with the flapping motion of the recirculation bubble. The effect of the cube roughness is to reverse the sign of the spatial mode from negative to positive. It is likely the high-speed inward moving u fluctuations represented by the positive Φ_u counteract the outward expansion of the recirculation bubble resulting in a smaller bubble in the case of CB compared to SM. The sharp contrast between the first POD mode and the higher-order modes is shown in the Figure. With increasing number of modes, smaller-scale structures arise as alternating positive and negative contours. These are considerably larger for the rough wall and their signs are reversed when compared to the smooth wall contours. The periodicity of the higher-order modes was also observed in previous investigations over a forward-facing step (Iftekhar and Agelin-Chaab 2016), an Ahmed body (Thacker et al. 2013) and flat plate turbulent boundary layer (Rempfer and Fasel 1994). The parity of the spatial modes reported by previous investigators can be noticed in the smooth wall contours. For instance, the smooth wall plots can be paired as follows: (Φ_u^2, Φ_u^3), (Φ_u^4, Φ_u^5), and so on, where each member of a pair is obtained by a streamwise shift of the other member. Following Thacker et al. (2013), the wavelength λ_Φ between two positive or negative extremum zones of fluctuating velocity can be estimated as indicated in Figure 4.39(c)

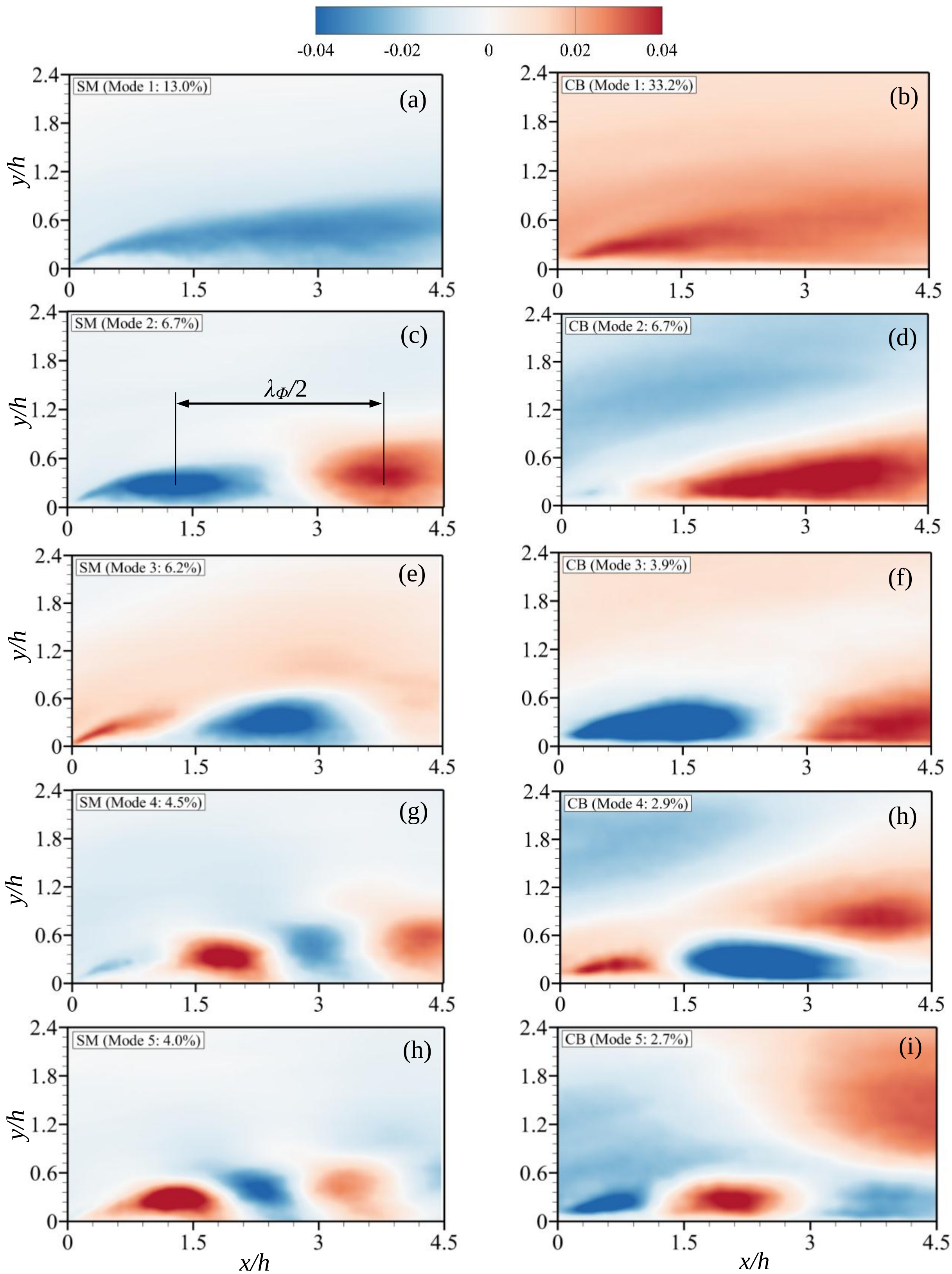

Figure 4.39: Iso-countours of the spatial eigenmodes in the recirculation region (Plane 2).

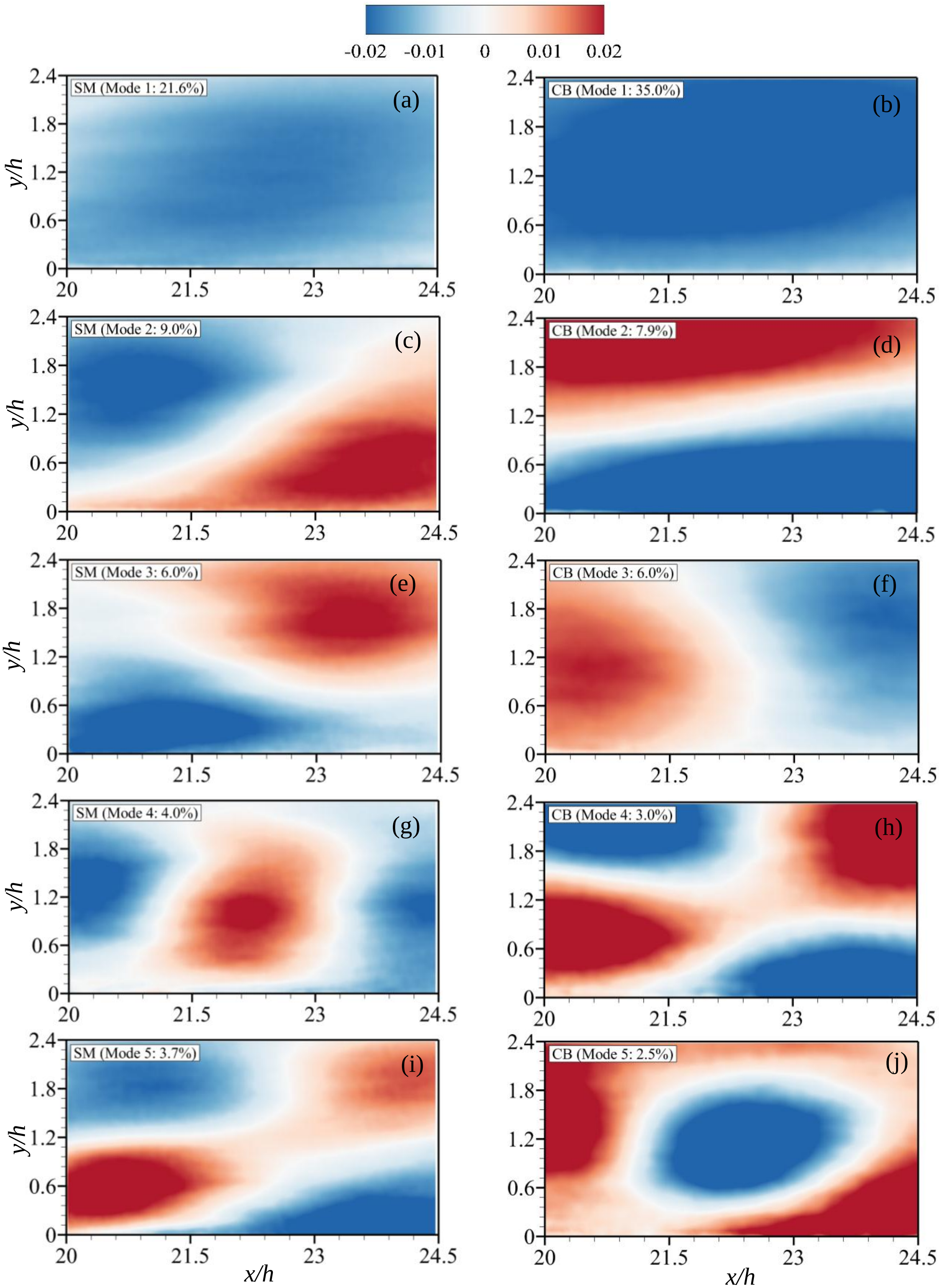

Figure 4.40: Iso-countours of spatial eigenmodes in the redevelopment region (Plane 5).

for SM. By using a convection velocity of U_c = 0.23 *m/s* measured from the plots in Figure 4.30(a) for the smooth wall, the frequency of the positive/negative alternation was estimated as $f_\Phi = U_c / \lambda_\Phi \approx 2.9$ Hz. This corresponds to a Strouhal number, $St = f_\Phi L_r / U_c$ of approximately 0.43 and reflects the relatively high frequency activity signature observed in this region for SM.

The iso-contours of $\Phi_u^n(x, y)$ in the redevelopment region (P5) are shown in Figure 4.40. The contour values of first POD mode are predominantly negative indicating the presence of more strongly coherent or larger-scale structures in the redevelopment region compared to the recirculation region. The higher-order modes show a similar streamwise periodicity but their orientation is more random than was observed in the recirculation region. Despite the randomness, the contour sizes are considerably larger than those observed in the recirculation region. The spatial structure of the second POD mode for CB closely resembles that reported for equilibrium turbulent boundary layers. This supports the earlier observation that the rough wall flow is recovering more quickly than the smooth wall flow.

The temporal modes of the POD (also known as chrono-modes) were investigated using temporal spectra of the POD coefficients. Figure 4.41 shows the frequency spectra of the first four chrono-modes in the recirculation region. The more energetic structures produced by the upstream roughness reflect in the temporal spectra of Figure 4.41(a) that indicate a larger spectral density at low frequencies for CB in comparison to SM. With increasing mode number, the spectral density is decaying. The decay is more rapid for the rough wall than the smooth wall due to the faster convergence of the rough wall POD. To obtain the dominant frequencies associated with the POD modes the pre-multiplied spectra of the chrono-modes were calculated. Those obtained in the recirculation region are shown in Figure 4.42. The dominant frequencies in the first chrono-modes are approximately 1.0 Hz and 0.8 Hz for SM and CB, respectively.

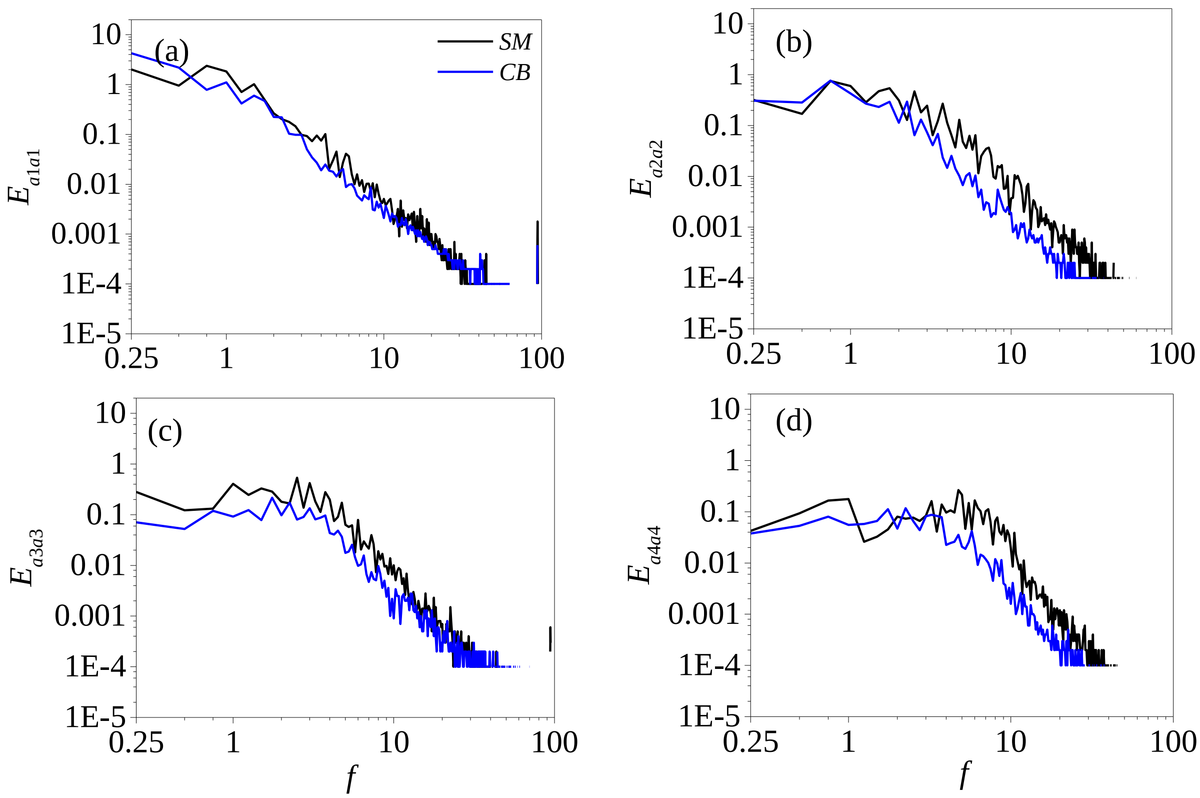

Figure 4.41: Frequency spectra of the temporal modes in the recirculation region.

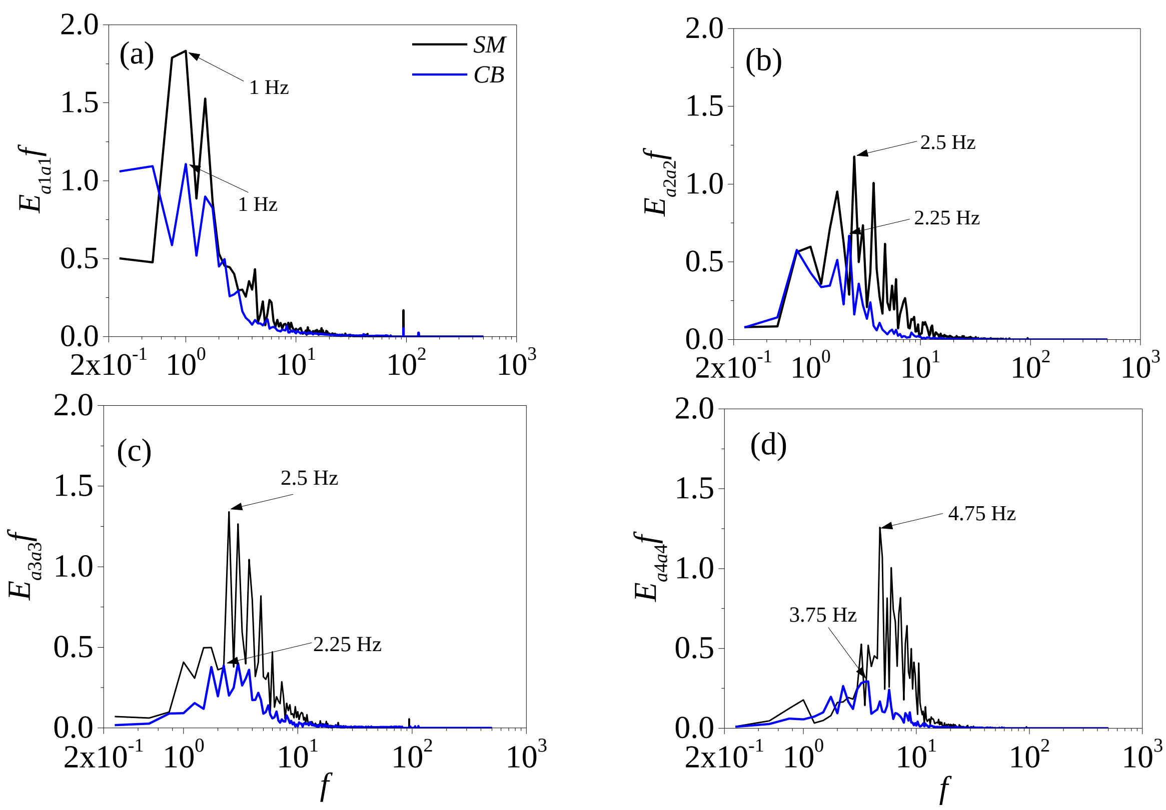

Figure 4.42: Pre-multiplied energy spectra of the temporal modes in the recirculation region.

Due to the parity rule, the dominant frequencies in the spectra are similar for successive pairs of temporal modes. For instance, the dominant frequency for the second and third is 2.5 Hz for SM and 2.3 Hz for the rough wall. It should be noted that the frequency of 2.5 Hz obtained for SM in Figure 4.42(b) is in good agreement with 2.9 Hz obtained for the positive/negative alternating contours of spatial mode 2 in Figure 4.39(c). A similar equality was observed for the fourth and fifth chrono-modes. The spectra for the fifth chrono-mode is not shown here for economy of space. The corresponding frequencies are approximately 5 Hz and 4 Hz for SM and CB, respectively. The consistently lower frequency values over the rough wall are indicative of the much larger structures over the rough wall than the smooth wall. Also, the increasingly smaller areas under the CB curves are consistent with the rapid convergence of energy for the rough wall.

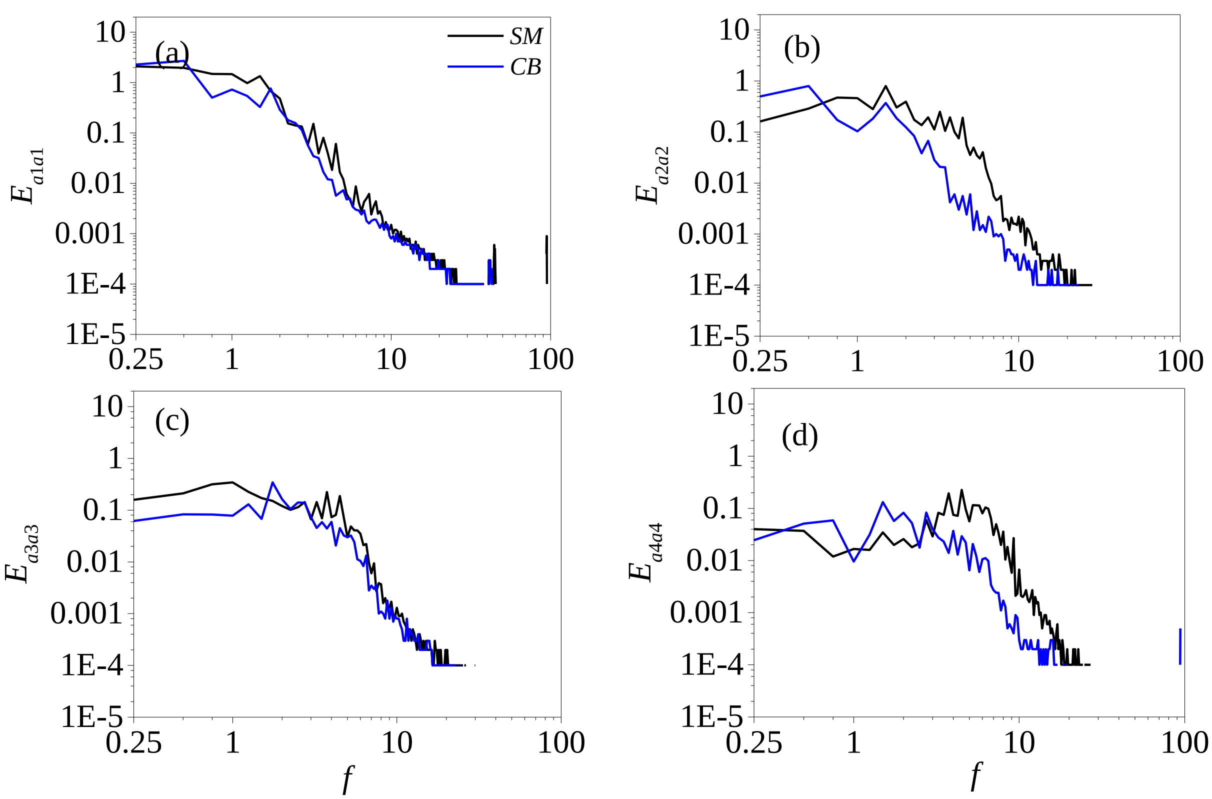

Figure 4.43: Frequency spectra of the temporal modes in the redevelopment region.

The chrono-modes in the redevelopment region are shown in Figure 4.43. The plots show a similar decay in spectral density with increasing mode number but there is no systematic dependency on upstream roughness. The profiles of the pre-multiplied spectra in the redevelopment region are displayed in Figure 4.44. Each of the plots shows that there are two dominant frequencies for the temporal characteristics of the modes in the redevelopment region. This illustrates the presence of smaller-scale eddies (higher frequencies) in the redevelopment region, which merge under the inverse cascade mechanism to form larger-scale structures (lower frequencies).

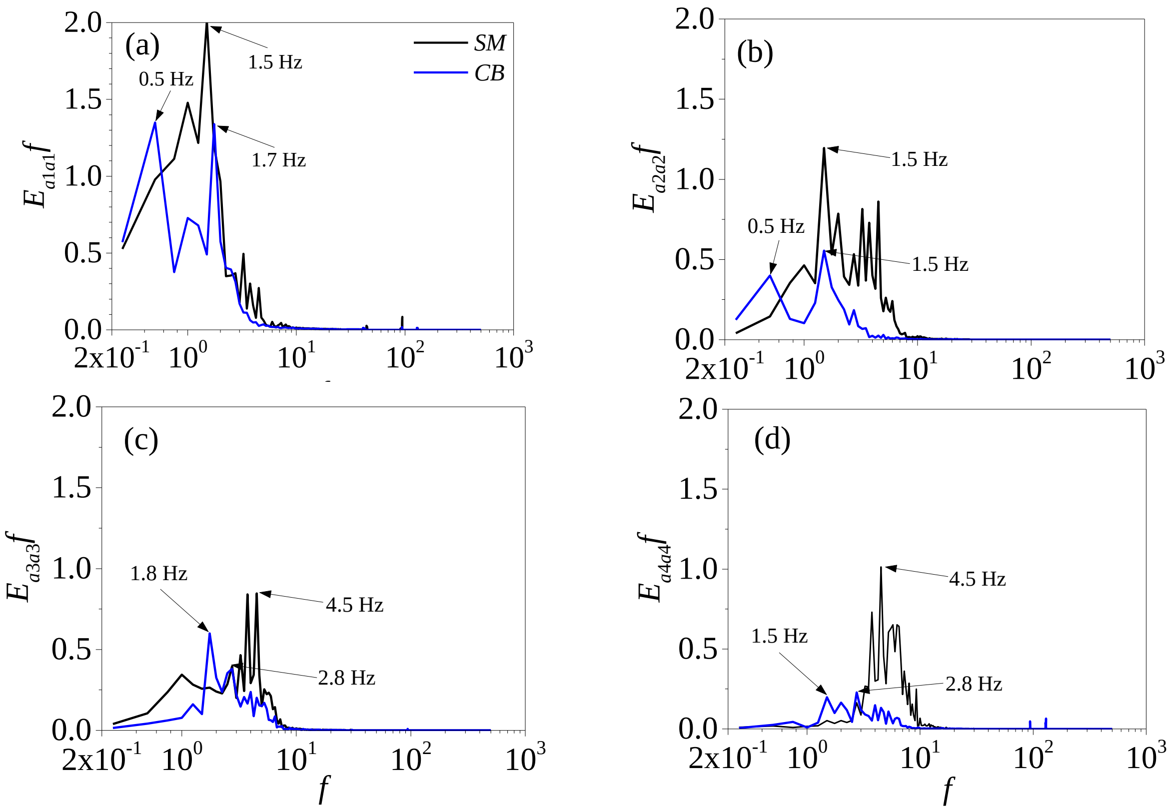

Figure 4.44: Pre-multiplied energy spectra of the temporal modes in the redevelopment region.

4.6 Implications for Turbulence Modelling

The measurements reported here revealed certain features of the forward-facing step flow that have important implications for turbulence modelling. The first of these, perhaps, with far reaching implications for RANS-based models is the existence of significant negative Reynolds shear stress near the leading edge of the step under the counter gradient diffusion mechanism. In the standard eddy viscosity model (EVM), the Reynolds stress tensor, $-\langle u_i' u_j' \rangle$, is related to the mean velocity gradients as

$$-\langle u_i' u_j' \rangle = \nu_t \left(\frac{\partial U_i}{\partial x_j} + \frac{\partial U_j}{\partial x_i} \right) - \frac{2}{3} K \delta_{ij} \tag{4.16}$$

where ν_t is the turbulence eddy viscosity, K is the turbulent kinetic energy and δ_{ij} is the Kronecker delta. Central to the eddy viscosity approximation is the requirement that both the Reynolds stress and strain rate tensors be in alignment with each other. This is to ensure that the eddy viscosity is always positive, since a negative eddy viscosity would have no physical meaning.

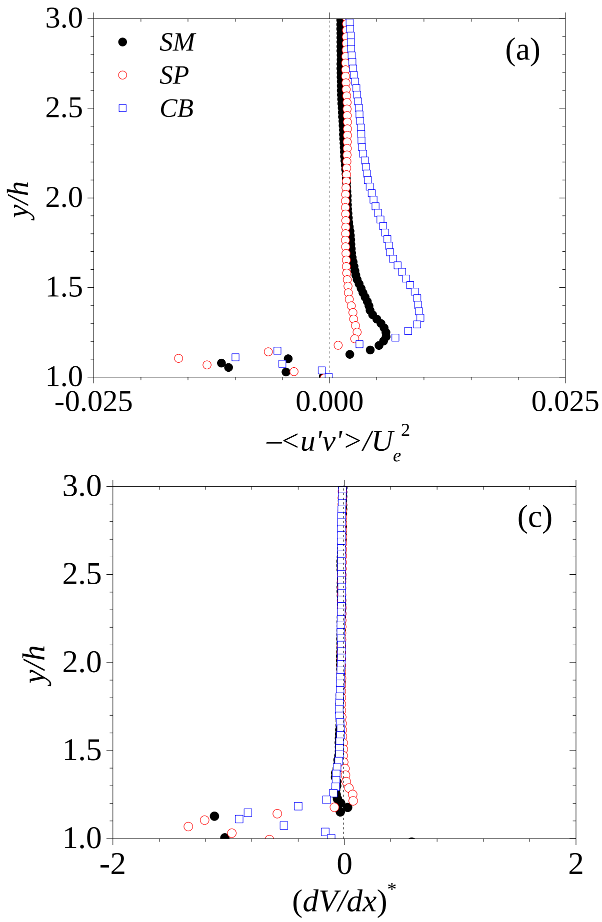

Figure 4.45: Distribution of Reynolds shear stress and velocity gradients at the leading edge of step.

To investigate the sign of the eddy viscosity, $\nu_t = -\langle u'v' \rangle / (\partial U/\partial y + \partial V/\partial x)$, in the present flow, profiles of the Reynolds shear stress and mean strain rate were plotted at the leading edge of the step. These are shown in Figure 4.45. In all cases, $-\langle u'v' \rangle$ is negative while $\partial U/\partial y + \partial V/\partial x$ is positive close to the wall ($1.0 \leq y/h \leq 1.3$). These values will contribute to negative eddy viscosity near the leading edge of the step. The occurrence of a negative eddy viscosity near the corner of the step suggests that RANS models based on equation (4.16) above are not appropriate for this flow.

In RANS simulations based on the two-equation turbulence model, the isotropy assumption ($\langle u'^2 \rangle \approx \langle v'^2 \rangle$) is made. In order to investigate the validity of this assumption, values of the anisotropy parameter, $\langle v'^2 \rangle / \langle u'^2 \rangle$, were calculated. Figures 4.46(a) and 4.46(b) show the streamwise evolution of $\langle v'^2 \rangle / \langle u'^2 \rangle$ in the recirculation and redevelopment regions, respectively, for SM, SP and CB. The results indicate a strong anisotropy between the Reynolds stresses in the shear layer. Within the recirculation and redevelopment regions, the wall-normal Reynolds stress is approximately one-half of the streamwise Reynolds stress. This high level of anisotropy in the flow suggests that RANS models employing isotropic stress assumption cannot be used to reproduce the turbulence intensities measured over the step.

Also, in the standard k-ε model, the turbulent eddy viscosity is evaluated as (Wilcox 1993):

$$\nu_t = C_\mu \frac{K^2}{\epsilon} \tag{4.17}$$

where C_μ is a dimensionless constant. The value of C_μ is obtained from experiments, typically two-dimensional turbulent boundary layer experiments. In the logarithmic region of the 2D turbulent boundary layer, where production balances dissipation, it can be shown that $C_\mu^{1/2} = -\langle u'v' \rangle / K$. The calculations by Bradshaw et al. (1975) have shown that $-\langle u'v' \rangle / (2K) \approx 0.15$. This yields $C_\mu \approx 0.09$. The values of the structure parameter, $-\langle u'v' \rangle / 2K$, were measured in the present experiments. In estimating the structure parameter, the turbulent kinetic energy (k) was estimated as $K = 0.75(\langle u'^2\rangle + \langle v'^2\rangle)$. The profiles of the structure parameter are shown Figures 4.46(c) and 4.46(d) for the three test cases in the recirculation and redevelopment regions, respectively. The structure parameter is negative at the leading edge of the step for all cases due the negative values of $-\langle u'v'\rangle$. The structure parameter is nearly independent of upstream roughness in both the recirculation and redevelopment regions. Except in a thin layer close to the wall, $-\langle u'v'\rangle/2K$ is approximately constant with a value approximately 0.15. This suggests that use of $C_\mu = 0.09$ is appropriate for this flow except near the step corner and very close to the wall.

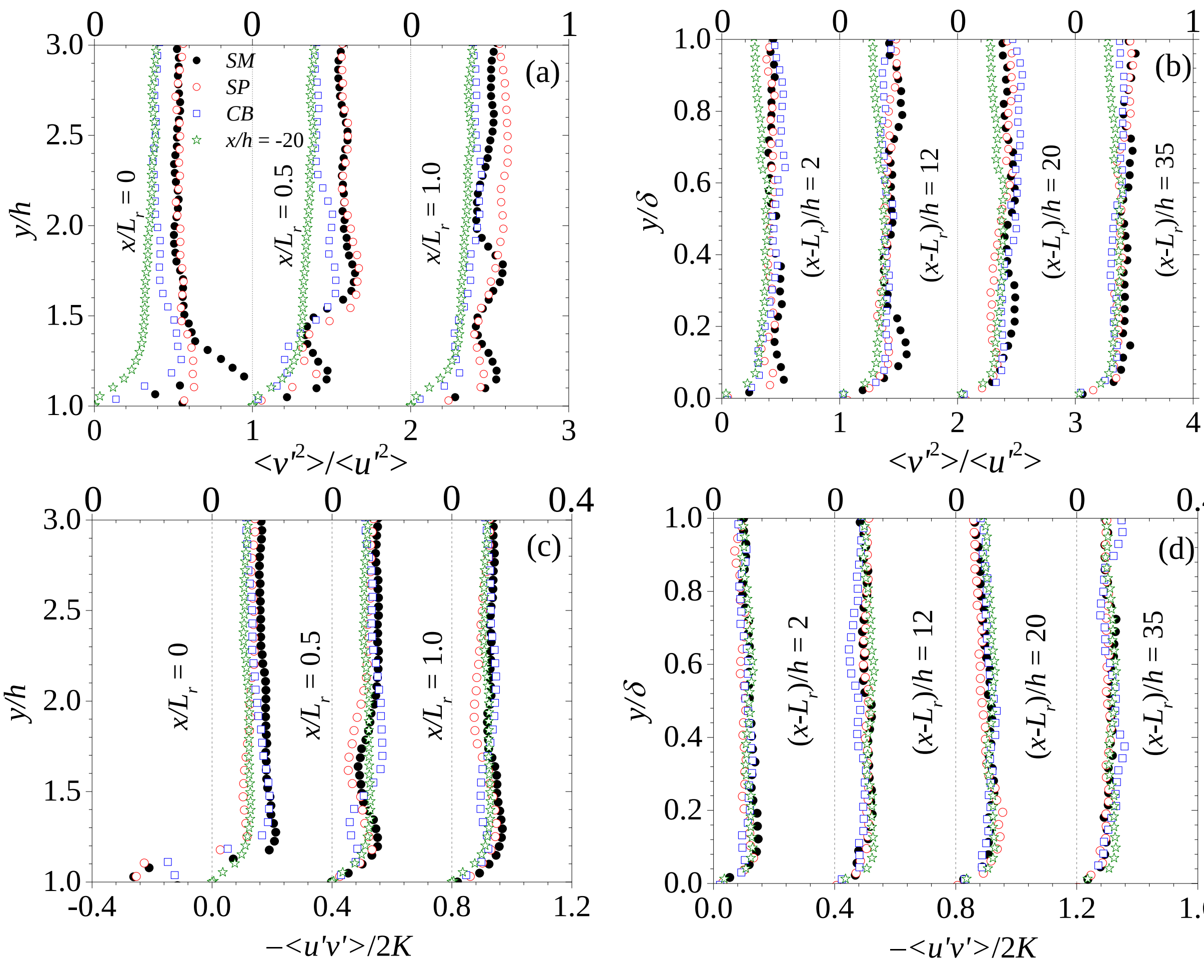

Figure 4.46: Distribution of (a,b) stress ratio; (c,d) structure parameter in the recirculation and redevelopment regions.

Finally, as shown in Figure 4.12(d), the near-wall values of wall-normal turbulent transport of the Reynolds shear stress ($\langle u'v'^2\rangle$) are predominantly positive near the step corner ($1.0 \leq y/h \leq 1.1$). This falls within the region where the counter-gradient diffusion phenomenon is observed. The positive near-wall values of $\langle u'v'^2\rangle$ suggest a turbulent transport of $u'v'$ away from the wall. In the k-ε model, the triple velocity products are modelled as (Skare and Krogstad 1994):

$$\langle u_k' u_i' u_j'\rangle = -C_s \frac{K}{\varepsilon} \langle u_k' u_l'\rangle \frac{\partial \langle u_i' u_j'\rangle}{\partial x_l} \tag{4.18}$$

where K and ε are the turbulent kinetic energy and turbulent kinetic dissipation rate, respectively, and $C_s = 0.08$ is a modelling constant. For a two-dimensional FFS flow, this equation can be expanded as

$$\langle u'v'^2\rangle = 0.08 \frac{K}{\varepsilon} \left[\langle u'v'\rangle \frac{\partial(-\langle u'v'\rangle)}{\partial x} + \langle v'^2\rangle \frac{\partial(-\langle u'v'\rangle)}{\partial y} \right] \tag{4.19}$$

Near the leading edge, the first term in the parenthesis is positive, while the second term is negative but of larger magnitude than the first. This would result in negative values of $\langle u'v'^2\rangle$ contrary to the positive values observed near the leading edge. These conditions imply that the gradient transport model will not be able to accurately predict the wall-normal transport of Reynolds shear stress near the corner of the step.

CHAPTER 5

CONCLUSIONS AND RECOMMENDATIONS

5.1 Summary and Conclusions

A planar time-resolved particle image velocimetry method was used to investigate the effects of upstream roughness on the flow characteristics of turbulent boundary layer over a forward-facing step. Two types of upstream roughness were investigated, including a transitionally rough 16-grit sandpaper and fully rough array of staggered cubes. Instantaneous flow fields and time-averaged quantities such as the mean velocities, Reynolds stresses, triple correlations, temporal auto-correlations and frequency spectra were measured. Quadrant decomposition and joint probability density functions of the velocity fluctuations were also measured to investigate the contribution of the dominant motions to mean Reynolds shear stress. To completely characterize the spatial and temporal evolution of the flow in the various regions of the flow, multi-point statistics such as two-point spatial and space-time correlations were calculated.

A Galilean decomposition of the instantaneous flow fields revealed that the flow downstream of the step is populated by streamwise-aligned spanwise vortices produced by the Kelvin-Helmholtz roll up the separated shear layer. These were found to be common features of the upstream smooth wall and sandpaper roughness but were replaced by large-scale ejections away from the step in the case of the staggered cubes. For the smooth wall and sandpaper roughness, the spanwise vortices were observed to be predominantly prograde-type vortices with instantaneous swirling strength that are of the same sign as the mean shear.

Turbulence spectra measurements near the leading edge of the step indicate that the upstream roughness reduced the vortex shedding frequency of the separated shear layer and at rate that increased with increasing roughness condition (k_s^+). A possible explanation for this reduction is the reduction of the mean streamwise velocity at the step height by the sandpaper and cube roughness.

The reattachment length of the recirculation bubble over the step decreases with increasing upstream roughness condition. This may be partly attributed to the reduction in magnitude of backflow with increasing roughness and the suppression of the frequency of vortex shedding from the leading edge. The upstream roughness also caused reductions in the height of the recirculation bubble and the distance of its centre from the leading edge of the step. The results also indicate that the flow accelerates more rapidly over the step for smooth wall than the rough walls, which will delay reattachment over the step for the smooth wall in comparison to the rough walls.

As the flow evolved in the recirculation region, the upstream roughness caused a decrease in the mean streamwise velocity in the outer layer and an increase in the shear layer. The Reynolds stresses remained relatively unchanged by the sandpaper roughness but showed significant modifications by the cube roughness. Downstream of the leading edge, the cubes increased the streamwise Reynolds stress both near the wall and outside the shear layer, while decreasing the wall-normal Reynolds stress and Reynolds shear stress near the wall but enhancing them in the outer layer. These changes are inversely proportional to distance in the recirculation region. Similar observations were made in the triple correlations measured for the three test cases. Near the leading edge, the wall-normal transport of the turbulent kinetic energy and Reynolds shear stress were attenuated by the sandpaper roughness in comparison to the smooth wall. Near the leading edge a counter-gradient diffusion of Reynolds shear stress was observed. The counter-gradient diffusion suggests that eddy-viscosity models based on the assumption of positive eddy viscosity will fail to properly predict the flow near the corner of the step.

The quadrant decomposition of the Reynolds shear stress and joint probability density function analysis reveals that the dominant contributors to the mean Reynolds shear stress near the leading edge are the inward (Q3) and outward (Q1) interaction terms. These are independent of upstream roughness. Downstream of the leading edge, the largest contributions to the mean Reynolds shear stress come from sweeps and ejections. The quadrant decomposition results also indicate that ejections (Q2) are the more dominant contributors to the Reynolds shear stress in the shear layer than sweeps (Q4). In the region of high Reynolds shear stress, this caused a shift in the maximum iso-probability contours of the joint probability density function in favour of the second quadrant. The cube roughness produced substantial enhancements in Q2 and Q4 in the outer layer but reductions in the near-wall region as was observed for the Reynolds shear stress.

In the recirculation region, the temporal auto-correlations show a more gradual decay with temporal separation at larger distances away from the wall. This is due to the increase in scale of the velocity fluctuations for reference locations away from the wall. Overall, away from the wall, the temporal correlations remain unaffected by the sandpaper roughness but were dramatically enhanced by the cube roughness. Also, the life times of the u' and v' fluctuations are considerably longer for the cube roughness within the shear layer. The two-point spatial and space-time correlations suggest that for the upstream cube roughness the vortical structures are more resilient to the presence of the step than the smooth wall. Convection velocity measurements in the recirculation region suggest a decrease in the propagation speed of the turbulence structures in the outer layer for a large upstream roughness condition. The convective velocities also revealed that larger-scale structures travel much slower than smaller-scale structures in the shear layer.

In the redevelopment region, the mean flow relaxes relatively quickly and recovers to the upstream distributions after some 12 step heights from the reattachment location. After recovery, the effects of upstream roughness on the mean velocities are negligible. The reduced influence of upstream roughness was supported by collapse of the streamwise profiles of the skin friction coefficient, boundary shape shaper factor and the Clauser shaper parameter. In the far downstream region (about 20 to 35 step heights from the reattachment point), the smooth- and rough-wall Reynolds stresses collapse reasonably well but do not recover to the upstream distributions. Also, in the redevelopment region, the turbulence generated by the step decays in intensity and grows in scale. The life time of u' and v' fluctuations increases with streamwise distance and are much larger in the redevelopment region than in the recirculation region. The measurements of the spatial and space-time correlations showed that structures are not only persistent but are spatially more coherent for the rough wall than the smooth wall. The spatial and space-time correlations were also helpful in showing that the turbulence structure recovers more quickly to the upstream conditions than indicated by the one-point statistics when the flow is subjected to large upstream roughness. The frequency spectra of wall-normal velocity fluctuations showed that energy is injected at the small scales for the cube roughness. This effect would lead to merging of the small scales to form larger scale structures.

A proper orthogonal decomposition (POD) of the flow fields was performed in order to reveal more relevant features of the separated and reattached shear layer. It was found that the enhanced growth of the vortical structures by the cubes caused a corresponding increase in fractional energy convergence of the POD modes. In the recirculation region, the most energetic eigenmode was found to be responsible for the large-scale dynamics of the recirculation bubble. The larger scale structures produced by amalgamation were confirmed by the POD results in the recirculation region.

5.2 Contributions and Recommendations for Future Work

5.2.1 Research Contributions

Although turbulent boundary layers subjected to a forward-facing step have been studied extensively in the past, this is the first time within the near-wall turbulence community when a time resolved PIV was used to characterize the influence of upstream roughness on the turbulence characteristics and flow structure of over the step.

To quantify roughness effects on the flow, a large set of metrics were used in probing the data. These include the time-averaged flow characteristics such as the mean velocities, Reynolds stresses, quadrant contributions, triple correlations, probability density functions, temporal correlations and spectra, and multi-point statistics such as the two-point spatial and space-time correlations. By examining the profiles of the single- and multipoint turbulence characteristics in both the recirculation and redevelopment regions, a more detailed picture of the temporally and spatially evolving flow has emerged in comparison to most previous investigations where measurements were limited to either the upstream region (e.g., Pearson et al. 2013) or the recirculation region (e.g., Largeau and Moriniere 2007; Sherry et al. 2010; Wu and Ren 2013). Thus, a large database of well-resolved measurements has been obtained that will invariably be useful to CFD researchers for calibrating and developing near-wall turbulence models.

Finally, this work employed some of the advanced statistical structure identification tools such as linear stochastic estimation and proper orthogonal decomposition to reveal the vortical structures in the smooth and rough wall flows. As a contribution to the FFS literature, the POD was used to confirm the results from the temporal and spatial correlations of smaller-scale vortices merging to form larger-scale structures in the redevelopment region, an inverse cascade process resulting in the “amalgamation” of the smaller-scale vortices. The POD also confirmed that the turbulent structure over the step recovers more rapidly to the equilibrium state when subjected to large upstream roughness.

5.2.2 Recommendations for Future Work

In this research a two-dimensional two-component time-resolved PIV was used to measure the flow characteristics of the FFS flow. Because of this, various turbulence characteristics such as the spanwise Reynolds stress, turbulence kinetic energy dissipation rate, and the complete three-dimensional velocity gradient tensor could not be measured. Also, due to the current planar measurements, flow visualization of the coherent structures and the statistical correlations are limited to the streamwise – wall-normal (*x*-*y*) plane of the fields of view. Based on the above shortfalls, the following recommendations are suggested for future research:

- A three-dimensional measurement system such as tomographic PIV will be very useful in gaining complete understanding of the complex nature of the separated and reattached flow over FFS. This will be very useful in measuring all three components of instantaneous velocity and in obtaining the complete velocity gradient tensor. These quantities are crucial in developing sub-grid scale models relevant to large eddy simulation.
- Additional measurements made in the spanwise (*x*-*z*) and cross-stream (*y*-*z*) planes will no doubt help to reveal three-dimensional structure of the spatially evolving flow over the step.
- Since time averaging tends to smear the educed structures, further structural identification methods such as dynamic mode decomposition (DMD) that provide both spatial and temporal decomposition without averaging will give further insight into the coherent structures in the shear layer.

APPENDIX A

CONVERGENCE AND SPATIAL RESOLUTION ANALYSIS

A.1 Convergence Analysis

In order to determine the adequacy of the sample size used in computing the statistics, a convergence test was performed by comparing profiles of the mean velocity and higher-order moments from samples of various sizes: N = 6000, 12000, 16000, 18000 and 24000. The statistics were calculated in the second measurement plane at the upstream location $x/h \approx -0.5$ and over the step at the three streamwise locations, $x/L_r \approx 0.0$, 0.5 and 1.0 for the smooth and rough walls. Figure A1 shows the one-dimensional wall-normal profiles of the mean streamwise velocity, Reynolds stresses, as well as profiles of the skewness and flatness factors for the upstream smooth-wall condition. The results indicate that the mean velocity is statistically converged both at the upstream location and over the step for $N \geq 6000$. Similar conclusions can be drawn for the Reynolds stresses as well as the skewness and flatness factors of the wall-normal velocity at the upstream location and over the step. For the skewness and flatness factors of the streamwise velocity, however, the data are statistically converged only in the inner region. In the outer parts of the flow, $S_{u'}$ and $F_{u'}$ are nearly Gaussian ($S_{u'} \approx 0$ and $F_{u'} \approx 3$) at the upstream location and over the step for N = 6000. The outer layer discrepancies are most dramatic for the flatness factor of the streamwise velocity both at the upstream location and over the step although these discrepancies reduce as the sample size increases. Figure A2 presents the convergence tests for the upstream sandpaper roughness. The results show that any of the sample sizes is sufficient for calculating the mean velocities, Reynolds stresses and the skewness and flatness factors of V. The profiles of $S_{u'}$ and $F_{u'}$, on the other hand, show a similar trend as observed for the smooth wall although the outer layer differences are smaller. Figure A3 shows the convergence results for the upstream cube roughness.

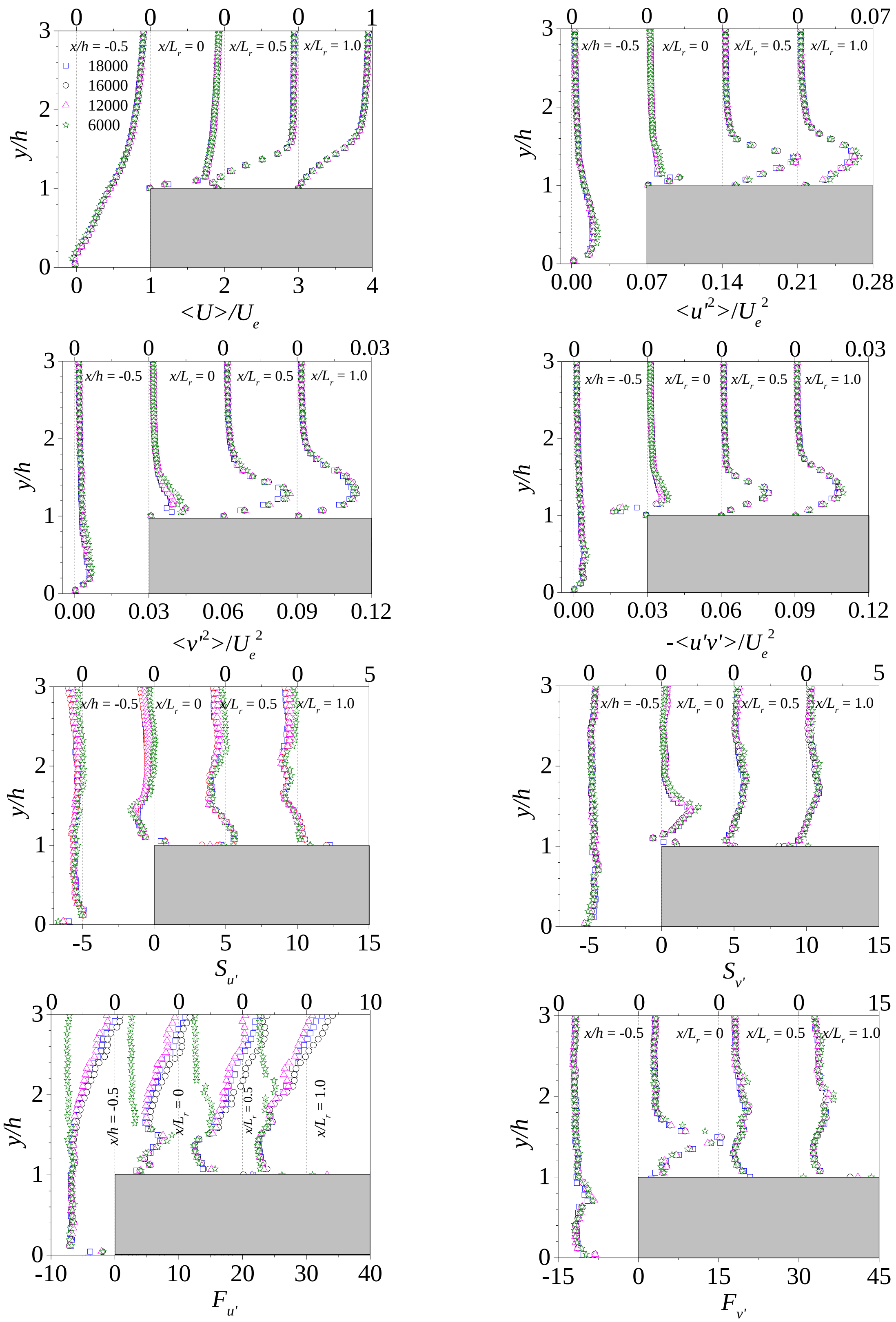

Figure A1: Comparison of profiles of the mean velocity and higher-order moments at various streamwise locations in plane 1 for the upstream smooth-wall condition calculated using samples of various sizes.

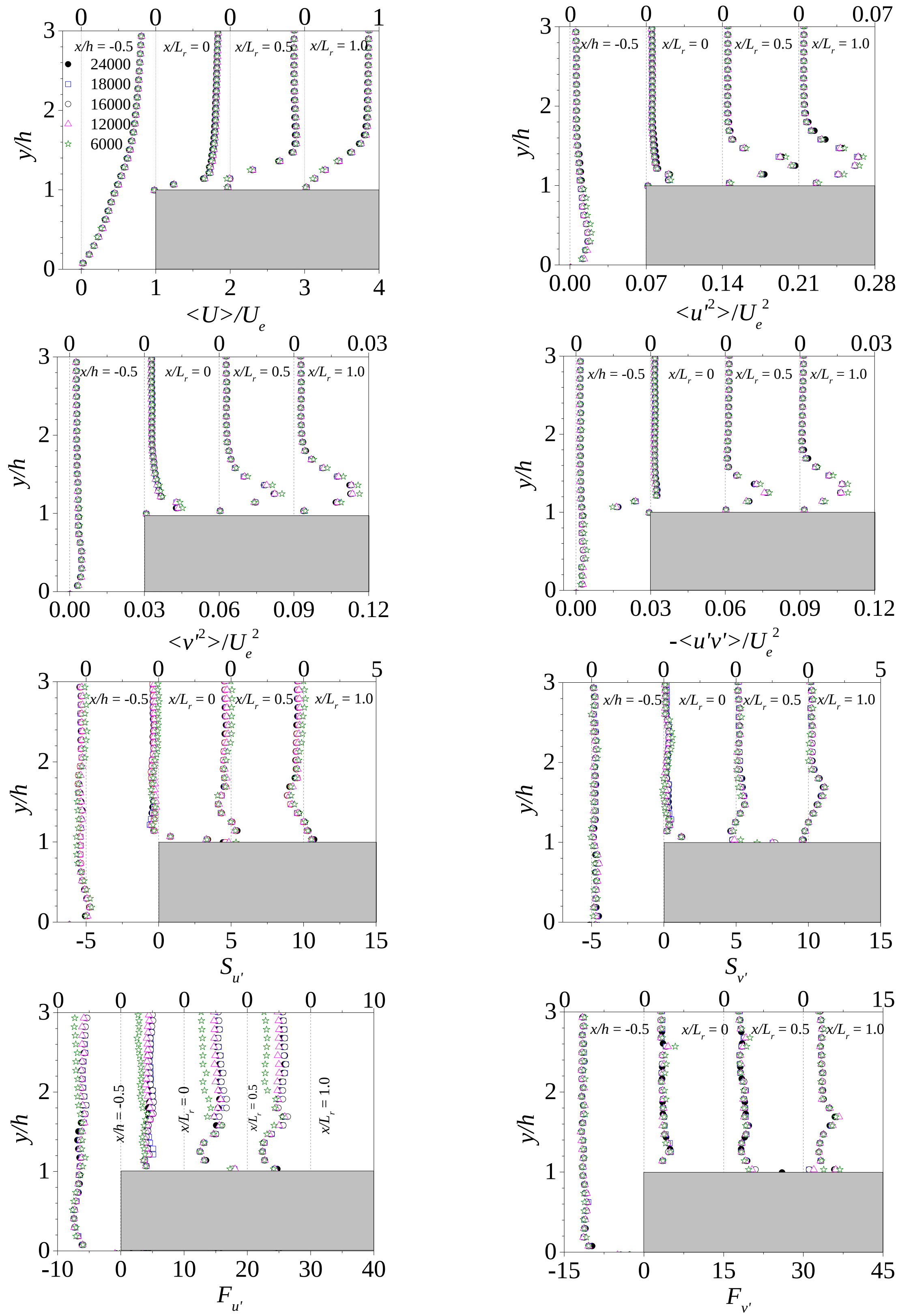

Figure A2: Comparison of profiles of the mean velocity and higher-order moments at various streamwise locations in plane 1 for the upstream sandpaper-roughness condition calculated using samples of various sizes.

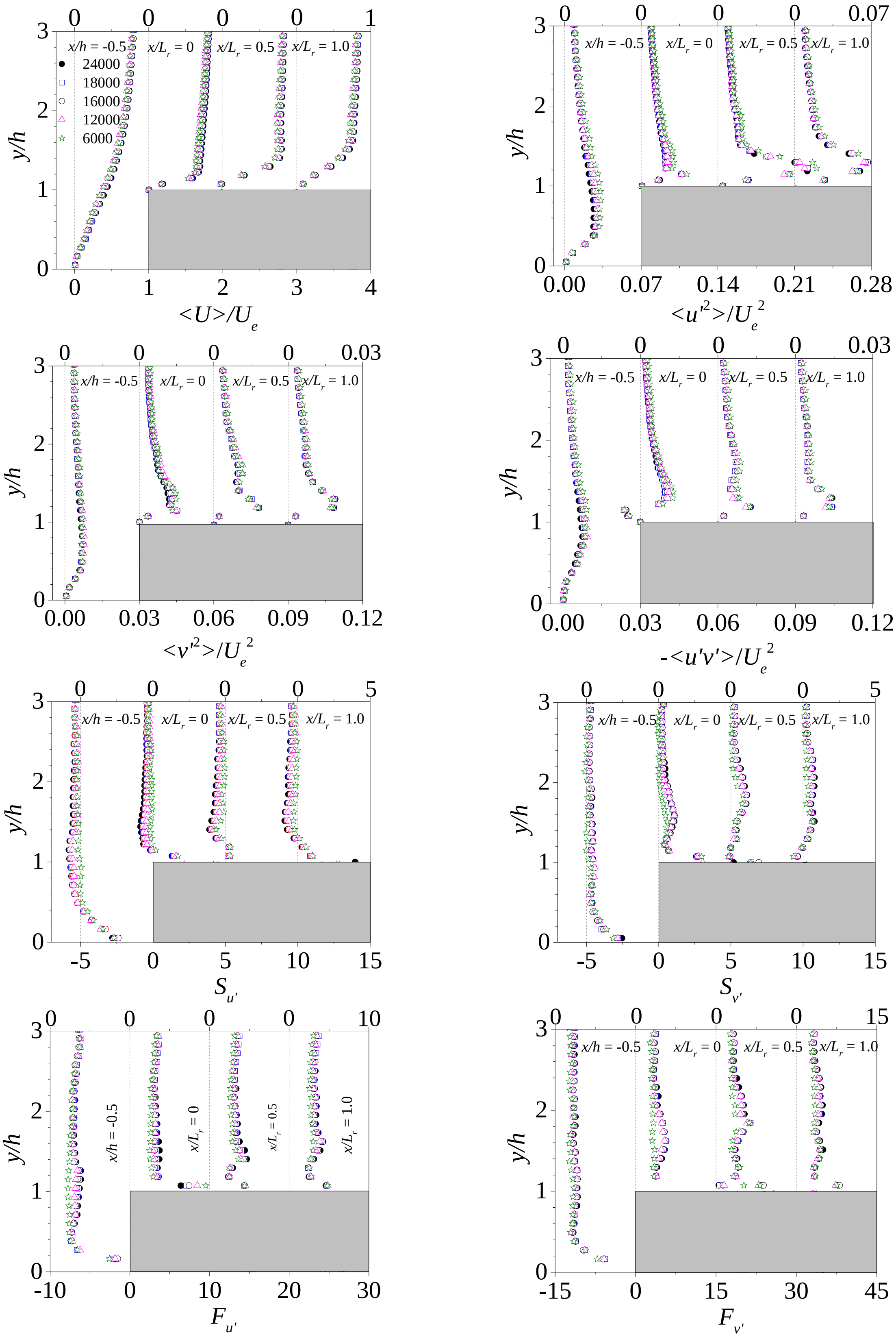

Figure A3: Comparison of profiles of the mean velocity and higher-order moments at various streamwise locations in plane 1 for the upstream cube-roughness condition calculated using samples of various sizes.

The results at the various sample sizes show reasonable collapse for the mean streamwise velocity, wall-normal stress and Reynolds shear stress, but the streamwise Reynolds stress at the upstream location and near the leading edge of the step shows differences as the sample size increases. Nevertheless, the skewness and flatness factors of the streamwise and wall-normal velocities are statistically converged for $N > 6000$ at the upstream location and over the rough wall. On the basis of the above results, it was decided to use a sample size of $N = 18000$ for statistical computations for the upstream smooth wall and $N = 24000$ for the upstream sandpaper and cube roughness. These sample sizes are significantly larger than twice the largest integral time scales in the smooth- and rough-wall experiments.

A.2 Spatial Resolution Analysis

Studies have shown that a low spatial resolution can underestimate the true values of the turbulent quantities in PIV (e.g., Piirto et al. 2003; Saikrishnan et al. 2006). In the present investigation, the smooth- and rough-wall statistics calculated at $x/h \approx -0.5$, and $x/L_r \approx 0.0$, 0.5 and 1.0 were used to examine spatial resolution effects in the experiments. Three special resolutions were tested corresponding to interrogation area sizes of 32 × 32, 24 × 24 and 16 × 16, with an overlap of 75% in each case. The number of samples for the upstream smooth and rough walls were $N = 18000$ and 24000, respectively. The spatial resolution tests for SM, SP and CB are presented in Figures A4, A5 and A6, respectively. The results indicate that the interrogation area size has negligible effect on the mean streamwise velocity, streamwise Reynolds stress, Reynolds shear stress, as well as the skewness and flatness factors. However, as the spatial resolution increases, the peak value of the wall-normal Reynolds stress increases both at the upstream location and over the step for the smooth- and rough-wall cases. Similar observations were reported by Shah et al. (2008).

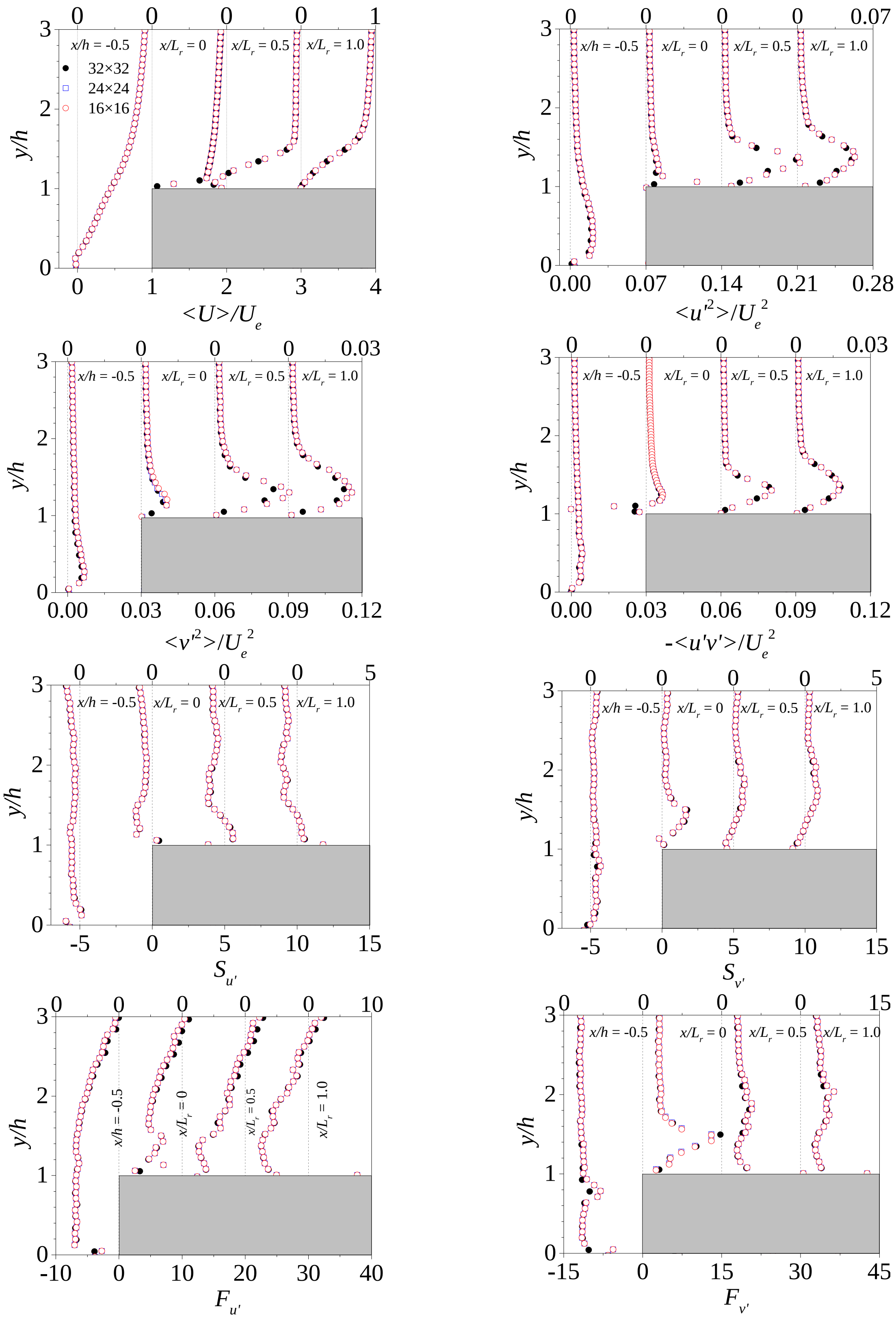

Figure A4: Comparison of profiles of the mean velocity and higher-order moments at various streamwise locations in plane 1 for the upstream smooth-wall condition calculated with data at various spatial resolutions.

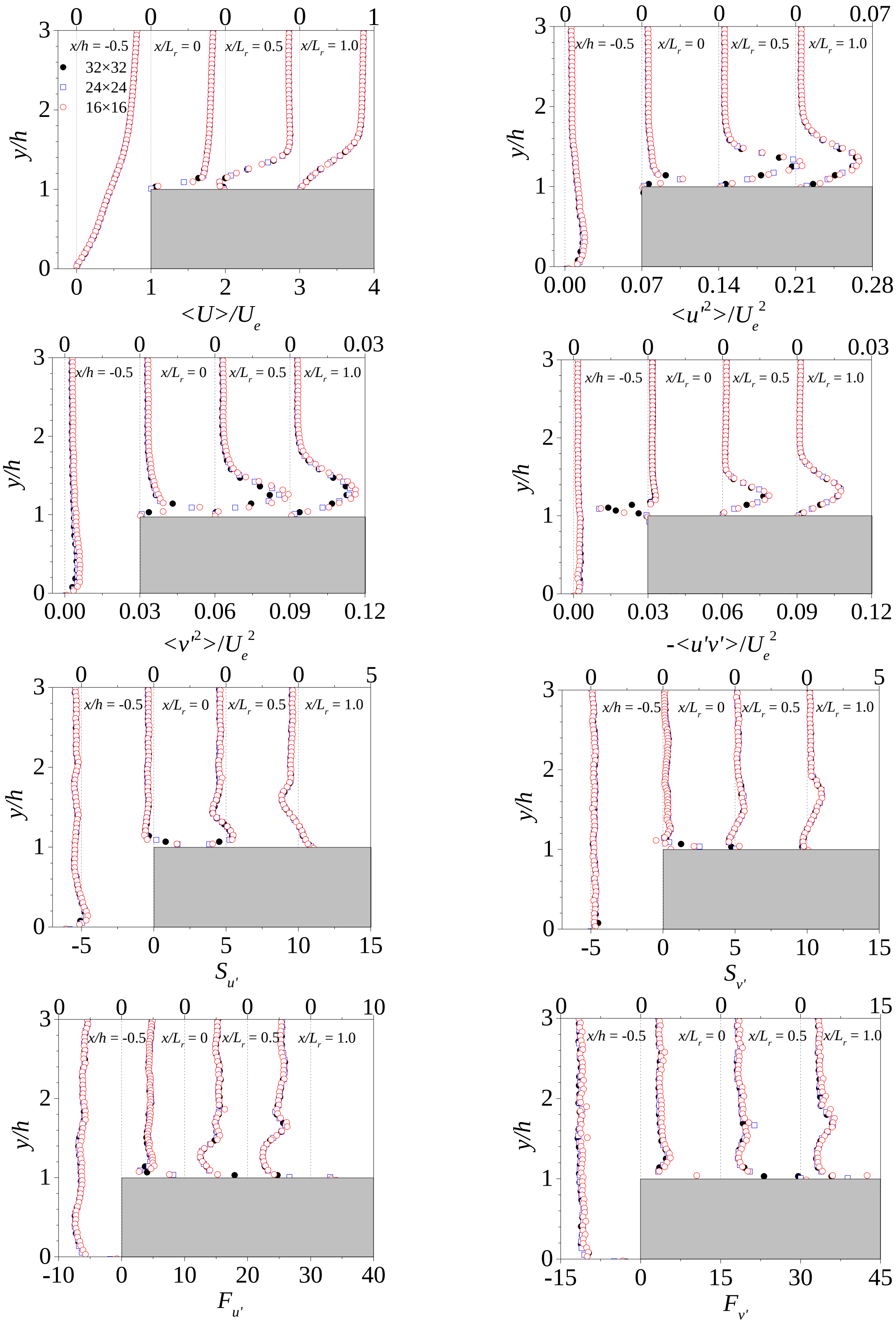

Figure A5: Comparison of profiles of the mean velocity and higher-order moments at various streamwise locations in plane 1 for the upstream sandpaper-roughness condition calculated with data at various spatial resolutions.

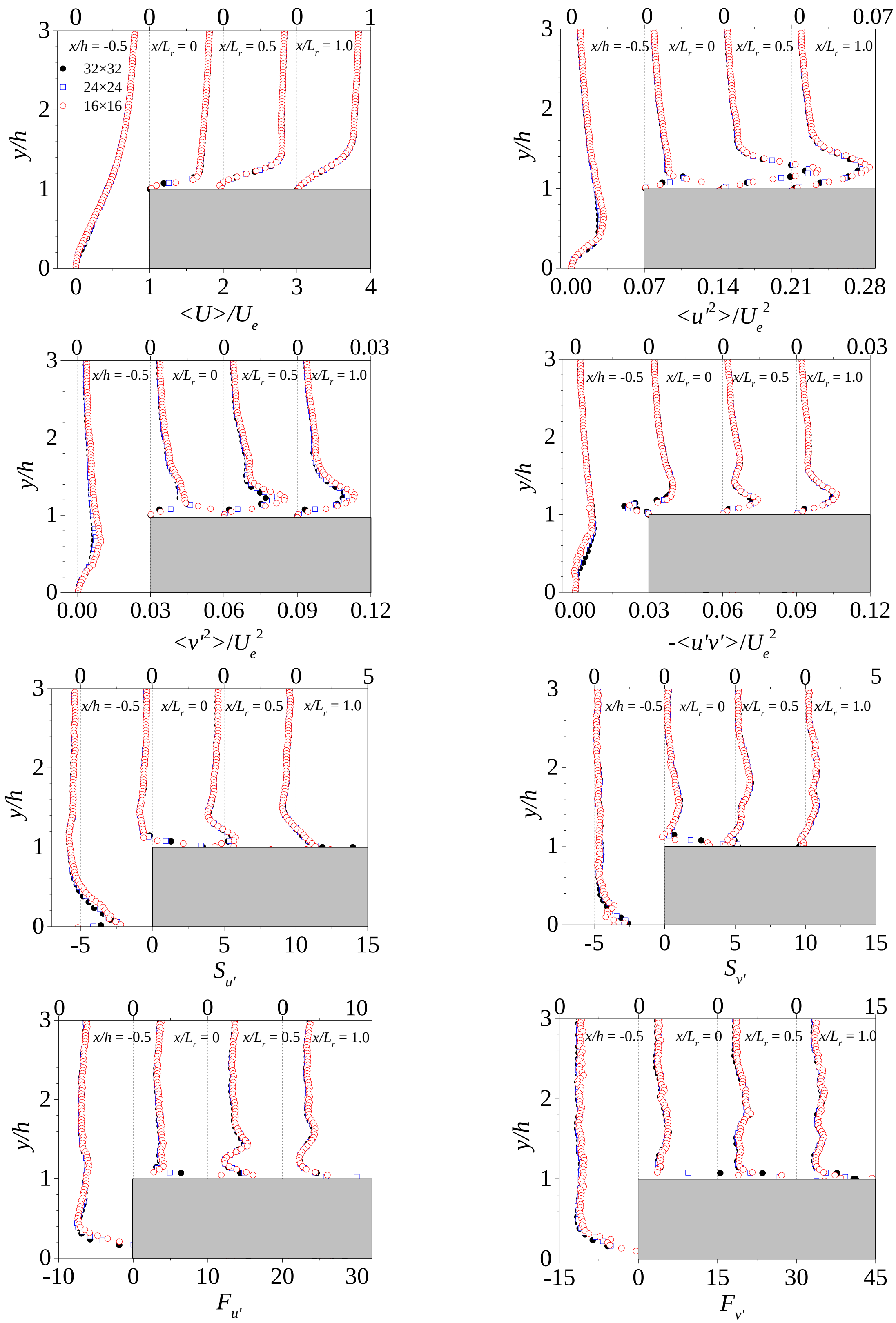

Figure A6: Comparison of profiles of the mean velocity and higher-order moments at various streamwise locations in plane 1 for the upstream cube-roughness condition calculated with data at various spatial resolutions.

APPENDIX B

EXPERIMENTAL UNCERTAINTY ANALYSIS

This appendix describes the correlation statistics procedure and the uncertainty propagation methodology used in estimating the uncertainties in the instantaneous velocities and time-averaged quantities. In the correlation statistics method, the measured displacement field, $s(x)$ is used to dewarp the second image back to the first image. This matches the pixel intensities in the IAs of the second image to corresponding intensities in the IAs of the first image. This is mathematically represented by the equation (Wieneke and Prevost 2014):

$$I_2^*(x) = I_2(x+s) \tag{B1}$$

which requires a sufficiently accurate high-order sub-pixel interpolation scheme.

Assuming that cross-correlation algorithm has sufficiently converged so that the residual given by

$$C(s) = \sum[I_1(x) - I_2(x+s)]^2 = \sum[I_1(x) - I_2^*(x)]^2 \tag{B2}$$

is at a minimum with zero slope *dC/ds*, then the following equality holds:

$$\Delta C = C(s+\Delta x) - C(s-\Delta x) \cong 0 \tag{B3}$$

where Δx is a small distance away from s.

A non-zero value of ΔC indicates that the correlation algorithm did not converge (Wieneke and Prevost 2014). This implies that taking the three points $C(s)$, $C(s - \Delta x)$, and $C(s + \Delta x)$, an improved optimal displacement $s + \delta s$ can be calculated, where δs is the residual displacement whose magnitude can be determined using any suitable peak-fitting algorithm. Fitting a second order polynomial, for instance, to the three points yields

$$\delta s = \frac{\Delta x}{2}\frac{\Delta C}{2C_0 - C_+ - C_-} \tag{B4}$$

where $C_0 = C(s)$, $C_+ = C(s + \Delta x)$ and $C_- = C(s - \Delta x)$.

Rewriting equation (B3) as (Wieneke and Prevost 2014):

$$\Delta C = \sum \Delta C_i = \sum [(I_1(x) - I_2^*(x + \Delta x))^2 - (I_1(x + \Delta x) - I_2^*(x))^2] \tag{B5}$$

ignoring small differences from shifting the second term by Δx. Equation (B5) implies that if $I_1 = I^*_2$, ΔC_i is exactly zero so that the residual displacement is zero. However, because of various sources of error, the values of I_1 and I^*_2 in actual experiments do not perfectly match. The standard deviation of ΔC is given by (Wieneke and Prevost 2014):

$$\sigma_{\Delta C} = \sqrt{N}\sigma_{\Delta C_i} = \sqrt{N}\left(\frac{\sum \Delta C_i^2}{N}\right)^{\frac{1}{2}} = \left(\sum \Delta C_i^2\right)^{\frac{1}{2}} \tag{B6}$$

Using equation (B4) and (B6), the standard deviation of the residual displacement is given by

$$\sigma_s = \frac{\Delta x}{2}\frac{(\sum \Delta C_i^2)^{\frac{1}{2}}}{2C_0 - C_+ - C_-} \tag{B7}$$

Equation (B7) yields the uncertainty estimate of the displacement field. The correlation statistics technique is implemented as a built-in tool in the LaVision DaVis software for direct computation of the experimental uncertainties in the instantaneous velocities. The uncertainty limits at the 95% confidence level in the instantaneous streamwise and wall-normal velocities at $y/h \approx 0.1$over the smooth and rough walls are summarized in Table B1 for the upstream location $x/h \approx -20$.

Table B1: Summary of uncertainty limits in the instantaneous velocities at $y/h = 0.1$ and $x/h = -20$

Test	***u* (m/s)**	***v* (m/s)**	**Uncertainty in *u***	**Uncertainty in *v***
SM	0.268	0.012	1.0%	1.0%
SP	0.017	0.005	2.1%	2.0%
CB	0.014	0.001	3.0%	2.0%

Using the methodology suggested by Sciacchitano and Wieneke (2016), the experimental uncertainties in the mean velocity and Reynolds stresses are given by:

Uncertainty of mean velocity:

$$E_{U_i} = \frac{\sigma_i}{\sqrt{N_{eff}}} \tag{B8}$$

Uncertainty of normal Reynolds stresses:

$$E_{R_{ii}} = R_{ii}\sqrt{\frac{2}{N_{eff}}} \tag{B9}$$

Uncertainty of Reynolds shear stress:

$$E_{R_{ij}} = \sigma_i\sigma_j\sqrt{\frac{1+\rho_{ij}^2}{N_{eff}-1}} \tag{B10}$$

where i, j = 1 and 2 are the Cartesian indices, σ denotes the standard deviation or root-mean-square value, ρ denotes the correlation coefficient, and N_{eff} denotes the effective number of independent samples.

The effective number of independent samples is given by (Sciacchitano and Wieneke 2016):

$$N_{eff} = \frac{T}{2T^u} \tag{B11}$$

where T is the total sampling time and T^u is the integral time scale. It should be noted that if the samples are independent, the effective number of independent samples can be replaced by the total number of samples N.

From equations (B8) to (B10) the uncertainties in the mean velocity and Reynolds stresses at $x/h \approx -20$ and $y/h \approx 0.1$ are summarized in Table B2.

Table B2: Summary of uncertainty limits in the mean velocities and Reynolds stresses at y/h = 0.1 and x/h = -20

Test	**Uncertainty in U**	**Uncertainty in $\langle u'^2\rangle$**	**Uncertainty in $\langle v'^2\rangle$**	**Uncertainty in $-\langle u'v'\rangle$**
SM	1.5%	1.8%	1.80%	3.5%
SP	2.0%	2.2%	2.2%	6.1%
CB	3.1%	2.3%	2.3%	7.9%

BIBLIOGRAPHY

Achenbach, E., and E. Heinecke, "On vortex shedding from smooth and rough cylinders in the range of Reynolds numbers 6×10^3 to 5×10^6". Journal of Fluid Mechanics, 109, 239-251, 1981.

Adams, E.W., and Johnston, J.P., "Flow structure in the near-wall zone of a turbulent separated flow", AIAA Journal 26, NO. 8, 1988.

Addad, Y., Laurence, D., Talotte, C., and Jacob, M., "Large eddy simulation of a forward-backward facing step for acoustic source identification", International Journal of Heat and Fluid Flow, 24, 562-571, 2003.

Adrian, R.J., "Particle imaging techniques for experimental fluid mechanics", Annual Review of Fluid Mechanics, 23, 261-304, 1991.

Adrian, R.J., "On the role of conditional averages in turbulence theory", Proceedings of the 4th biennal symposium on turbulence in liquids, Science Press, Princeton 323-332, 1977.

Adrian, R. J., Jones, B. G., Chung, M. K., Hassan, Y., Nithanandan, C. K., and Tung, A. T. C., "Approximation of turbulent conditional averages by stochastic estimation", Physics of Fluids A, 1, 992, 1989.

Adrian, R. J., Meinhart, C. D., and Tomkins, C. D., "Vortex organization in the outer region of the turbulent boundary layer", Journal of Fluid Mechanics, 422, 1–54, 2000.

Ausoni, P., Farhat, M., Escaler, X., Egusquiza, E., Avellan, F., "Cavitation influence on von kármán vortex shedding and induced hydrofoil vibrations", Journal of Fluids Engineering, 129(8), 966-973, 2007.

Awasthi1, M., Devenport, W.J., Glegg, S.A.L., and Forest, J.B., "Pressure fluctuations produced by forward steps immersed in a turbulent boundary layer", Journal of Fluid Mechanics, 756, 384-421, 2014.

Bagheri, S., "Koopman-mode decomposition of the cylinder wake", Journal of Fluid Mechanics, 726, 596-623, 2013.

Becker, S., Kniesburges, S., Hahn, C., Castelain, T., "Flow induced sound radiated by a forward facing step with different geometries", 15th Int Symp on Applications of Laser Techniques to Fluid Mechanics Lisbon, Portugal, 05-08 July, 2010.

Berkooz, G., Holmes, P., and Lumley, J. L., "The proper orthogonal decomposition in the analysis of turbulent flows", Annual Review of Fluid Mechanics, 25, 539, 1993.

Blackwelder, R.F. and Eckelmann, H., "Streamwise Vortices Associated with the Bursting Phenomenon", Journal of Fluid Mechanics, 94, 577-594, 1979.

Blackwelder, R. F., and Kovasznay, L. S. G., "Large-scale motion of a turbulent boundary layer during relaminarization", Journal of Fluid Mechanics, 53(1), 61-83, 1972.

Blackwelder, R.F. and Kaplan, R.E., "On the wall structure of the turbulent boundary layer", Journal of Fluid Mechanics, 76, 89-112, 1976.

Bowen, A., Lindley, D., "A wind-tunnel investigation of the wind speed and turbulence characteristics close to the ground over various escarpment shapes", Boundary-Layer Meteorology, 12, 259–271, 1977.

Bradshaw, P., Wong, F.Y.F., "The reattachment and relaxation of a turbulent shear layer", Journal of Fluid Mechanics, 52, part 1, 113-135, 1972.

Brederode, V., Bradshaw, P., "Three-dimensional flow in nominally two-dimensional separation bubbles: flow behind a rearward-facing step", Imp. Coll. Aeronaut. Rep., 72–19, 1972.

Browand, F. K., and Weidman P. D., "Large scales in the developing mixing layer", Journal of Fluid Mechanics, 76(01), 127 – 144, 1976.

Brown, G.L., and Roshko, A., "On density effects and large structure in turbulent mixing layers", Journal of Fluid Mechanics, 64, part 4, 775-816, 1974.

Brown, G.L. Thomas, A.S.W., "Large structure in a turbulent boundary layer", Physics of Fluids, 20(10), S243-S252, 1977.

Camussi, R., Felli M., Pereira, F., Aloisio G., Di Marco A., "Statistical properties of wall pressure fluctuations over a forward-facing step", Physics of Fluids, 20, 075113, 2008.

Castro, I. P., and Haque, A., "The structure of a turbulent shear layer bounding a separation region", Journal of Fluid Mechanics, 179, 439-468, 1987.

Castro, I.P., Epik, E., "Boundary layer development after a separated region", Journal of Fluid Mechanics, 374, 91-116, 1998.

Cherry. N. J., Hillier, R. and Latour, P. M. "Unsteady measurements in a separated and reattaching flow", Journal of Fluid Mechanics, 144, 13-46, 1984.

Chong, M. S., Perry, A. E. and Cantwell, B. J., "A general classification of three-dimensional flow fields", Physics of Fluids, 2, 765-777, 1990.

Chou JH, Chao SY, "Branching of horseshoe vortex around surface-mounted rectangular cylinders", Experiments in Fluids, 28:394–402, 2000.

Choi H., Moin, P., "On the space-time characteristics of wall-pressure fluctuations", Physics of Fluids A: Fluid Dynamics 2 (8), 1450, 1990.

Christensen K. T. & Adrian, R.J., "Statistical evidence of hairpin vortex packets in wall turbulence", Journal of Fluid Mechanics, 431, 433–443, 2001.

Coleman, H. W., Steele, W. G., "Experimentation, validation, and uncertainty analysis for engineers", Third Edition, 2009.

Coles, D. E., “The turbulent boundary layer in a compressible fluid. R 403-PR. The RAND Corporation, Santa Monica, CA, 1962.

Coles, D., “The law of the wake in the turbulent boundary layer”, Journal of Fluid Mechanics, 1, 191–226, 1956.

Coles, D.E., Hirst, E.A., “Proceedings computation of turbulent boundary layer”, AFOSR-IFP-Stanford Conference, Thermoscience Division, Stanford University, 2, 47-54, 1969.

Corino, E.R. and Brodkey, R.S., “A visual investigation of the wall region in turbulent flow”, Journal of Fluid Mechanics, 37, 1-30, 1969.

Del Álamo, J.C., Jiménez, J., “Estimation of turbulent convection velocities and corrections to Taylor's approximation”, Journal of Fluid Mechanics, 640, 5-2, 2009.

Dimaczek, G., Kessler, R., Martinuzzi, R, and Tropea, C., "The flow over two-dimensional, surface-mounted obstacles at high Reynolds numbers” Proc. 7th Symposium on Turbulent Shear Flows, Standford, CA, 1989.

Djilali N., Gratshore IS., “Turbulent flow around a bluff rectangular plate. Part I: Experimental Investigation”, Journal of Fluids Engineering, 113, 51-59, 1991.

Doron, P., Bertuccioli, L., Katz, J., and Osborn, T.R., “Turbulence characteristics and dissipation estimates in the coastal ocean bottom boundary layer from PIV data”, Journal of Physical Oceanography, 31(8), 2108-2134, 2001.

Driver, D.M. and Seegmiller, H.L., “Features of a reattaching turbulent shear layer in divergent channel flow”, AIAA Journal, 23, 163-171, 1985.

Driver, D.M., Seegmiller, H.L., Marvinf, J.G., “Time-dependent behavior of a reattaching shear layer”, AIAA Journal, 5(7), 914-919, 1987.

Eaton J.K. and Johnston J.P., “A review of research on subsonic turbulent-flow reattachment”, AlAA 13th FLUID & PLASMA DYNAMICS CONFERENCE July 14-16, 1980/Snowmass, Colorado, 1980.

Eaton, J.K., Johnston, J.P., “A review of research on subsonic turbulent flow reattachment”, AIAA Journal 19, 1093-1100, 1981.

Efimtsov, B., Kozlov, N., Kravchenko, S., Andersson A., “Wall pressure-fluctuation spectra at small forward-facing steps”, AIAA Journal, 1054-1064, 1999.

Essel, E.E., Nematollahi, A., Thacher, E.W., Tachie, M.F., “Effects of upstream roughness and Reynolds number on separated and reattached turbulent flow”, Journal of Turbulence, 16, 872–899, 2015.

Essel, E.E., and Tachie, M.F., “Upstream roughness and Reynolds number effects on turbulent flow structure over forward facing step”, International Journal of Heat and Fluid Flow, 66, 226-242, 2015.

Farabee TM, Casarella MJ., "Effects of surface irregularity on turbulent boundary layer wall pressure fluctuations", Journal of Vibration, Acoustics, Stress, and Reliability in Design, 106, 343–350, 1984.

Favre, A., Gaviglio, J., Dumas, R., "Further space–time correlations and spectra in a turbulent boundary layer", Journal of Fluid Mechanics, 3, 344–356, 1958.

Favre, A., Gaviglio, J., Dumas, R., "Structure of velocity space–time correlations in a boundary layer", Physics of Fluids, 10, S138–S145, 1967.

Fiorentini E, Camussi R, Pereira F, Felli M, Aloisio G, Di Marco A., "Velocity and wall pressure correlations over a forward facing step", Roma (Italy): Atti 14 Convegno Nazionale AIVELA; 2006.

Fisher, M.J., Davies, P.O.A.L., "Correlation measurements in a nonfrozen pattern of turbulence", Journal of Fluid Mechanics, 18, 97-116, 1964.

Goldschmidt, V.W., Young, M.F., Ott, E.S., "Turbulent convective velocities (broadband and wavenumber dependent) in a plane jet", Journal of Fluid Mechanics, 105, 327-345, 1981.

Gordeyev, S.V., and Thomas, F.O., "Coherent structure in the turbulent planar jet. Part 1. Extraction of proper orthogonal decomposition eigenmodes and their self-similarity", Journal of Fluid Mechanics, 414, 145–194, 2000.

Grass, A.J., "Structural features of turbulent flow over smooth and rough boundaries," Journal of Fluid Mechanics, 50, 233-255, 1971.

Hattori, H., Nagano, Y., "Investigation of turbulent boundary layer over forward-facing step via direct numerical simulation", International Journal of Heat and Fluid Flow, 31, 284–294, 2010.

Head, M.R. and Bandyopadhyay, P., "New aspects of turbulent boundary layer structure", Journal of Fluid Mechanics, 107, 297-338, 1981.

Hillier, R., and Cherry, N.J., "The effects of stream turbulence on separation bubbles", Journal of Wind Engineering and Industrial Aerodynamics, 8, 49-58, 1981.

Hong, J., Katz, J., and Schultz, M.P., "Near-wall turbulence statistics and flow structures over three-dimensional roughness in turbulent channel flow," Journal of Fluid Mechanics, 667, pp. 1–37, 2011.

Humble, R. A., Scarano, F., and van Oudheusden, B. W., "Unsteady aspects of an incident shock wave/turbulent boundary layer interaction", Journal of Fluid Mechanics, 635, 47-74, 2009.

Hussain, F., "Coherent structures—reality and myth", Physics of Fluids, 26, 2816, 1983.

Hutchins, N., Hambleton, W. T. and Marusic, I., "Inclined cross-stream stereo PIV measurements in turbulent boundary layers", Journal of Fluid Mechanics, 541, 21–54, 2005.

Iftekhar, H., and Agelin-Chaab, M., “Characteristics of turbulent flows over forward facing steps in adverse pressure gradients based on two-point analyses” Journal of Fluids Engineering, 139(11), 114501, 2016.

Iqbal M.O., and Thomas, F.O., “Coherent structure in a turbulent jet via a vector implementation of the proper orthogonal decomposition”, 571, 281-326, 2007.

Jiménez, J., “The largest scales of turbulence”, In: CTR Annual Research Briefs, edited by Moin, P., 137-154, 1998.

Jovic, S., and Driver D., “Backward-facing step measurement at low Reynolds number”, Tech. rep. NASA, 1994.

Jovic, S., “An experimental study on the recovery of a turbulent boundary layer downstream of the reattachment”. Proceedings of the Second International Symposium on Engineering Turbulence Modelling and Measurements, Florence, Italy, 31 May-2 June, 1993.

Jovic, S., “Recovery of reattached turbulent shear layers”, Experimental Thermal and Fluid Science, 17, 57–62, 1998.

Karlsson, R. I., “Similarity of longitudinal turbulence intensity in flat plate turbulent boundary layers”, Chalmers Technical High School Internal Report, 7811, 1978.

Kim, J., and Hussain, F., “Propagation velocity of perturbations in turbulent channel flow”, Physics of Fluids, 5(3), 695, 1993

Kim, K.C. and Adrian, R.J., “Very large-scale motion in the outer layer”, Physics of Fluids, 11(2), 417-422, 1999.

Kiya, M., and Sasaki, K., “Structure of a turbulent separation bubble”, Journal of Fluid Mechanics, 137, 83-113, 1983.

Kiya, M., and Sasaki, K., “Structure of large-scale vortices and unsteady reverse flow in the reattaching zone of a turbulent separation bubble”, Journal of Fluid Mechanics, 154, 463-491, 1985.

Kline, S.J., Reynolds, W.C., Schraub, F.A., and Runstadler, P.W., “The structure of turbulent boundary layers”, Journal of Fluid Mechanics, 30, 741-773, 1967.

Kolmogorov, A.N., “The local structure of turbulence in incompressible viscous fluids at very large Reynolds numbers”, Dokl. Akad. Nauk. SSSR 30, 299-303. Reprinted in Proc. R. Soc. London A 434, 9-13, 1941.

Kostas, J., Soria, J., Chong, M.S., “A comparison between snapshot POD analysis of PIV velocity and vorticity data”, Experiment in Fluids, 38, 146–160, 2005.

Kovasznay, L. S. G., Kibens, V., and Blackwelder, R. F., “Large-scale motion in the intermittent region of a turbulent boundary layer”, 41(2), 283-325, 1970.

Krogstad, P.-Å., Antonia, R.A. and Browne, L.W.B., “Comparison between rough-and smooth-wall turbulent boundary layers”, Journal of Fluid Mechanics, 245, 599 – 617, 1992.

Krogstad, P. A., Kaspersen, J. H., and Rimestad, S., “Convection velocities in a turbulent boundary layer”, Physics of Fluids, 10(4), 1998.

Largeau, J., Moriniere, V., “Wall pressure fluctuations and topology in separated flows over a forward facing step”. Experiments in Fluids, 42, 21–40, 2007.

Leclercq, D., Jacob, M., Louisot, A., and Talotte, C., “Forward-backward facing step pair: Aerodynamic flow, wall pressure and acoustic characterisation”, AIAA Pap, 2001–2249, 2001.

Lin, C. C., “On Taylor’s hypothesis and the acceleration terms in the Navier–Stokes equations” Quarterly of Applied Mathematics, 10 (4), 295–306, 1953.

Lu, S. S., Willmarth, W. W., “Measurements of the structure of the Reynolds stress in a turbulent boundary layer”, Journal of Fluid Mechanics, 60, 481-511, 1973.

Ludwieg, H., and Tillman, W., “Investigation of the wall-shearing stress in turbulent boundary layer”, NACA Technical Memorandum, No. 1285, 1950.

Lumley, J.L., “The structure of inhomogeneous turbulence”, In: Atmospheric Turbulence and Wave Propagation, ed. Yaglom, A.M., Tatarski, 166-178, 1967.

Marino, L., and Luchini, P., “Adjoint analysis of the flow over a forward-facing step”, Theoretical and Computational Fluid Dynamics, 23, 37–54, 2009.

Millikan, C.B., “A critical discussion of turbulent flows in channels and circular tubes”, Proceedings of the Fifth International Congress on Applied Mechanics, Editors: Den Hartog, J.P. and Peters, H., Wiley, New York, 1938.

Mizuno, Y., Duke, D., Atkinson, C. and Soria, J., “Investigation of wall-bounded turbulent flow using dynamic mode decomposition”, 13th European Turbulence Conference, 318, 042040, 2011.

Mohammed-Taifour, A., and Weiss, J., “Unsteadiness in a large turbulent separation bubble”, 799, 383-412, 2016.

Mohsen M, “Experimental investigation of the wall pressure fluctuations in subsonic separated flows”, (Renton: Boeing Commercial Airline Co.), 1967.

Monin, AS., and Yaglom, AM., “Statistical Fluid Mechanics: Mechanics of Turbulence”, vol. 2, 874 pp MIT Press, Cambridge, 1975.

Moretti, F. H., and Kays, W. M., “Heat transfer in turbulent boundary layer with varying free stream velocity and varying surface temperature- an experimental study”, International Journal of Heat and Mass Transfer, 8, 1187, 1965.

Moss, W., and Baker, S., “Re-circulating flows associated with two-dimensional steps”, Aeronaut. Q., 31, 151-172, 1980.

Mueller, T. J., and J. M. Robertson, “A study of the mean motion and turbulence downstream of a roughness element”, Modern Developments in Theoretical and Applied Mechanics, 1, 326–340, 1963.

Na, Y., and Moin, P., “Direct numerical simulation of a separated turbulent boundary layer”, Journal of Fluid Mechanics, 374, 379-405, 1998.

Nakamura, Y., and Ozono, S., “The effects of turbulence on a separated and reattaching flow”, Journal of Fluid Mechanics, 178, 477-490, 1987.

Nakagawa, H., and Nezu, I., “Structure of space-time correlations of bursting phenomena in an open-channel flow”, Journal of Fluid Mechanics, 104, 1-43, 1981.

Nelkin M. “Universality and scaling in fully developed turbulence”, Adv. Phys. 43, 143–181, 1994.

Nikuradse, J., “Laws of Flow in Rough Pipes”, NACA TM 1292, 1933.

O'Gorman, P. A. and Pullin, D. I., “On modal time correlations of turbulent velocity and scalar fields”, Journal of Turbulence, 5, 035, 2004.

Ota, T., Asano, Y., Okawa, J.I., “Reattachment length and transition of the separated flow over blunt flat plates”. Bull. JSME, 24 (192), 941–947, 1981.

Ota, T., Motegi, H., “Measurements of spatial correlations and autocorrelations in separated and reattached flow over a blunt flat plate”, Journal of Wind Engineering and Industrial Aerodynamics, 12, 297-312, 1983.

Pearson, D. S., Goulart, P. J., Ganapathisubramani, B., “Investigation of turbulent separation in a forward-facing step flow”, Journal of Physics, Conference Series 318 Section 2, 2011.

Pearson, D.S., Goulart, P.J., Ganapathisubramani, B., “Turbulent separation upstream of a forward facing step”, Journal of Fluid Mechanics, 724, 284–304, 2013.

Piirto, M., Saarenrinne, P., Eloranta, H., and Karvinen, R., “Measuring turbulence energy with PIV in a backward-facing step flow” Experiments in Fluids, 35, 219-236, 2003.

Pollard, A., Wakarani, N. & Shaw, J., “Genesis and morphology of erosional shapes associated with turbulent flow over a forward-facing step”, In Coherent Flow Structures in Open Channels, pp. 249–265. Wiley, 1996.

Pope, S.B., “Turbulent Flows”, Cambridge University Press, 2000.

Prandtl, L., “Zur Turbulenten Strömung in Roren und langs Plätten”, Ergeb Aerod Versuch Gottingen, 4, 18-29, 1932.

Raffel, M., Willert, C., Kompenhans, J., “Particle image velocimetry, a practical guide”, Springer, Berlin Heidelberg New York, 1998.

Rempfer, D., and Fasel H.F., “Evolution of three-dimensional coherent structures in a flat-plate boundary layer”, Journal of Fluid Mechanics, 260, 351-375, 1994.

Ren, H., Wu, Y., “Turbulent boundary layers over smooth and rough forward-facing steps”. Physics of Fluids, 23, 045102, 2011.

Rifat, S.M., Marchildon, A., and Tachie, M., “Effects of Upstream Wall Roughness on Separated Turbulent Flow over a Forward Facing Step in an Open Channel”, International Journal of Mechanical, Aerospace, Industrial, Mechatronic and Manufacturing Engineering, 10(2), 250-255, 2016.

Robinson, S. K., “Coherent motion in the turbulent boundary layer”, Annual Review of Fluid Mechanics, 23, 601-639, 1991.

Rowley, C.W., Mezic, I., Bagheri, S., Schlatter, P., and Henningson, D.S., “Spectral analysis of nonlinear flows”, Journal of Fluid Mechanics, 641, 115–127, 2009.

Ruderich, R. and Fernholz, H.H., “An experimental investigation of a turbulent shear flow with separation, reverse flow, and reattachment”, Journal of Fluid Mechanics, 163, 283-322, 1986.

Ruhe, A., “Rational Krylov sequence methods for eigenvalue computation”, Linear Algebra and its Applications, 58, 391-405, 1984.

Saikrishnan, N., Marusic, I., Longmire, E.K., “Assessment of dual plane PIV measurements in wall turbulence using DNS data”, Experiments in Fluids, 41, 265–278, 2006.

Samimy, M., and Lele, S. K., “Motion of particles with inertia in a compressible free shear layer”, Physics of Fluids, 3(8), 1915-1923, 1991.

Sampath, R., and Chakravarthy, S.R., Proper orthogonal and dynamic mode decompositions of time-resolved PIV of confined backward-facing step flow”, Experiments in Fluids, 55:1792, 2014.

Sanada, T., and Shanmugasundaram, V., “Random sweeping effect in isotropic numerical turbulence”, Physics of Fluids A: Fluid Dynamics, 4, 1245, 1992.

Sandborn, V. A. and Kline, S. J. “Flow model in boundary-layer stall inception”, Journal of Basic Engineering, 83, 317-327, 1961.

Sasaki, K., and Kiya, M., “Three-dimensional vortex structure in a leading-edge separation bubble at moderate Reynolds numbers”, Journal of Fluids Engineering, 113(3), 405-410, 1991.

Scheit, C., Esmaeili, A., Becker, S., “Direct numerical simulation of flow over a forward-facing step – Flow structure and aeroacoustic source regions”, International Journal of Heat and Fluid Flow, 43, 184–193, 2013.

Schlichting, H., 1979, “Boundary-Layer Theory,” 7th Edition, McGraw-Hill, New York.

Schmid, P.J., “Dynamic mode decomposition of numerical and experimental data”, Journal of Fluid Mechanics, 656, 5–28, 2010.

Schoppa, W. and Hussain, F., “Coherent structure dynamics in near-wall turbulence”, Fluid Dynamics Research, 26, 119-139, 2000.

Sciacchitano, A., Wieneke, B., “PIV uncertainty propagation”, Measurement Science and Technology, 27(8), 084006, 2016.

Sen, M., Bhaganagar, K., and Juttijudata, V., “Application of proper orthogonal decomposition to investigate a turbulent boundary layer in a channel with rough walls”, Journal of Turbulence, 8(41), 1–21, 2007.

Shah, M.K., and Tachie, M.F., “PIV investigation of an open channel flow over a forward facing step”, Proceedings of FEDSM2007 5th Joint ASME/JSME Fluids Engineering Conference July 30 August 2, 2007 San Diego, California USA.

Shah, M.K., Agelinchaab, M., Tachie, M.F., “Influence of PIV interrogation area on turbulent statistics up to 4th order moments in smooth and rough wall turbulent flows”, Experimental Thermal and Fluid Science, 32(3), 725-747, 2008.

Shao, W., and Agelin-Chaab, M., “Turbulent flows over forward facing steps with surface roughness”. Journal of Fluids Engineering, 138(2), 021103, 2016.

Sherry, M., Lo Jacono, D., Sheridan, J., “An experimental investigation of the recirculation zone formed downstream of a forward facing step”, Journal of Wind Engineering and Industrial Aerodynamics, 98, 888–894, 2010.

Shinneeb, A.M., Bugg, J.D., and Balachandar, R., “Quantitative investigation of vortical structures in the near-exit region of an axisymmetric turbulent jet”, Journal of Turbulence, 9, 1–20, 2008.

Shu, Z.R., and Lia, Q.S., “An experimental investigation of surface pressures in separated and reattaching flows: effects of freestream turbulence and leading edge geometry”, Journal of Wind Engineering & Industrial Aerodynamics, 165, 58–66, 2017.

Simpson, R.L., “Turbulent boundary-layer separation”, Annual Review of Fluid Mechanics, 21: 205-234, 1989.

Sirovich, L., “Turbulence and the dynamics of coherent structures. Part 1: Coherent structures”, Quarterly of Applied Mathematics, 45, 561–571, 1987.

Sirovich, L., “Analysis of turbulent flows by means of the empirical eigenfunctions”, Fluid Dynamics Research, 8, 85-100, 1991.

Skare, P.E., Krogstad, P., “A turbulent equilibrium boundary layer near separation”, Journal of Fluid Mechanics, 272, 319-348, 1994.

Smith, R. W. and Smits, A. J., “Effect of Reynolds number on the large structure of turbulent boundary layers”, AIAA Journal, 91-0526, 1994.

Sokolov, M., Hussain, A. K. M. F., Kleis, S. J., Husain, Z. D., “A ‘turbulent spot’ in an axisymmetric free shear layer. Part 1”, Journal of Fluid Mechanics, 28, 65-95, 1980

Song, S., DeGraaff, D. B., Eaton, J. K., “Experimental study of a separating, reattaching, and redeveloping flow over a smoothly contoured ramp”, International Journal of Heat and Fluid Flow, 21, 512–519, 2000.

Song, S., Eaton, J. K., “Reynolds number effects on a turbulent boundary layer with separation, reattachment, and recovery”, Experiments in Fluids, 36, 246–258, 2004.

Sreenivasan, K. R., “Laminarescent, relaminarizing and retransitional Flows”, Acta Mechanica, 44, 1–48 (1982).

Swamy, N. V. C. and Gowda, b. H. L., “Auto-correlation measurements and integral time scales in three-dimensional turbulent boundary layers”, Applied Scientific Research, 35, 265-316, 1979.

Tachie, M.F., Balachandar, R., Bergstrom, D.J., “Open channel boundary layer relaxation behind a forward facing step at low Reynolds number”, Journal of Fluids Engineering, 123, 539-544, 2001.

Tachie, M.F., Bergstrom, D.J., and Balachandar, R., “Rough-wall turbulent boundary layers in shallow open channel flow,” Journal of Fluids Engineering, 122, 533–541, 2000.

Tani, I., Iuchi, M., Komoda, H., “Experimental investigation of flow separation associated with a step, or a groove”, Aeronautical Research Institute, University of Tokyo, Report No. 364, 1961.

Tay, G.F.K., Kuhn, D.C.S., Tachie M.F., “Effects of sedimenting particles on the turbulence structure in a horizontal channel flow”, Physics of Fluids, 27, 025106, 2015.

Taylor, G. I., “The Spectrum of Turbulence”, Proceedings of the Royal Society of London. Series A, Mathematical and Physical Sciences, 164 (919), 476-490, 1938.

Tennekes, H., “Eulerian and Lagrangian time microscales in isotropic turbulence”, Journal of Fluid Mechanics, 67(3), 561-567, 1975.

Thacker, A., Aubrun, S., Leroy, A., and Devinant, P., “Experimental characterization of flow unsteadiness in the centerline plane of an Ahmed body rear slant”, Experiments in Fluids, 54 (3), 1–16, 2013.

Theodorsen, T., “Mechanism of Turbulence”, In: Proceedings of the Second Midwestern Conference of Fluid Mechanics, Ohio State University, 1-18, 1952.

Tinney, C. E., and Ukeiley, L. S., “A study of a 3-D double backward facing step”, Experiments in Fluids, 47(3), 427–438, 2009.

Tomkins, C.D., Adrian, R.J., "Spanwise structure and scale growth in turbulent boundary layers", Journal of Fluid Mechanics, 490, 37–74, 2003.

Volino, R.J., Schultz M.P., Flack, K.A., "Turbulence structure in a boundary layer with two-dimensional roughness", Journal of Fluid Mechanics, 635, 75–101, 2009.

Volino, R.J., Schultz M.P., Flack, K.A., "Turbulence structure in boundary layers over periodic two- and three-dimensional roughness", Journal of Fluid Mechanics, 676, 172–190, 2011.

Volino, R. J., Schultz, M. P., and Flack, K. A., "Turbulence structure in rough- and smooth-wall boundary layers", Journal of Fluid Mechanics, 592, 263-293, 2007.

von Karman, T., "Mechanishe Aehnlichkeit and Turbulenz", Nachr Ges Wiss Göttingen, 58-76, 1930.

Wallace, J.M., "Space–time correlations in turbulent flow: A review", Theoretical & Applied Mechanics Letters, 4, 022003, 2014.

Wallace, J.M., Eckelmann, H., and Brodkey, R. S., "The wall region in turbulent shear flow", Journal of Fluid Mechanics, 54, 39-48, 1972.

Wallace, J.M., Brodkey, R.S., "Reynolds stress and joint probability density distributions in the u-v plane of a turbulent channel flow", Physics of Fluids, 20, 351, 1977.

Weiss, J., Mohammed-Taifour, A., and Schwaab, Q., "Unsteady behavior of a pressure-induced turbulent separation bubble", AIAA Journal, 53(9), 2634-2645, 2015.

Westerweel, J., "Fundamentals of digital particle image velocimetry" Measurement Science and Technology, 8, 1379–1392, 1997.

Wieneke, B., Prevost, R., "DIC uncertainty estimation from statistical analysis of correlation values", Advancement of Optical Methods in Experimental Mechanics, 3, 125–36, 2014.

Wilcox D.C., "Turbulence modeling for CFD", 1st ed. DCW Industries, La Canada, 1993.

Wilhelm, D., Hartel, C., Kleiser, L., "Computational analysis of the two-dimensional–three-dimensional transition in forward-facing step flow", Journal of Fluid Mechanics, 489, 1–27, 2003.

Wu, Y. and Christensen, K. T., "Population trends of spanwise vortices in wall turbulence", Journal of Fluid Mechanics, 568, 55-76, 2006.

Wu Y., and Christensen, K.T., "Spatial structure of a turbulent boundary layer with irregular surface roughness", Journal of Fluid Mechanics, 655, 380-418, 2010.

Wu Y., Ren H., "On the impacts of coarse-scale models of realistic roughness on a forward-facing step turbulent flow", International Journal of Heat and Fluid Flow, 40, 15–31, 2013.

Wygnanski, I., Sokolov, M., and Friedmann, D., “On a turbulent 'spot' in a laminar boundary layer”, Journal of Fluid Mechanics, 78, 785-819, 1976.

Yaghoubi M., Mahmoodi S., “Experimental study of turbulent separated and reattached flow over a finite blunt plate”. Experimental Thermal and Fluid Science, 29, 105–112, 2004.

Yoo, J.Y., Baik, S.J. “Redeveloping turbulent boundary layer in the backward-facing step flow”, Journal of Fluid Engineering, 114, 522- 529, 1992.

Zhou, J., Adrian, R. J., Balachandar, S., Kendall, T. M., “Mechanisms for generating coherent packets of hairpin vortices in channel flow”, Journal of Fluid Mechanics, 387, 353–396, 1999.

Zhao, X., and He, G. W., “Space-time correlations of fluctuating velocities in turbulent shear flows”, Physical Review E, 79, 046316, 2009.

Zhou, Y., and Rubinstein, R., “Sweeping and straining effects in sound generation by high Reynolds number isotropic turbulence”, Physics of Fluids, 8, 647, 1996.

Home | Account Info | Help

Title:	Vortex organization in the outer region of the turbulent boundary layer
Author:	R. J. ADRIAN, C. D. MEINHART, C. D. TOMKINS
Publication:	The Journal of Fluid Mechanics
Publisher:	Cambridge University Press
Date:	Nov 6, 2000

Logged in as:
Ali Nematollahi
LOGOUT

Review Order

Please review the order details and the associated terms and conditions.

No royalties will be charged for this reuse request although you are required to obtain a license and comply with the license terms and conditions. To obtain the license, click the Accept button below.

Licensed Content Publisher	Cambridge University Press
Licensed Content Publication	The Journal of Fluid Mechanics
Licensed Content Title	Vortex organization in the outer region of the turbulent boundary layer
Licensed Content Author	R. J. ADRIAN, C. D. MEINHART, C. D. TOMKINS
Licensed Content Date	Nov 6, 2000
Licensed Content Volume	422
Licensed Content Issue	undefined
Start page	1
End page	54
Type of Use	Dissertation/Thesis
Requestor type	Not-for-profit
Portion	Text extract
Number of pages requested	21
Order reference number	
Territory for reuse	World
Title of your thesis / dissertation	Effects of Upstream Roughness on Turbulent Flow over a Forward Facing Step
Expected completion date	Oct 2018
Estimated size(pages)	200
Attachment	
Requestor Location	108-1000 Markham Rd. 108-1000 Markham Rd. Winnipeg, MB R3T 2M2 Canada Attn: 108-1000 Markham Rd.
Publisher Tax ID	123258667RT0001
Total	0.00 CAD

Edit Order Details
Edit Requestor Location This location may be used to determine your tax liability.

☑ I agree to these terms and conditions.

☑ I understand this license is for reuse only and that no content is provided.

Copyright Clearance Center RightsLink®

Home | Account Info | Help

CAMBRIDGE JOURNALS

Title: Structure of large-scale vortices and unsteady reverse flow in the reattaching zone of a turbulent separation bubble

Author: Masaru Kiya, Kyuro Sasaki

Publication: The Journal of Fluid Mechanics

Publisher: Cambridge University Press

Date: Apr 20, 2006

Logged in as:
Ali Nematollahi
LOGOUT

Review Order

Please review the order details and the associated terms and conditions.

No royalties will be charged for this reuse request although you are required to obtain a license and comply with the license terms and conditions. To obtain the license, click the Accept button below.

Licensed Content Publisher	Cambridge University Press
Licensed Content Publication	The Journal of Fluid Mechanics
Licensed Content Title	Structure of large-scale vortices and unsteady reverse flow in the reattaching zone of a turbulent separation bubble
Licensed Content Author	Masaru Kiya, Kyuro Sasaki
Licensed Content Date	Apr 20, 2006
Licensed Content Volume	154
Licensed Content Issue	undefined
Start page	463
End page	491
Type of Use	Dissertation/Thesis
Requestor type	Not-for-profit
Portion	Text extract
Number of pages requested	473
Order reference number	
Territory for reuse	World
Title of your thesis / dissertation	Effects of Upstream Roughness on Turbulent Flow over a Forward Facing Step
Expected completion date	Oct 2018
Estimated size(pages)	200
Attachment	
Requestor Location	108-1000 Markham Rd. 108-1000 Markham Rd. Winnipeg, MB R3T 2M2 Canada Attn: 108-1000 Markham Rd.
Publisher Tax ID	123258667RT0001
Total	0.00 CAD

Edit Order Details

Edit Requestor Location This location may be used to determine your tax liability.

☑ I agree to these terms and conditions.

Title: Journal of fluids engineering
Article ID: 1528-901X
Publication: Publication1
Publisher: CCC Republication
Date: Jan 1, 1973

Order Completed

Thank you for your order.

This Agreement between Ali Nematollahi ("You") and American Society of Mechanical Engineers ASME ("American Society of Mechanical Engineers ASME") consists of your order details and the terms and conditions provided by American Society of Mechanical Engineers ASME and Copyright Clearance Center.

License number	Reference confirmation email for license number
License date	Apr, 05 2018
Licensed content publisher	American Society of Mechanical Engineers ASME
Licensed content title	Journal of fluids engineering
Licensed content date	Jan 1, 1973
Type of use	Thesis/Dissertation
Requestor type	Academic institution
Format	Print, Electronic
Portion	chart/graph/table/figure
Number of charts/graphs/tables/figures	2
The requesting person/organization	Ali Nematollahi
Title or numeric reference of the portion(s)	Figure 9 (a) Side view of vortices in regime III, Figure 10 (b) Top view of vortices in regime III
Title of the article or chapter the portion is from	Three-Dimensional Vortex Structure in a Leading-Edge Separation Bubble at Moderate Reynolds Numbers
Editor of portion(s)	N/A
Author of portion(s)	Kyuro Sasaki and Masaru Kiya
Volume of serial or monograph	113
Issue, if republishing an article from a serial	3
Page range of portion	408 and 409
Publication date of portion	SEPTEMBER 1991
Rights for	Main product
Duration of use	Life of current edition
Creation of copies for the disabled	no
With minor editing privileges	no
For distribution to	Worldwide
In the following language(s)	Original language of publication
With incidental promotional use	no
Lifetime unit quantity of new product	Up to 499
Title	Effects of Upstream Roughness on Turbulent Flow over a Forward Facing Step
Instructor name	n/a
Institution name	University of Manitoba
Expected presentation date	Oct 2018
Requestor Location	108-1000 Markham Rd. 108-1000 Markham Rd.